UNIVERSITY
OF OSLO

Siri Fløgstad Svensson

MR Elastography of the Brain

In healthy subjects and patients with glioblastoma

Thesis submitted for the degree of Philosophiae Doctor

Department of Physics
Faculty of Mathematics and Natural Sciences

Department of Physics and Computational Radiology
Oslo University Hospital

2023

© Siri Fløgstad Svensson, 2023

Series of dissertations submitted to the
Faculty of Mathematics and Natural Sciences, University of Oslo
No. 2609

ISSN 1501-7710

All rights reserved. No part of this publication may be
reproduced or transmitted, in any form or by any means, without permission.

Cover: UiO.
Print production: Graphic Center, University of Oslo.

Welcome to the detectors with names made of letters: MRI, CT, PET. Earmuffs on, gown on, gown removed, arms up, arms down, breathe in, breathe out, blood drawn, dye injected, wand in, wand on, moving or being moved - radiology turns a person made of feelings and flesh into a patient made of light and shadows. There are quiet technicians, loud clatters, warmed blanket, cinematic beeps.

— *Anne Boyer*
The Undying: A Meditation on Modern Illness

Summary

Magnetic resonance elastography (MRE) is a magnetic resonance technique that enables the noninvasive measurement of the viscoelastic properties of tissue. MRE functions by measuring tissue displacement induced by mechanical vibrations. MRE is an established technique for liver examinations, while the use of MRE in the brain is gaining more interest. MRE may be a powerful tool for understanding brain tumors and for planning brain surgeries. MRE has the potential to help surgeons by providing information about brain tumor heterogeneity before surgery. The contribution of this thesis is therefore to help establish the viability of MRE in the evaluation of brain cancer, in particular glioblastoma.

In the first paper, we test the repeatability of MRE stiffness measurements in healthy subjects. We find a whole-brain coefficient of variation of 4 %. Brain MRE thus appears to be a robust technique. We use two different reconstruction methods to calculate the viscoelastic properties, and find that the choice of reconstruction method affects the stiffness estimates. We therefore recommend normalizing MRE measurements to a reference tissue, such as normal-appearing white matter. For most subjects, the difference in tissue stiffness between the two scans was small, even when the MRE data quality differed between scans. MRE data quality was highest in the part of the brain closest to the skull, and decreased toward the central parts of the brain. However, there were no significant correlations between MRE data quality and the stiffness measurements.

In the second paper, we examine ten patients with glioblastoma using a combination of MRE and perfusion and diffusion MR imaging. We find that mean values of stiffness and viscosity are lower in tumors than in normal-appearing white matter, and lower in necrotic tumor regions than in contrast-enhancing tumor regions. We calculate gradients of all MR measurements. Moving outwards from the tumor core, we find that stiffness, viscosity, perfusion and diffusion parameters approach the values in normal tissue. However, three cm away from the edge of the lesion, several of the patients displayed abnormal measurements, illustrating the infiltrative nature of the disease. We also construct a model of cerebral blood flow as a function of diffusion and MRE parameters and find that the model performs better when both stiffness and viscosity are included. This model reveals that increased perfusion is associated with decreased stiffness and viscosity.

In the third paper, we use MRE in combination with surgical evaluation to further explore the heterogeneity of brain tissue properties. During tumor resection, the operating neurosurgeon extracted tissue biopsies. The surgeon evaluated the tissue stiffness of the biopsies as stiffer, softer, or similar to healthy brain. The same biopsies were also classified by MRE as ‘stiff’ and

'soft' relative to the mean biopsy stiffness in each patient. The surgeon's evaluations did not correlate with MRE stiffness measurements. This suggests that the MRE measurements and the surgeon's measurements describe different properties of the tissue. We also performed RNA sequencing of the biopsies. Gene set enrichment analysis showed that genes upregulated in 'stiff' biopsies were associated with extracellular matrix reorganization and immune processes. Genes upregulated in 'soft' biopsies were mainly associated with normal neuronal function. Dimensionality reduction was used to find genes that separated 'stiff' biopsies from 'soft' biopsies. To further understand the impact on patients of this gene expression, we evaluated the transcriptomic profiles of 265 patients with glioblastoma in two public data sets. Expression patterns of the genes selected by the dimensionality reduction were used to classify the tumors with this gene expression signal and tumors without it. The median survival time of patients with tumors that expressed the gene expression signal associated with 'stiff' biopsies was 100 days shorter than that of patients whose tumors did not express it (360 versus 460 days). The gene expression signal had a significant negative impact on survival also after adjusting for age, sex, and treatment.

In total, these papers deliver three main conclusions. First, MRE is a robust technique for measuring brain tissue stiffness. Second, the biomechanical properties of glioblastoma tumors are heterogeneous and differ from those of healthy tissues. And third, intra-tumor stiffness differences are associated with differences in aggressive behavior: Stiffer biopsies within the tumor were associated with a more aggressive behavior and shorter survival time.

Sammendrag

Magnetisk resonans-elastografi (MRE) er en ikke-invasiv metode for å måle vevets viskoelastiske egenskaper. Hovedprinsippet går ut på å måle vevsforflytning skapt av mekaniske vibrasjoner. MRE er mest brukt i leverundersøkelser, men har de siste årene også være brukt i forskning på hjernen. MRE kan være et nyttig verktøy for å øke forståelsen vår av hjernesvulster og for planlegging av nevrokirurgi. Informasjon om tumorens heterogenitet og hvilke områder som kan være spesielt aggressive, er nyttige for en kirurg å få i forkant av operasjonen. Denne doktorgradsavhandlingen bidrar til å etablere bruken av MRE for hjernekreft, og spesielt i glioblastom.

I vår første artikkel testet vi repeterbarheten i MRE-målingene av friske forsøkspersoner. Variasjonskoeffisienten for stivhetsmålingen i hele hjernen var på 4 %. På bakgrunn av dette konkluderer vi at MRE er en robust teknikk. Vi brukte to ulike rekonstruksjonmetoder til å beregne de viskoelastiske egenskapene til vevet, og fant at stivhetsestimatet avhang av rekonstruksjonsteknikk. Vi anbefaler derfor å normalisere MRE-målinger til et referansevev, som hvit substans. For de fleste forsøkspersonene var det liten forskjell i målt stivhet mellom de to opptakene, også i tilfellene der datakvaliteten på MRE-opptaket varierte mellom opptakene. Datakvaliteten var høyest i de ytre delene av hjernen, nærmest skallen, og falt innover mot midten av hjernen. Vi fant ingen signifikante korrelasjoner mellom MRE-datakvalitet og stivhetmålene.

I den andre artikkelen undersøkte vi ti pasienter med glioblastom med MRE, perfusjons- og diffusjons-MR. Stivhet og viskositet var lavere i svulsten enn i normal hvit substans. Videre var verdiene lavere i nekrotiske svulstområder enn i områdene som ladet kontrast. Vi beregnet gradienter for alle MR-målingene fra svulstkjernen og utover i vevet. Jo lenger ut man kom fra svulstens kjerne, jo mer nærmet målingene av MRE, perfusjon og diffusjon seg verdiene i friskt vev. Tre cm utenfor patologisk vev hadde imidlertid flere pasienter fremdeles abnormale verdier. Dette illustrerer hvor infiltrativ denne krefttypen er. Vi laget også en modell for cerebral blodstrøm som funksjon av MRE, perfusjons- og diffusjonsparametre, og fant at modellen ble bedre av å inkludere stivhet og viskositet. Modellen viste at økt blodstrøm er forbundet med redusert stivhet og viskositet.

I den tredje artikkelen sammenlignet vi MRE med en nevrokirurgs vudering av stivhet for å undersøke heterogeniteten til vevets biomekaniske egenskaper nærmere. Nevrokirurgen tok ut vevsbiopsier under operasjonen hvor svulsten ble fjernet. Han evaluerte biopsiene som stivere, mykere eller like stive som normal hjerne. MRE-målingene ble brukt til å klassifisere biopsiene som «stive» eller «myke», sammenlignet med den gjennomsnittlige målte stivheten for biopsiene for hver pasient. Kirurgens stivhetsevalueringer samsvarte ikke med MRE-

målingene i de samme posisjonene. Dette tyder på at MRE måler noe annet enn det kirurger bedømmer som stivhet under operasjonen. Biopsiene ble i tillegg RNA-sekvensert, og en anrikelseanalyse av dette gensettet viste at oppregulerte gener i «stive» biopsier var assosiert med reorganisering av den ekstracellulære matrisen og immunprosesser. Genene som var oppregulert i «myke» biopsier var stort sett assosiert med normal nevrofunksjon. Dimensjonsreduksjon ble brukt til å finne gener som separerte «stive» fra «myke» biopsier. For å forstå mer om hvilken bertydning disse genene har for pasienter evaluerte vi genuttrykksprofilen til 265 pasienter med glioblastom i to offentlige datasett. Genuttrykket vi fant i dimensjonsreduksjonen ble brukt til å dele pasientene i to: de som hadde høyt uttrykk av disse genene og de med lavt uttryk. Median overlevelse for pasienter som uttrykte genene forbundet med «stive» biopsier var hundre dager kortere enn for pasienter uten disse genene uttrykt (360 versus 460 dager). Uttrykk av disse genene i tumor hadde en signifikant negativ påvirkning på overlevelse også etter justering for alder, kjønn og type behandling.

Fra dette arbeidet trekker jeg tre hovedkonklusjoner. For det første er MRE en robust teknikk for å måle stivhet i hjernen. For det andre er de biomekaniske egenskapene til et glioblastom heterogene og skiller seg fra friskt vev. For det tredje er stive områder innad i svulsten forbundet med høyere aggressivitet og kortere overlevelse.

Acknowledgements

The research presented in this thesis was conducted at the Department for Physics and Computational Radiology, Oslo University Hospital between 2018 and 2022. Funding was provided by the Research Council of Norway (grant 261984), South-Eastern Norway Regional Health Authority (grant 2017073), and the European Research council's Horizon 2020 Framework Programme (project 758657).

This PhD would not have been possible without the contributions of many colleagues:

First and foremost, thank you, Kyrre Eeg Emblem. I could not have asked for a better main supervisor. Your scientific knowledge and experience is a true inspiration. You always have good ideas, you are thorough in your feedback, and a very empathetic and encouraging supervisor and colleague. Whenever I have come into your office with a problem, I have left with a higher spirit and the belief that it could be solved.

Thank you, co-supervisor Sverre Holm. It has great to have someone with which to discuss the technical aspects of elastography. Thank your for your thorough reading, and all of your support.

I am honored to have worked with great co-authors. Elies Fuster-Garcia, you are a brilliant researcher and I have truly enjoyed our collaboration, both in Oslo, and over Skype. Ralph Sinkus, I feel very lucky to have worked so close to a true MRE guru. It is inspiring to see the accomplishments in MRE theory, hardware, and software from you and your group in London and Paris. Thank you for sharing your knowledge, and always being friendly and pedagogic. Einar Vik-Mo; some of the most exciting days these last years have been when I joined you in the operating room, watching you operating one of the patients in our study. I am impressed by your skill both as a surgeon and a researcher, and how you combine that with a curious and friendly character. Skarphéðinn Halldórsson, I am very happy to have worked so closely with you on the last paper of this thesis. I have learnt a lot about analyses that I knew nothing about, and hope to do more interdisciplinary science in the future.

To the radiographers at the Intervention center – Grethe, Kenneth, Janne, Jorunn, and Svein Are – it has been great spending time at the MR lab with you. Thank you for teaching me about imaging, being welcoming, and all the coffee! Anna Latysheva, it has been great to work close to a skilful neuroradiologist. You have taught me a lot about glioma imaging, and your work is always thorough and effective.

Thank you, colleagues at the Department of Physics and Computational Radiology for your community during my nine years at the department. Meeting friendly faces for lunches and coffee during the workday is always a highlight.

Many of you have also helped me directly in my work with this thesis, including helping me carry the MRE equipment in and out of my car during the period where we scanned on both Rikshospitalet and Ullevål, with only one MRE setup. Thanks to Robin and Gunnhild for a great collaboration on setting up MRE on a new scanner, and for filling in for me while I was on maternity leave. The section of MRI physics is a very nice and competent group, and it has been great to be able to stick my head inside all of your offices whenever a technical MRI question needed answering. A special thanks to Atle Bjørnerud for your help with nordicICE throughout the years. Trine Hjørnevik, thank you for help with the survival analysis. To my PhD colleagues Ivar Thokle Hovden and Elisabeth Kirkeby Lysvik, I have appreciated being in the same boat as you while figuring out MRI, coding and PhD life in general.

An enjoyable part of this work was to be at the MR lab on my own, scanning healthy subjects for the first papers. I am thankful toward all volunteers that were scanned, and through some trial and error helped me make the scan run more smoothly when we started examining patients.

I am thankful that I had the opportunity to work close to the patients with glioblastoma whose images we base our research on. I have been impressed and humbled by the individuals who, facing such a dire diagnosis, agree to participate in research and spend more time in the MR scanner than they already need to. Meeting the people in question has made this work even more meaningful.

There have also been frustrating times, where things didn't work or I was stuck. On those days, it has been a relief and joy to meet great friends for a beer and discussions about life, politics or philosophy.

My family is always there for me. Eva and Sveinung, thank you for everything you have given me and for showing me which things in life are important. My dear sister Åshild, I am happy to have been living so close with you for these years. During everything that has been going on, you are the kindest and have always supported me.

Thank you to Monica and Allen Joslin for your kind support during these years.

Lastly, I wish to thank my partner Knut-Eric for all love and support. You have been there for me all the way: you have laid in the scanner, you have helped me with statistics, you have corrected my English. It is always a joy coming home to you and to Ragnar.

Siri Fløgstad Svensson
Oslo, December 2022

Contents

Summary iii

Sammendrag v

Acknowledgements vii

Contents ix

List of Papers xiii

List of Figures xiv

Acronyms xv

1 Introduction 1

2 Background 3
- 2.1 Magnetic resonance imaging . . . 3
  - 2.1.1 The MRI technique . . . 3
  - 2.1.2 Perfusion imaging . . . 5
  - 2.1.3 Diffusion-weighted imaging . . . 6
- 2.2 MR elastography . . . 7
  - 2.2.1 The MRE technique . . . 7
  - 2.2.2 Tissue displacement . . . 8
  - 2.2.3 Imaging the tissue displacement . . . 9
  - 2.2.4 Conversion into biomechanics . . . 11
  - 2.2.5 Measured values . . . 12
  - 2.2.6 Frequency dependency . . . 12
  - 2.2.7 MRE of the brain . . . 12
- 2.3 Glioblastoma . . . 13
  - 2.3.1 Standard MRI of GBM . . . 14
  - 2.3.2 Biomechanics in glioma . . . 16

3 Aims 19
- 3.1 Paper I . . . 19
- 3.2 Paper II . . . 19
- 3.3 Paper III . . . 19

4 Material and methods 21
- 4.1 Study design and population . . . 21

4.2 Ethical approval . . . 21
4.3 MRI protocol . . . 22
4.3.1 MRE acquisition . . . 22
4.3.2 Other MRI sequences . . . 23
4.4 Image processing . . . 24
4.4.1 MRE analysis . . . 24
4.4.2 Image processing, other sequences . . . 25
4.4.3 Regions of interest used in analysis . . . 26
4.5 Biopsy extraction, Paper III . . . 28
4.6 RNA sequencing, Paper III . . . 29
4.7 External patient data sets, Paper III . . . 29
4.8 Statistical analysis . . . 29

5 Summary of papers 33
5.1 Paper I . . . 33
5.2 Paper II . . . 33
5.3 Paper III . . . 37

6 Discussion 41
6.1 Robustness of brain MRE . . . 41
6.1.1 Repeatability . . . 41
6.1.2 The effect of different reconstruction methods . . . 43
6.1.3 MRE data quality . . . 44
6.2 MRE of the healthy brain . . . 46
6.3 MRE of GBM . . . 48
6.3.1 Relationship between biomechanical and functional parameters . . . 49
6.3.2 The peritumoral zone . . . 50
6.3.3 Tumor heterogeneity . . . 50
6.4 Understanding (more of) GBM stiffness . . . 51
6.4.1 The surgeon's evaluation of stiffness . . . 52
6.4.2 Microscopic stiffness measurements . . . 54
6.4.3 Genetical meaning of MRE signal . . . 55
6.5 The potential gain of MRE in GBM . . . 56
6.6 Technical considerations and limitations of MRE . . . 57
6.6.1 Frequency dependency . . . 58
6.6.2 MRE parameters . . . 58
6.6.3 Anisotropy . . . 59
6.7 Limitations in our work . . . 60

7 Conclusion and future perspectives 63
7.1 Conclusions . . . 63
7.2 Future perspectives . . . 63

Bibliography 65

Papers **84**

I Robustness of MR elastography in the healthy brain: Repeatability, reliability, and effect of different reconstructions **85**

II Decreased tissue stiffness in glioblastoma by MR elastography is associated with increased cerebral blood flow **99**

III MR elastography identifies regions of extracellular matrix reorganization associated with shorter survival in glioblastoma patients **113**

Appendices **137**

A Supplementary material Paper II **139**

B Supplementary material Paper III **143**

List of Papers

I

Robustness of MR elastography in the healthy brain: Repeatability, reliability, and effect of different reconstruction methods. S.F. Svensson, J. De Arcos, O.I. Darwish, J. Fraser-Green, T.H. Storås, S. Holm, E.O. Vik-Mo, R. Sinkus and K.E. Emblem. In: *Journal of Magnetic Resonance Imaging.* Vol. 53, no. 5 (2021), pp. 1510-1521 DOI: 10.1002/jmri.27475.

II

Decreased tissue stiffness in glioblastoma by MR elastography is associated with increased cerebral blood flow. S.F. Svensson, E. Fuster-Garcia, A. Latysheva, J. Fraser-Green, W. Nordhøy, O.I. Darwish, I.T. Hovden, S. Holm, E.O. Vik-Mo, R. Sinkus and K.E. Emblem. In: *European Journal of Radiology.* Vol. 147, article 110136 (2022), DOI: 10.1016/j.ejrad.2021.110136.

III

MR elastography identifies regions of extracellular matrix reorganization associated with shorter survival in glioblastoma patients. S.F. Svensson*, S. Halldórsson*, A. Latysheva, E. Fuster-Garcia, T. Hjørnevik, J. Fraser-Green, R.A.B Bugge, J. Grinband, S. Holm, E.O. Vik-Mo, R. Sinkus and K.E. Emblem. *Submitted for publication. *Shared first-authorship* DOI: 10.1101/2022.11.07.22282021.

Both published papers are open access articles distributed under the terms of the Creative Commons CC-BY license, which permits unrestricted use, distribution, and reproduction in any medium, provided the original work is properly cited. The third paper, which has not yet been peer-reviewed, is published on Medrxiv, an online archive and distribution server for unpublished manuscripts in the medical, clinical, and related health sciences.

List of Figures

2.1 T1- and T2-weighted images 5
2.2 MRE workflow 8
2.3 MRE pulse sequence diagram 9
2.4 MRE magnitude, phase and elastograms 11
2.5 MR images of GBM 15

4.1 The transducer 23
4.2 Regions of interest 26
4.3 Location of tissue biopsy 28

5.1 Results Paper I 34
5.2 Results Paper II, Peritumor gradients 36
5.3 Results Paper III, Biopsy example 37
5.4 Results Paper III, Gene set enrichment analysis 38

Symbols and acronyms

$\mathbf{G}''$ Shear loss modulus ('viscosity')

$\mathbf{G}'$ Shear storage modulus ('stiffness')

ϕ Shear phase angle

$|\mathbf{G}^*|$ Magnitude of shear modulus ('stiffness')

ADC Apparent diffusion coefficient

AFM Atomic force microscopy

ASL Arterial spin labelling

CBF Cerebral blood flow

CBV Cerebral blood volume

CE-T1w Contrast-enhanced T1-weighted

CPTAC Clinical proteomic tumor analysis consortium

CV Coefficient of variation

DSC Dynamic susceptibility contrast

DTI Diffusion tensor imaging

ECM Extracellular matrix

EPI Echo-planar imaging

FA Fractional anisotropy

FEM Finite element method

FLAIR Fluid-attenuated inversion recovery

GBM Glioblastoma

GRE Gradient echo

ICC Intraclass correlation coefficient

IDH Isocitrate dehydrogenase

MEG Motion-encoding gradient

MRE Magnetic resonance elastography

MRI Magnetic resonance imaging

NAWM Normal-appearing white matter

PCA Principal component analysis

PLS-DA Partial least-squares differential analysis

RC Repeatability coefficient

RF Radiofrequency

RNA Ribonucleic acid

ROI Region of interest

SE Spin echo

TCGA The cancer genome atlas

TE Echo time

TR Repetition time

VAI Vessel architecture imaging

Chapter 1

Introduction

Glioblastoma (GBM) is the most aggressive type of brain tumor. Even with standard treatment that includes surgery, radiation therapy, and chemotherapy, the median survival time is only 12-15 months [1]. Tumors of this type have been extensively studied in the pursuit of new treatment strategies.

Magnetic resonance imaging (MRI) is an invaluable tool for examining the biology of tumors. MRI is used to guide the diagnosis and treatment of cancer, determine response to therapy, and monitor recurrence. Advanced MRI techniques can provide functional information about the tumor, such as its blood supply and cellularity.

During the progress of cancer, the biomechanical properties of tissue may change. A familiar example is breast cancer. The discovery of a a hard lump in previously soft tissue might indicate a tumor. A physician can evaluate solid tumors in other parts of the body using her fingers. This technique is called palpation and has been used in medical practice since at least Hippocrates (ca. 460–370 BCE) [2]. Palpation has been shown to contribute significantly to breast cancer detection [3].

However, palpation is subjective, not quantifiable, and not always possible to perform. The brain, for instance, is encapsulated by the skull, and manual probing is only possible during surgery.

The benefit of magnetic resonance elastography (MRE) is that the biomechanical properties of tissue can be quantified noninvasively and *in vivo* [4]. By placing a vibrating device on the patient's head while in the MR scanner, it is possible to image the displacement of the tissue as a shear wave traverses the brain. Such a wave travels faster in stiffer tissue than in soft tissue. This enables the acquisition of stiffness maps.

In this thesis, I use MRE to explore the biomechanical properties of tumors. Together with my co-authors, I performed MRE in both the healthy brain and in patients with GBM. Here, I present results regarding the robustness of the technique, and discuss practical aspects of performing MRE successfully. We explore heterogeneity of biomechanical properties of the tumor, and how biomechanics relate to tissue function. Finally, we study the molecular mechanisms involved in GBM stiffness, and explore the potential implications for the patients.

Chapter 2

Background

2.1 Magnetic resonance imaging

2.1.1 The MRI technique

The MRI technique has substantially enriched our knowledge of brain anatomy and physiology, and is an indispensable tool for diagnosing pathology. This technique exploits a quantum mechanical property of nuclei in our bodies, namely their spin. Briefly explained, particles with nonzero spins have a magnetic moment, and can absorb and re-emit electromagnetic radiation by interaction with a magnetic field [5, 6]. These interactions can take place at the resonance frequency of the particle $\omega_0 = \gamma B_0$, called the Larmor frequency. The Larmor frequency is proportional to the magnitude of the magnetic field $\mathbf{B_0}$, and the gyromagnetic ratio, a constant which for protons is $\gamma = 2\pi \cdot 42.6 \cdot 10^6$ Hertz/Tesla. This nuclear magnetic resonance forms the basis for MRI.

There are several nuclei with nonzero spins in the body, but the hydrogen atom is by far the most abundant. The hydrogen nucleus, which consists of a single proton, is the basis for the signal predominantly used in MRI. On the proton level, a complete description of the interaction between the particle and the magnetic field requires quantum mechanics. However, when a large number of protons is considered, their net magnetization is well explained by classical physics. When placed in a strong magnetic field $\mathbf{B_0}$, the proton magnetic moment will either be aligned with $\mathbf{B_0}$ or pointing in the opposite direction of $\mathbf{B_0}$. More protons will be in the low-energy state, parallel to $\mathbf{B_0}$, than pointing in the opposite direction, causing a net magnetization along $\mathbf{B_0}$. We denote this sum of the individual proton magnetic moments the macroscopic magnetization $\mathbf{M}$. The behavior of the macroscopic magnetization vector as a result of magnetic interactions is described classically by the Bloch equation: $d\mathbf{M}/dt = \gamma(\mathbf{M} \times \mathbf{B})$.

The Bloch equation states that the rate of change in $\mathbf{M}$ is perpendicular to the magnetic field $\mathbf{B}$ and $\mathbf{M}$, and hence describes the precession of $\mathbf{M}$ around $\mathbf{B}$. We let the direction of $\mathbf{B_0}$ be the z-direction of our coordinate system. When in equilibrium, the net magnetization $\mathbf{M}$ will be equal to M_z, pointing along $\mathbf{B_0}$, as the M_x- and M_y-components average out.

In order to detect an MR signal, the magnetization needs to be excited from its equilibrium state. By generating a smaller, transient magnetic field $\mathbf{B_1}$ near the Larmor frequency, $\mathbf{M}$ is excited to precess around $\mathbf{B_1}$ temporarily. The component of $\mathbf{M}$ in the xy-plane, M_{xy}, will be detected as an oscillation in $\mathbf{M}$, and such a change in magnetization can be detected as a current in a coil.

The applied $\mathbf{B_1}$ field is in the radiofrequency range (RF) and commonly called an RF pulse. After the application of such an RF pulse, the net magnetization will gradually return to the equilibrium state. The following signal decay is due

to proton relaxation processes. These cause the longitudinal component M_z to recover with a time constant T1. In the xy-plane, the spins will quickly dephase, so the M_{xy} signal disappears with a shorter time constant T2. T1 and T2 are the characteristic relaxation times and are a product of the molecular structure of the tissue. Different relaxation patterns in different tissues provide the basis for the ability of MRI to differentiate between tissue types, such as as water and fat.

In MRI, a long train of RF pulses is applied in what is called a pulse sequence, and the signal is built up from what happens to the magnetization between the pulses before the readout of the signal. In order to spatially encode the emitted signal, magnetic gradients are applied in all three spatial directions. By varying the magnetic field along a direction, the Larmor frequency becomes a function of position along that axis, making it possible to excite specific volumes only. The reemitted radiation can then be traced back based on the emitted frequency.

A pulse sequence is a combination of RF pulses and gradients in order to obtain images with different contrast. The interval between the RF pulses is called the repetition time (TR). The echo time (TE) is the time between the excitation pulse and the readout of the signal in the receiver coil. In general terms, TR determines how much longitudinal magnetization recovers between excitation and TE determines how much T2 relaxation that occurs before signal readout. Hence, by adjusting TR and TE one can tune the T1- and T2-weighting of an image. T1- and T2-weighted images, shown in Figure 2.1, are the most important anatomical brain images.

There are many pulse sequences available, but two basic sequences are called spin echo and gradient echo. In a spin-echo sequence, the RF pulse flips the magnetization $\mathbf{M}$ by 90°, resulting in the full magnetization in the xy-plane. As mentioned, the spins rotating in the xy-plane will soon be dephased, but by applying another RF pulse, this one rotating the spins $\mathbf{M}$ by 180°, the spins will rotate into phase again. At the moment they are all in phase again, we obtain a maximal signal. We refer to this as an echo.

An alternative way of producing an echo is to use gradients. By turning on a gradient, the spins will experience slightly different magnetic fields and the dephasing is accelerated. By turning on a rephasing gradient with the same strength and opposite polarity, the dephasing is reversed, resulting in an echo.

Gradients can also be used to make the MR sequence sensitive to spins in motion, as gradients have a different effect on the MR signal of moving spins relative to stationary spins. This is utilized in diffusion imaging and in MRE, as will be described in following sections.

The readout of the MRI signal is a vast topic. Briefly, MRI is a time-consuming image modality, and various tactics are used to speed up scan times. Echo-planar imaging (EPI) is a common readout method when rapid imaging is required. EPI can accelerate the data encoding severalfold [7].

Readers who are interested in the details of the physics of MRI should dig deeper in textbooks written on the topic [8, 9]. In addition to imaging anatomy, MRI can provide information on brain function. In the next sections, I will

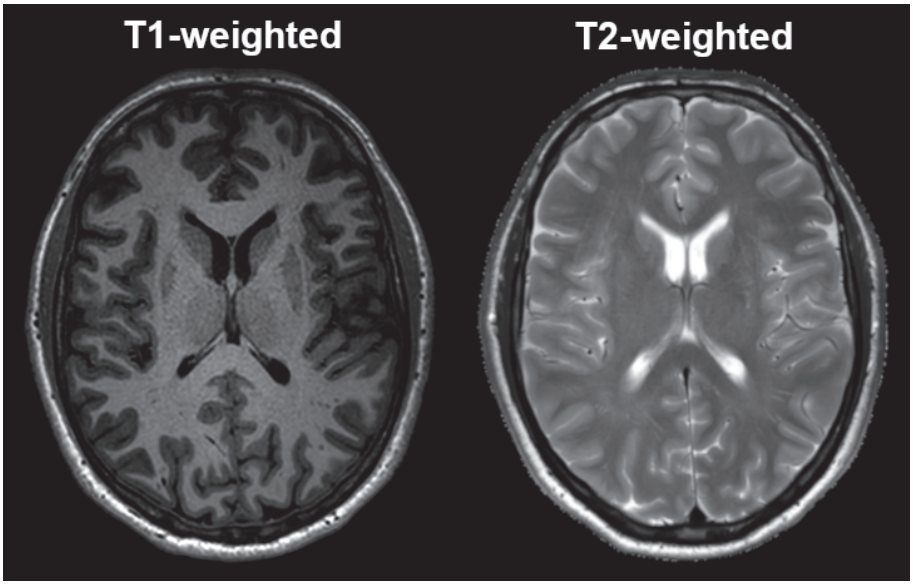

Figure 2.1: Example of T1-weighted (left) and T2-weighted (right) images. T1-weighted images are taken with short TR and TE, in this case 5.2 and 2.3 ms, respectively. On T1-weighted images, gray matter is darker than white matter, and cerebrospinal fluid is completely dark. T2-weighted images are taken with long TR and TE, in this case 3000 and 80 ms, respectively. On T2-weighted images, gray matter is brighter than white matter, and cerebrospinal fluid is very bright. Here, the T2-weighted image has a higher in-plane resolution than the T1-weighted image.

describe methods used in the subsequent papers that provide specific information about brain tissue function.

2.1.2 Perfusion imaging

Perfusion is the process by which blood delivers nutrients and oxygen to the tissue. There are several perfusion MRI methods that measure tissue blood flow and other perfusion-related parameters from MR images [10]. In the diagnosis of brain cancer, dynamic susceptibility contrast (DSC) may be used, utilizing intravenous injection of a contrast agent. An alternative noninvasive method that does not require any injection is arterial spin labeling (ASL). Both methods are briefly described below.

2.1.2.1 Dynamic susceptibility contrast

Due to inhomogeneities in the magnetic field experienced by the protons, different protons experience different Larmor frequencies. The phase coherence in the xy-plane is therefore lost in a time even shorter than T2. This effect gives rise to T2* relaxation, which is faster than T2 relaxation. This signal loss can be taken advantage of by using a paramagnetic contrast agent. When such an agent is injected intravenously and passes through the blood vessels, the magnetic field

experienced by the surrounding spins will vary, accelerating the dephasing of spins. The resulting signal drop can be measured by successive MR acquisitions during a rapid injection of the contrast agent.

By analysing the signal intensity change in the brain over time, one can derive maps of cerebral blood volume (CBV), cerebral blood flow (CBF) and the average time it takes the contrast agent to pass through the image voxel of interest (mean transit time) [11]. DSC usually uses EPI readout for fast imaging, and it is recommended using a gradient-echo sequence because of higher signal-to-noise ratio [12].

More advanced versions of DSC have been developed, in which both gradient and spin echoes are acquired during the bolus passage. The signal responses of the two sequences differ depending on underlying microvascular properties of the tissue, due to different sensitivity to susceptibility variations. Vessel size estimations can be performed utilizing the variation in spin and gradient echo signal dependency on vessel size [13]. There is also a temporal shift between the peaks of the contrast concentration-time curve in the tissue, and further analysis of this time shift can provide information about vessel type and function [14].

2.1.2.2 Arterial spin labeling

ASL can provide perfusion images without the injection of a exogeneous contrast agent. Instead, protons in the blood are used as an endogeneous, diffusible tracer. In pseudo-continuous ASL used in our work, RF pulses are used to excite the blood as it passes through the arteries of the neck [15]. After a delay to allow for the labeled blood to flow into the brain tissue, labeled images of the brain are acquired, containing signal both from spins that were labeled and static spins in the brain tissue. Separate control images are also acquired without prior labeling of the arterial spins. The signal difference between the control and labeled images provides a measure of labeled blood from arteries delivered to the tissue by perfusion [15]. By also acquiring proton density images, the signal intensities can be scaled to quantify CBF [15]. ASL thus produces maps of CBF measured in ml/100 g/min.

2.1.3 Diffusion-weighted imaging

Diffusion-weighted imaging sequences are sensitive to the intrinsic random thermal movement of water in tissue. To measure the rate of water movement along one direction, an RF pulse is applied, flipping the spins 90°. Then a strong gradient along the direction in question is applied for a short amount of time before a 180° refocusing pulse is applied. By reapplying the short, strong gradient, the sum of these gradients will be zero for voxels containing nonmoving water. For such a voxel, the resultant signal intensity is the same as it would be without the gradients. Water molecules that move along said direction are subjected to the two gradients at different locations, and they no longer cancel each other out. Faster-moving spins undergo a larger dephasing compared to

stationary spins. For a voxel containing moving spins, the signal intensity is decreased by an amount related to the rate of diffusion [16].

Diffusion weighting of images can be adjusted by varying the strength, duration, and spacing of the gradients. When these measurements are made with gradients along at least six directions, diffusion tensor imaging (DTI) can be performed, which also provides information on tissue water anisotropy [17]. Resulting maps from DTI are of apparent diffusion coefficient (ADC) and of the fractional anisotropy (FA).

2.2 MR elastography

The most common clinical application of elastography is to evaluate chronic liver disease. Chronic liver disease often features progressive hepatic fibrosis with the possible development of cirrhosis, liver failure or cancer [18]. Staging the fibrosis is important in order to find appropriate treatment. Liver biopsy is considered the gold standard for assessing liver fibrosis, but noninvasive techniques for detecting and staging the fibrosis are in demand [18]. Elastography was first developed using ultrasound technology, and ultrasound elastography has been widely used to detect liver fibrosis [19]. Ultrasound elastography is fast to perform and inexpensive. However, the published literature generally indicates that MRE has a higher diagnostic performance in assessing hepatic fibrosis, fewer technical failures, in addition to covering a larger volume [20]. According to the American College of Radiology, MRE is currently the most accurate imaging modality for the diagnosis and staging of hepatic fibrosis, and the technique has been approved by the American Food and Drug Administration for liver fibrosis grading [18, 21].

2.2.1 The MRE technique

In addition to the liver, MRE has been used in the brain, the heart, skeletal muscle, the breast and other organs, but the use has so far been for research purposes [22]. From here the text will focus on MRE in the brain, which is the topic of this thesis.

The main idea behind MRE is to cause a shear wave to travel through brain tissue. Stated simply, this wave will propagate more quickly through a stiff material than a soft material and hence make it possible to assess the stiffness of the tissue. Technically, MRE is performed by combining three elements: The first step is to cause displacement of the brain tissue (Figure 2.2A). This is usually performed by placing a vibrational device beneath on the patient's head. The vibration causes shear waves to pass through the tissue, displacing the tissue on a micrometer scale [23]. Next, the tissue displacement is imaged using a modified phase-contrast MRI sequence with motion-encoding gradients (MEGs) in synchronization with the vibration [24] (Figure 2.2B). Finally, inversion algorithms are used to calculate the shear modulus from the tissue displacements [25]. The resulting viscoelastic maps are known as elastograms (Figure 2.2C).

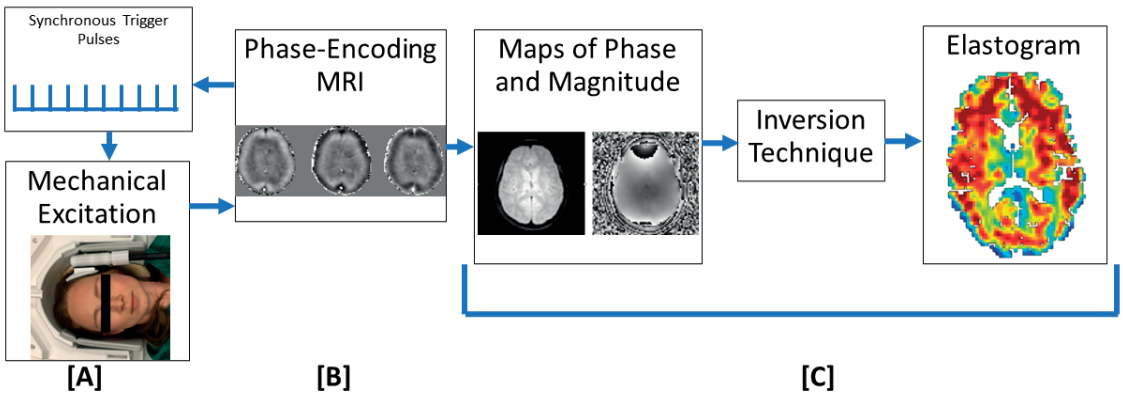

Figure 2.2: Workflow of MRE used in our studies: A mechanical vibration of brain tissue [A] synchronized to an MR phase-encoding sequence [B] causes a shear wave to pass through the brain tissue. This produces maps of phase and magnitude. These are the input in reconstruction algorithm which ultimately produce elastograms [C].

All three steps can be performed in different ways, and will be described in the next sections.

2.2.2 Tissue displacement

The first step in elastography is to apply a stress to deform the tissue of interest. This deformation can be static or dynamic and has been performed using internal sources such as heart motion or pulsation of blood vessels. More commonly, the deformation is caused by an external mechanical source, where the timing can be controlled and the displacement is larger. Various external vibration sources have been used to produce low-frequency shear waves, including electromechanical voice coils, piezoelectric bending elements, and pneumatically powered actuators [26].

In brain MRE, the vibrational device, commonly called a transducer, is placed underneath or on the side of the patient's head, causing harmonic vibrations to be transmitted through the skull. Compressional waves from the vibration are converted into shear waves when passing the tissue interface, causing tissue displacement from both compressional and shear waves.

The frequency of the vibrations used in the brain is typically between 20 and 60 Hz, with a small vibration amplitude on the order of 100 μm or less. The choice of vibration frequency is a balance between resolution and penetration: Lower frequency waves attenuate less rapidly than higher frequency waves, but high frequency waves, having a shorter wavelength, can in theory provide higher spatial resolution [23].

The tissue displacement caused by the shear waves is well within the safety limits set by the occupational safety standards of the European Union [27]. The vibration typically lasts between five and ten minutes.

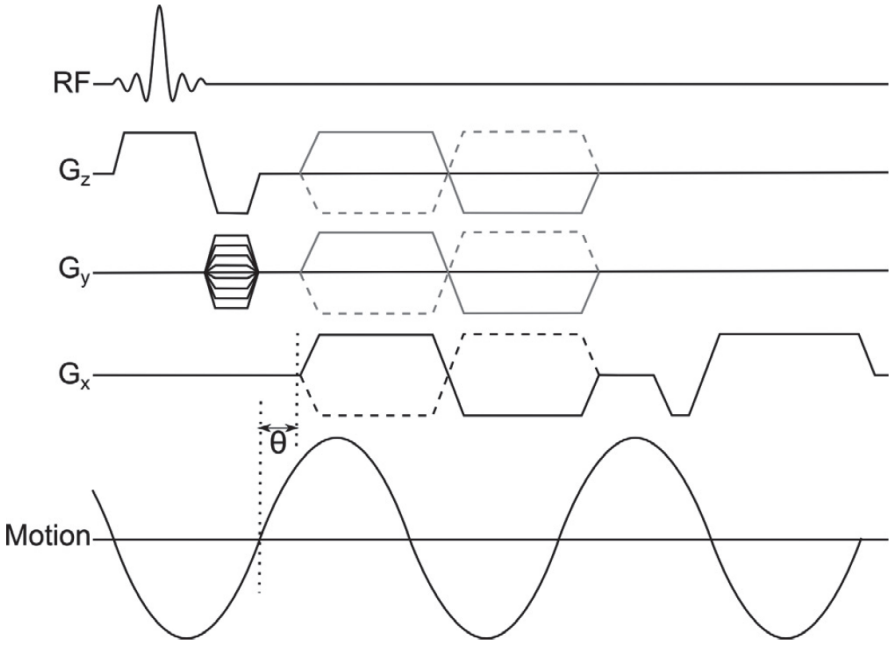

Figure 2.3: Pulse sequence diagram for a gradient-echo MRE pulse sequence. The diagram shows the RF pulse, and spatial encoding gradients in the x, y- and z-direction. Sensitivity to tissue motion is achieved by adding bipolar MEGs that are synchronized to the applied motion in the x-, y-, and z-directions. The positive (solid line) and negative (dotted line) MEGs are used for phase-contrast imaging. A temporal relationship between tissue motion and the MEGs is achieved by varying the phase offset θ. Figure from [26], with permission.

2.2.3 Imaging the tissue displacement

As the shear wave moves through the brain, it displaces the brain tissue it passes through on its way. This is analogous to the ripples caused by throwing a stone into a body of water. Whatever is floating on the surface will move up and down as the ripples pass by. In the same way, brain tissue moves synchronously with the mechanical wave that is applied. By synchronizing the MR acquisition and the mechanical vibration, using a trigger signal between the MR scanner and the vibration generator, this displacement can be captured using an MR phase-contrast sensitive technique. By applying a rapidly alternating bipolar MEG with the same frequency as the vibration of the transducer, spins moving due to this displacement will acquire a phase shift compared to stationary spins or spins moving in another way. This way, the tissue motion can be encoded into the phase of the MR signal. Figure 2.3 shows an MRE pulse sequence diagram.

A temporal relationship can be acquired by varying the phase offset θ between the applied shear wave frequency and the oscillating MEGs at three to eight evenly spaced time points. The amplitude of tissue motion is recorded in the

phase of the magnetization by the following equation [28]:

$$\phi(\mathbf{r}, \theta) = \frac{\gamma N T(\mathbf{MEG} \cdot \xi_\mathbf{0})}{2} \cos(\mathbf{k} \cdot \mathbf{r} + \theta) \tag{2.1}$$

where $\mathbf{r}$ is the position vector, θ is the phase offset between the applied motion and the MEG, γ is the gyromagnetic ratio of protons in the tissue, N is the number of gradient pairs, and T is the period of the MEG. $\mathbf{MEG}$ is the motion-sensitizing magnetic gradient vector, $\xi_\mathbf{0}$ is the displacement amplitude vector, and $\mathbf{k}$ is the wave vector.

By measuring the phase over a full period of motion ($\theta \in [0, 2\pi]$), the peak phase amplitude can be correlated to the maximum displacement amplitude in the direction of the MEG. The proportionality between the maximum phase and the maximum displacement is therefore $MEG\gamma NT\xi/2$. Since this response is proportional to the number of gradient cycles (N) and the period of the gradient waveform (T), high sensitivity to small amplitude synchronous motion can be achieved by accumulating phase shifts over multiple cycles of mechanical excitation and the motion-sensitizing gradient waveform [29].

Adjusting the phase offset θ between the mechanical excitation and the oscillating magnetic gradient allows the extraction of the harmonic component at the frequency of interest, providing the amplitude and phase of the harmonic displacement at each point in space. This results in a complex displacement field, used as input for the inversion methods described in the next section.

The cyclic MEGs described above can be implemented in many different pulse sequences. Motion can be recorded using modified 2D or 3D, gradient echo, spin echo, EPI, balanced steady-state free precession, spiral, and stimulated echo pulse sequences [22]. To capture three-dimensional motion, MEGs are applied in minimally three orthogonal directions. In order to decouple the phase difference caused by the cyclic motion from the phase effect of inhomogeneities in B_0 and susceptibility effects, a reference scan without motion encoding is typically also acquired [30].

To sum up, the harmonic tissue motion is captured by accumulating phase shifts over multiple cycles of mechanical excitation, with multiple phase offsets θ, and in several motion-encoding directions. The recorded motion - the MRE signal - therefore increases with scan duration. The duration may become lengthy, especially if one wishes to acquire a large brain coverage. As the vibration may over time become intense for the patient, the patient comfort places a limit on the scan resolution, coverage and MRE signal.

When an MR signal is acquired, the signal is a complex number. For all the sequences described in Chapter 2.1, only the magnitude of the signal is of interest. In MRE, however, motion information is stored in the phase image. Hence, in MRE, both the magnitude and phase image are used, shown in Figure 2.4. As the phase ϕ is encoded between $-\pi$ and π, phase wrapping occurs at high MEG amplitudes, where the phase jumps abruptly with $2\pi k$, with k being an integer number. In order to recuperate the true measured phase, phase unwrapping algorithms are applied before the analysis of the data [23].

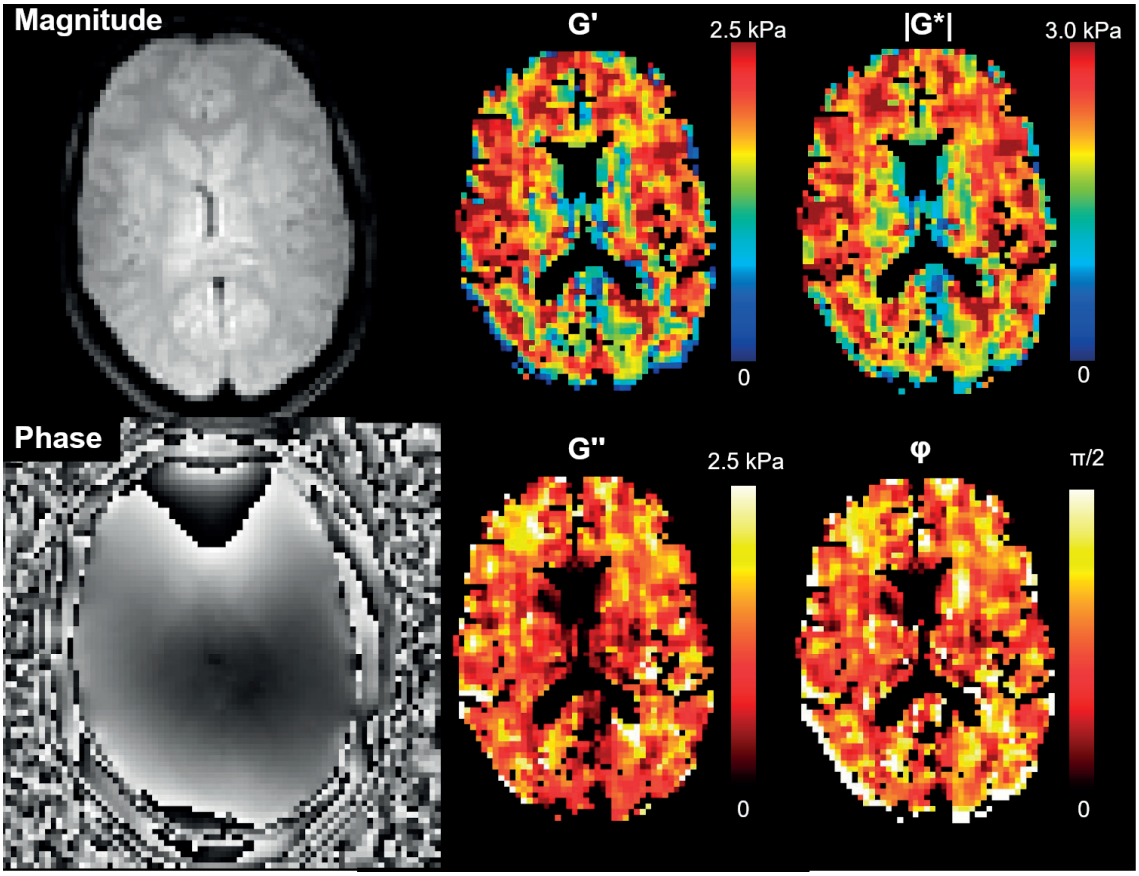

Figure 2.4: MRE input and output. Left: MRE magnitude and phase image of a healthy subject. Middle: Resulting maps of shear storage modulus G' and shear loss modulus G''. Right: Magnitude of shear modulus $|G^*|$ and shear phase angle ϕ.

2.2.4 Conversion into biomechanics

The third step, after deforming the tissue and imaging that displacement, is to translate the measurements into biomechanical properties. The mechanical quantities we wish to characterize are those that relate the strain to stress, and since the displacements in MRE are very small (on the order of micrometers), a linear relationship can be assumed between them [29]. Typically, several physical assumptions are made about the brain tissue: that it can be modeled as an isotropic, linearly viscoelastic, and locally homogeneous material. This results in the following wave equation for the harmonic motion:

$$G\nabla^2\mathbf{u}(f) + (\lambda + G)\nabla(\nabla \cdot \mathbf{u}(f)) = -\rho\omega^2\mathbf{u}(f) \tag{2.2}$$

where G and λ are the two Lamé constants that describe the shear and compressive strain, $\mathbf{u}$ is the vector displacement of the material, ρ is the density of the material (1000 kg/m^3) and $\omega = 2\pi f$, where f is the applied mechanical frequency [26]. MRE reconstruction is considered an inverse problem. The goal of reconstruction is to solve equation 2.2 for G based on the measured

displacement field $\mathbf{u}$.

Compressional waves in soft tissue propagate at high velocities ($\sim$ 1540 m/s) and the velocity does not vary significantly for different tissues. Conversely, shear waves in soft tissue propagate at 1-5 m/s in the MRE frequency range [24]. Their propagation speed can vary significantly across tissues, and therefore shear waves are well suited to characterize tissue.

The large difference in magnitude of λ and G makes it difficult to estimate both parameters simultaneously [29]. The most common techniques to remove the contribution of compressional waves are to apply a spatial high-pass filter to remove the very long wavelengths [29], or to apply the curl operator to equation 2.2 [31]. As the curl of a divergence is zero, this removes the term containing the compressional component λ, at the cost of third-order spatial derivatives.

2.2.5 Measured values

Soft tissue has both elastic and viscous properties. This means that the shear modulus in equation 2.2 is a complex quantity G^*, which can be decomposed into a real and imaginary component: $G^* = G' + iG''$. The real part of the shear modulus, G', is a measure of the mechanical energy stored in the system, and the imaginary component G'' provides a measure of the energy dissipated. G' and G'' may be interpreted by considering a dampened spring with an attached weight. The stiffness (G') of the spring is inversely related to the extension of the spring when the weight is attached. Any decrease in amplitude associated with harmonic motion of the mass will incur energy losses and these losses are related to G'' [32]. G' and G'' are also called the elasticity and the viscosity moduli, respectively.

The viscoelastic properties are commonly reported using G' and G'', both measured in kPa. However, many studies report the magnitude of the shear modulus, $|G^*| = \sqrt{G'^2 + G''^2}$ (also measured in kPa), and the shear phase angle, $\phi = \tan^{-1}(G''/G')$ (measured in radians). Both G' and G'', and $|G^*|$ and ϕ are illustrated for a healthy subject in Figure 2.4.

2.2.6 Frequency dependency

In a purely elastic material, the shear modulus is simply given by the material density ρ and the shear wave speed c: $G = \rho \cdot c^2$. In this case, there is only one wave velocity c for all frequencies. In a viscoelastic material, where the wave is attenuated, the wave speed and the shear modulus becomes a function of frequency [33]. The shear modulus has been reported to be approximately 1/3 higher at 50 Hz than at 25 Hz [34]. Therefore, reported values of G' and G'' measured at a specific frequency are only valid at that frequency.

2.2.7 MRE of the brain

During the last 15 years, MRE has been used to probe the biomechanical properties of the healthy brain and neurological diseases.

Multiple studies in healthy subjects have shown that brain stiffness decreases with age [35–38]. This was first showed in adults, but a recent study found that brain stiffness decreases from early childhood to adulthood as well [39]. Sex differences in viscoelasticity have been reported [35], but later studies have not found an overall effect [36, 38]. Two studies have found sex differences in specific regions of the brain, so a regional sex difference could explain the disharmonious findings between different studies [37, 40].

Several studies have demonstrated the sensitivity of brain stiffness to neurodegeneration. Brain viscoelasticity has been shown to decrease in patients with multiple sclerosis [41–43], Parkinson's disease [44], and dementia [45–48].

A few studies have also examined the relationship by MRE measures and brain function [49, 50]. By performing a series of MRE measurements while a subject performs a visual task, functional MRE links increased local tissue stiffness to neuronal activity [51].

2.3 Glioblastoma

The Global Cancer Observatory database reported that roughly 300,000 patients (1.6 % of all new cancer cases) were diagnosed with a brain tumor in 2018, and 241,000 patients (2.5 % of all cancer deaths) died from this disease [52]. In Norway, there are about 400 new cases annually of cancer in the central nervous system [53]. Despite their relatively low frequency of occurrence compared with other cancers, brain tumors cause a disproportionate amount of morbidity and mortality, partly because of the critical location of the tumor mass [54]. The 5-year survival rates for malignant brain tumors are the third lowest among all types of cancer [55].

The most commonly occurring malignant brain tumor is GBM, which accounts for 14 % of all primary central nervous system tumors [56]. GBMs are the most aggressive of glioma tumors, which arise in the glial cells of the brain. The World Health Organization has categorized gliomas into grade 1-4, with higher grades meaning increasingly aggressive behavior, shorter survival time and more rapid disease progression [57]. The diagnosis is based on histology and molecular characteristics. Astrocytomas and oligodendrogliomas present mutations of isocitrate dehydrogenase (IDH), and oligodendrogliomas are in addition defined by their chromosomal 1p/19q co-deletion. Astrocytomas can be of WHO grade 2,3, or 4, while oligodendrogliomas are of grade 2 or 3. GBMs are IDH-wildtype and WHO grade 4.

GBM is a highly infiltrating tumor, with tumor cells also encountered far from areas displayed as pathological in the images [58]. Therefore, complete surgical resection is impossible. Patient survival increases by maximal possible resection of the visible tumor [59]. However, the surgeon must balance this against maintaining healthy tissue in important functional areas of the brain. Despite removal of all macroscopic disease visible in images and during surgery, the infiltrative nature will eventually cause tumor recurrence.

The current standard treatment for newly diagnosed GBM consists of surgery followed by six weeks of radiation in combination with daily temozolomide chemotherapy, followed by at least six cycles of adjuvant temozolomide [1, 60]. The addition of temozolomide improves overall survival by ∼2.5 months compared with radiation only [1, 60]. MRI is used both for obtaining an initial diagnosis and for assessment of therapy response [61].

Another distinctive feature of GBM is heterogeneity, both between and within tumors [62]. The ultimate goal of cancer research, using imaging as well as molecular and genetic analyses, is to discover new tumor properties that can be targeted for treatment. Although GBMs share histological characteristics, tumors are highly variable from patient to patient on a molecular level [63]. Understanding more of the differences between tumors can hopefully lead to development of treatments that will be effective for subgroups of patients.

Heterogeneity within tumors is believed to be one of the key determinants of therapy failure [62, 64]. Different parts of the tumor may be hypoxic, while others have a more normal oxygen supply. Some regions are very proliferative and infiltrate surrounding tissues, while other regions may be more quiescent [58]. These phenotypic characteristics are accompanied by genotypic differences [65]. GBM tumor cells are inherently plastic and adapt to various microenvironmental factors [66]. In combination with intrinsic genetic alterations and immune response, this results in intratumoral heterogeneity [67]. The molecular properties of a recurrent GBM may differ substantially from the initial tumor due to this plasticity, leading to a temporal heterogeneity as well [63].

While tumor diagnosis is typically based on a small tissue sample from one part of the tumor, imaging has the unique ability to show intratumor heterogeneity.

2.3.1 Standard MRI of GBM

To obtain an initial diagnosis of a suspected brain tumor, recommended MRI includes a T1-weighted sequence before and after injection of a gadolinium-based contrast-agent, a T2-weighted sequence, a fluid-attenuated inversion recovery T2-weighted (FLAIR-T2w) sequence and a diffusion-weighted imaging sequence [68]. Figure 2.5 shows images of a patient with GBM, displaying images from the anatomical sequences, as well as maps from diffusion, perfusion, and MRE imaging.

GBMs appear bright on contrast-enhanced T1-weighted images (Figure 2.5B). This is due to the breakdown of the blood-brain barrier, causing bleeding to appear as contrast-enhancing tumor. There are also necrotic regions in GBM tumors. These appear dark on T1-weighted images. Tumor cells are assumed to exist also outside the contrast-enhancing region, in the so-called peritumoral zone, which is nonenhancing on contrast-enhanced T1-weighted images. In this peritumoral zone, there is usually significant vasogenic edema, which shows a high signal on T2-weighted images (Figure 2.5C).

FLAIR MRI is another important sequence. By utilizing a combination of T1- and T2-weighting, the fluid signal originating from the cerebrospinal fluid

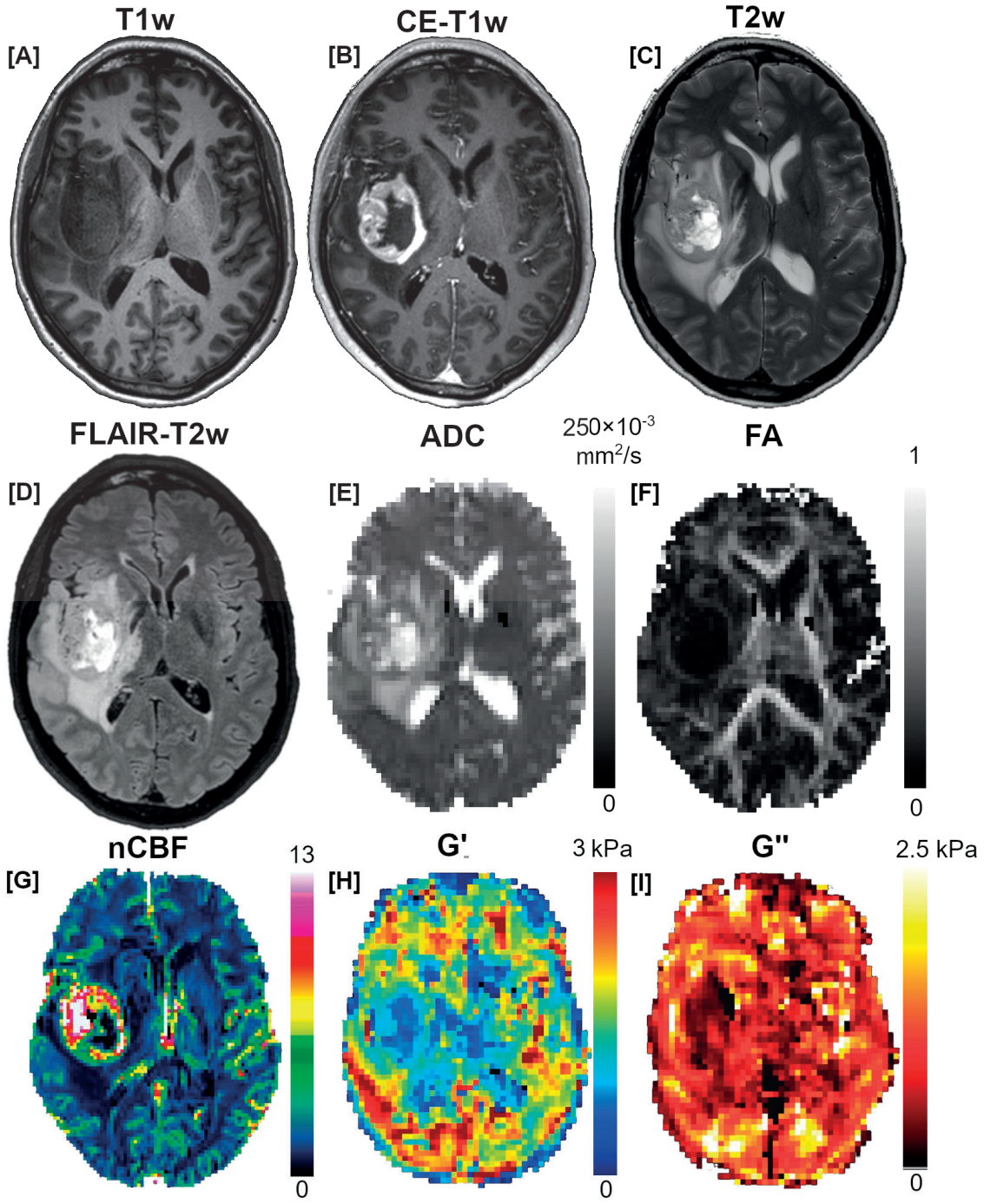

Figure 2.5: MR images of patient with GBM. The tumor is visible as an oval mass on the left side of the images. A) T1-weighted (T1w), B) contrast-enhanced T1-weighted (CE-T1w), C) T2-weighted (T2w), D) fluid-attenuated inversion recovery (FLAIR-T2w), E) apparent diffusion coefficient (ADC), F) fractional anisotropy (FA), G) normalized cerebral blood flow (nCBF), H) shear storage modulus G', I) shear loss modulus G''

is suppressed. FLAIR-T2w MRI allows for visualization of vasogenic edema surrounding the tumor, as well as surgery-induced and radiation-induced gliosis and infiltrating tumor (Figure 2.5D) [68].

The ADC map from diffusion-weighted imaging sheds further light on the tumor characteristics, as ADC normally is inversely related to tissue cellularity. ADC is typically low in tumor regions with high cellularity and high in edematous and necrotic regions where water diffusion is elevated [69], as illustrated in Figure 2.5E. FA can provide information about white matter integrity and dislocation (Figure 2.5F). In addition, white matter tractography obtained from DTI can be useful for planning tumor resection, making it possible to spare eloquent regions [70].

Perfusion MRI is also used in brain tumor imaging. Angiogenesis is a hallmark of aggressive tumors [71]. Newly formed vasculature is highly abnormal and leaky, resulting in contrast agent leakage from the vascular to the extravascular, extracellular space. The new tumor vessels are typically disorganized, highly permeable, and with abnormal blood flow [72]. These changes can be measured by perfusion MRI. Cerebral blood flow maps have been shown to be useful in tumor grading [73–75] and treatment response monitoring [76, 77] (Figure 2.5G).

2.3.2 Biomechanics in glioma

Cancer research has historically mainly focused on genetic and biochemical aspects of tumor progression. Over the last decade, the mechanical tumor microenvironment has received more attention, and physical stimuli have been shown to affect cells as profoundly as biochemical and genetic signals do [78]. The mechanical properties of a GBM tumor and its microenvironment have been shown to contribute to tumor invasion [79].

Previous MRE studies have found gliomas to typically be softer than normal-appearing white matter (NAWM) [80–85]. This is illustrated in Figure 2.5, where both G' and G'' shows lower values in the tumor. In a review of MRE in patients with brain tumors, the softening of gliomas compared to NAWM were calculated across published studies: the mean reduction in stiffness was 17 % in GBM (n = 36), 14 % in WHO grade 3 gliomas (n=5), and 34 % in low-grade gliomas (n = 5) [32]. The average decrease of ϕ compared to NAWM was 30 % in GBMs, 4 % in grade 3 gliomas and 1 % in low-grade gliomas [32].

Most studies of MRE in brain tumors only present average values of stiffness and viscosity for the whole tumor. One study noted that the stiffness maps of GBMs are heterogeneous and composed of stiff and soft compartments. The authors suggest that $|G^*|$ heterogeneity may be attributed to GBMs consisting of both solid masses and possibly cystic and necrotic fractions [81].

So far, no studies using MRE in gliomas have measured the heterogeneity of tumor biomechanics. Furthermore, in the handful of studies of MRE in patients with glioma, none present perfusion or diffusion measurements.

While the importance of biomechanical forces in GBM is gaining attention, the underlying mechanisms are still not well understood, nor their clinical implications. Several methods exist to assess tissue stiffness, but MRE is unique

in allowing measurements of stiffness *in vivo*, with the tumor still within the brain.

Chapter 3

Aims

This thesis uses brain MRE in healthy subjects and patients with GBM to explore the biomechanical properties of the tumor and how the biomechanics relate to tissue function and genetics.

3.1 Paper I

In order to determine true biological changes in tissue stiffness caused by disease, the inherent variation in the measurements must be quantified. The aim of the first study was to assess the repeatability and test-retest reliability of MRE in the healthy human brain, and to evaluate the effect of different reconstruction methods and variation in MRE data quality on stiffness estimates.

3.2 Paper II

The aim of the second study of MRE in patients with GBM and healthy subjects was to map the differences between tumor and healthy tissue with regard to biomechanical and functional properties. The spatial distribution of these properties was examined, and the relationship between biomechanical and functional parameters assessed.

3.3 Paper III

The aim of the third study was to further explore the biomechanical heterogeneity of GBMs. By performing ribonucleic acid (RNA) sequencing of biopsies from different locations within tumors, we examined the genetic mechanisms that govern stiffness within GBM tumors. Further, we explored possible associations between patient outcome and the information obtained from MRE.

Chapter 4

Material and methods

4.1 Study design and population

All three studies in the thesis were prospective studies. For the first study, healthy volunteers were recruited. Persons between 20 and 40 years and without a history of neurological disease were included. For studies II and III, patients were included after being referred to the neurosurgery department at Rikshospitalet, Oslo University Hospital. Preliminary inclusion criteria for patients were suspected new GBM, and the neurosurgeon evaluating the patient as capable of undergoing the MRE examination in addition to their planned preoperative MRI. The final inclusion of patients was done after confirmation of GBM with IDH wild-type diagnosis based on histological and molecular examinations of specimens obtained during tumor resection [57].

In Paper I, 15 healthy subjects were examined, between the ages of 21 and 33 years (median 27 years). Of these, there were six women and nine men. In Paper II, 17 healthy subjects were scanned, between 21 and 34 years, (median 25 years). Of these, there were eight women and nine men. Twelve of the volunteers featured in both Papers I and II. In Paper II, ten patients between 44 and 74 years (median 55 years) were included, five men and five women. In Paper III, thirteen patients between 38 and 75 years (median 56 years) were included, eight women and five men. Eight patients were included in both Paper II and Paper III, as the assessment in the two studies were non-overlapping.

A power analysis with correlated paired means, an estimated mean MRI parameter spread of 20 % between groups, a within-group standard deviation of 15 %, and α=0.05, β=0.20, yields N=10. This suggests the number of subjects included in each study was sufficient, under the assumption that the estimated parameter spread and standard deviation are valid. Varying β between 0.15 and 0.2, and varying the parameter spread within 15 % and 20 %, yielded sample sizes between 8 and 12.

4.2 Ethical approval

All studies were approved by the institutional review board and the Regional Research Ethics Committee, with reference ID 2018/1093 (healthy subjects) and 2017/1875 (patients) before data acquisition. All examinations were performed in accordance with the Helsinki Declaration of ethical principles for medical research involving human subjects [86]. Both patients and volunteers signed an informed consent form for the use of their clinical data for research purposes.

4.3 MRI protocol

4.3.1 MRE acquisition

4.3.1.1 Hardware

We used a mechanical transducer to cause harmonic brain tissue displacement, shown in Figure 4.1. This transducer contains an asymmetric mass which is rotated mechanically. This results in a vibration, which was set to a frequency of 50 Hz [21]. A motor placed in the scanner operating room produces the mechanical rotation, which is then transmitted by a rotating axis inside a cable running through a waveguide to the transducer in the MR scanner.

The motor is controlled by a stepper motor controller that is synchronized to transistor–transistor logic signals sent by the MR system at the start of the slice selection loop. The trigger signals account for lag in the control system and motor. By using microsteps to perform a full turn of the motor, any angular position drift is nulled [21]. The transducer setup, including the motor and the cable, was developed by our collaborating research group in King's College London through the EU Horizon 2020 project H2020-PHC-2014-2015 (Imaging the Force of Cancer, grant number 668039).

The transducer was placed on the side of the subject's head, with cushioning to keep it in place while scanning. To ensure contact between the transducer and the head, the transducer was modified with a curved piece of plastic that lay flush with the side of the subject's head, slightly behind and above the temple. This piece of plastic was 3D-printed to match the average curvature of the human head, and lined with a thin gel pad. The gel pad transmits the compressional waves originating from the transducer without attenuation [21]. The vibrations were well tolerated by all healthy subjects and patients.

4.3.1.2 Image acquisition

MRE image acquisition was performed using a multishot gradient-echo MRE sequence [87]. In MRE, it is common to apply motion-encoding gradients along three orthogonal directions, in addition to a reference scan without motion encoding. An alternative encoding strategy is to encode along the four diagonals of a cube. In that case, a reference scan with simultaneous motion encoding along all three encoding directions is acquired and, in the subsequent three measurements, one gradient direction at a time is inverted. The phase is then decoded by subtraction of the reference from each encoded direction. We used a variant of this method, called Hadamard encoding, with bipolar 13 mT/m MEGs at 115 Hz in four directions [88]. Nineteen slices were scanned, but due to second-order derivatives used in the reconstruction, results are only obtained for slices 3-17, resulting in 15 elastogram slices.

Eight equally distributed wave phases were sampled over one oscillation period at 25 Hz. As some harmonics of vibration frequency appear (see smaller peaks on the right in Figure 4.1), the actual mechanical vibration frequency was shifted to the second index of the Fourier transform, 50 Hz, thereby filtering

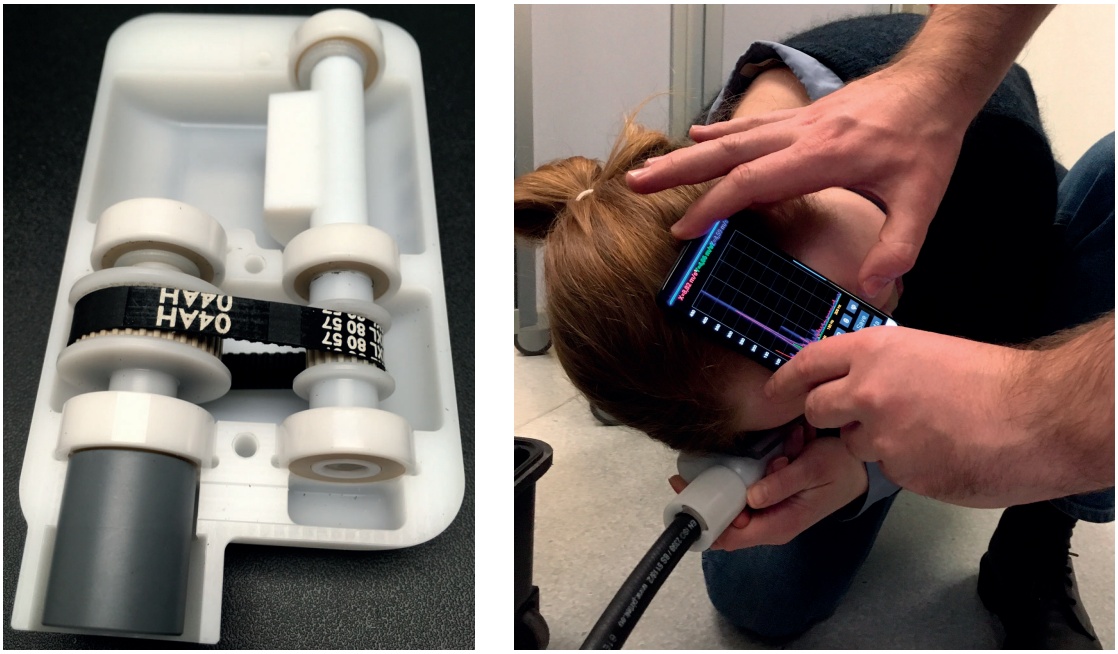

Figure 4.1: The gravitational transducer. Left: The vibration is caused by an asymmetric rotating mass inside the transducer. Right: An accelerometer measuring the frequency on the left side of the head with the transducer vibrating at the right side of the head. The high peak shown in purple is at the applied 50 Hz.

out potential contributions from the 25 Hz, 75 Hz and 100 Hz frequencies. The MRE acquisition lasted 5.5 minutes. In Paper I, two MRE acquisitions were performed, one after the T1-weighted sequence, the other after additional DTI and ASL imaging. For patients, the MRE sequence was performed last, after all preoperative MRI sequences.

4.3.2 Other MRI sequences

A full preoperative MRI protocol was used for the patients included in Paper II and III. At our institution, this includes a T1-weighted sequence, acquired before and after intravenous injection of a gadolinium-based contrast agent (Gadovist, Bayer Pharma AG, Germany), with a dose of 0.1 mmol/kg body weight, followed by a 20 ml flush of saline (BB. Melsungen AG, Melsungen, DE). During contrast injection, 100 dynamic volumes were acquired in a gradient- and spin-echo DSC sequence [89]. In addition, an axial T2-weighted sequence, a 3D FLAIR sequence, and a DTI sequence were acquired (Table 4.1).

For healthy subjects, the same T1-weighted and DTI sequences were used, in addition to an ASL acquisition for perfusion imaging. Proton-density-weighted images were acquired using the same parameters as the ASL images, in order to scale the signal intensities of the subtracted ASL images to absolute CBF units [90].

Sequence	Technique	Resolution (mm^3)	TR/TE (ms)	Used in
T_{2w}	2D Turbo SE	$0.6 \times 0.6 \times 4$	3000/80	Patients
FLAIR	3D Turbo SE	$1 \times 1 \times 1$	4800/320	Patients
DSC	2D GRE/SE-EPI	$1.8 \times 1.8 \times 5$	1500/25(GRE),105(SE)	Patients
T_{1w}	3D IR TFE	$1 \times 1 \times 1$	5.2/2.3	All subjects
DTI	2D SE-EPI	$2.5 \times 2.5 \times 2.5$	9800/60	All subjects
MRE	2D GRE	$3.1 \times 3.1 \times 3.1$	295/12	All subjects
ASL	2D GRE-EPI	$3.6 \times 3.6 \times 5.5$	4400/14.8	Healthy subjects
PD	2D GRE-EPI	$3.6 \times 3.6 \times 5.5$	12000/12	Healthy subjects

Table 4.1: Key scan parameters for patients and healthy subjects. Abbreviations: T_{2w} - T2-weighted image series, SE - spin-echo, FLAIR - fluid-attenuated inversion recovery, DSC - dynamic susceptibility contrast, GRE - gradient-echo, EPI - echo-planar imaging, T_{1w} - T1-weighted image series, IR - inversion recovery, TFE - turbo field echo, DTI - diffusion tensor imaging, MRE - magnetic resonance elastography, ASL - arterial spin labeling, PD - proton-density weighted

4.4 Image processing

4.4.1 MRE analysis

MRE data were reconstructed using dedicated in-house software (ROOT environment, CERN; Meyrin, Switzerland) developed by Ralph Sinkus, our collaborator at King's College London. The MRE phase images were unwrapped by a method based on the mathematical problem of minimum cost flow analysis [91]. Next, pixel-wise Fourier transformation of the data was performed in order to obtain the tissue displacement in the frequency domain, before each component of the complex-valued displacement vector $\mathbf{u}$ was filtered.

As mentioned in the Background chapter, there are several methods used to obtain viscoelastic properties from the displacement data. In Paper I, two of these methods were used and compared, called the curl and the FEM method. Both methods are state-of-the-art reconstruction methods, and have been used in recent scientific work [21, 50, 87, 92]. The first method used in Paper I applies the curl operator on equation 2.2 [31]:

$$\nabla \times (G^* \nabla^2 \mathbf{u}(f) + (\lambda + G^*) \nabla(\nabla \cdot \mathbf{u}(f))) = \nabla \times (-\rho \omega^2 \mathbf{u}(f)) \tag{4.1}$$

As the curl of the divergence is zero, the second term, accounting for the compressional waves, disappears. Equation 2.2 then simplifies to the Helmholtz equation:

$$G^* = \frac{-\rho\omega(\nabla \times \mathbf{u})}{\nabla^2(\nabla \times \mathbf{u})} \tag{4.2}$$

This equation is then solved for G^* by least-squares polynomial fitting [93].

The second method used in Paper I is a finite-element method, here referred to as FEM reconstruction. Details are thoroughly described elsewhere [94]. Briefly, the method computes a value for G^* at every voxel of the wave image data using a moving local finite-element mesh and assuming that G^* is locally homogeneous. Data leading to negative shear modulus values are removed, and a weighted averaging of the shear modulus based on residual error is also

performed. In this case, only first-order spatial derivatives are required since no curl operator is applied.

In Papers II and III, a variation of the curl method was used: The data was filtered in Fourier space using a 11^{th} order Blackman-Harris filter [95] before the curl operator was applied in the image space. The final choice of reconstruction method to be used in patients was based on the recommendation of the developer of the reconstruction methods, deeming the curl method more robust [31]. The MRE analysis resulted in maps of the shear storage modulus G', the shear loss modulus G'', the magnitude of the shear modulus $|G^*|$ and the shear phase angle ϕ.

After reconstruction of MRE maps, further image analysis as described below was performed using Matlab (version R2021a, MathWorks, Natick, MA, USA).

In Paper I, MRE data quality was assessed by the shear-compression wave ratio, meaning the ratio between the amplitude of the curl and the amplitude of the divergence of the displacement data. This ratio quantifies the signal (curl) to noise (divergence) since the divergence of the displacement is approximately zero due to the incompressible nature of tissue [31]. Hence, a higher shear-compression wave ratio indicates better data quality. In Paper II and III, all included scans had a mean shear-compression wave ratio above 5. This threshold was found to satisfyingly separate scans with high and low data quality, based on empirical experience, both from Paper I, but also in MRE data from another research project.

In Paper II, another data quality requirement was added, evaluating the degree of temporal nonlinearity. By performing a Fourier transform on the displacement data, a temporal nonlinearity value can be calculated as the proportion of energy that is not at the driving frequency (50 Hz, in our case) at each pixel [96]. A higher percentage of energy at higher frequencies (high temporal nonlinearity) indicates poorer data quality. In Paper II, masks were made to exclude any pixel with temporal nonlinearity above 50 %, a cut-off value also used in another brain MRE study [96].

As fluid in the ventricles is not modeled by the MRE inversion, voxels containing mostly cerebrospinal fluid was therefore excluded from all analysis after elastogram reconstruction (Figure 4.2) [39]. To avoid artefacts from MRE reconstruction at the edge of the brain, the outmost brain mask of the MRE maps were eroded by 2 pixels [97].

4.4.2 Image processing, other sequences

ASL images of healthy subjects were analyzed in the nordicICE software (NordicNeuroLab AS, Bergen, Norway). This produced maps of cerebral blood flow, measured in $ml/100g/min$. Perfusion values were obtained for gray matter only. The blood flow is lower in white than in gray matter, and ASL has a low sensitivity for white matter perfusion [15].

The DTI and DSC images were corrected for EPI distortion effects prior to analysis using the geometric distortion correction method FSL TOPUP [98, 99]. Thereafter, DTI analysis was performed in nordicICE using default settings

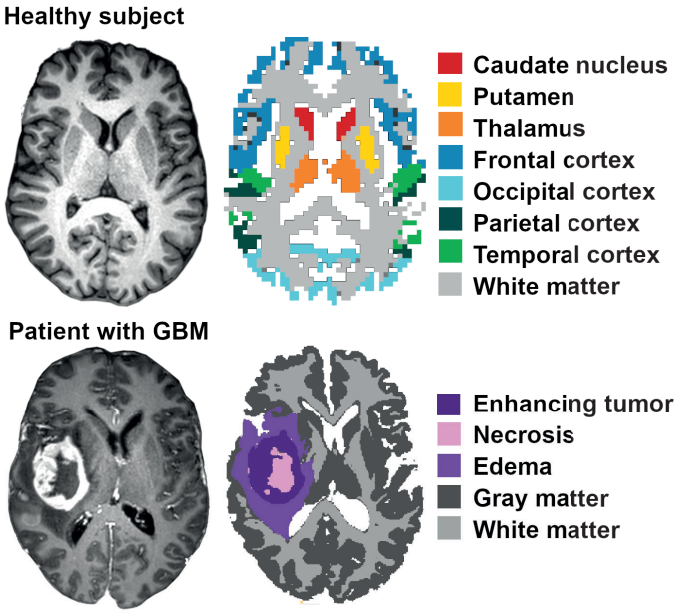

Figure 4.2: Regions of interest used in the analyses. Upper row: Gray and white matter regions of interest in healthy subject. Lower row: Tumor and normal-appearing regions of interest in patient with GBM. Voxels classified as mainly cerebrospinal fluid were not used in the analysis.

for motion correction, automatic detection of noise threshold, and noise level cutoff. The diffusivity of the tissue was measured by ADC and the anisotropy of the tissue was measured by FA. The DSC images of the patients were also analyzed in nordicICE using default settings for motion and leakage correction [100]. This produced maps of cerebral blood flow normalized to white matter (nCBF), leakage, and vessel size index (VSI) [101].

4.4.3 Regions of interest used in analysis

4.4.3.1 Regions of interest in healthy subjects, Papers I and II

All image registrations in healthy subjects were performed using Matlab and SPM12 (version 7487, Wellcome Trust Centre for Neuroimaging, London). First, anatomical T1-weighted images were warped to the Montreal Neurological Institute brain region template [102]. The inverse deformation fields of the transformations were then used to reorient the binary maps of the brain regions of interest (ROIs) into the anatomical space of each subject. T1-weighted images and labels were then co-registered by affine transformations, using nearest-neighbour interpolation, into the native spaces of the MRE, DTI and the ASL images to preserve pixel integrity. Analysis was performed in the whole brain, in white matter, in four cortical gray matter regions (frontal, occipital, parietal, and temporal) and in four deep gray matter regions (caudate nucleus, hippocampus, putamen, and thalamus).

4.4.3.2 Tumor and healthy regions for patients, Papers II and III

Segmentations of ROIs in the patients was performed automatically using a convolutional neural network. This network is based on the 3D-Unet architecture defined by Juan-Albarracín et al. [103], trained with 262 presurgical BRATS exams [104, 105], and 222 follow-up exams from Oslo University Hospital.

Segmentations were made for each patient based on pre- and post-contrast T1-weighted images, T2-weighted and FLAIR images.

Contrast-enhancing and necrotic tumor regions were defined as the enhancing and nonenhancing tumor regions on post-contrast T1-weighted images, respectively. Edema was defined as the nonenhancing region appearing hyperintense on the FLAIR images. Gray- and white-matter masks were eroded by one voxel, and only the opposite hemisphere of the brain from the tumor was used for the normalization masks. For cases where the tumor affected both hemispheres, a 3 cm margin from the distal edge of the tumor and edema was used for the gray and white matter masks.

4.4.3.3 Biopsy regions of interest, Paper III

During tumor resection, biopsies were extracted by the surgeon. Stereotactic guidance was provided by preoperative contrast-enhanced T1-weighted and FLAIR images on a neuronavigation system (Brainlab Curve; Brainlab, Feldkirchen, Germany). Biopsy locations were recorded by a screenshot image on the neuronavigation system, illustrated in Figure 4.3.

A semi-automated 2D to 3D co-registration algorithm was then used to convert the cross-hairs from the neuronavigation system screenshot image into an MR imaging coordinate [106]. The following steps were performed: First, a cropped subimage of the biopsy crosshair in the axial, coronal and sagittal orientations was obtained. Then, each slice of the contrast-enhanced T1-weighted images in the three planes were displayed sequentially and visually matched to the biopsy crosshair in each plane. Together, the position in all three planes yielded the coordinates of the image voxel in the MR images. Next, a binary ROI was made for each coordinate by expanding one voxel in all three directions from this coordinate point. Finally, the positions of all ROIs were controlled by an experienced neuroradiologist. The contrast-enhanced T1-weighted images were then co-registered to the space of the MRE images, utilising a nearest-neighbor interpolation in nordicICE. The same transforms were applied to the binary ROI masks in T1-weighted space, resulting in a one-voxel seed point in the MRE space. In order to make the analysis more robust to brain shift and co-registration issues, this voxel was morphologically dilated in 2D to a ROI of nine pixels. From these a trimmed mean was calculated, where the pixel with the lowest and the highest values were removed. This resulted in a measured $|G^*|$ values for all biopsies, which was normalized to the mean value in each patient's NAWM ROI. The biopsies were classified as 'stiff' or 'soft' based on MRE, i.e., higher or lower $|G^*|_{norm}$ than the mean value of all biopsies within each tumor, respectively.

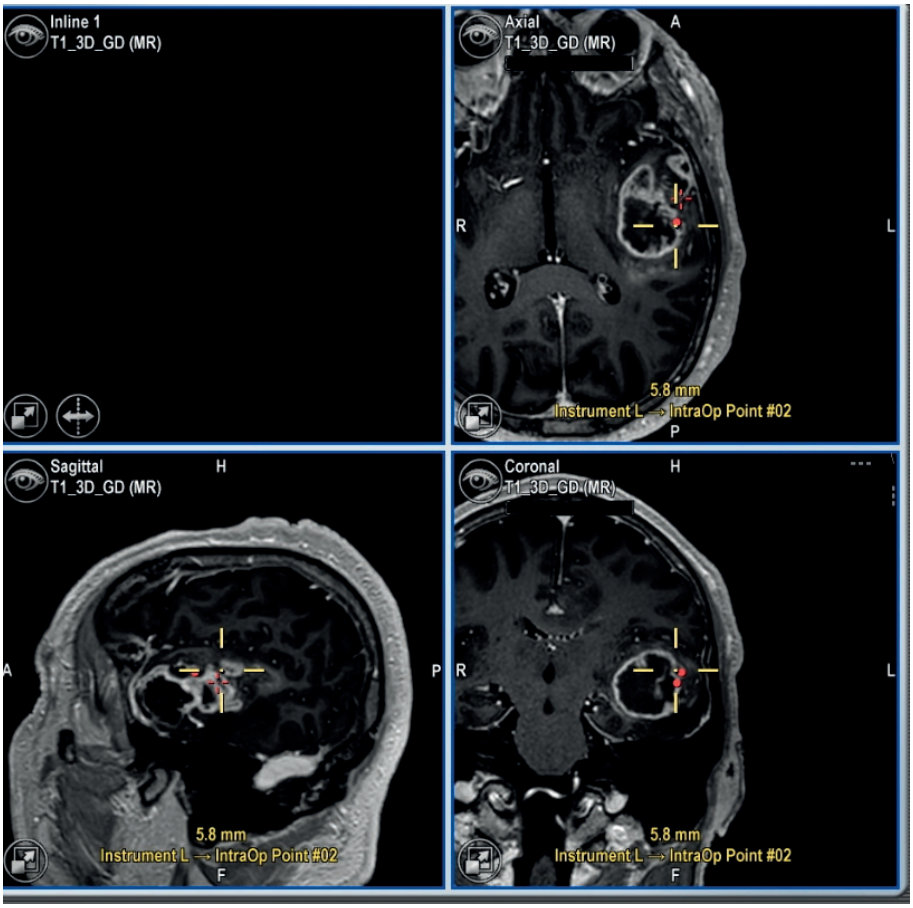

Figure 4.3: Location of tissue biopsy. The location of the biopsy was recorded by screen capture of the navigation system at the time of tissue sampling. The yellow cross shows the location of the biopsy in all planes: axial, sagittal and coronal. In this case, the biopsy was taken from the contrast-enhancing tumor. The crosshairs on the screenshot images were then transformed into MRI coordinates.

4.5 Biopsy extraction, Paper III

Surgery was performed by a single experienced neurosurgeon, except for one patient. Biopsies were taken from regions within the preplanned volume amenable for surgery, and covered both T1-weighted-contrast enhancing regions, and regions with hyperintense FLAIR signal that were nonenhancing on T1-weighted images. From each tumor, 2–7 biopsies were taken. Biopsies were taken early in the resection, before any major change in navigational precision. The surgeon evaluated tumor consistency as 1) softer than normal brain tissue, 2) similar in consistency as normal brain tissue, or 3) firmer than normal brain tissue [107]. Biopsies were snap frozen immediately after extraction. The surgeon was shown the MRE data before the surgery, but the biopsy locations were chosen according to the surgeon's evaluation of tissue with differing stiffness.

4.6 RNA sequencing, Paper III

In order to make proteins, a cell makes an RNA copy of a piece of DNA in a process called transcription. This copy carries the genetic information needed to make proteins in a cell. The transcriptome is the set of all RNA transcripts in an individual or a population of cells, and can be analyzed using RNA sequencing. Simply stated, RNA sequencing can show to which extent the genes in our DNA are expressed. Understanding the transcriptome is essential for interpreting the functional elements of the genome and revealing the molecular constituents of cells and tissues [108].

In Paper III, RNA sequencing was performed on 2–4 biopsies from the first eight patients. By comparing the expression levels of genes in 'stiff' and 'soft' biopsies, my molecular biologist colleague performed a differential gene expression analysis. Further details about the RNA sequencing analysis can be found in the submitted manuscript of Paper III [109].

4.7 External patient data sets, Paper III

In Paper III, we analyzed survival data and transcriptomic profiles of patients in publicly available data sets. Data were retrieved from two data sets: The Cancer Genome Atlas (TCGA) and the Clinical Proteomic Tumor Analysis Consortium (CPTAC) [110, 111]. TCGA contains genomic, epigenomic, transcriptomic and proteomic data and is publicly available for the research community. The CPTAC database has as its main focus proteomic profiling using mass spectroscopy. Through the National Cancer Institute Genomic Data Commons Data Portal, we could access RNA transcription profiles from 265 patients, 168 from TCGA and 97 from CPTAC [112].

4.8 Statistical analysis

Statistical analysis was performed using Matlab, where nothing else is noted. A p-value of 0.05 was used as a statistical significance threshold throughout the thesis. Holm-Bonferroni corrections were made for multiple comparisons in Papers I and II.

A Wilcoxon signed rank test was used when comparing paired measurements. The Wilcoxon signed rank test is a nonparametric version of the paired Student's t-test, which assumes a normal distribution of the data. Due to our small sample sizes, we cannot assume a normal distribution of measurements, making the Wilcoxon signed rank test the appropriate choice. In Paper I, the test was used to compare the stiffness values of the two different reconstruction methods. In Paper II, the Wilcoxon signed rank test was used to compare functional measurement in different brain regions pairwise and to compare different regression models. In Paper III, comparisons of MRE measurements in tumor and NAWM were performed using the Wilcoxon signed rank test.

Spearman rank-order correlation is a nonparametric test of the strength and direction of association between two variables. In Paper I, Spearman rank-order correlation was used to assess the correlation between stiffness and MRE data quality. In Paper II, the correlation between the different functional measurements was assessed by this test. In Paper III, MRE measurements and tumor volumes were compared using the Spearman's rank order test.

In Paper I, test–retest reliability was estimated using both absolute and relative indices. Relative reliability was calculated in Stata (release 16, StataCorp, College Station, TX) using intraclass correlation coefficients (ICC) with 95 % confidence intervals, based on an absolute-agreement, two-way mixed effects model [113]. Within-subject coefficients of variation (CV) for repeated measurements x_1 and x_2 for n subjects were calculated as [114]:

$$CV(\%) = 100 \times \frac{\sqrt{\frac{\sum (x_1 - x_2)^2}{2n}}}{mean\ of\ all\ measurements} \tag{4.3}$$

Repeatability coefficients (RC) were calculated as $1.96 \cdot \sqrt{2\sigma}$, where σ is the standard deviation of the measurement differences between the two scans [115, 116].

In Paper II, two regression models were used to study cerebral blood flow as a function of MRE and DTI measurements using all voxels for all patients. Both a linear and a random forest model were used, and comparisons were made between the CBF predictions using DTI measurements alone and CBF predictions including MRE measurements. The performance of the regression models was evaluated by their root mean square error with a leave-one-patient-out cross-validation strategy.

In Paper III, logistic regression using Stata was used to compare the surgeon's stiffness assessment with the MRE stiffness measurement. Differential expression analysis of RNA sequencing data and dimensionality reduction was performed using the DESeq2 package of R (version 4.1.1, R Core Team 2021).

To examine whether stiffness was a strong source of variance within RNA sequencing data in Paper III, we performed dimensionality reduction by both principal component analysis (PCA) and partial least-squares discriminant analysis (PLS-DA). The purpose of dimensionality reduction methods is to separate data points according to the variables that vary the most between different groups (in our case, biopsies). Using a linear transformation, the data is converted to a lower dimensional space with as small an error as possible. The new features representing the reduced dimensions are referred to as principal components [117]. PCA is an unsupervised technique, meaning the method is looking for new variables that better separate data points without considering which data properties we are interested in (stiffness in our case). In PCA, the first principal component contains as much variance in the original data as possible. In contrast, PLS-DA is a supervised method, where the information of each sample's group is given. With the objective of separating 'stiff' and 'soft' biopsies, PLS-DA can be used to find the genes that best separate the samples.

The first principal component of PLS-DA contains as much covariance between the original data and the given label as possible [117].

In Paper III, data from the TCGA and the CPTAC were used in a survival analysis. Kaplan Meier curves were calculated in R and a Cox regression analysis was performed using SPSS (version 28.0, IBM Corp, Armonk, NY).

In survival analyses, we study time until an event occurs, with the event of interest often being death. The survival probability can be estimated nonparametrically from observed survival times in the data set. Plotting the survival $S(t)$ as a function of time will produce a stepwise decreasing plot, showing the probability of survival at any point t. During the follow-up time of the study, we usually do not have information about the time of death for all patients. The patient can survive longer than the follow-up period or drop out of the study during the follow-up period. This phenomenon is called censoring, and these cases are included in the Kaplan Meier plots and displayed as marks on the plotted survival curve [118].

This way, survival curves for two patient groups can be compared (for instance with or without a specific genotype). However, there might be other differences between the patients in each group. For example, the patients in one group could be older than in the other group, which could influence survival. By using a multivariate model, several factors affecting survival can be considered at once. The Cox regression model is the most commonly used multivariate approach for analysing survival time data in medical research [119]. Examples of covariates that can be included in the model are age, sex, or tumor size. In Cox regression, covariates act multiplicatively on the hazard at any point in time. A hazard ratio above one indicates a covariate that is negatively associated with the length of survival. By finding hazard ratios for all covariates, one can find which covariate contributes the most to patient survival, and present hazard ratios for one covariate adjusted for the others.

Chapter 5

Summary of papers

5.1 Paper I – Robustness of MR elastography in the healthy brain: Repeatability, reliability, and effect of different reconstruction methods

Mean stiffness was measured in the whole brain, and in gray and white matter ROIs, using the curl and FEM reconstruction. FEM reconstruction resulted in 39 %higher stiffness than the curl reconstruction (Figure 5.1A, $p<0.05$).

Figure 5.1B shows the mean values in all ROIs in scan 1 versus in scan 2. The repeatability analysis of CV was 4.3 %and 3.8 %in the whole brain for the curl and the FEM reconstruction, respectively, with 4.0 %—12.8 %for subregions. The whole-brain ICC was 0.60—0.74, ranging from 0.20 to 0.89 in different regions. RC for the whole brain was 0.14 kPa and 0.17 kPa for the curl and FEM method, respectively.

No significant correlations were observed between MRE data quality and the stiffness estimates. For most subjects, the difference in tissue stiffness between the two scans was small, even when the MRE data quality of the two scans differed (Figure 5.1C). For a subset of subjects, data quality varied substantially between the two scans. Half of the subjects had a relative difference in shear-compression wave ratio of more than 20 %between scans. Despite differences in data quality, the median difference in measured brain stiffness for these cases was only 2 %.

Regions of low stiffness, such as the caudate nucleus and thalamus, tended toward low shear compression wave ratios, whereas regions of high stiffness, such as white matter, tended to have higher shear-compression wave ratios. MRE data quality was higher in the peripheral regions than in the central regions of the brain ($p<0.05$, Figure 5.1D).

In conclusion, MRE was found to be a reliable method for assessing brain stiffness. The results suggest that MRE can be used to track changes in tissue stiffness caused by disease and to track the biomechanical effects of treatment.

5.2 Paper II – Decreased tissue stiffness in glioblastoma by MR elastography is associated with increased cerebral blood flow

Ten patients with GBM and 17 healthy subjects were examined using MRE, perfusion, and diffusion MRI. G', G'', CBF, ADC and FA were measured in

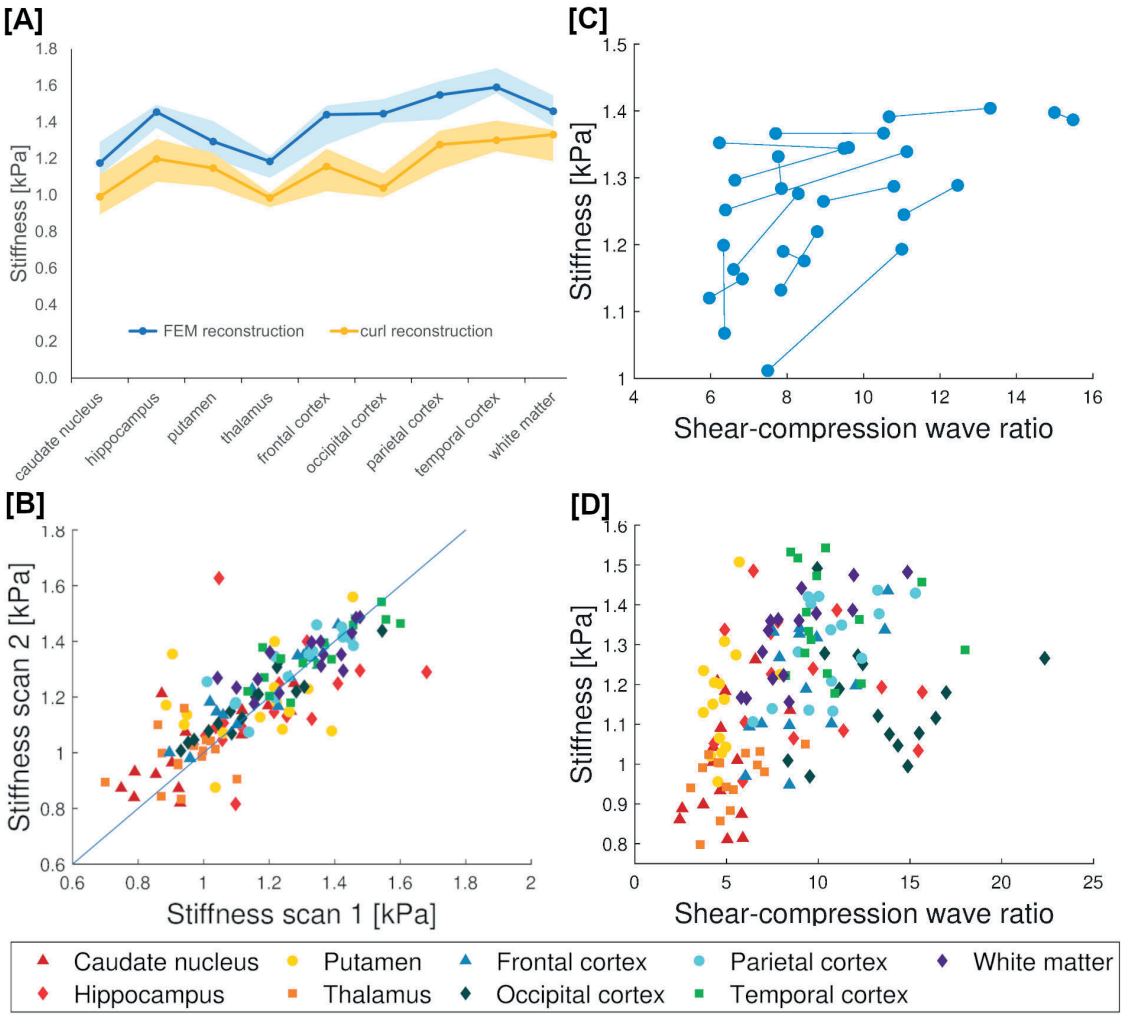

Figure 5.1: Results Paper I. A) Median stiffness estimates (average of both scans for each subject), ribbon showing the first and third quartile range, from both the curl reconstruction and the FEM reconstruction for all the investigated brain regions. B) Parametric plot of stiffness in each ROIs in scan 1 versus scan 2 for the curl reconstruction, C) The MRE data quality versus stiffness in the whole-brain ROI for the curl reconstruction, showing both scans for each subject linked with a line. D) MRE data quality for each subregion versus the stiffness in that region for the curl reconstruction, where every entry corresponds to the average of the two scans, and shown for all subjects (n=15).

contrast-enhancing tumor, necrosis, edema, and gray and white matter of patients, and gray and white matter (with the exception of CBF) of healthy subjects.

GBM tissue was found to be structurally degraded compared to healthy tissue, with a median G' and G'' in contrast-enhancing tumor 13 %and 37 %lower than in NAWM ($p<0.01$), respectively. Tumor stiffness was found to be heterogeneous, both between patients and within tumors. The median value of G' and G'' was 18 %and 6 %lower in necrosis than in contrast-enhancing tumor, respectively ($p<0.05$). The differences in voxel distributions between patients were larger in the lesion regions than in normal-appearing gray matter, illustrating the interpatient tumor heterogeneity. Measurements in tumor and edema showed greater variability between patients than the values in white and gray matter.

Tracking the voxel distributions radially from the tumor core outward, G' and G'' started with low values within the tumor and increased to values found in contralateral NAWM at the distal edge of the edema region for most patients. ADC was high in necrosis, tumor and edema, and was still 29 %(median value) higher than in NAWM at the edema edge — although with large variation among patients. FA was low in the tumor core and increased away from it; the median value was 46 %lower at the edema edge than in NAWM. CBF, leakage and vessel size were highest in the contrast-enhancing tumor and gradually decreased toward the mean NAWM value at the edema edge. For several of the patients, the properties of the tissue remained abnormal (outside the 25^{th} and 75^{th} percentile of NAWM) for more than 3 mm into the normal-appearing tissue (Figure 5.2).

No correlations across patients were found in the contrast-enhancing tumor between the mean G' and the mean CBF, ADC, leakage or vessel size, nor between G'' and the perfusion and diffusion parameters. To further explore any relationship between the MRE measurements and functional parameters in patients, we estimated voxel-by-voxel regressions to explain CBF as a function of the other measurements, all normalized to NAWM. Our baseline model was a linear model with ADC_{norm} and FA_{norm} as predictors. Using root-mean-square error as a criterion, we investigated how predictive power increased as we added first G'_{norm} and then both G'_{norm} and G''_{norm} to the model. Predictive power increased significantly with the inclusion of each additional predictor ($p<0.01$). After the assessment of each model, the linear model was trained using all data, resulting in the following final linear model, where CBF decreases with higher G' and G'':

$$CBF = 1.7 - 0.16 \cdot G'_{norm} - 0.15 \cdot G''_{norm} + 0.35 \cdot ADC_{norm} - 0.44 \cdot FA_{norm}$$

In addition to the linear model, we investigated the predictive capacity of a random-forest model. Again, we compared a baseline model that included ADC_{norm} and FA_{norm} with models that included G'_{norm}, and both G'_{norm} and G''_{norm}. All three random-forest models performed better than the linear models ($p<0.01$). In addition, the performance of the random-forest model improved by including G'_{norm} ($p<0.01$), and further improved by including both G'_{norm} and G''_{norm} ($p<0.01$).

In summary, we found that GBM tumors differed from healthy tissue in terms of G' and G'', CBF, ADC, and FA, with heterogeneity both between patients

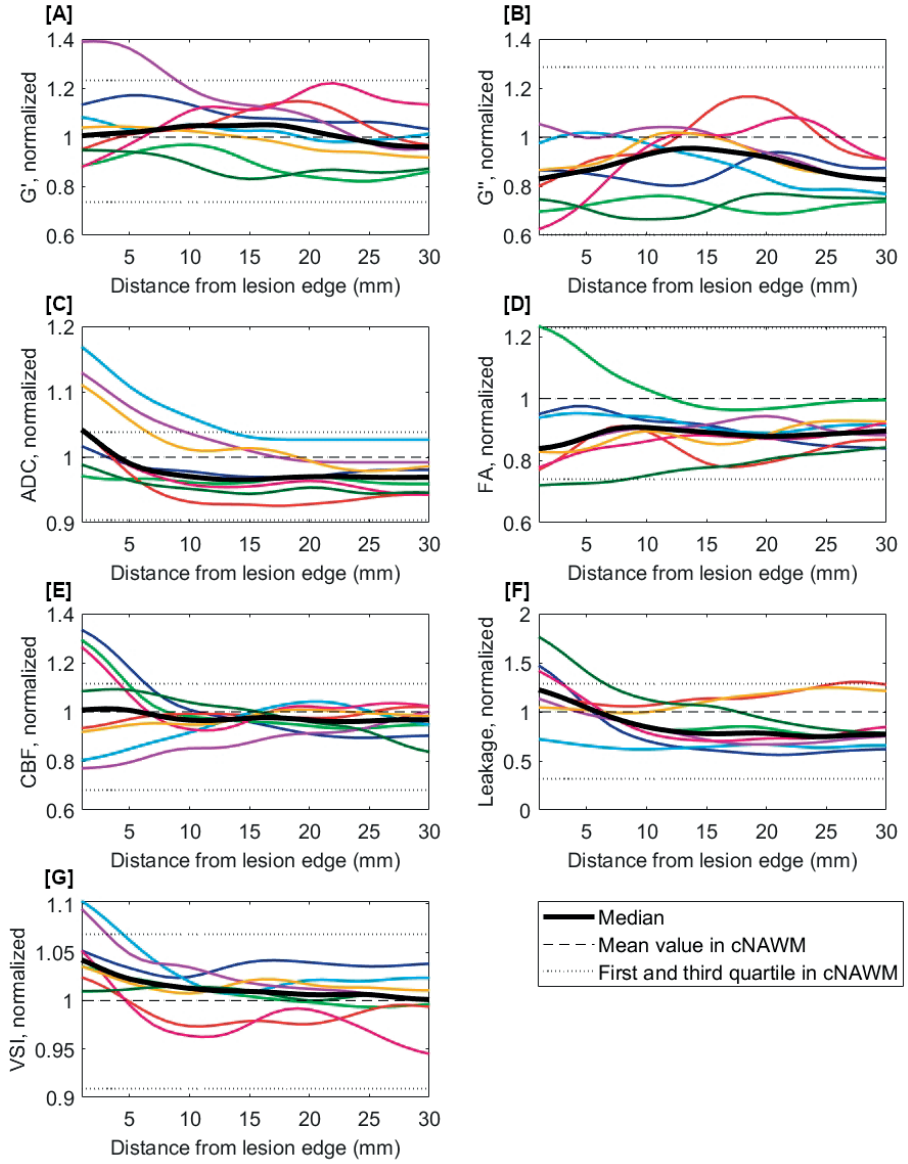

Figure 5.2: Results Paper II. Gradients of the different measurements, moving radially outwards from the lesion edge. Measurements in tissue segmented as white matter, normalized to each patient's mean value in contralateral NAWM. The colored lines show individual patients (n=8 included), and the black line shows patient median.

and within tumors. Abnormal tissue properties were present in regions that appeared normal on anatomical images. Finally, we showed that the inclusion of MRE measurements in statistical models helped predict perfusion, with stiffer tissue associated with lower perfusion values.

5.3 Paper III – MR elastography identifies regions of extracellular matrix reorganization associated with shorter survival in glioblastoma patients

Thirteen patients with GBM were examined using MRE before tumor resection. The mean whole-tumor $|G^*|$ and ϕ were both lower than in NAWM. Figure 5.3 shows shows an example of a biopsy location on a contrast-enhanced T1-weighted image and the corresponding $|G^*|$ map.

We found no association between the neurosurgeon's evaluation of biopsy stiffness and $|G^*|_{norm}$ as assessed by logistic regression (Odds ratio=0.91, p=0.91), suggesting the two entities are independent measures.

To evaluate the molecular differences between 'stiff' and 'soft' tissue biopsies, we performed total RNA sequencing on 22 biopsies with variable stiffness from eight GBM tumors.

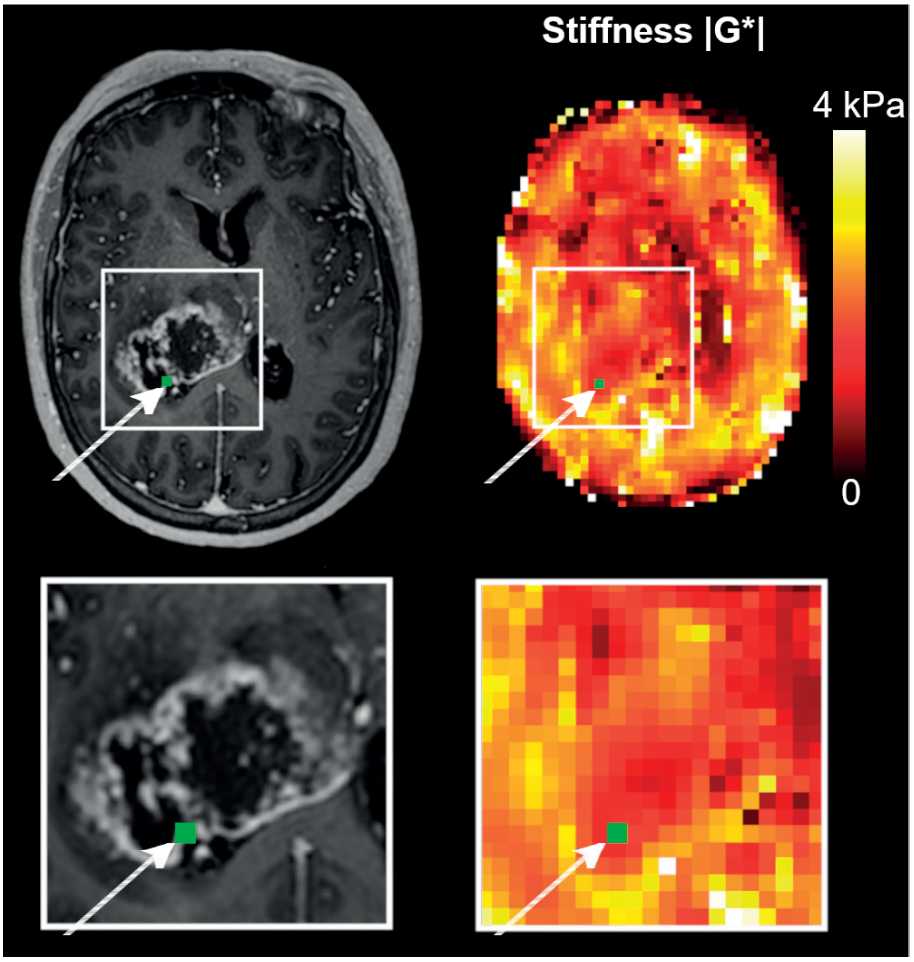

Figure 5.3: Example of MRE imaging in Paper III. The location of the tissue biopsy is shown in green in the contrast-enhanced T1-weighted image (CE-T1w) and the MRE stiffness map ($|G^*|$).

Differential gene expression analysis between the 'stiff' and the 'soft' biopsies

per patient found that 196 genes were differentially expressed (adjusted $p<0.05$). Of these, 122 were upregulated in 'stiff' biopsies while 74 were upregulated in 'soft' biopsies. Normalized expression levels of differentially expressed genes in every biopsy showed that 'stiff' or 'soft' biopsies tend to cluster together, and biopsies within individual patients also showed similar expression profiles. Patient-wise leave-one-out cross-validation identified a set of 43 genes that were found to be differentially expressed in every iteration.

To evaluate the structural and functional importance of the differentially expressed genes, we performed a gene set enrichment analysis of genes associated with increased biopsy stiffness using the Gene Ontology and Reactome databases [120–122]. The Gene Ontology terms with highest association to 'stiff' biopsies represent extracellular matrix (ECM) components, cellular adhesion, and innate immunity (Figure 5.4).

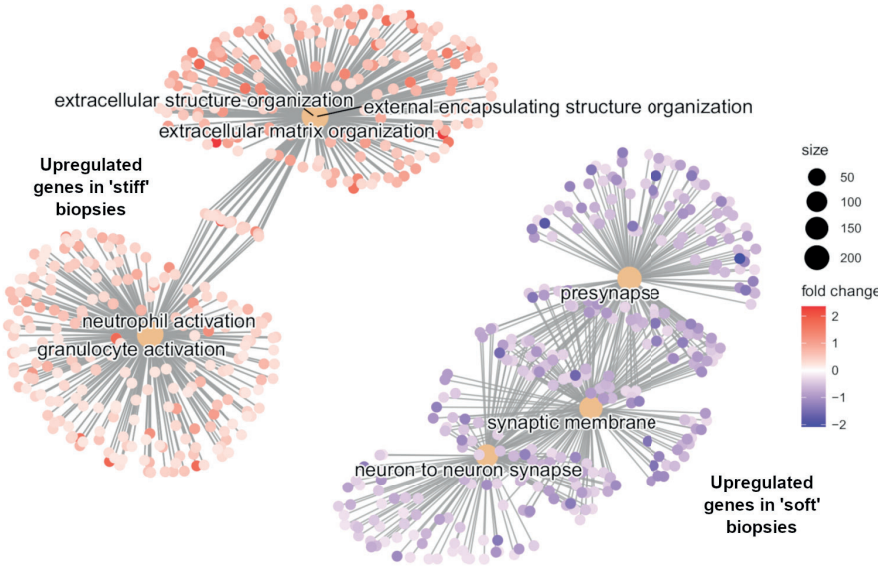

Figure 5.4: Results Paper III. Gene set enrichment analysis of differentially expressed genes in 'soft' and 'stiff' tumor biopsies. Central nodes represent Gene Ontology terms, colored dots represent differentially expressed genes. The terms upregulated in 'stiff' biopsies (red) are associated with ECM organization and effector cells of the innate immune system (neutrophils and granulocytes). In contrast, 'soft' biopsies (blue) are associated with normal neuronal functions.

In contrast, Gene Ontology terms and Reactome pathways with the highest association with 'soft' biopsies largely represented normal neuronal functions such as regulation of membrane potential and neurotransmitter receptor complex, although associations with DNA methylation and rRNA regulation were also found. On the basis of our findings, we hypothesize that stiffer tumor areas are important for tumor progression and hence patient survival.

Unsupervised dimensionality reduction by principal component analysis did not identify tissue stiffness as a strong source of variance within the

data. However, supervised dimensionality-reduction with partial least-squares discriminant analysis identified a robust expression signal that separated 'stiff' from 'soft' biopsies within each tumor. Tuning of the PLS-DA parameters indicated that a minimal sparse PLS-DA model containing 22 genes was sufficient to separate the patient samples based on the measured tissue stiffness.

To study the effect of this gene expression signal on patient survival, we used RNA transcription profiles of 265 GBM tumors from two studies available in the National Cancer Institute Genomic Data Commons Data Portal [112]. The expression patterns of the 22 stable genes selected by the dimensionality reduction were used to classify tumors with this gene expression signal (n=63) and tumors without it (n=202). Survival analysis showed that the median survival time of patients carrying tumors expressing this gene signal (360 days) was 100 days shorter than that of patients without this gene expression signal (460 days). Cox regression analysis showed that this gene expression signal had a significant impact on survival, with a 45 %higher risk of death at any given time for patients with this gene expression signal. This result was significant after adjusting for age, gender, and type of treatment (hazard ratio: 1.45, 95 %confidence interval: 1.043–2.015, $p<0.05$).

Chapter 6

Discussion

The primary objective of this PhD project was to use MRE in patients with GBM to explore the biomechanical properties of tumors and to probe how biomechanics relate to tissue function and genetics. In Paper I, we scanned healthy subjects twice to assess repeatability of MRE in the healthy human brain. We also evaluated the effect of different reconstruction methods and varying MRE data quality on stiffness estimates. In Paper II, we used MRE, DSC, and DTI in healthy subjects and patients with GBM and mapped the differences between tumor and healthy tissue. In Paper III, we further examined tumor heterogeneity by performing RNA sequencing of biopsies from different locations in the tumor. These are our main findings:

- MRE in brain is robust in terms of repeatability. Absolute stiffness values vary with the reconstruction method.
- The biomechanical properties of GBM tumors differ from those of healthy tissue. In patients, lower stiffness is associated with higher perfusion.
- Within a tumor, stiffer regions express genes related to ECM reorganization. The gene expression signal found in 'stiff' biopsies is associated with shorter survival in patients with GBM.

6.1 Robustness of brain MRE

6.1.1 Repeatability

The repeatability coefficients we found in Paper I suggest that to track whole-brain changes in a patient over time, the change in G' must be greater than 0.14 kPa for curl reconstruction and greater than 0.17 kPa for the FEM reconstruction. For regions deep in the brain, with higher measurement errors, the changes would have to be greater than 0.4 kPa.

Differences in stiffness between patients with neurological disorders and healthy controls have been shown to range from -3 % to -21 % [23]. As we have shown that a significant change in whole-brain stiffness would have to be 11 % (0.14 kPa) for the curl reconstruction, this could pose a challenge. However, as brain tumors are localized in one part of the brain, local stiffness changes are more apparent than subtle global changes. For the patients in Paper II, the difference in G' between the tumor and NAWM ranged from -3 % to -30 % for the contrast-enhancing tumor and +11 % to -50 % for the necrotic tumor regions. The biomechanical properties of the tissue seem to be less affected for some patients than for others. Tracking changes in biomechanical properties

over time can be challenging with our current technique if the differences are small.

Our repeatability results are in line with other studies of brain MRE, although repeatability assessment varies between studies. In a study with five repeated scans of one healthy subject, CVs ranged from 1.7 % to 8.5 % [123]. The authors do no, however, clarify whether the scans were performed subsequently or with a longer time interval and equipment reassembly between scans. In a second study, a single subject was scanned five times over two months. The repeatability of MRE was assessed in global gray and white matter, as well as in substructures such as the corpus collosum. With CVs ranging from 4.6 % to 8.7 %, the repeatability was denoted excellent by the authors [124]. The same authors published repeatability measures in deep gray matter regions from eight scans of one healthy subject over four days. They found CVs in deep gray matter regions to range from 2.4 % to 7.1 %, and CVs of 1.4 % and 2.1 % for global white and gray matter [125]. In a fourth study, 10 volunteers were scanned three times in one day, with subjects removed from the scan table and the MRE apparatus reassembled between each exam. They obtained a CV of 1 % for global brain stiffness and a maximum CV of 4.5 % for brain subregions [97].

In our study, we perform a test and retest during the same session. If we had scanned the subjects with a longer time interval and repositioning between scans, the study setup would resemble the clinical situation in a more realistic way. However, we choose to do the measurements within a single session in order to minimize the factors that could influence the results and thereby demonstrate the inherent repeatability of the technique. A somewhat larger difference between scans would be expected if the scans had been performed further apart in time and with subject repositioning between scans.

The repeatability of brain MRE is comparable to measurements in liver MRE. A study of four patients with Hepatitis C and five healthy subjects scanned twice in one day found an ICC of 0.88 and CVs ranging from 6 % to 11 %[126]. Similarly, G' was found to not differ more than 10 %, with an average variation of 3 %, in a study of liver tumor stiffness carried out in nine patients scanned twice with repositioning between scans [127].

Our study and the studies described above focused on repeatability, with the goal of measuring the same subject multiple times in an identical fashion. However, variation in measurements associated with differences in procedure or methodology, so called reproducibility, is also of interest. Reproducibility could be assessed by scanning the same patient on different scanners, using different pulse sequences and possibly also different field strengths. No such study has been performed in brain MRE, but a reproducibility study of liver MRE examined variation across different imaging systems from different vendors, spin- and gradient echo sequences, and 1.5 T and 3 T scanners. They found a mean variance in liver stiffness measurement across all manufacturers, field strengths, and pulse sequence combinations of 0.042 kPa (range: 0.008—0.11 kPa) for 24 subjects, with CVs ranging from 4.7 % to 20.7 % [128].

In general, we find MRE to be a robust technique.

6.1.2 The effect of different reconstruction methods

In Paper I, the estimated G' depended on the reconstruction method. The FEM reconstruction yielded a 39 % higher value than the curl reconstruction. This is consistent with earlier results, which found 10-–42 % higher stiffness values in phantom regions when the data were reconstructed using the FEM compared to the curl approach [94]. This may be due to noise sensitivity. The curl method requires third-order derivatives, and is therefore more sensitive to noise. Removing the compressional waves by applying the curl to the displacement field works perfectly in theory, in a homogeneous isotropic object. In practice, noise-corrupted empirical estimates of the displacement field $\mathbf{u}$ are used when solving for stiffness, and differential operations amplify this noise [129].

Both methods in Paper I are direct inversion methods. Direct methods assume that the measured wave displacement is sufficiently accurate that insertion into the wave equation leaves the stiffness distribution as the principal unknown that can be found by error minimization. Direct methods are therefore inherently sensitive to data quality [94].

An alternative to direct reconstruction methods is iterative techniques. Iterative techniques solve a forward problem rather than inversely solving the wave equation. The stiffness parameters are iteratively adapted in order to minimize the difference between the resulting forward solution and the measured wave field [94]. Iterative methods are less sensitive to noise, but strongly depend on the forward problem and the assumption that it correctly models the wave behavior. This approach is therefore sensitive to model assumptions. Furthermore, they are typically more computationally expensive than direct methods, as they require many solutions of the forward problem, with the stiffness estimate updated each time, instead of acting directly on the data [94].

Both the curl and the FEM reconstruction methods also assume local stiffness homogeneity. This assumption is less valid close to tissue boundaries, where it may cause artifacts [24]. To mitigate this, the elastograms in our studies were eroded to remove the pixels furthest out in the brain.

The alternative to assuming local homogeneity is to account for spatial stiffness variations [123]. In principle, global models allow for more accurate modeling of the physics of motion [24]. However, such methods are more computationally expensive, yielding longer reconstruction times. Furthermore, methods that consider stiffness heterogeneity typically require the tuning of regularization parameters [94].

In addition to the two reconstruction methods used in Paper I, a wide range of other reconstruction algorithms are available, including the commonly used local frequency estimation method [130], the multifrequency dual elastovisco inversion [131] and nonlinear inversion [132]. The different methods are based on different underlying physical assumptions, which may result in different stiffness estimates [25].

Reconstruction methods are not the only aspect that differs between studies. Brain MRE is performed using different types of vibration-generating hardware and different MRI pulse sequences. Estimates of tissue stiffness in the brain

may vary with experimental design, hardware, vibration frequency, acquisition methods and processing pipelines, as well as physiological variations between individuals [133]. Consequently, reproducibility of tissue stiffness estimates across sites is challenging. Therefore, circumspection is required when comparing stiffness values obtained with different techniques. A way to mitigate this issue is to normalize stiffness measurements to a reference tissue in each subject, usually NAWM.

6.1.3 MRE data quality

In Paper I, we defined MRE data quality as the shear-compression wave ratio. By this measure, we did not find a correlation between MRE data quality and estimated stiffness. This is encouraging in regard to method robustness, given that the scans we included in our study were deemed successful. Five subjects were excluded from the studies in Papers I and II due to subject movement during the scan or insufficient wave propagation, resulting in low shear-compression wave ratios. If poor quality data is used as input, the reconstruction yields low stiffness measurements. So if cases with truly low data quality had been included, we would expect to see a correlation between MRE data quality and stiffness estimates.

The transducer needs to adequately transfer the vibration to the head in order to ensure proper shear wave propagation. Therefore, careful positioning of the equipment and proper padding to keep the transducer in place during the scan are important. With our setup, the transducer was attached on the side of the subject's head. Even with padding on both sides of the head, there is a risk of movement of the transducer relative to the head. The only commercial MRE hardware available uses a passive acoustic driver beneath the head of the subject [45], which minimizes movement between the transducer and the subject. However, a patient lying on top of it could possibly silence the passive driver [21]. MRI head coils differ in design and shape. Whether it is more practical to place the transducer on the side of the head or underneath it also depends on which head coil is used.

As the mechanical vibration of the transducer is transmitted by a cable with a rotating axis, the vibration is sensitive to the placement of the cable. Sharp bends will perturb the vibration. In our studies, we therefore laid the cable as smoothly as possible from the motor to the transducer in the scanner isocenter. Compared to the commercial MRE system that use pneumatic pipes to transmit vibration, our system has higher frequency accuracy [134]. However, some higher harmonics were present in the vibration (illustrated in Figure 4.1), leading to noise in the displacement data. In order to account for higher harmonics, the mechanical wave was sampled eight times across the period of the 25 Hz component of the vibration. Had there been no or very low-amplitude higher harmonics, fewer samples of the waveform would have been required, and the scan time could have been shorter. To reduce the effect of the higher harmonics, we used ROI masks excluding pixels with temporal nonlinearity above 50 % in Paper II.

The MRE quality could be improved by stronger and longer-lasting MEGs, motion encoding in more directions, more gradient cycles and phase offset samples of the mechanical wave, and higher image resolution. The strength and duration of MEGs is limited by the MRI hardware and the number of gradient cycles is constrained by the sequence timing [88]. Longer scan time could improve MRE data quality, but this should be balanced with patient comfort. In our studies, we have used a gradient-echo sequence. It is also common to use a spin-echo EPI sequence, which is quicker [23]. However, EPI sequences are susceptible to distortion effects which then needs to be corrected for [99].

As for any MRI exam, patient movement can severely affect the quality of the data. MRE is a motion-sensitive technique, so unwanted subject motion can cause phase errors that appear as inconsistent phase between volumes and cause signal loss [135]. The MRE acquisition can be challenging for the patients, especially if they find the vibration uncomfortable. For the patients in our studies, the MRE was acquired after all preoperative MRI scans. The standard preoperative examination at this lab includes pre- and post-contrast T1-weighted sequences, T2-weighted and FLAIR sequences, in addition to DTI and DSC acquisitions. These acquisitions are important for the planning of surgery and further treatment, while MRE was only to be used for research. Therefore, all standard scans were taken first, in case the patient was unable to complete the full exam. The full exam lasted more than an hour for most patients. This could cause patients to feel tired or not ready for one last scan. However, MRE acquisition was well tolerated in all patients and volunteers. When asked, most said that it felt okay, while some commented that the sensation was 'strange' or 'not very comfortable'.

To obtain good data quality and a better experience for the subject, it is important to provide proper information in advance of the procedure. I told all the subjects about the vibration and how long it would last. I also ran a test vibration that lasted less than ten seconds before the actual MRE scan. This way, I prepared the subjects for how the vibration would feel and asked them if they were comfortable with going through with the MRE exam.

MRI in general is sensitive to artifacts and MRE is also affected by such general artifacts. For example, one patient was excluded due to artifacts from a cranium fixation item from an earlier surgery. The presence of this object led to susceptibility differences, causing signal loss in the magnitude images. In another study, a meningioma was so densely calcified that it barely had any MR signal, disqualifying the patient from MRE.

In Paper I, we found that the MRE data quality was higher in the brain regions lying closest to the skull, and decreased toward the center of the brain. As shear waves propagate from the skull inward, the waves are attenuated, causing a lower MRE signal for the central regions. Most brain MRE studies use a vibration frequency of 50–60 Hz to balance the trade-off between depth of penetration, resolving power and noise levels. A slightly lower vibration frequency might lead to higher data quality in the central brain, as lower frequency waves are less attenuated than higher frequency waves [23].

There is no consensus as to which measure to use for signal-to-noise ratios

in MRE data [24]. Besides the one that we use, there are several alternatives: phase-to-noise ratio, displacement-to-noise ratio, and octahedral shear strain signal-to-noise ratio [30, 136]. Further standardization of how to report data quality and recommended cutoff values would be valuable to make MRE studies more comparable. Sharing of raw data could also enable research reproducibility and method comparison. To this end, we have shared our MRI data from both healthy subjects and patients with GBM on the open respository Zenodo: DOI 10.5281/zenodo.4926005 [137].

6.2 MRE of the healthy brain

In Papers I and II, we used data from healthy subjects to examine the healthy brain and its subregions.

We found white matter to be stiffer than gray matter. This is consistent with the findings in most publications on MRE in the healthy brain [40, 124, 138–141]. This can be explained by the fact that white matter consists of bundles of myelinated axons and therefore is more structured than gray matter [40].

We found cortical gray matter to be stiffer than deep gray matter. This is different from what was measured in a study of 134 healthy subjects, where deep gray matter was reported to be stiffer than white and cortical gray matter [40]. An earlier study reported that stiffness was lower in deep gray matter than in white matter [140], while a third study found that stiffness of white and gray matter was very similar in both adults and pediatric subjects [96]. This last study also noted a data quality bias in the calculations due to the attenuation of the applied shear waves causing low MRE signal in the central regions of the brain, similar to our findings [96, 142]. The studies described above used a higher resolution than we did, with 1 mm^3, 2 mm^3 and $2mm \times 2mm \times 3mm$, respectively. With our current image resolution in MRE ($3.1mm \times 3.1mm \times 3.1mm$), we expect some partial-volume effects. This might contribute to less precise measurements in small regions and thin structures, such as the cerebral cortex, which is in the order of 2.5 mm [143]. In addition, neighboring voxels are used for calculating spatial derivatives in the stiffness reconstruction. The ventricles are filled with cerebrospinal fluid, which is not viscoelastic, and this leads to very low shear modulus values in these regions [96]. We excluded these voxels from the analysis, but the proximity of deep gray matter regions to the ventricles may have contributed to partial volume effects.

In addition to differing resolutions, all studies described above use different MRE hardware and reconstruction methods. It is therefore challenging to conclude about the reasons for the discrepancies between studies.

In Paper II, we also examined possible correlations between MRE and functional parameters at the brain subregion level. We did not find a simple relationship between biomechanical and functional parameters in the healthy subjects. When pathology causes changes in tissue microstructure, the relationship between properties can change. A study of hippocampal stiffness and ADC in patients with Alzheimer's disease and healthy controls found an

inverse correlation between both $|G^*|$ and ϕ, and mean ADC in the hippocampus when considering patients and healthy controls together [144]. Considering only the healthy subjects in their study, no clear correlation was observed, which is similar to our results in the hippocampus. Yeung *et al.* similarly found that brain stiffness did not vary with FA or ADC in a study on both children and adults [96]. A third study performed MRE and DTI in specific regions of white matter and found a negative correlation between G'' and radial diffusivity in the corpus callosum and corona radiata, and a positive correlation between G'' and FA in corpus callosum. The only correlation between G' and the DTI measures was a positive correlation between G' and radial diffusivity in corpus callosum [124]. The lack of correlation between MRE and DTI measures in our study could be due to the averaging over all white matter. Hetzer *et al.* did not find a significant correlation between CBF and stiffness or viscosity in deep gray matter structures in the healthy brain, consistent with our findings [145].

The perfusion imaging in patients was performed by DSC, while ASL was used in healthy subjects. This hindered direct comparisons between the two groups in terms of perfusion. ASL is noninvasive, in contrast to DSC, where a contrast agent must be administered intravenously. In a potential future study comparing MRE and perfusion in both patients and healthy subjects, ASL could be used for all participants. The acquisition of ASL could further be improved by employing a state-of-the-art 3D ASL sequence. Compared to the 2D technique used in our study, a 3D acquisition would be quicker and improve background suppression [15]. Because ASL in general has low sensitivity to the subtle perfusion levels in white matter, our study includes ASL measurements only in deep and cortical gray matter regions [15]. White matter was used as a region for measurement normalization in patients, but could not be used for normalization of perfusion measurements in healthy subjects.

A contralateral region of white matter which showed no pathology on the anatomical images was used as a normalization region for the patients. However, G' and G'' in this region differed significantly from the measurements in white matter in healthy subjects. This could be due to the age differences between the two cohorts. The median age of the healthy subjects in our study was 25 years, and the median age of the patients was 53 years. The difference between the median white matter G' between patients and healthy subjects was 0.22 kPa, corresponding to -0.008 kPa/year (ranging from -0.002 to -0.012 kPa/year). It is well documented that adult brain stiffness decreases with age [35–39]. A study found that the decrease in stiffness varied with brain region, and ranged from -0.014 $\pm$ 0.002 kPa/year in the temporal lobe to nonsignificant in deep gray and white matter [37]. In this study, stiffness was defined as $G = \rho \cdot c^2$, ignoring the viscoelastic tissue properties (see Chapter 2.2.6). Another study found that the largest decrease in $|G^*|$ was in sensorimotor areas, with a decrease of -0.0136 $\pm$ 0.0016 kPa/year, and -0.008$\pm$0.0025 kPa/year in the deep gray and white matter regions [38]. Although stiffness measurements varied between studies, the amount of change is roughly comparable between our studies and can explain the differences in the two study populations.

It is common to use relatively young volunteers in studies of healthy subjects,

in part because they are easy to recruit, and because there is on average lower variations between young subjects, an important point for a test-retest study. Had we instead used an age-matched cohort of healthy subjects, it could have shed light on whether the differences we observed were caused by age or possibly that the patient's NAWM is affected by the disease. The age dependency of stiffness is one reason to normalize measured values to values in NAWM rather than use absolute G' and G'' values measured in kPa for tumors.

For healthy subjects, the 19 MRE slices were positioned in an identical region of the brain for all scans. The same coverage and angulation was used for all patients, but the slices were placed symmetrically around the contrast-enhancing tumor. This means that the part of the brain that was imaged was not identical between patients or between patients and healthy subjects. Therefore, different portions of the white matter were imaged between the patients and between the groups. This could also contribute to nonidentical MRE measurements of NAWM between patients and healthy subjects.

In Paper I, there were six female and nine male subjects. In Paper II, there were eight female and nine male subjects. In our studies, we did not consider potential sex differences in brain stiffness. Sex differences in the biomechanical properties of the healthy brain have been reported, but are not found in all studies [35, 36, 38]. Potential studies exploring differences between sexes should include more subjects than in our studies, as any effect is expected to be small.

6.3 MRE of GBM

In Paper II, we found that both G' and G'' were significantly lower in the tumor than in the NAWM of patients. Similarly, in Paper III, both mean $|G^*|$ and ϕ were lower in the tumor than in NAWM (with some overlap between patients in the two studies). This is consistent with previous reports: Gliomas have been found to have lower viscoelastic properties than normal brain tissue [80–83, 85]. A reduction in both G' and G'' can be interpreted as a softening of the mechanical rigidity of the tissue. A decrease in the ratio between the two, when G'' is reduced more than G', indicates that the material turns more springlike. It has been proposed to interpret such a change in ϕ as a reduction in the complexity of the tissue architecture and the degradation of the tissue [146]. This has not been shown at the molecular level.

Our results related to FA, ADC, and CBF are consistent with previous findings in the literature. We observed lower values of FA in the contrast-enhancing and necrotic tumor, and in the hyperintense FLAIR region, relative to NAWM. This is expected as glioma infiltration disrupts the organization of white matter tracts, which is reflected in a reduction in FA. Regarding ADC, we found high values in the edematous and necrotic regions, suggesting the presence of unrestricted water movement [69]. Finally, our results showed high CBF in the tumor compared to NAWM. Newly formed tumor vessels are typically leaky and structurally abnormal, known to cause high local tissue blood volume and irregular blood flow [147]. Furthermore, our CBF results also illustrate

the heterogeneity between patients: The patient with the most vascularized tumor had three times higher normalized CBF in the contrast-enhancing tumor compared to the least vascularized tumor.

6.3.1 Relationship between biomechanical and functional parameters

Contrary to our expectations, we found no evidence of association between region-wise mean values of biomechanical and functional parameters in patients in Paper II.

Cancer-related factors such as cellularity, increased vessel density, and interstitial fluid pressure are hypothesized to influence macroscopic tumor stiffness [83]. ADC is a measure of cellularity, and FA measures white matter tract integrity. When cellularity and integrity of the white matter tracts change in the tumor, this should affect the biomechanical properties of the tissue. Tumor stiffness is also expected to be influenced by the architecture of the blood vessels [148]. However, we found no correlation between the regional mean values of biomechancial and functional parameters. A study using animal models also noted a lack of correlation between MRE parameters and cellularity [149].

Due to the proliferation of cancer cells and tumor growth, solid pressure is also increased in tumors [150]. Both increased interstitial fluid pressure and solid pressure lead to decreased treatment efficacy and may promote tumor progression and increased invasion [150]. There is currently no method to measure tumor pressure *in vivo*, but a study using MRE to infer tumor pressure shows promising results in phantom data [151].

The lack of measured correlation between measurements (for instance between G' and CBF) on the region level (such as mean values in the contrast-enhancing tumor) may be due to small sample size and low power. However, it may also be due to the spatial variation of biomechanical and functional properties within brain regions. If tissue perfusion is related to diffusion and stiffness properties, the relationship might be more complex than what can be observed via mean values. Taking the spatial distribution of all voxels into account, we considered an indirect measure of correlation between parameters in Paper II. Regression models were made of all voxels in the patient brains. We constructed a model of perfusion as a function of ADC and FA, and investigated the effect of including MRE parameters in the model. Even in a simple linear model, MRE added to the performance of the model. The model showed that CBF decreased when G' and G'' increased, an effect that could be caused by vessels being compressed by stiff tissue and therefore reduced perfusion [150].

Of course, there might be a more complex relationship between the tissue characteristics. A linear model is probably too simple, but has the advantage that it is interpretable; we can see from the resulting model that CBF increases when G' and G'' decreases. We also tested a random-forest model using machine learning. Such models generally perform better at prediction than classical linear regression models, but are less interpretable [152]. As measured by the

root-mean-square error, the random-forest model performed better than the linear model, and again the model performed better by including G' and G''.

6.3.2 The peritumoral zone

All patients included in Paper II had a region of nonenhancing hyperintensity on FLAIR images (labeled 'edema' in the paper and the following discussion). In this peritumoral region, the median G' was similar to in NAWM (p=0.6), while G'' was 16 % lower than in NAWM (p<0.01). FA was 48 % lower (p<0.05) and ADC was 53 % higher in edema than in NAWM (p<0.01). CBF was similar in edema and NAWM (p=0.3).

To investigate any infiltration outside the contrast-enhancing tumor, we studied the spatial distribution of the biomechanical and functional parameters from the tumor core out to the tumor edge. This was done by calculating smoothed radial gradients of mean values from all voxels in increasing radii from the tumor core in regions segmented as necrotic tumor, contrast-enhancing tumor, and edema. We found that the properties of the tissue in the edema had characteristics different from those of the NAWM, but that the properties approached those of the healthy tissue further out in the edema. The gradients did not show an abrupt edge when going from the contrast-enhancing tumor to the edema, illustrating the infiltrative character of the tumors.

To investigate the possibly infiltrated area outside the tumor and the edema, we similarly made gradients from the outer edge of the edema radially to three cm outside (Figure 5.2). Here, the measurements gradually approached those for NAWM. For some patients, abnormal tissue measurements were also found even further away from the tumor core, in regions that appeared normal on anatomical scans, implying that infiltration may extend beyond the increased FLAIR signal. Although we have some partial volume effects at our current resolution, they cannot explain the measurements several cm from the lesion.

One other study has examined the peritumoral area of GBM by MRE [81]. Here, a perifocal zone was defined as a three-pixel wide rim outside the tumor, partly overlapping with edema. The authors did not find significant differences in $|G^*|$ between this zone and the tumor, but ϕ increased in the perifocal region, compared to the tumor. They found a significant correlation between $|G^*|$ in the tumor and the perifocal region, suggesting the extension of the viscoelastic properties of the tumor to surrounding tissue [81]. This supports our findings.

For simplicity, the term edema was used in Paper II, but as this region also may contain infiltrating tumor cells, edema is not a completely accurate description. In Paper III, we hence avoided the term edema to describe these regions.

6.3.3 Tumor heterogeneity

In Paper II, we segmented the tumor into contrast-enhancing and necrotic parts. We found significantly lower G' and G'' in necrotic regions of the tumor than in the contrast-enhancing tumor regions, showing that the heterogeneity of GBMs

is also apparent in their biomechanical properties. The low values measured in necrotic regions may be caused by necrosis leading to tissue liquefaction [153]. Low values of both elastic and viscous properties in necrotic brain tumor regions have also been found by MRE in animal models [149, 153], in shear wave elastography using ultrasound [154, 155] and by atomic force microscopy (AFM) [156].

In a longitudinal MRE study in glioma mouse models, Schregel *et al.* found that tumors became softer and more heterogeneous over time as the cancer progressed [153]. Specifically, the soft subregions of the tumor were characterized by high heterogeneity. Stiffer subregions of the tumor differed in histopathological characteristics from the central tumor core, but differently from case to case. In one animal, stiffer tumor regions corresponded to a higher density of viable tumor cells and in another animal to a slightly elevated microvessel density [153].

Why is tumor heterogeneity important? Molecular heterogeneity in cancer is believed to contribute to the poor prognosis for patients. GBMs contain multiple distinct populations of tumor cells with the potential to convey survival advantage and resistance to therapy, and these can be selected and enriched through successive cycles of treatment [63]. Spatial heterogeneity can confound histopathological classification, which is typically based on a single biopsy. Additionally, spatial heterogeneity may have a large impact for targeted therapies if the biopsy is not taken from a representative part of the tumor. Mechanical heterogeneity within a tumor may also contribute to the intratumoral heterogeneity of tumor cells, which again may affect tumor evolution [157].

In Paper III, we further examined the tumor heterogeneity by measuring stiffness in different locations in the tumors. Even if the tumor as a whole had a mean stiffness value lower than NAWMW, we found that the biopsies with the highest stiffness within each tumor expressed genes that code for the reorganization of the ECM. That softer tumor regions, in contrast, expressed genes related to normal neuronal functions illustrates the tumor heterogeneity: some parts of the tumor may be more aggressive, while others are in a more inactive state.

Imaging has the unique potential to assess tumor heterogeneity before surgery. If we could obtain biomarkers that pinpoint tumor malignancy and hence patient survival, this would be useful in guiding surgery, and particularly aid in deciding which parts of the tumor biopsies should be taken from.

6.4 Understanding (more of) GBM stiffness

For nonbrain cancer, there is a consensus that solid tumors are associated with tissue stiffening [150, 158]. In breast tumors, increased tissue stiffness is associated with an invasive phenotype and can compromise treatment [159]. Malignant breast tumors are stiff due to their modulated ECM being rich in cross-linked collagen fibers [160].

The characteristic softness of malignant brain tumors stands out compared to other forms of cancer. However, the brain itself is also much softer than

other body tissues [161]. Compared to the body, the healthy brain ECM is characterized by high concentrations of hyaluronic acid and scarcity of fibrillar networks such as collagen, fibronectin, and vitronectin, and basement membrane proteins such as laminin, which are only found in the vascular or perivascular space [162, 163]. In gliomas, this may change, and levels of laminin, collagen IV and fibronectin increase [164].

Previous MRE studies of glioma present several hypotheses to explain the apparent softness of gliomas. The shear modulus is interpreted as capturing the degree of microstructural integrity of tissues [165]. Demyelination and degradation of the ECM structure lead to a decrease in tissue stiffness [166]. Simon *et al.* conclude that tumors soften compared to healthy tissue due to a reduction the cross-linking network structure [80]. The rapid and chaotic tumor cell growth decreases structural anisotropy, causing lower viscoelastic properties in brain tumors [162].

In a preclinical study of GBM, decreased $|G^*|$ in necrotic tumor subregions was explained by hemorrhage and necrosis that compromised microstructural integrity and caused tissue liquefaction [153]. In the study, $|G^*|$ and ϕ values increased in subregions consisting of densely packed viable tumor cells or blood vessels, where the mechanical network remained comparatively intact [153].

Solid tumors elsewhere in the body typically become aggressive by their displacing growth and metastatic spread [85]. The softening of tumors has generally been considered an obstacle to cancer cell proliferation [167]. The soft nature of gliomas shows that the infiltrative mechanism must be different in these tumors. Streitberger *et al.* propose that the abnormally low ϕ values measured in GBM suggest that the fluid properties of the tumor may be the mechanism for infiltrative tumor growth [85]. Their study compared GBMs to meningiomas, which are predominantly benign brain tumors. Although stiffness was reduced in both types of tumors, compared to healthy tissue, ϕ was only reduced in GBMs [85]. In their review of MRE of brain tumors, Bunevicius *et al.* state that ϕ might be more affected by malignant tissue changes than the stiffness [32]. *In vitro*, the viscosity of the microenvironment has been shown to affect the efficacy of temozolomide treatment in GBM cells [168].

In Paper III, we found that the stiffer regions within the overall soft tumors were associated with more aggressive behaviour. We hypothesize that regional stiffening might occur in parts of the tumor as it evolves and remodels its environment. However, while the biomechanical properties of the tissue might contribute to the tumor development, they might also be a product of this behavior, such as an overall softening caused by tissue degradation. As changed biomechanical properties could be both cause and effect of tumor aggressiveness, it is not possible to conclude from our results that for instance a further tissue softening would improve patient outcome.

6.4.1 The surgeon's evaluation of stiffness

MRE is usually compared to manual palpation. How do we explain the lack of correlation between measured $|G^*|$ and the surgeon's stiffness evaluation in

Paper III?

Previous studies have compared neurosurgeons' evaluation of tumor stiffness with MRE in meningiomas and in pituitary adenomas, and found that measured stiffness correlated positively with the surgeon's evaluation [169–172]. A study of MRE in 34 patients with meningiomas, pituitary adenomas, vestibular schwannomas and gliomas found a correlation between the surgeon's grading and the maximal measured stiffness in the tumor, but not the mean tumor stiffness [84]. A recent intraoperative study using ultrasound shear-wave elastography in a wide range of brain tumors also found a correlation between the measured stiffness and the surgeon's evaluation [173]. However, in these studies, the mean stiffness value for the entire tumor was reported. While gliomas are reported to be soft, both meningiomas and pituitary adenomas are known to vary in stiffness, from very firm to very soft tumors [171, 174]. In addition, the consistency of meningiomas has been reported as mostly homogeneous [171].

In our study, we did not ask the surgeon to rate the entire tumor as stiff or soft. As all tumors had a lower mean $|G^*|$ than healthy tissue, the whole-tumor comparison is of less interest. It is rare to find published descriptions of how surgeons experience the stiffness of GBM, but several papers anecdotally mention that surgeons find high-grade gliomas to be stiffer than the healthy brain [78, 79, 175]. The neurosurgeon co-authoring my papers has stated that GBMs typically are soft, but may have stiff — even hard — regions. Previous MRE studies of patients with glioma did not correlate measurements with the surgeon's evaluation, stating that the subjective haptic impression of the surgeons in the study varied widely, preventing them from using their scores as a gold standard for tumor consistency [81, 82].

This illustrates the challenge of comparing MRE measurements with the surgeon's evaluation, and especially for small ROIs. I believe that an experienced neurosurgeon's evaluation of whether tumor tissue is softer or stiffer than normal brain tissue is reliable, but this measure does not appear to be directly comparable with MRE measurements. MRE exclusively measures the shear properties of tissue. When a material is probed using surgical tools to assess consistency, a more complex process takes place, as the tissue is not exclusively sheared, but also compressed. Therefore, the two measures are not completely similar.

Additionally, the MRE was acquired preoperatively, with the skull and dura still intact. Tumor growth is known to compress surrounding tissue, generating solid stress due to tumor growth and swelling [176, 177]. Even though GBMs may be soft, their expansion within the skull may cause the tumors to compress ventricles and shift the brain midline [178]. The strain generated by a pressurized tumor has been shown to shift the measured shear modulus of the surrounding host tissue, due to the nonlinear stress-strain behavior typically exhibited by soft tissue when subjected to large-scale deformations [179]. Capilnasiu *et al.* have shown that materials appear increasingly stiffer by MRE with increasing compression and also that the heterogeneity of the stiffness increases with compression [180].

In one of the studies comparing MRE and the surgeon's stiffness evaluation in patients with meningioma, the tumor with the highest measured stiffness was

evaluated as mostly soft by the surgeon [169]. The authors noted that this may be due to compressed brain tissue behaving stiffer than tissue without a preload. That compressive stress increased brain stiffness as measured by MRE was also shown in a porcine model [181]. Additionally, an *in vitro* study by Pogoda *et al.* found that glioma tissue was not stiffer than normal brain when measured at low strains without compression, but that compression caused glioma tissue samples to became stiffer than normal brain [182]. Opening the skull during a craniotomy affects the pressure conditions in the brain. This may affect the perceived stiffness of the tissue compared to the MRE measurements, which were performed while the skull was still intact. Perfusion and drainage may also be different from those in the preoperative situation.

Further work is warranted to probe the effect of compression on the tissue biomechanics and to understand the effect of these forces on the tumor environment.

6.4.2 Microscopic stiffness measurements

MRE measures stiffness on a macroscopic scale. However, stiffness has also been examined on the single-cell level. The findings on different scales may not agree. For example, for breast cancer, malignancy is found to be associated with increased stiffness measured on the macroscale, whereas single-cell analysis has shown that cancer aggressiveness is associated with softening of cancer cells [183].

For GBM, single glioma cells were measured by a microfluidic cell squeezer device and found to be stiffer than benign brain cells [184]. Another study using a microfluidic device found that compared to healthy astrocytes, most types of astrocytoma cells were stiffer than their healthy counterparts [185].

On a larger, yet still microscopic scale, AFM quantifies local stiffness properties at the molecular level across an entire biopsy using [183]. Using AFM, Miroshnikova *et al.* found GBMs to be stiffer than low-grade gliomas, which again were stiffer than nontumor gliosis tissue. The stiffness of healthy or normal-appearing brain tissue was not measured in their study. The study also reports a correlation between the proportion of highly stiff areas within a GBM tissue and worse patient prognosis, suggesting that elevated ECM stiffness can promote GBM aggression [186]. This supports our findings. Luo *et al.* found GBMs to be stiffer than IDH1-mutated WHO grade 4 gliomas by AFM, and further found the tumor area to be stiffer than a nontumor area, with lowest stiffness in the necrotic area [156].

A third study using AFM found that GBM tissue was almost three times stiffer than healthy tissue and much more heterogeneous in terms of stiffness [187]. A stiffer mechanical microenvironment, measured by AFM, has been shown to promote glioma aggression [188].

However, the literature is not conclusive as to whether GBM is associated with softening or stiffening of tissue on a microscopic scale. Using AFM in an animal model, GBMs have been found to be softer than normal brain [189]. Another study found GBM cells to be softer compared to normal fibroblast

cells seeded on polymeric nanostructures [190]. In a study where GBM and WHO grade 3 astrocytoma cells were compared using two different microrheology techniques, GBM cells were softer than WHO grade 3 cells on a global level, but stiffer at the intracellular level [191].

AFM has also been used to investigate the viscoelastic properties of necrotic and non-necrotic regions of GBM tumors. Ciasca *et al.* found the non-necrotic tumor core to have a markedly different biomechanical response than the necrotic regions of the tumors. While necrotic regions had quite a uniform spatial distribution, the non-necrotic regions appeared highly heterogeneous. The authors suggest this shows a complex tissue organization, consisting of structures with different biomechanical responses [78]).

It is also contested whether tissue softening or stiffening is associated with increased malignancy. *In vitro*, cells can proliferate more or less in stiffer hydrogels, depending on whether the hydrogels are in 2D or 3D [79, 192]. As multiple studies on glioma stiffness have led to conflicting results *in vitro* and *in vivo*, Pogoda *et al.* suggest that biomechanical changes in gliomas might depend more strongly on geometry or measurement conditions than for other tumor types. The macroscopic rheometry measurements of excised specimens may not reflect the local stiffness encountered by cells in intact tissue. For instance, *in vivo* microstructures such as blood vessel boundaries can exert greater resistance to cell-generated forces than the average stiffness measured for the tissue as a whole [193].

AFM only measures elastic properties without taking into account viscous effects [187]. In contrast to MRE, AFM is an indentation method, which probes the tissue in a quasi-static manner [194]. As the viscoelastic properties of tissue depend on the frequency at which they are measured, different results in AFM and MRE studies are expected. In addition, tissue in pathological states may have different frequency characteristics [33, 165]. In that case, the contrast between healthy and pathological tissue may differ between AFM and other microrheology techniques operated at zero frequency, and MRE.

Finally, in contrast to the microscale techniques mentioned above, MRE measures viscoelasticity both *in vivo* and *in situ*; without removing the tissue of interest from its surroundings.

There may be correlations between stiffness measurements using different techniques and on different scales. Sauer *et al.* compared macroscopic MRE measurements of brain tumors to single-cell measurements of stiffness, and found that single cell stiffness was correlated with $|G^*|$, but that viscosity parameters of individual cells and bulk tissue were not correlated [195]. More work is needed to understand the relationship between the microscopic stiffness of cancer cells and the tumor microenvironment, and the macroscopic whole-tumor stiffness in gliomas.

6.4.3 Genetical meaning of MRE signal

In Paper III, we observed a general softening of GBM tumors. Most biopsies had a lower $|G^*|$ than NAWM, while some had a higher $|G^*|$. Biopsies were classified

as 'stiff' or 'soft' compared to the average biopsy stiffness value for each patient to account for differences between patients and between groups in the statistical analysis. This way, all patients had at least one biopsy classified as 'stiff' and one as 'soft'.

When comparing the two groups defined in this way, the 'stiff' biopsies expressed genes coding for remodeling of the ECM, while 'soft' biopsies expressed genes that coded for more normal neuronal functions. Invasive glioma cells are known to actively remodel their microenvironment [196]. Tumor development is characterized by changes in tissue stiffness due to extensive ECM remodeling processes, including degradation of ECM proteins by enzymes, overproduction of ECM proteins, or secretion of novel ECM proteins by tumor stromal cell types [197]. We hypothesize that regional stiffening might occur in parts of the tumor as the tumor evolves and remodels its environment.

The metabolic process and binding of collagen was also associated with 'stiff' biopsies. Levels of collagens in the healthy brain are low compared to the rest of the body, but in glioma, collagen levels are elevated and play a vital role in driving tumor progression [198]. Gene sets associated with innate immune processes, such as neutrophil activation, were also upregulated in 'stiff' biopsies, indicating that these are active regions of the tumor [199].

Several of the genes found in our study to be upregulated in 'stiff' biopsies have previously been shown to play a role in glioma malignancy. NRP1 and DAB2 have been linked to glioma progression [200, 201], PECAM1 correlates with GBM aggressiveness [202], CD163 is positively associated with the glioma malignancy grade [203], and Flt1 promotes invasion and migration of GBM cells [204]. CR1, PLAGL1, COL4A1, and COL5A2 have all been shown to correlate with shorter survival [205–208].

To understand what our findings mean for patient outcome, we used independent patient cohorts to study the importance of genes expressed in 'stiff' tumor biopsies. We found that median survival was significantly shorter in patients with tumors that expressed these genes. This indicates that the genetic and molecular processes that we detect in 'stiff' tumor biopsies play a role in the malignant progression of tumors. If MRE can provide a biomarker to identify particularly aggressive tumor regions, this may help guide surgery and identify pathways for targeted therapies. For instance, the genes CD163 and COL4A1 were both overexpressed in 'stiff' biopsies and have been proposed as new therapeutic targets for glioma [203, 207].

6.5 The potential gain of MRE in GBM

Initially, viscoelasticity changes measured by MRE was envisioned as a potential direct predictive marker for brain tumor malignancy [80]. For gliomas, we are not quite there yet. A review paper on brain tumor MRE reported a substantial overlap of the reported shear modulus values across different brain tumor diagnoses. Hence, based on the clinical evidence so far, MRE is not yet

recommended for discriminating between different types of brain tumor in the clinical environment [32].

Although MRE cannot currently be used for tumor diagnosis on its own, investigating the biomechanical properties of GBM helps understanding the role mechanical forces play in the course of cancer. Mechanical forces have received much less attention than genes and other biomolecules in cancer studies. But considering only genes and biomolecules may be 'trying to write a book with only half the letters of the alphabet' [209]. The mechanical tumor microenvironment with its physical stimuli may affect cells as dramatically as biochemical and genetic cues do [78].

Mathematical models of tumor growth are used to study and predict tumor progression [210]. Including MRE data in a mathematical model results in more accurate predictions of the distribution of mechanical stresses in tumors, and the developments related to this stress, such as tumor vasculature heterogeneity and drug delivery [211].

Our findings in Paper III indicate that MRE can provide *in vivo* information about more aggressive regions of the tumor. Using advanced MRI techniques, we can obtain abundant information about the tumor before a possible surgery. If the tumor is a suspected GBM, a total resection is planned. However, the extent of resection must be balanced against preservation of brain tissue important for function. If preoperative MRI could provide *a priori* information on aggressiveness in different parts of the tumor and help guide tissue sampling, that could be of great advantage. In the event of tumor recurrence, the patient may not be reoperated. Imaging biomarkers that provide important information on tumor subregion aggressiveness may then be valuable in the planning of radiotherapy.

All cancer research is ultimately about the pursuit of new possible treatment strategies. In extracranial tumors, some treatment approaches target solid stress in the tumor microenvironment. In breast and pancreatic tumors, angiotensin inhibition by the drug losartan decompresses tumor blood vessels and reduces stromal collagen [212]. This has been shown to increase vascular perfusion and improve drug delivery.

We are currently performing an ongoing clinical trial at Oslo University Hospital on the use of losartan in patients with GBM and brain metastases (ClinicalTrials.gov Identifier: NCT03951142). The hypothesis of the study is that losartan will improve the effect of traditional cancer treatment by alleviating solid stress of the tumor microenvironment to improve tissue perfusion. MR imaging, including MRE, will be used to assess the effect of the drug [213].

6.6 Technical considerations and limitations of MRE

MRE of the brain is not yet routinely available and its use is currently limited to research.

After decades (liver) and years (brain) of use, there is no reported risk associated with the MRE technique. In general, patients tolerate the mechanical

vibrations well [32]. The frequency of the vibrations is typically between 20 and 60 Hz, with a vibration amplitude on the order of 100 µm or less. The sensation has been compared to holding an electric toothbrush to one's head [32]. For the gravitational transducer used in our studies, the force exerted by the transducer scales linearly with the mass within the transducer and quadratically with rotational frequency [21]. Therefore, tissue displacement, and hence MRE signal, could be increased by increasing the rotating mass or the frequency. We chose both to be at a comfortable level of vibration for the patients.

Current acquisitions are typically between five and ten minutes [135]. With a longer scan time, we could have achieved higher resolution and increased brain coverage using our technique, but this should be weighed against possible patient discomfort in what is already a lengthy scan session.

Continued focus on hardware, acquisition sequences, and reconstruction methods will bring the technique closer to clinical viability. For instance, there are several proposed methods that accelerate scan time significantly [214–216]. With quicker data acquisition, the gain can be used for faster scans, greater coverage, or better resolution.

In addition, there are a few technical considerations that must be taken into account in the transition to a more clinically available technique.

6.6.1 Frequency dependency

In all three of our studies, the MRE was performed using a vibration of 50 Hz. However, as mentioned in Chapter 2.2.6, the viscoelastic properties of tissue makes the shear modulus dependent of frequency. Many studies use vibration frequencies of 50 or 60 Hz and the results are comparable at the same frequencies. However, one should be careful to check at which frequencies the experiments were carried out with when reading the literature, whether it is MRE studies performed at different frequencies, or quasi-static rheology techniques.

The frequency dependence of the shear modulus can also be explored as a potentially useful biomarker. Several studies perform MRE at multiple frequencies in order to probe this behavior [165], but the frequencies spanned are usually in a narrow range of 20–60 Hz, limiting the determination of material model coefficients [24]. Other studies acquire data using multiple frequencies to improve data quality, and report an average stiffness over the used frequencies [131].

6.6.2 MRE parameters

MRE measures the complex shear storage modulus, $G^* = G' + iG''$. Some articles report measurements of the shear storage and loss modulus G' and G'', others report the magnitude $|G^*|$ and the shear phase angle ϕ. In Paper II, we reported G' and G'' in order to separate the mechanisms of energy storage and loss. In Paper III, we report $|G^*|$, as it is believed to be the MRE parameter most closely related to the haptic distinction between stiff and soft materials [23]. For the mean tumor values, we also provide ϕ. However, the calculation of

ϕ is more sensitive to noise and was considered less robust when only using a few voxels per biopsy [23].

In soft tissue, the shear storage modulus G' is larger than G'', and hence G' dominates $|G^*| = \sqrt{G'^2 + G''^2}$. The maps of G' and $|G^*|$ often resemble each other, as do maps of G'' and ϕ, illustrated in Figure 2.4. Ideally, we would include both sets of parameters in the papers and perform all analyses using both sets of parameters. This would increase comparability within the MRE milieu, but in order to communicate a comprehensive story in a paper, it is more practical to pick one pair and use the term stiffness, which is more intuitive to a broad audience.

To further complicate things, these are not the only reported MRE measures used in the literature. Many articles report the so-called shear stiffness $\mu = 2|G^*|^2/(G' + |G^*|)$ and the damping ratio $\xi = G''/2G'$ [40]. Other research groups acquiring multifrequency data require rheological models to analyze the data and therefore report model-dependent measures of stiffness and viscosity [24].

The word 'stiffness' is commonly used, as it makes sense to most people and clinicians [24]. Using a familiar word makes it easier to communicate results and concepts, but stiffness is not a precise term. As I have shown, the stiffness measured by MRE may differ from the stiffness assessed manually by a surgeon. As the measurement method and scale also affects results, using the term stiffness may be confusing. There are many types of stiffness, such as compressional stiffness, bending stiffness, and torsional stiffness [217]. Shear modulus is a property of the constituent material, but in in biomechanics and engineering applications, stiffness refers to a property of a structure, depends on the physical dimensions that describe that structure, and has units different from the shear modulus [24].

In each of the papers, I have defined which parameters I refer to as stiffness. The specific parameters G', G'', $|G^*|$ or ϕ were used when presenting results, and I have tried to mostly use the term stiffness when making qualitative statements, as recommended in a recent overview of guidelines for MRE [24]. In Paper III, I have used the terms 'stiff' and 'soft' to separate MRE measurements from the surgeon's evaluation, and to emphasize that these are labels defined relative to the other biopsies for each patient, rather than quantitative values.

6.6.3 Anisotropy

Both MRE reconstruction methods used in our papers, and most others, assume tissue isotropy. However, brain tissue is actually anisotropic, especially in white matter. A study assessing both isotropic and anisotropic stiffness in white and gray matter, found a strong positive correlation between isotropic and anisotropic stiffness in gray matter, while no significant correlation was found between isotropic stiffness and anisotropic stiffness in white matter [218]. This means that assessing an anisotropic measure of stiffness would add value to the analysis, especially for white matter. Disease-related biological processes may

affect anisotropic parameters with more sensitivity than the averaged stiffness recovered through isotropic inversion [219].

6.7 Limitations in our work

The applicability of the results from our studies is limited by the relatively small sample of patients and healthy subjects.

In Paper III, the sample size of biopsies per tumor is also small. With a handful of biopsies taken of a large and heterogeneous tumor, it is difficult to ensure that the sampling is representative of the whole tumor. While the surgeon had access to the MRE data prior to surgery, the MRE images were not consulted during surgery, and the chosen locations of the biopsies were based on varying tissue stiffness as evaluated by the neurosurgeon. The classification of biopsies used in the differential gene expression analysis was based on MRE measurements, which did not correlate with the surgeon's evaluation. Had the biopsy locations been chosen based on MRE, we could have sampled tumor regions that differed even more from each other in terms of $|G^*|$.

In traditional linear regression, the number of samples n must always be larger than the number of features p used to describe, or in our case, separate the data points [220]. In molecular biology, it is common to analyse thousands of features, such as genes or proteins, far exceeding the number of biological samples. Even if we had included 200 patients in a study, there would still be many features compared to the number of samples. Machine learning methods can be used for high-dimensional data with thousands of genes, where the number of samples is bound to be smaller than the number of features [221]. Dimension reduction techniques are typically used to overcome this problem. PLS-DA enables the selection of the most discriminatory features in the data to classify the samples [222]. By using Lasso regularization to reduce the number of features, sparse PLS-DA can be used in the case of $n < p$ [117]. Through repeated cross-validation, the algorithm is run many times with different number of features in the model. There is no exact spot to choose the cut-off of how many features should be used for the classification, but we found that there was no significant improvement with a higher number of features than 22 genes.

We normalized MRE measurements to mean values of all contralateral NAWM. Another normalization option would be to use a mirror ROI in the contralateral hemisphere to study the differences between tumor and healthy tissue [223]. This way, we could have compared the tumor properties not only to white matter, but to the tissue specific for that region. But as the tumors are located in different parts of the brain, results for different patients would be harder to combine or compare. Using a mirror ROI might be a more viable option for tracking a tumor over time.

As mentioned, we expect some partial-volume effects with our current resolution. To reduce interpolation effects due to low resolution, the MRE, diffusion, and perfusion data were all analyzed in their native spaces for the calculation of mean values.

In Papers II and III, tumor and normal tissue ROIs were segmented automatically using a convolutional neural network [103]. Currently, manual delineations of ROIs by neuroradiologists are considered the gold standard. However, manual delineation is a very time-consuming process, and not perfectly reproducible among radiologists. During the last years, computational techniques have enabled increased accuracy and speed of tumor segmentation. The errors of the algorithms are now comparable with human interrater variability [104].

In Paper III, the biopsies were classified as 'stiff' or 'soft' compared to the other biopsies of that patient. Alternatively, the biopsies could be classified as stiff or soft compared to NAWM. However, for some patients, all biopsies were softer than NAWM ($|G^*|_{norm}<1$), while others had both stiffer and softer biopsies than NAWM. Therefore, an absolute division based on $|G^*|_{norm}$ would disregard the information of which patient the biopsies were from and make interpretation less meaningful and useful, as differences between patients could be greater than differences between stiff or soft biopsies. Biopsies were classified using $|G^*|_{norm}$ values rather than the surgeon's division of soft or stiff biopsies because we wanted to examine the biological significance of MRE measurements. We also performed the differential gene expression analysis with biopsies classified according to the surgeon's evaluation, but no significant differences in gene expression was found using this definition of stiff and soft biopsies.

To understand the importance of differentially expressed genes in 'stiff' versus' soft' biopsies, we evaluated independent survival data from public data sets. For these patients, only one tissue biopsy is recorded, and in our analysis, we therefore had to assume this tissue biopsy to be representative of the entire tumor. Unfortunately, there are no biomechanical data for these data sets, so we cannot claim that the tumors in these data sets are stiff or soft. The use of the external data was therefore solely to examine the prognostic relevance of the gene expression signal for patients with GBM.

Chapter 7

Conclusion and future perspectives

7.1 Conclusions

The role biomechanics plays in cancer is gaining more attention, and MRE uniquely enables us to measure tissue biomechanical properties *in vivo*. From our results, we conclude that MRE of the brain is a robust technique, although stiffness estimates depend on how the data is analyzed.

We have shown that the biomechanical properties of GBM differs from healthy brain tissue, and that the characteristic heterogeneous nature of GBM is also found in its biomechanical properties. We found perfusion to decrease with lower G' and G'' in patients. Our analysis of the peritumoral tissue, where tissue displayed abnormal properties several centimeters from the tumor, illustrates the infiltrative nature of the disease.

Through RNA sequencing of tissue from different locations within the tumor, we showed that MRE imaging of GBM can provide unique information about tumor heterogeneity not readily observed on conventional anatomical images. MRE can help identify possibly more aggressive regions of active extracellular matrix reorganization that may influence patient survival.

7.2 Future perspectives

Because there are only a handful studies of MRE in patients with glioma, there are many aspects that should be further examined.

The variation between different GBM tumors can be assessed by performing MRE in a larger cohort of patients with GBM. By following a large group of patients over time, we could explore how the biomechanical characteristics of the tumor affects patient outcome.

No longitudinal study with MRE examinations at several time points has been performed in patients with brain cancer. Such a study would shed light on how the biomechanical properties evolve during treatment and as the disease ultimately recurs. A longitudinal study following treatment could also examine whether MRE can provide additional information to help separate true progression of the disease from the pseudoprogression often occurring after radiation therapy [224].

As a GBM grows, it exerts local pressure on its surroundings and displaces peritumoral tissue. The compression of peritumoral tissue in brain tumor patients is considered a major cause of the patients' life-threatening neurologic symptoms [225]. Using anatomical MR images from several time points, tissue displacement and compression can be quantified, and these measures are associated with

patient survival [176]. Combining compression measurements with MRE in peritumoral tissue could increase the understanding of mechanical forces at play.

By using RNA sequencing in tumor biopsies, we explored the molecular background for the stiff and soft parts of the tumors. Histology analyses of spatially localized biopsies would add to this analysis, and potentially strengthen the association between ECM reorganization and proliferation which we now infer from public data sets.

Combining MRE with other methods can help us understand more of the measured signal. For instance, performing rheometric testing of excised tumors after preoperative MRE could relate the MRE measurements to solid stress [177].

So far, repeatability studies in MRE have been performed using the same MRE hardware and acquisition for all scans. It would also be interesting to compare measurements across systems, by scanning the same subjects using different MRE techniques.

In our studies, our primary aim was to apply the technique in patients and healthy subjects, rather to work on method development. On the technical side, much can be gained by improving the MRE acquisition. For instance, there are several methods for accelerating MRI scans that are suitable for MRE. With data acquisition repeated for several MEG directions and at several time points during the mechanical wave, there is a high degree of data redundancy in MRE [216]. This opens possibilities for sparse sampling of the signal and accelerating scans. Machine learning has the potential to reconstruct full MRE magnitude and phase images from sparsely sampled data. Machine learning could also play a future role in reconstruction of elastograms [226].

Bibliography

[1] Stupp, R. et al. “Radiotherapy plus concomitant and adjuvant temozolomide for glioblastoma”. In: *N Engl J Med* vol. 352, no. 10 (2005), pp. 987–96.

[2] “The Origins of the History and Physical Examination”. In: *Clinical Methods: The History, Physical, and Laboratory Examinations*. Ed. by H.K., W., W.D., H., and J.W., H. 3rd ed. Boston: Butterworths, 1990. Chap. 1.

[3] Provencher, L. et al. “Is clinical breast examination important for breast cancer detection?” eng. In: *Current oncology (Toronto)* vol. 23, no. 4 (2016), e332–e339.

[4] Muthupillai, R. et al. “Magnetic resonance elastography by direct visualization of propagating acoustic strain waves”. In: *Science* vol. 269, no. 5232 (1995), pp. 1854–7.

[5] Bloch, F. “Nuclear Induction”. In: *Physical Review* vol. 70, no. 7-8 (1946), pp. 460–474.

[6] Purcell, E. M., Torrey, H., and Pound, R. V. “Resonance Absorption by Nuclear Magnetic Moments in a Solid”. In: *Physical Review* vol. 69, no. 11-1 (1946), pp. 37–38.

[7] Poustchi-Amin, M. et al. “Principles and applications of echo-planar imaging: a review for the general radiologist”. eng. In: *Radiographics* vol. 21, no. 3 (2001), pp. 767–779.

[8] Vlaardingerbroek, M. T. and Boer, J. A. d. *Magnetic Resonance Imaging: Theory and Practice*. Third Edition. Berlin, Heidelberg: Berlin, Heidelberg: Springer Berlin Heidelberg, 2003.

[9] Flower, M. A. and Webb, S. *Webb’s physics of medical imaging*. 2nd ed. Series in medical physics and biomedical engineering. Boca Raton, Fla: CRC Press, 2012.

[10] Barbier, E. L., Lamalle, L., and Decorps, M. “Methodology of brain perfusion imaging”. In: *J Magn Reson Imaging* vol. 13, no. 4 (2001), pp. 496–520.

[11] Rosen, B. R. et al. “Perfusion imaging with NMR contrast agents”. In: *Magn Reson Med* vol. 14, no. 2 (1990), pp. 249–265.

[12] Boxerman, J. et al. “Consensus recommendations for a dynamic susceptibility contrast MRI protocol for use in high-grade gliomas”. eng. In: *Neuro-oncology (Charlottesville, Va.)* vol. 22, no. 9 (2020), pp. 1262–1275.

[13] Dennie, J. et al. “NMR imaging of changes in vascular morphology due to tumor angiogenesis”. eng. In: *Magn Reson Med* vol. 40, no. 6 (1998), pp. 793–799.

[14] Emblem, K. E. et al. “Vessel architectural imaging identifies cancer patient responders to anti-angiogenic therapy”. In: *Nat Med* vol. 19, no. 9 (2013), pp. 1178–83.

[15] Alsop, D. C. et al. “Recommended implementation of arterial spin-labeled perfusion MRI for clinical applications: A consensus of the ISMRM perfusion study group and the European consortium for ASL in dementia”. In: *Magn Reson Med* vol. 73, no. 1 (2015), pp. 102–16.

[16] Schaefer, P., Grant, P., and Gonzalez, R. “Diffusion-weighted MR imaging of the brain”. In: *Radiology* vol. 217, no. 2 (2000), pp. 331–345.

[17] Le Bihan, D. et al. “Diffusion tensor imaging: Concepts and applications”. In: *J. Magn. Reson* vol. 13, no. 4 (2001), pp. 534–546.

[18] Bashir, M. R. et al. “ACR Appropriateness Criteria® Chronic Liver Disease”. eng. In: *Journal of the American College of Radiology* vol. 17, no. 5 (2020), S70–S80.

[19] Sigrist, R. M. S. et al. “Ultrasound Elastography: Review of Techniques and Clinical Applications”. In: *Theranostics* vol. 7, no. 5 (2017), pp. 1303–1329.

[20] Yin, M. and Venkatesh, S. K. “Ultrasound or MR elastography of liver: which one shall I use?” In: *Abdom Radiol (NY)* vol. 43, no. 7 (2018), pp. 1546–1551.

[21] Runge, J. H. et al. “A novel magnetic resonance elastography transducer concept based on a rotational eccentric mass: preliminary experiences with the gravitational transducer”. In: *Phys Med Biol* vol. 64, no. 4 (2019), p. 045007.

[22] Venkatesh, S. and Ehman, R. *Magnetic Resonance Elastography*. Springer New York, 2014.

[23] Hiscox, L. V. et al. “Magnetic resonance elastography (MRE) of the human brain: technique, findings and clinical applications”. In: *Phys Med Biol* vol. 61, no. 24 (2016), R401–R437.

[24] Manduca, A. et al. “MR elastography: Principles, guidelines, and terminology”. In: *Magn Reson Med* vol. 85, no. 5 (2021), pp. 2377–2390.

[25] Fovargue, D., Nordsletten, D., and Sinkus, R. “Stiffness reconstruction methods for MR elastography”. In: *NMR Biomed* vol. 31, no. 10 (2018), e3935.

[26] Pepin, K. M., Ehman, R. L., and McGee, K. P. “Magnetic resonance elastography (MRE) in cancer: Technique, analysis, and applications”. In: *Prog Nucl Magn Reson Spectrosc* vol. 90-91 (2015), pp. 32–48.

[27] Ehman, E. C. et al. “Vibration safety limits for magnetic resonance elastography”. In: *Phys Med Biol* vol. 53, no. 4 (2008), pp. 925–35.

[28] Muthupillai, R. and Ehman, R. L. “Magnetic resonance elastography”. In: *Nat Med* vol. 2, no. 5 (1996), pp. 601–3.

[29] Manduca, A. et al. “Magnetic resonance elastography: non-invasive mapping of tissue elasticity”. In: *Med Image Anal* vol. 5, no. 4 (2001), pp. 237–54.

[30] Guenthner, C. and Kozerke, S. “Encoding and readout strategies in magnetic resonance elastography”. In: *NMR Biomed* vol. 31, no. 10 (2018), e3919.

[31] Sinkus, R. et al. “Viscoelastic shear properties of in vivo breast lesions measured by MR elastography”. In: *Magnetic Resonance Imaging* vol. 23, no. 2 (2005), pp. 159–165.

[32] Bunevicius, A. et al. “REVIEW: MR elastography of brain tumors”. In: *Neuroimage Clin* vol. 25 (2019), p. 102109.

[33] Parker, K. J., Szabo, T., and Holm, S. “Towards a consensus on rheological models for elastography in soft tissues”. eng. In: *Phys Med Biol* vol. 64, no. 21 (2019), pp. 215012–215012.

[34] Sack, I. et al. “Non-invasive measurement of brain viscoelasticity using magnetic resonance elastography”. In: *NMR Biomed* vol. 21, no. 3 (2008), pp. 265–271.

[35] Sack, I. et al. “The impact of aging and gender on brain viscoelasticity”. In: *Neuroimage* vol. 46, no. 3 (2009), pp. 652–7.

[36] Sack, I. et al. “The influence of physiological aging and atrophy on brain viscoelastic properties in humans”. In: *PLoS One* vol. 6, no. 9 (2011), e23451.

[37] Arani, A. et al. “Measuring the effects of aging and sex on regional brain stiffness with MR elastography in healthy older adults”. In: *Neuroimage* vol. 111 (2015), pp. 59–64.

[38] Takamura, T. et al. “Influence of Age on Global and Regional Brain Stiffness in Young and Middle-Aged Adults”. In: *J Magn Reson Imaging* vol. 51, no. 3 (2020), pp. 727–733.

[39] McIlvain, G. et al. “Mapping brain mechanical property maturation from childhood to adulthood”. eng. In: *NeuroImage (Orlando, Fla.)* vol. 263 (2022), p. 119590.

[40] Hiscox, L. V. et al. “Standard-space atlas of the viscoelastic properties of the human brain”. In: *Hum Brain Mapp* vol. 41, no. 18 (2020), pp. 5282–5300.

[41] Wuerfel, J. et al. “MR-elastography reveals degradation of tissue integrity in multiple sclerosis”. In: *Neuroimage* vol. 49, no. 3 (2010), pp. 2520–5.

[42] Streitberger, K. J. et al. “Brain viscoelasticity alteration in chronic-progressive multiple sclerosis”. In: *PLoS One* vol. 7, no. 1 (2012), e29888.

[43] Herthum, H. et al. “In vivo stiffness of multiple sclerosis lesions is similar to that of normal-appearing white matter”. In: *Acta Biomater* vol. 138 (2022), pp. 410–421.

[44] Lipp, A. et al. “Progressive supranuclear palsy and idiopathic Parkinson’s disease are associated with local reduction of in vivo brain viscoelasticity”. In: *Eur Radiol* vol. 28, no. 8 (2018), pp. 3347–3354.

[45] Murphy, M. C. et al. “Decreased brain stiffness in Alzheimer’s disease determined by magnetic resonance elastography”. In: *J Magn Reson Imaging* vol. 34, no. 3 (2011), pp. 494–8.

[46] Huston J., 3. et al. “Magnetic resonance elastography of frontotemporal dementia”. In: *J Magn Reson Imaging* vol. 43, no. 2 (2016), pp. 474–8.

[47] Murphy, M. C. et al. “Regional brain stiffness changes across the Alzheimer’s disease spectrum”. In: *Neuroimage Clin* vol. 10 (2016), pp. 283–90.

[48] ElSheikh, M. et al. “MR Elastography Demonstrates Unique Regional Brain Stiffness Patterns in Dementias”. In: *AJR Am J Roentgenol* vol. 209, no. 2 (2017), pp. 403–408.

[49] Schwarb, H. et al. “Structural and Functional MRI Evidence for Distinct Medial Temporal and Prefrontal Roles in Context-dependent Relational Memory”. In: *Journal of cognitive neuroscience* vol. 31, no. 12 (2019), pp. 1857–1872.

[50] Patz, S. et al. “Imaging localized neuronal activity at fast time scales through biomechanics”. In: *Sci Adv* vol. 5, no. 4 (2019), eaav3816.

[51] Lan, P. S. et al. “Imaging brain function with simultaneous BOLD and viscoelasticity contrast: fMRI/fMRE”. In: *NeuroImage* vol. 211 (2020), pp. 116592–116592.

[52] Bray, F. et al. “Global cancer statistics 2018: GLOBOCAN estimates of incidence and mortality worldwide for 36 cancers in 185 countries”. In: *CA: a cancer journal for clinicians* vol. 68, no. 6 (2018), pp. 394–424.

[53] Kreftregisteret. *Cancer in Norway 2015 - cancer incidence, mortality, survival and prevalence in Norway.* Ed. by Larsen, I. (Oslo: Cancer Registry of Norway, 2016.

[54] Taghizadeh, H. et al. “Applied Precision Cancer Medicine in Neuro-Oncology”. In: *Scientific reports* vol. 9, no. 1 (2019), pp. 20139–8.

[55] England, P. H. *Cancer survival in England for patients diagnosed between 2014 and 2018, and followed up to 2019. National statistics.* National Statistics. London, England: Public Health England, 2021.

[56] Ostrom, Q. T. et al. “CBTRUS Statistical Report: Primary Brain and Other Central Nervous System Tumors Diagnosed in the United States in 2014-2018”. In: *Neuro-oncology* vol. 23, no. 12 Suppl 2 (2021), pp. iii1–iii105.

[57] Louis, D. N. et al. “The 2021 WHO classification of tumors of the central nervous system: A summary”. In: *Neuro-oncology* vol. 23, no. 8 (2021), pp. 1231–1251.

[58] Prados, M. D. et al. “Toward precision medicine in glioblastoma: The promise and the challenges”. In: *Neuro-oncology*. Editor’s choice vol. 17, no. 8 (2015), pp. 1051–1063.

[59] Molinaro, A. M. et al. “Association of Maximal Extent of Resection of Contrast-Enhanced and Non-Contrast-Enhanced Tumor With Survival Within Molecular Subgroups of Patients With Newly Diagnosed Glioblastoma”. In: *JAMA Oncol* vol. 6, no. 4 (2020), pp. 495–503.

[60] Stupp, R. et al. “Effects of radiotherapy with concomitant and adjuvant temozolomide versus radiotherapy alone on survival in glioblastoma in a randomised phase III study: 5-year analysis of the EORTC-NCIC trial”. In: *Lancet Oncol* vol. 10, no. 5 (2009), pp. 459–66.

[61] Wen, P. Y. and Kesari, S. “Malignant gliomas in adults”. In: *N Engl J Med* vol. 359, no. 5 (2008), pp. 492–507.

[62] Patel, A. P. et al. “Single-cell RNA-seq highlights intratumoral heterogeneity in primary glioblastoma”. In: *Science* vol. 344, no. 6190 (2014), pp. 1396–401.

[63] Parker, N. R. et al. “Molecular heterogeneity in glioblastoma: Potential clinical implications”. In: *Frontiers in oncology* vol. 5 (2015), pp. 55–55.

[64] Qazi, M. A. et al. “Intratumoral heterogeneity: pathways to treatment resistance and relapse in human glioblastoma”. In: *Ann Oncol* vol. 28, no. 7 (2017), pp. 1448–1456.

[65] Sottoriva, A. et al. “Intratumor heterogeneity in human glioblastoma reflects cancer evolutionary dynamics”. In: *Proc Natl Acad Sci U S A* vol. 110, no. 10 (2013), pp. 4009–14.

[66] Dirkse, A. et al. “Stem cell-associated heterogeneity in Glioblastoma results from intrinsic tumor plasticity shaped by the microenvironment”. In: *Nat Commun* vol. 10, no. 1 (2019), p. 1787.

[67] Lombardi, M. Y. and Assem, M. “Glioblastoma Genomics: A Very Complicated Story”. In: *Glioblastoma*. Ed. by De Vleeschouwer, S. Brisbane, Australia: Codon Publications, 2017.

[68] Ellingson, B. M. et al. “Consensus recommendations for a standardized Brain Tumor Imaging Protocol in clinical trials”. In: *Neuro-oncology* vol. 17, no. 9 (2015), pp. 1188–98.

[69] Maier, S. E., Sun, Y., and Mulkern, R. V. “Diffusion imaging of brain tumors”. In: *NMR Biomed* vol. 23, no. 7 (2010), pp. 849–64.

[70] Romano, A. et al. “Pre-surgical planning and MR-tractography utility in brain tumour resection”. In: *Eur Radiol* vol. 19, no. 12 (2009), pp. 2798–808.

[71] Folkman, J. “Tumor angiogenesis: therapeutic implications”. In: *N Engl J Med* vol. 285, no. 21 (1971), pp. 1182–6.

[72] Jain, R. K. et al. “Angiogenesis in brain tumours”. In: *Nat Rev Neurosci* vol. 8, no. 8 (2007), pp. 610–22.

[73] Law, M. et al. “Glioma grading: sensitivity, specificity, and predictive values of perfusion MR imaging and proton MR spectroscopic imaging compared with conventional MR imaging”. In: *AJNR Am J Neuroradiol* vol. 24, no. 10 (2003), pp. 1989–98.

[74] Shin, J. H. et al. “Using relative cerebral blood flow and volume to evaluate the histopathologic grade of cerebral gliomas: preliminary results”. In: *AJR Am J Roentgenol* vol. 179, no. 3 (2002), pp. 783–9.

[75] Hakyemez, B. et al. “High-grade and low-grade gliomas: differentiation by using perfusion MR imaging”. In: *Clin Radiol* vol. 60, no. 4 (2005), pp. 493–502.

[76] Dijken, B. R. J. van et al. “Perfusion MRI in treatment evaluation of glioblastomas: Clinical relevance of current and future techniques”. In: *J Magn Reson Imaging* vol. 49, no. 1 (2019), pp. 11–22.

[77] Patel, P. et al. “MR perfusion-weighted imaging in the evaluation of high-grade gliomas after treatment: a systematic review and meta-analysis”. In: *Neuro-oncology* vol. 19, no. 1 (2017), pp. 118–127.

[78] Ciasca, G. et al. “Nano-mechanical signature of brain tumours”. In: *Nanoscale* vol. 8 (47 2016), pp. 19629–19643.

[79] Ulrich, T. A., De Juan Pardo, E. M., and Kumar, S. “The mechanical rigidity of the extracellular matrix regulates the structure, motility, and proliferation of glioma cells”. In: *Cancer Research* vol. 69, no. 10 (2009), pp. 4167–4174.

[80] Simon, M. et al. “Non-invasive characterization of intracranial tumors by magnetic resonance elastography”. In: *New Journal of Physics* vol. 15 (2013).

[81] Streitberger, K. J. et al. “High-resolution mechanical imaging of glioblastoma by multifrequency magnetic resonance elastography”. In: *PLoS One* vol. 9, no. 10 (2014), e110588.

[82] Reiss-Zimmermann, M. et al. “High Resolution Imaging of Viscoelastic Properties of Intracranial Tumours by Multi-Frequency Magnetic Resonance Elastography”. In: *Clinical Neuroradiology* vol. 25, no. 4 (2015), pp. 371–378.

[83] Pepin, K. M. et al. “MR Elastography Analysis of Glioma Stiffness and IDH1-Mutation Status”. In: *AJNR Am J Neuroradiol* vol. 39, no. 1 (2018), pp. 31–36.

[84] Sakai, N. et al. “Shear Stiffness of 4 Common Intracranial Tumors Measured Using MR Elastography: Comparison with Intraoperative Consistency Grading”. In: *American Journal of Neuroradiology* vol. 37, no. 10 (2016), pp. 1851–1859.

[85] Streitberger, K. J. et al. “How tissue fluidity influences brain tumor progression”. In: *Proc Natl Acad Sci U S A* vol. 117, no. 1 (2020), pp. 128–134.

[86] World Medical, A. “World Medical Association Declaration of Helsinki. Ethical principles for medical research involving human subjects”. In: *Bull World Health Organ* vol. 79, no. 4 (2001), pp. 373–4.

[87] Guenthner, C. et al. “Ristretto MRE: A generalized multi-shot GRE-MRE sequence”. In: *NMR Biomed* vol. 32, no. 5 (2019), e4049.

[88] Guenthner, C. et al. “Analysis and improvement of motion encoding in magnetic resonance elastography”. In: *NMR Biomed* vol. 31, no. 5 (2018), e3908.

[89] Digernes, I. et al. “A theoretical framework for determining cerebral vascular function and heterogeneity from dynamic susceptibility contrast MRI”. In: *J Cereb Blood Flow Metab* vol. 37, no. 6 (2017), pp. 2237–2248.

[90] Alsop, D. C. and Detre, J. A. “Reduced transit-time sensitivity in noninvasive magnetic resonance imaging of human cerebral blood flow”. In: *J Cereb Blood Flow Metab* vol. 16, no. 6 (1996), pp. 1236–49.

[91] Costantini, M. “A novel phase unwrapping method based on network programming”. In: *IEEE Transactions on Geoscience and Remote Sensing* vol. vol. 36, no. no. 3 (1998), pp. 813–821.

[92] Garteiser, P. et al. “Rapid acquisition of multifrequency, multislice and multidirectional MR elastography data with a fractionally encoded gradient echo sequence”. In: *NMR Biomed* vol. 26, no. 10 (2013), pp. 1326–35.

[93] Savitzky, A. and Golay, M. “Smoothing and Differentiation of Data by Simplified Least Squares Procedures”. In: *American Chemical Society* vol. 36, no. 8 (1964), pp. 1627–1639.

[94] Fovargue, D. et al. “Robust MR elastography stiffness quantification using a localized divergence free finite element reconstruction”. In: *Med Image Anal* vol. 44 (2018), pp. 126–142.

[95] Albrecht, H.-H. “A family of cosine-sum windows for high-resolution measurements”. In: *2001 IEEE International Conference on Acoustics, Speech, and Signal Processing. Proceedings (Cat. No.01CH37221)* vol. 5 (2001), 3081–3084 vol.5.

[96] Yeung, J. et al. “Paediatric brain tissue properties measured with magnetic resonance elastography”. In: *Biomech Model Mechanobiol* vol. 18, no. 5 (2019), pp. 1497–1505.

[97] Murphy, M. C. et al. “Measuring the characteristic topography of brain stiffness with magnetic resonance elastography”. In: *PLoS One* vol. 8, no. 12 (2013), e81668.

[98] Andersson, J. L., Skare, S., and Ashburner, J. “How to correct susceptibility distortions in spin-echo echo-planar images: application to diffusion tensor imaging”. In: *Neuroimage* vol. 20, no. 2 (2003), pp. 870–88.

[99] Hovden, I. T. et al. “The impact of EPI-based distortion correction of dynamic susceptibility contrast MRI on cerebral blood volume estimation in patients with glioblastoma”. In: *Eur J Radiol* vol. 132 (2020), p. 109278.

[100] Bjørnerud, A. and Emblem, K. E. “A fully automated method for quantitative cerebral hemodynamic analysis using DSC-MRI”. In: *J Cereb Blood Flow Metab* vol. 30, no. 5 (2010), pp. 1066–78.

[101] Kiselev, V. G. et al. “Vessel size imaging in humans”. eng. In: *Magn Reson Med* vol. 53, no. 3 (2005), pp. 553–563.

[102] Tzourio-Mazoyer, N. et al. “Automated anatomical labeling of activations in SPM using a macroscopic anatomical parcellation of the MNI MRI single-subject brain”. In: *Neuroimage* vol. 15, no. 1 (2002), pp. 273–289.

[103] Juan-Albarracin, J. et al. “ONCOhabitats: A system for glioblastoma heterogeneity assessment through MRI”. In: *Int J Med Inform* vol. 128 (2019), pp. 53–61.

[104] Menze, B. H. et al. “The Multimodal Brain Tumor Image Segmentation Benchmark (BRATS)”. In: *IEEE Trans Med Imaging* vol. 34, no. 10 (2015), pp. 1993–2024.

[105] Bakas, S. et al. “Advancing The Cancer Genome Atlas glioma MRI collections with expert segmentation labels and radiomic features”. In: *Sci Data* vol. 4 (2017), p. 170117.

[106] Petridis, P. D. et al. “BOLD asynchrony elucidates tumor burden in IDH-mutated gliomas”. In: *Neuro-Oncology* vol. 24, no. 1 (July 2021), pp. 78–87.

[107] Zada, G. et al. “A proposed grading system for standardizing tumor consistency of intracranial meningiomas”. In: *Neurosurg Focus* vol. 35, no. 6 (2013), E1.

[108] Snyder, M., Wang, Z., and Gerstein, M. “RNA-Seq: a revolutionary tool for transcriptomics”. eng. In: *Nature reviews. Genetics* vol. 10, no. 1 (2009), pp. 57–63.

[109] Svensson, S. F. et al. “MRI Elastography Identifies Regions of Extracellular Matrix Reorganization Associated with Shorter Survival in Glioblastoma Patients”. In: *medRxiv* (2022). eprint: https://www.medrxiv.org/content/early/2022/11/13/2022.11.07.22282021.full.pdf.

[110] Institute, N. C. *The cancer genome atlas*. https://www.cancer.gov/tcga. Accessed: 2022-08-18.

[111] Institute, N. C. *Clinical Proteomic Tumor Analysis Consortium*. https://proteomics.cancer.gov/programs/cptac. Accessed: 2022-08-18.

[112] Grossman, R. L. et al. "Toward a Shared Vision for Cancer Genomic Data". In: *N Engl J Med* vol. 375, no. 12 (2016), pp. 1109–1112.

[113] Shrout, P. E. and Fleiss, J. L. "Intraclass correlations: uses in assessing rater reliability". In: *Psychol Bull* vol. 86, no. 2 (1979), pp. 420–8.

[114] Jones, R. and Payne, B. *Clinical Investigation and Statistics in Laboratory Medicine*. London: ACB Venture Publications, 1997.

[115] Klein, R. *Bland-Altman and Correlation Plot*. https://se.mathworks.com/matlabcentral/fileexchange/45049-bland-altman-and-correlation-plot. [Online; accessed May 24th, 2022]. 2022.

[116] Barnhart, H. X. and Barboriak, D. P. "Applications of the repeatability of quantitative imaging biomarkers: a review of statistical analysis of repeat data sets". In: *Transl Oncol* vol. 2, no. 4 (2009), pp. 231–5.

[117] Ruiz-Perez, D. et al. "So you think you can PLS-DA?" In: *BMC bioinformatics* vol. 21, no. Suppl 1 (2020), pp. 2–2.

[118] Clark, T. et al. "Survival Analysis Part I: Basic concepts and first analyses". eng. In: *British journal of cancer* vol. 89, no. 2 (2003), pp. 232–238.

[119] Bradburn, M. J. et al. "Survival Analysis Part II: Multivariate data analysis – an introduction to concepts and methods". In: *British Journal of Cancer* vol. 89 (2003), pp. 431–436.

[120] Botstein, D. et al. "Gene Ontology: tool for the unification of biology". In: *Nature genetics* vol. 25, no. 1 (2000), pp. 25–29.

[121] Logie, C. and Gene Ontology Consortium, T. "The Gene Ontology resource: enriching a GOld mine". In: *Nucleic acids research* vol. 49, no. D1 (2021), pp. D325–D334.

[122] Gillespie, M. et al. "The reactome pathway knowledgebase 2022". In: *Nucleic Acids Research* vol. 50 (2021), pp. D687–D692.

[123] McGarry, M. et al. "Including spatial information in nonlinear inversion MR elastography using soft prior regularization". In: *IEEE Trans Med Imaging* vol. 32, no. 10 (2013), pp. 1901–9.

[124] Johnson, C. L. et al. "Local mechanical properties of white matter structures in the human brain". In: *Neuroimage* vol. 79 (2013), pp. 145–52.

[125] Johnson, C. L. et al. "Viscoelasticity of subcortical gray matter structures". In: *Hum Brain Mapp* vol. 37, no. 12 (2016), pp. 4221–4233.

[126] Shire, N. J. et al. "Test-retest repeatability of MR elastography for noninvasive liver fibrosis assessment in hepatitis C". In: *J Magn Reson Imaging* vol. 34, no. 4 (2011), pp. 947–55.

[127] Garteiser, P. et al. “MR elastography of liver tumours: value of viscoelastic properties for tumour characterisation”. In: *Eur Radiol* vol. 22, no. 10 (2012), pp. 2169–77.

[128] Trout, A. T. et al. “Liver Stiffness Measurements with MR Elastography: Agreement and Repeatability across Imaging Systems, Field Strengths, and Pulse Sequences”. In: *Radiology* vol. 281, no. 3 (2016), pp. 793–804.

[129] Manduca, A. et al. “Waveguide effects and implications for cardiac magnetic resonance elastography: A finite element study”. In: *NMR Biomed* (2018), e3996.

[130] Manduca, A. et al. “Image processing for magnetic-resonance elastography”. In: *Medical Imaging 1996: Image Processing*. Ed. by Loew, M. H. and Hanson, K. M. Vol. 2710. International Society for Optics and Photonics. SPIE, 1996, pp. 616–623.

[131] Hirsch, S. et al. “MR Elastography of the Liver and the Spleen Using a Piezoelectric Driver, Single-Shot Wave-Field Acquisition, and Multifrequency Dual Parameter Reconstruction”. In: *Magn Reson Med* vol. 71, no. 1 (2014), pp. 267–277.

[132] McGarry, M. D. J. et al. “Multiresolution MR elastography using nonlinear inversion”. eng. In: *Medical physics (Lancaster)* vol. 39, no. 10 (2012), pp. 6388–6396.

[133] Murphy, M. C., Huston, J., and Ehman, R. L. “MR elastography of the brain and its application in neurological diseases”. In: *Neuroimage* vol. 187 (2019), pp. 176–183.

[134] Gnanago, J.-L. et al. “Actuators for MRE: New Perspectives With Flexible Electroactive Materials”. In: *Frontiers in Physics* vol. 9 (2021).

[135] Johnson, C. L. and Telzer, E. H. “Magnetic resonance elastography for examining developmental changes in the mechanical properties of the brain”. In: *Dev Cogn Neurosci* vol. 33 (2018), pp. 176–181.

[136] McGarry, M. D. et al. “An octahedral shear strain-based measure of SNR for 3D MR elastography”. In: *Phys Med Biol* vol. 56, no. 13 (2011), N153–64.

[137] Svensson, S. F., Emblem, K. E., and Fuster-Garcia, E. *MR Elastography, perfusion and diffusion data in 9 patients with glioblastoma and 17 healthy subjects*. Zenodo, June 2021.

[138] Braun, J. et al. “High-resolution mechanical imaging of the human brain by three-dimensional multifrequency magnetic resonance elastography at 7T”. In: *Neuroimage* vol. 90 (2014), pp. 308–14.

[139] Kruse, S. A. et al. “Magnetic resonance elastography of the brain”. In: *Neuroimage* vol. 39, no. 1 (2008), pp. 231–7.

[140] Guo, J. et al. “Towards an elastographic atlas of brain anatomy”. In: *PLoS One* vol. 8, no. 8 (2013), e71807.

[141] Zhang, J. et al. “Viscoelastic properties of human cerebellum using magnetic resonance elastography”. In: *J Biomech* vol. 44, no. 10 (2011), pp. 1909–13.

[142] Green, M. A., Bilston, L. E., and Sinkus, R. “In vivo brain viscoelastic properties measured by magnetic resonance elastography”. In: *NMR Biomed* vol. 21, no. 7 (2008), pp. 755–64.

[143] Fischl, B. and Dale, A. M. “Measuring the Thickness of the Human Cerebral Cortex from Magnetic Resonance Images”. eng. In: *Proceedings of the National Academy of Sciences - PNAS* vol. 97, no. 20 (2000), pp. 11050–11055.

[144] Gerischer, L. M. et al. “Combining viscoelasticity, diffusivity and volume of the hippocampus for the diagnosis of Alzheimer’s disease based on magnetic resonance imaging”. In: *Neuroimage Clin* vol. 18 (2018), pp. 485–493.

[145] Hetzer, S. et al. “Perfusion alters stiffness of deep gray matter”. In: *J Cereb Blood Flow Metab* vol. 38, no. 1 (2018), pp. 116–125.

[146] Riek, K. et al. “Magnetic resonance elastography reveals altered brain viscoelasticity in experimental autoimmune encephalomyelitis”. In: *Neuroimage Clin* vol. 1, no. 1 (2012), pp. 81–90.

[147] Carmeliet, P. and Jain, R. K. “Angiogenesis in cancer and other diseases”. In: *Nature* vol. 407, no. 6801 (2000), pp. 249–57.

[148] Juge, L. et al. “Colon tumor growth and antivascular treatment in mice: complementary assessment with MR elastography and diffusion-weighted MR imaging”. In: *Radiology* vol. 264, no. 2 (2012), pp. 436–44.

[149] Li, J. et al. “Investigating the Contribution of Collagen to the Tumor Biomechanical Phenotype with Noninvasive Magnetic Resonance Elastography”. In: *Cancer Res* vol. 79, no. 22 (2019), pp. 5874–5883.

[150] Jain, R. K., Martin, J. D., and Stylianopoulos, T. “The role of mechanical forces in tumor growth and therapy”. In: *Annu Rev Biomed Eng* vol. 16 (2014), pp. 321–46.

[151] Fovargue, D. et al. “Towards noninvasive estimation of tumour pressure by utilising MR elastography and nonlinear biomechanical models: a simulation and phantom study”. In: *Sci Rep* vol. 10, no. 1 (2020), p. 5588.

[152] Song, L., Langfelder, P., and Horvath, S. “Random generalized linear model: A highly accurate and interpretable ensemble predictor”. eng. In: *BMC bioinformatics* vol. 14, no. 1 (2013), pp. 5–5.

[153] Schregel, K. et al. “Characterization of glioblastoma in an orthotopic mouse model with magnetic resonance elastography”. In: *NMR Biomed* vol. 31, no. 10 (2018), e3840.

[154] Chauvet, D. et al. “In Vivo Measurement of Brain Tumor Elasticity Using Intraoperative Shear Wave Elastography”. In: *Ultraschall in der Medizin* vol. 37, no. 6 (2015), pp. 584–590.

[155] Yin, L. et al. “Application of intraoperative B-mode ultrasound and shear wave elastography for glioma grading”. In: *Quantitative imaging in medicine and surgery* vol. 11, no. 6 (2021), pp. 2733–2743.

[156] CH, L. et al. “High levels of TIMP1 are associated with increased extracellular matrix stiffness in isocitrate dehydrogenase 1-wild type gliomas”. In: *Lab Invest* (2022).

[157] Northey, J. J., Przybyla, L., and Weaver, V. M. “Tissue force programs cell fate and tumor aggression”. In: *Cancer discovery* vol. 7, no. 11 (2017), pp. 1224–1237.

[158] Stylianopoulos, T. “The Solid Mechanics of Cancer and Strategies for Improved Therapy”. In: *J Biomech Eng* vol. 139, no. 2 (2017).

[159] Butcher, D. T., Alliston, T., and Weaver, V. M. “A tense situation: forcing tumour progression”. In: *Nat Rev Cancer* vol. 9, no. 2 (2009), pp. 108–22.

[160] Levental, K. R. et al. “Matrix Crosslinking Forces Tumor Progression by Enhancing Integrin Signaling”. In: *Cell* vol. 139, no. 5 (2009), pp. 891–906.

[161] Bilston, L. E. “Brain Tissue Mechanical Properties”. In: *Biomechanics of the Brain*. Ed. by Miller, K. New York, NY: Springer New York, 2011, pp. 69–89.

[162] Jamin, Y. et al. “Exploring the biomechanical properties of brain malignancies and their pathologic determinants in vivo with magnetic resonance elastography”. In: *Cancer Res* vol. 75, no. 7 (2015), pp. 1216–1224.

[163] Bellail, A. C. et al. “Microregional extracellular matrix heterogeneity in brain modulates glioma cell invasion”. In: *Int J Biochem Cell Biol* vol. 36, no. 6 (2004), pp. 1046–69.

[164] Huijbers, I. J. et al. “A role for fibrillar collagen deposition and the collagen internalization receptor endo180 in glioma invasion”. eng. In: *PloS one* vol. 5, no. 3 (2010), e9808–e9808.

[165] Sack, I. et al. “Structure-sensitive elastography: on the viscoelastic powerlaw behavior of in vivo human tissue in health and disease”. In: *Soft matter* vol. 9, no. 24 (2013), pp. 5672–568.

[166] Schregel, K. et al. “Demyelination reduces brain parenchymal stiffness quantified in vivo by magnetic resonance elastography”. In: *Proc Natl Acad Sci U S A* vol. 109, no. 17 (2012), pp. 6650–5.

[167] Höckel, M. et al. “Are biomechanical changes necessary for tumour progression?” In: *Nature physics* vol. 6, no. 10 (2010), pp. 730–732.

[168] Cieśluk, M. et al. “Substrate viscosity impairs temozolomide-mediated inhibition of glioblastoma cells’ growth”. In: *Biochimica et Biophysica Acta (BBA) - Molecular Basis of Disease* (2022), p. 166513.

[169] Murphy, M. C. et al. “Preoperative assessment of meningioma stiffness using magnetic resonance elastography”. In: *J Neurosurg* vol. 118, no. 3 (2013), pp. 643–8.

[170] Hughes, J. D. et al. “Higher-Resolution Magnetic Resonance Elastography in Meningiomas to Determine Intratumoral Consistency”. In: *Neurosurgery* vol. 77, no. 4 (2015), 653–8, discussion 658–9.

[171] Shi, Y. et al. “Use of magnetic resonance elastography to gauge meningioma intratumoral consistency and histotype”. eng. In: *NeuroImage clinical* vol. 36 (2022), pp. 103173–103173.

[172] Hughes, J. D. et al. “Magnetic resonance elastography detects tumoral consistency in pituitary macroadenomas”. In: *Pituitary* vol. 19, no. 3 (2016), pp. 286–92.

[173] Chan, H. W. et al. “Clinical Application of Shear Wave Elastography for Assisting Brain Tumor Resection”. In: *Front Oncol* vol. 11 (2021), p. 619286.

[174] Lagerstrand, K. et al. “Virtual magnetic resonance elastography has the feasibility to evaluate preoperative pituitary adenoma consistency”. eng. In: *Pituitary* vol. 24, no. 4 (2021), pp. 530–541.

[175] Koizumi, S. and Kurozumi, K. “NI-01 Usefulness of preoperative evaluation of glioma elasticity by the magnetic resonance elastography”. In: *Neuro-Oncology Advances* vol. 2, no. Supplement_3 (Nov. 2020), pp. ii12–ii13.

[176] Fuster-Garcia, E. et al. “Quantification of Tissue Compression Identifies High-Grade Glioma Patients with Reduced Survival”. In: *Cancers (Basel)* vol. 14, no. 7 (2022).

[177] Nia, H. T. et al. “Solid stress and elastic energy as measures of tumour mechanopathology”. In: *Nat Biomed Eng* vol. 1 (2016).

[178] Steed, T. C. et al. “Quantification of glioblastoma mass effect by lateral ventricle displacement”. eng. In: *Scientific reports* vol. 8, no. 1 (2018), pp. 2827–8.

[179] Fiorito, M. et al. “Impact of axisymmetric deformation on MR elastography of a nonlinear tissue-mimicking material and implications in peri-tumour stiffness quantification”. In: *PLoS One* vol. 16, no. 7 (2021), e0253804.

[180] Capilnasiu, A. et al. “Magnetic resonance elastography in nonlinear viscoelastic materials under load”. In: *Biomech Model Mechanobiol* vol. 18, no. 1 (2019), pp. 111–135.

[181] Arani, A. et al. “Acute pressure changes in the brain are correlated with MR elastography stiffness measurements: initial feasibility in an in vivo large animal model”. In: *Magn Reson Med* vol. 79, no. 2 (2018), pp. 1043–1051.

[182] Pogoda, K. et al. “Compression stiffening of brain and its effect on mechanosensing by glioma cells”. In: *New J Phys* vol. 16 (2014), p. 075002.

[183] Zanetti-Dällenbach, R. et al. “Length Scale Matters: Real-Time Elastography versus Nanomechanical Profiling by Atomic Force Microscopy for the Diagnosis of Breast Lesions”. In: *BioMed research international* vol. 2018 (2018), pp. 3840597–12.

[184] Khan, Z. S. and Vanapalli, S. A. “Probing the mechanical properties of brain cancer cells using a microfluidic cell squeezer device”. In: *Biomicrofluidics* vol. 7, no. 1 (2013), pp. 11806–11806.

[185] Graybill, P. M. et al. “A constriction channel analysis of astrocytoma stiffness and disease progression”. In: *Biomicrofluidics* vol. 15, no. 2 (2021), pp. 024103–024103.

[186] Miroshnikova, Y. A. et al. “Tissue mechanics promote IDH1-dependent HIF1α-tenascin C feedback to regulate glioblastoma aggression”. In: *Nature cell biology* vol. 18, no. 12 (2016), pp. 1336–1345.

[187] Cieśluk, M. et al. “Nanomechanics and Histopathology as Diagnostic Tools to Characterize Freshly Removed Human Brain Tumors”. In: *International journal of nanomedicine* vol. 15 (2020), pp. 7509–7521.

[188] Chen, X. et al. “A Feedforward Mechanism Mediated by Mechanosensitive Ion Channel PIEZO1 and Tissue Mechanics Promotes Glioma Aggression”. In: *Neuron* vol. 100, no. 4 (2018), 799–815.e7.

[189] Seano, G. et al. “Solid stress in brain tumours causes neuronal loss and neurological dysfunction and can be reversed by lithium”. In: *Nature biomedical engineering* vol. 3, no. 3 (2019), pp. 230–245.

[190] Ning, D. et al. “Mechanical and Morphological Analysis of Cancer Cells on Nanostructured Substrates”. In: *Langmuir* vol. 32, no. 11 (2016), pp. 2718–2723.

[191] Alibert, C. et al. “Multiscale rheology of glioma cells”. In: *Biomaterials* vol. 275 (2021), pp. 120903–120903.

[192] Wang, C., Tong, X., and Yang, F. “Bioengineered 3D Brain Tumor Model To Elucidate the Effects of Matrix Stiffness on Glioblastoma Cell Behavior Using PEG-Based Hydrogels”. In: *Molecular pharmaceutics* vol. 11, no. 7 (2014), pp. 2115–2125.

[193] Pogoda, K. et al. “Soft Substrates Containing Hyaluronan Mimic the Effects of Increased Stiffness on Morphology, Motility, and Proliferation of Glioma Cells”. In: *Biomacromolecules* vol. 18, no. 10 (2017), pp. 3040–3051.

[194] Cartagena, A. and Raman, A. “Local Viscoelastic Properties of Live Cells Investigated Using Dynamic and Quasi-Static Atomic Force Microscopy Methods”. eng. In: *Biophysical journal* vol. 106, no. 5 (2014), pp. 1033–1043.

[195] Sauer, F. et al. “Whole tissue and single cell mechanics are correlated in human brain tumors”. In: *Soft Matter* vol. 17 (47 2021), pp. 10744–10752.

[196] Nakada, M. et al. “Molecular targets of glioma invasion”. In: *Cell Mol Life Sci* vol. 64, no. 4 (2007), pp. 458–78.

[197] Viapiano, M. and Lawler, S. *Chapter 49: Glioma Invasion: Mechanisms and Therapeutic Challenges*. 2009, pp. 1219–1252.

[198] Payne, L. S. and Huang, P. H. “The pathobiology of collagens in glioma”. In: *Mol Cancer Res* vol. 11, no. 10 (2013), pp. 1129–40.

[199] Lin, Y.-J. et al. “Roles of Neutrophils in Glioma and Brain Metastases”. eng. In: *Frontiers in immunology* vol. 12 (2021), pp. 701383–701383.

[200] HU, B. et al. “Neuropilin-1 promotes human glioma progression through potentiating the activity of the HGF SF autocrine pathway”. eng. In: *Oncogene* vol. 26, no. 38 (2007), pp. 5577–5586.

[201] Güven, E., Afzal, M., and Kazmi, I. “Screening the Significant Hub Genes by Comparing Tumor Cells, Normoxic and Hypoxic Glioblastoma Stem-like Cell Lines Using Co-Expression Analysis in Glioblastoma”. eng. In: *Genes* vol. 13, no. 3 (2022), p. 518.

[202] Musumeci, G. et al. “Enhanced expression of CD31/platelet endothelial cell adhesion molecule 1 (PECAM1) correlates with hypoxia inducible factor-1 alpha (HIF-1α) in human glioblastoma multiforme”. eng. In: *Experimental cell research* vol. 339, no. 2 (2015), pp. 407–416.

[203] Liu, S. et al. “Molecular and clinical characterization of CD163 expression via large-scale analysis in glioma”. eng. In: *Oncoimmunology* vol. 8, no. 7 (2019), pp. 1601478–1601478.

[204] Jiang, K. et al. “Fms related tyrosine kinase 1 (Flt1) functions as an oncogene and regulates glioblastoma cell metastasis by regulating sonic hedgehog signaling”. eng. In: *American journal of cancer research* vol. 7, no. 5 (2017), pp. 1164–1176.

[205] Pilgaard, L. et al. “Cripto-1 Expression in Glioblastoma Multiforme: CR-1 Expression in Glioblastoma Multiforme”. eng. In: *Brain pathology (Zurich, Switzerland)* vol. 24, no. 4 (2014), pp. 360–370.

[206] Li, C. et al. “Tumor edge-to-core transition promotes malignancy in primary-to-recurrent glioblastoma progression in a PLAGL1/CD109-mediated mechanism”. eng. In: *Neuro-Oncology Advances* vol. 2, no. 1 (2020), vdaa163–vdaa163.

[207] Wang, H. et al. “COL4A1 as a novel oncogene associated with the clinical characteristics of malignancy predicts poor prognosis in glioma”. eng. In: vol. 22, no. 5 (2021).

[208] Pencheva, N. et al. “Identification of a Druggable Pathway Controlling Glioblastoma Invasiveness”. eng. In: *Cell reports (Cambridge)* vol. 20, no. 1 (2017), pp. 48–60.

[209] Dance, A. “The secret forces that squeeze and pull life into shape”. In: *Nature* vol. 589, no. 7841 (2021), pp. 186–188.

[210] Falco, J. et al. “In Silico Mathematical Modelling for Glioblastoma: A Critical Review and a Patient-Specific Case”. eng. In: *Journal of clinical medicine* vol. 10, no. 10 (2021), p. 2169.

[211] Harkos, C. et al. “Inducing Biomechanical Heterogeneity in Brain Tumor Modeling by MR Elastography: Effects on Tumor Growth, Vascular Density and Delivery of Therapeutics”. eng. In: *Cancers* vol. 14, no. 4 (2022), p. 884.

[212] Chauhan, V. P. et al. “Angiotensin inhibition enhances drug delivery and potentiates chemotherapy by decompressing tumour blood vessels”. In: *Nature communications* vol. 4, no. 1 (2013), p. 2516.

[213] Emblem, K. E. *Imaging perfusion restrictions from extracellular solid stress - an open-label losartan study - full text view*. 2019.

[214] Sui, Y. et al. “TURBINE-MRE: A 3D hybrid radial-Cartesian EPI acquisition for MR elastography”. eng. In: *Magn Reson Med* vol. 85, no. 2 (2021), pp. 945–952.

[215] Peng, X. et al. “Fast 3D MR elastography of the whole brain using spiral staircase: Data acquisition, image reconstruction, and joint deblurring”. eng. In: *Magn Reson Med* vol. 86, no. 4 (2021), pp. 2011–2024.

[216] McIlvain, G. et al. “OSCILLATE: A low-rank approach for accelerated magnetic resonance elastography”. eng. In: *Magn Reson Med* vol. 88, no. 4 (2022), p. 1659.

[217] Baumgart, F. “Stiffness – an unknown world of mechanical science?” In: *Injury* vol. 31, no. 2 (2000), pp. 14, 72, 76, 80, 84–23, 72, 76, 80, 84.

[218] Kalra, P. et al. “Magnetic resonance elastography of brain: Comparison between anisotropic and isotropic stiffness and its correlation to age”. In: *Magn Reson Med* vol. 82, no. 2 (2019), pp. 671–679.

[219] McGarry, M. et al. “Mapping heterogenous anisotropic tissue mechanical properties with transverse isotropic nonlinear inversion MR elastography”. eng. In: *Medical image analysis* vol. 78 (2022), pp. 102432–102432.

[220] Johnstone, I. M. and Titterington, D. M. “Statistical challenges of high-dimensional data”. eng. In: vol. 367, no. 1906 (2009), pp. 4237–4253.

[221] Bühlmann, P. and Geer, S. van de. “Introduction”. In: *Statistics for High-Dimensional Data: Methods, Theory and Applications*. Berlin, Heidelberg: Springer Berlin Heidelberg, 2011, pp. 1–6.

[222] Lê Cao, K.-A., Boitard, S., and Besse, P. “Sparse PLS discriminant analysis: Biologically relevant feature selection and graphical displays for multiclass problems”. eng. In: *BMC bioinformatics* vol. 12, no. 1 (2011), pp. 253–253.

[223] Feng, Y. et al. “A longitudinal magnetic resonance elastography study of murine brain tumors following radiation therapy”. In: *Phys Med Biol* vol. 61, no. 16 (2016), pp. 6121–31.

[224] Thust, S., Bent, M. van den, and Smits, M. “Pseudoprogression of brain tumors”. eng. In: *J. Magn. Reson* vol. 48, no. 3 (2018), pp. 571–589.

[225] Gamburg, E. S. et al. “The prognostic significance of midline shift at presentation on survival in patients with glioblastoma multiforme”. eng. In: *International journal of radiation oncology, biology, physics* vol. 48, no. 5 (2000), pp. 1359–1362.

[226] Murphy, M. C. et al. “Artificial neural networks for stiffness estimation in magnetic resonance elastography”. eng. In: *Magn Reson Med* vol. 80, no. 1 (2018), pp. 351–360.

Papers

Paper I

Robustness of MR elastography in the healthy brain: Repeatability, reliability, and effect of different reconstructions

I

Siri F. Svensson, José De Arcos, Omar I. Darwish, Jorunn Fraser-Green, Tryggve H. Storås, Sverre Holm, Einar O. Vik-Mo, Ralph Sinkus and Kyrre E. Emblem

Published in: *Journal of Magnetic Resonance Imaging*. Vol. 53, no. 5 (2021), pp. 1510-1521 DOI: 10.1002/jmri.27475.

ORIGINAL RESEARCH

Robustness of MR Elastography in the Healthy Brain: Repeatability, Reliability, and Effect of Different Reconstruction Methods

Siri F. Svensson, MS,[1,2*] José De Arcos, PhD,[3,4] Omar Isam Darwish, BEng,[3] Jorunn Fraser-Green, RT,[5] Tryggve H. Storås, PhD,[1] Sverre Holm, PhD,[2] Einar O. Vik-Mo, MD, PhD,[6] Ralph Sinkus, PhD,[3,4] and Kyrre E. Emblem, PhD[1]

Background: Changes in brain stiffness can be an important biomarker for neurological disease. Magnetic resonance elastography (MRE) quantifies tissue stiffness, but the results vary between acquisition and reconstruction methods.
Purpose: To measure MRE repeatability and estimate the effect of different reconstruction methods and varying data quality on estimated brain stiffness.
Study Type: Prospective.
Subjects: Fifteen healthy subjects.
Field Strength/Sequence: 3T MRI, gradient-echo elastography sequence with a 50 Hz vibration frequency.
Assessment: Imaging was performed twice in each subject. Images were reconstructed using a curl-based and a finite-element-model (FEM)-based method. Stiffness was measured in the whole brain, in white matter, and in four cortical and four deep gray matter regions. Repeatability coefficients (RC), intraclass correlation coefficients (ICC), and coefficients of variation (CV) were calculated. MRE data quality was quantified by the ratio between shear waves and compressional waves.
Statistical Tests: Median values with range are presented. Reconstruction methods were compared using paired Wilcoxon signed-rank tests, and Spearman's rank correlation was calculated between MRE data quality and stiffness. Holm–Bonferroni corrections were employed to adjust for multiple comparisons.
Results: In the whole brain, CV was 4.3% and 3.8% for the curl and the FEM reconstruction, respectively, with 4.0–12.8% for subregions. Whole-brain ICC was 0.60–0.74, ranging from 0.20 to 0.89 in different regions. RC for the whole brain was 0.14 kPa and 0.17 kPa for the curl and FEM methods, respectively. FEM reconstruction resulted in 39% higher stiffness than the curl reconstruction ($P < 0.05$). MRE data quality, defined as shear-compression wave ratio, was higher in peripheral regions than in central regions of the brain ($P < 0.05$). No significant correlations were observed between MRE data quality and stiffness estimates.
Data Conclusion: MRE of the human brain is a robust technique in terms of repeatability. Caution is warranted when comparing stiffness values obtained with different techniques.
Level of Evidence: 1
Technical Efficacy Stage: 1

J. MAGN. RESON. IMAGING 2021.

CHANGES IN BRAIN STIFFNESS can be a biomarker for neurological disease, and biomechanical information about brain tumors may be valuable in surgical planning and tumor characterization.[1,2] Magnetic resonance elastography (MRE) is an emerging technique for quantifying tissue stiffness in a noninvasive manner.[3]

View this article online at wileyonlinelibrary.com. DOI: 10.1002/jmri.27475

Received Sep 3, 2020, Accepted for publication Nov 30, 2020.

*Address reprint requests to: S.F.S., Department for Diagnostic Physics, Oslo University Hospital, Building 20 Gaustad, PB 4959 Nydalen, 0424 Oslo, Norway. E-mail: siriflo@uio.no

Contract grant sponsor: European Union's Horizon 2020 Programme: ERC Grant Agreement No. 758657-ImPRESS, and Research and Innovation Grant Agreement No. 668039-FORCE, South-Eastern Norway Regional Health Authority (Grant Agreement No. 2017073 and 2013069), The Research Council of Norway FRIPRO (Grant Agreement No. 261984), the National Institute of Health R21 grant (Grant Agreement No. EB030757), and the German Research Foundation (DFG, SCHR 1542/1-1).

From the [1]Department of Diagnostic Physics, Oslo University Hospital, Oslo, Norway; [2]Department of Physics, University of Oslo, Oslo, Norway; [3]Division of Imaging Sciences and Biomedical Engineering, King's College, London, UK; [4]INSERM U1148, LVTS, University Paris Diderot, Paris, France; [5]The Intervention Centre, Oslo University Hospital, Oslo, Norway; and [6]Vilhelm Magnus Laboratory, Department of Neurosurgery, Oslo University Hospital, Oslo, Norway

This is an open access article under the terms of the Creative Commons Attribution License, which permits use, distribution and reproduction in any medium, provided the original work is properly cited.

© 2021 The Authors. *Journal of Magnetic Resonance Imaging* published by Wiley Periodicals LLC. on behalf of International Society for Magnetic Resonance in Medicine.

MRE is usually performed using an external mechanical transducer that vibrates on the surface of the body. Compressional waves from the vibration are converted into shear waves when passing the tissue interface, causing tissue displacement from both compressional and shear waves. This tissue displacement is encoded into the phase of the magnetization by a modified phase-contrast MRI sequence, using motion-encoding gradients synchronized with the vibrational movement. Next, quantitative maps of tissue stiffness and viscosity are created by applying inversion algorithms to the phase images.[4]

MRE is a well-established technique in the liver. However, its primary application in brain studies has been in research.[5] To use brain MRE for diagnostic purposes, the robustness and the reliability of the technique needs to be established. In order to determine true biological changes in tissue stiffness, as caused by therapy, the inherent variation in the measurements needs to be quantified.

Estimates of tissue stiffness in the brain may vary with experimental design, study timing, hardware, vibrational frequency, acquisition methods, and processing pipelines, as well as physiological variations between individuals.[1] Consequently, reproducibility of tissue stiffness estimates across sites is challenging. Moreover, a wide range of reconstruction algorithms are available, all with different underlying physical assumptions.[6] Within one experimental design, both reliability and repeatability should be high in order to track changes over time or to separate between normal and abnormal tissue stiffness. Researchers have reported brain MRE repeatability as measured by coefficients of variation (CV), with values below 10% for subregions in the healthy brain, and below 2% for the brain as a total.[7–10]

In order to trust stiffness estimates, the underlying data need to be of sufficient quality, both in terms of wave propagation and data acquisition.[11] As the tissue displacement caused by the shear waves are the underlying signal prior to processing, MRE data quality is here quantified by the ratio between the shear waves and the compressional waves.

The aim of this study was to assess repeatability and test–retest reliability of MRE in the human brain, and to evaluate the effect of different reconstruction methods and varying MRE data quality on stiffness estimates.

Materials and Methods

Image Acquisition

The study was approved by the national Research Ethics Committee and the Institutional Review Board. Informed consent was obtained from healthy test subjects. The study used a test–retest design with MRI exams performed on a 3T scanner (Ingenia, Philips Medical Systems, Best, the Netherlands) using a 32-channel head coil. A T_1-weighted anatomical reference scan for tissue segmentation was acquired by an 3D inversion recovery turbo field echo acquisition with flip angle = 8°, repetition time (TR) = 5.2 msec, echo time (TE) = 2.3 msec, shot interval = 3000 msec, inversion delay = 853 msec, with field of view (FOV) = 256 mm × 256 mm × 368 mm and 1 mm isotropic resolution.

The MRE was performed using a mechanical transducer placed on the side of the subject's head (Fig. 1). This device induced shear waves at 50 Hz into the brain.[12] Image acquisition was performed with a multishot gradient-echo MRE sequence[10] using a Hadamard encoding scheme[13] with bipolar 13 mT/m motion-encoding gradients in three orthogonal directions at 115 Hz. Synchronization to the external wave generator was achieved using a transistor-transistor logic (TTL) trigger signal. A reference scan without motion encoding gradients was used as a phase reference. Fifteen contiguous transversal slices were scanned using an isotropic 3.1 mm

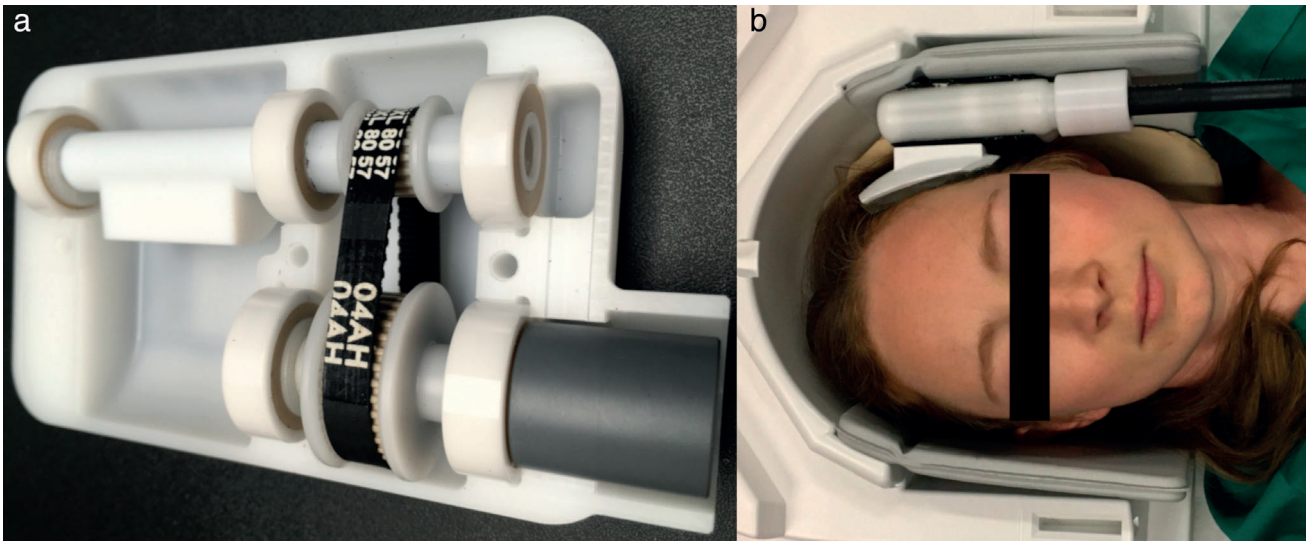

FIGURE 1: The transducer setup, thoroughly described previously.[12] (a) The mechanical transducer contains an asymmetrical mass which is rotated by a timing belt on a rod connected to the rotating axis. (b) Illustration of the transducer placement in the head coil illustrated. The transducer is connected to the motor by a flexible rotating axis, shown in black, and a curved plastic head holder connects the head and the transducer. Hearing protection and extra padding to stabilize the head not shown in picture.

resolution, a matrix size of 72 × 70, and FOV = 22 cm. Other scan parameters were: flip angle = 20°, TR = 384 msec, TE = 12 msec, Cartesian readout, and a sensitivity encoding factor of 2.[14] Eight equally distributed wave phases were sampled over one oscillation period at 25 Hz. The actual mechanical vibration frequency was shifted to the second index of the Fourier transform, thereby filtering out potential contributions from the frequencies 25 Hz, 75 Hz, and 100 Hz. The total MRE acquisition time was 5.5 minutes. Two MRE acquisitions were performed during the MR exam, ~25 minutes apart. The same image geometry was used for both scans. No repositioning of the subject was allowed and the same operator acquired all scans.

In addition to MRE, diffusion tensor images were acquired. These images were acquired using a diffusion-weighted spin-echo, single-shot, echo-planar imaging sequence with Cartesian readout, accelerated by a sensitivity encoding factor 2. Fifty slices of 2.5 mm isotropic resolution were acquired with an acquisition matrix of 94 × 94, FOV = 240 × 240 mm, TR = 9.8 sec, and TE = 60 msec. Fifteen gradient directions and b-values 0 sec/mm^2 and 800 sec/mm^2 were used, with a total scan duration of 6 minutes.

Image Processing

In this study the MRE phase images were unwrapped by a method based on the mathematical problem of minimum cost flow analysis.[15] Next, pixelwise Fourier transformation of the data was performed in order to obtain the tissue displacement in the frequency domain, before each component of the complex-valued displacement vector **u** was Gaussian filtered, using a 3D filter of width σ = 0.75 pixels with 3 × 3 × 3 pixels support. The viscoelasticity was then solved using two different state-of-the-art reconstruction methods, both of which have been used in recent scientific work.[12,16–18] Both are direct inversion methods that assume incompressibility, local isotropy, and stiffness homogeneity. The following linear time-harmonic viscoelastic equations governs the wave behavior:

$$\rho\omega^2 u + \nabla \cdot \left[G^* \left(\nabla u + (\nabla u)^T\right]\right. + \nabla p = 0 \qquad (1)$$

$$\nabla \cdot \mathrm{u} = 0 \qquad (2)$$

where ρ is the tissue density, ω is the angular frequency of the transducer, **u** are the complex-valued wave displacements, and p is the complex hydrostatic pressure. G* is the complex-valued shear modulus, G* = G′ + iG″, where G′ is the shear *storage modulus* or *stiffness*, and G″ is the shear *loss modulus* or *viscosity*.

The first method performs the inversion by applying the curl operator on the displacement data **u**. This eliminates the pressure term in Eq. (1) and separates the shear waves from the compressional waves.[19] Equation (1) is then replaced by Eq. (3):

$$\rho\omega^2 \nabla \times u + G^* \nabla^2 (\nabla \times u) = 0 \qquad (3)$$

which is then solved for G* by least squares polynomial fitting.[20] As the reconstruction is performed on the curl field, this method will be denoted curl reconstruction.

The second method is a finite element method (FEM) reconstruction. Details are thoroughly described elsewhere.[21] Briefly, however, the method uses a compact FEM with divergence-free basis functions. Data leading to negative shear modulus values are removed and a weighted averaging of the shear modulus based on residual error is also performed. In this case, only first-order spatial derivatives are needed, since no curl operator is applied. The derivatives of **u** were computed by least squares polynomial fitting.[20]

Final stiffness maps were spike-filtered for both reconstructions using a sliding 3 × 3 pixel window. If the central pixel of the sliding window carried the largest or the smallest entry of all values within the sliding window, and this entry was 3 standard deviations away from the average value of the surrounding eight values, this central value was replaced by the average value of the neighboring pixels.

Diffusion analysis was performed in nordicICE (NordicNeuroLab, Bergen, Norway) using the following preprocessing steps: automatic detection of noise threshold, noise level cutoff, and motion correction. Maps of apparent diffusion coefficient (ADC) were produced as previously described.[22]

Image Registration and Analysis

Image registration was performed using MatLab (v. R2018a, MathWorks, Natick, MA) and SPM12 (v. 7487, Wellcome Trust Centre for Neuroimaging, London, UK). First, anatomical T_1-weighted images were coregistered by affine transformations into the native spaces of each MRE scan. Second, the downsampled images were warped to the Montreal Neurological Institute (MNI) brain region template,[23] and the inverse deformation field was used to reorient the binary maps of the brain regions of interest (ROIs) into the space of the MRE data for each scan. The diffusion images were also warped into the same space.

The following ROIs of the brain were pulled from the MNI template: white matter, the deep gray matter regions caudate nucleus, thalamus, putamen, and hippocampus, the cortical gray matter in the frontal, occipital, parietal, and temporal regions (Fig. 2a–c), as well as an ROI of the entire brain. To avoid artifacts from MRE reconstruction at the edge of the brain, the outermost voxels in the brain were removed. This was performed using a mask from each MRE scan's magnitude image, which was segmented in nordicICE, morphologically closed, and then eroded at a depth equaling two pixels. ADC maps from the diffusion acquisition were used to reduce any potential errors from partial volume effects. A binary mask with a cutoff ADC value of $<1.2 \times 10^{-3}$ mm^2/s was used to exclude voxels with a high content of cerebrospinal fluid.[24] The size of the masked MRE ROIs ranged from 100 to 15,000 voxels.

For the gray matter regions, tissue stiffness normalized to each subject's white matter was calculated in addition to the absolute stiffness measurements.

Statistical Analysis

Mean values of the stiffness in the ROIs were calculated for all subjects, and median values with range were calculated for the 15 subjects. Ratios between white and gray matter were calculated by the median of the ratio of values for white and gray matter based on the average value of both scans for each volunteer.

Test–retest reliability was estimated using both absolute and relative indices. Relative reliability was measured by intraclass

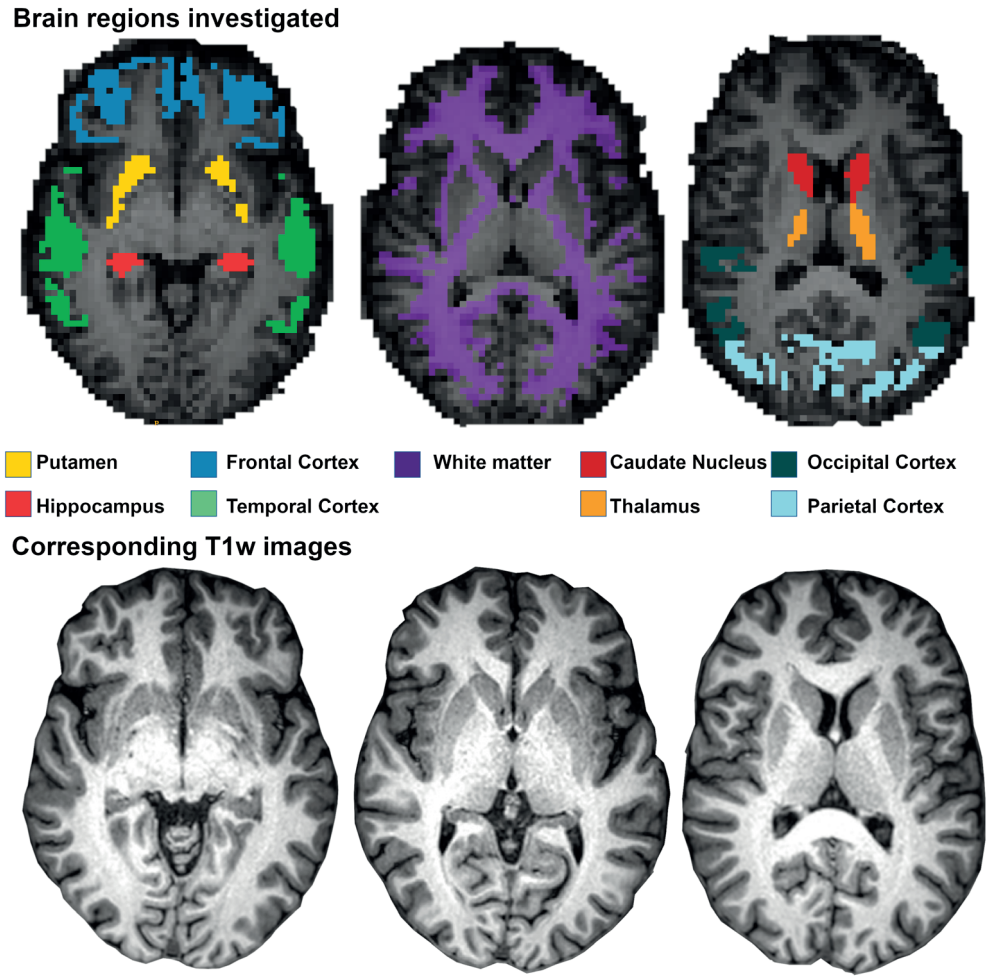

FIGURE 2: Illustration of the ROIs used in the analysis. (a) The brain ROIs overlaid on T_1-weighted images downsampled to the MRE resolution. (a) Putamen and hippocampus, frontal and temporal cortex. (b) White matter. (c) Caudate nucleus, thalamus, occipital, and parietal cortex. (d–f) High resolution T_1-weighted images of corresponding slices.

correlation coefficients (ICCs) with 95% confidence intervals (CIs), calculated using Stata (release 16, StataCorp, College Station, TX) based on an absolute-agreement, two-way mixed-effects model.[25] Repeatability coefficients (RC) were calculated in MatLab and are defined as $1.96 \cdot \sqrt{2}\sigma$, where σ is equal to the standard deviation of the measurement differences between the two scans.[26,27]

The comparisons of stiffness values from different reconstruction methods were assessed using a paired Wilcoxon signed-rank test. Correlations between shear-compression wave ratio and stiffness were measured using Spearman's rank correlation. A significance level of $P < 0.05$ was assumed after Holm–Bonferroni corrections for multiple comparisons.

Results

Fifteen healthy volunteers were examined in the study, between the ages of 21 and 33 years (median 27). Of these, six were female and nine male. Figure 3 shows stiffness maps for three subjects, reconstructed using both the curl and the FEM reconstruction method.

Repeatability and Reliability

CURL RECONSTRUCTION. Using the curl reconstruction, the median tissue stiffness in the whole-brain ROI was 1.29 kPa (range 1.01–1.39 kPa, $N = 15$) in the first scan and 1.28 kPa (range 1.15–1.40 kPa, $N = 15$) in the second scan (Table 1). The CV for the measured tissue stiffness in the whole-brain ROI was 4.3%. The CV in the gray matter regions was 4.2–12.8% and 5.1% for the white matter (Table 2). The ICC between the tissue stiffness of the whole-brain ROI for scans 1 and 2 was 0.74. The ICC for the subregion ROIs ranged from 0.20 in thalamus to 0.89 in the frontal cortex. The RC was 0.14 kPa (95% CI: 0.10–-0.19 kPa) for the whole-brain ROI, while the lowest RC was observed for the frontal cortex (0.11 kPa) and the highest for hippocampus (0.43 kPa).

FEM RECONSTRUCTION. Using the FEM reconstruction, the median of average tissue stiffness estimates for the whole-brain ROI was 1.76 kPa (range 1.53–1.91 kPa) in the first

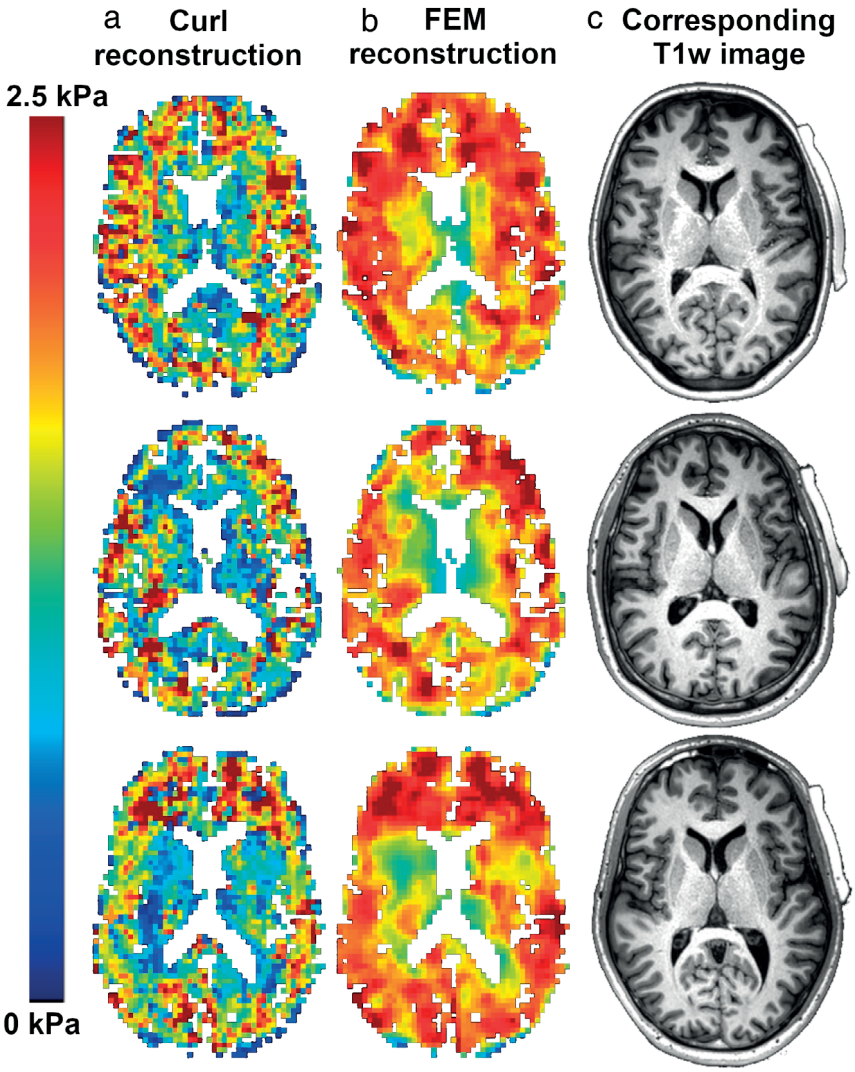

FIGURE 3: Stiffness (G′) maps of the whole-brain ROI using both (a) curl and (b) FEM reconstruction. (c) The corresponding T_1-weighted image of the slice, with the transducer pad visible to the right. First row: a 23-year-old female subject; second row: a 33-year-old male subject; third row: a 31-year-old male subject. The FEM reconstruction yields higher stiffness in all cases.

scan and 1.78 kPa (range 1.67–1.96 kPa) in the second scan (Table 1). The corresponding median CV was 3.8%. The CV was 4.0–9.6% for the gray matter ROIs and 4.5% for white matter (Table 2). The ICC between the tissue stiffness of the whole–brain ROI for scans 1 and 2 was 0.60, and ranged from 0.15 in putamen to 0.75 in the occipital cortex. The RC for the whole-brain ROI was 0.17 kPa (95% CI: 0.12–0.24 kPa), while the lowest RC was observed in the occipital and the temporal cortex (0.19 kPa) and the highest RC in the putamen (0.48 kPa).

There were no significant differences in the reliability and repeatability measurements between the curl and FEM reconstruction methods: ICC (P = 0.16), CV (P = 0.82) and RC (P = 0.10).

Figure 4 shows the stiffness estimates in each scan for all subjects, and Fig. 5 shows the correlation plot and the Bland–Altman plot for tissue stiffness estimates in the subregions of the brain.

FEM RECONSTRUCTION YIELDS HIGHER STIFFNESS ESTIMATES THAN THE CURL RECONSTRUCTION. For the whole-brain ROI, the FEM reconstruction resulted in 39% higher estimated stiffness compared to the curl reconstruction (P < 0.05). For the individual subregions, no significant difference was found in stiffness estimates from the FEM and the curl reconstruction (P = 0.004) (Fig. 4b).

STIFFNESS VALUES NORMALIZED TO WHITE MATTER. For the curl reconstruction, white matter was 8% stiffer than gray matter (cortical and deep combined) (P < 0.05). For the FEM reconstruction, white matter was 5% stiffer than gray matter (P < 0.05). Figure 4b shows the distribution of stiffness in ROIs after normalization to white matter. Normalizing to white matter did not lead to significant differences in ICC (curl: P = 0.008, FEM: P = 0.20), CV (curl: P = 0.46, FEM: P = 0.74), or RC (curl: P = 0.008, FEM: P = 0.016) regardless of reconstruction.

TABLE 1. Stiffness Estimates and MRE Data Quality of the Scans

ROI	Median stiffness G' [kPa] (range)				Median shear-compression wave ratio (range)	
	Curl		FEM			
	Scan 1	Scan 2	Scan 1	Scan 2	Scan 1	Scan 2
Whole-brain	1.29 (1.01–1.39)	1.28 (1.15–1.40)	1.76 (1.53–1.91)	1.78 (1.67–1.96)	7.7 (5.9–15.5)	9.5 (6.3–14.9)
Caudate nucleus	0.93 (0.75–1.28)	1.04 (0.82–1.25)	1.53 (1.13–1.87)	1.55 (1.24–1.96)	4.2 (1.8–9.4)	4.8 (2.2–9.7)
Hippocampus	1.21 (1.01–1.68)	1.13 (0.82–1.63)	1.87 (1.65–2.07)	1.76 (1.62–2.08)	8.2 (3.4–17.4)	7.4 (4.4–16.0)
Putamen	1.22 (0.89–1.46)	1.15 (0.88–1.56)	1.75 (1.42–2.07)	1.72 (1.53–2.11)	4.9 (3.3–6.8)	4.8 (2.3–9.0)
Thalamus	0.94 (0.70–1.10)	1.00 (0.83–1.16)	1.43 (1.01–1.65)	1.47 (1.26–1.87)	4.6 (2.5–9.0)	5.2 (2.8–9.6)
Frontal cortex	1.23 (0.90–1.41)	1.23 (0.98–1.46)	1.63 (1.33–1.92)	1.78 (1.49–1.98)	8.3 (5.3–14.3)	10.0 (4.1–15.4)
Occipital cortex	1.12 (0.93–1.55)	1.15 (1.01–1.44)	1.54 (1.32–2.05)	1.68 (1.49–1.95)	10.3 (6.9–19.7)	13.5 (8.7–23.3)
Parietal cortex	1.32 (1.01–1.46)	1.35 (1.07–1.46)	1.78 (1.48–1.95)	1.82 (1.55–2.00)	9.0 (5.8–13.2)	11.8 (6.3–17.7)
Temporal cortex	1.35 (1.13–1.60)	1.34 (1.18–1.54)	1.85 (1.58–2.10)	1.91 (1.81–2.09)	8.6 (6.3–17.5)	11.7 (8.0–19.4)
White matter	1.36 (1.04–1.48)	1.35 (1.18–1.49)	1.82 (1.56–1.99)	1.84 (1.69–2.03)	7.3 (5.7–15.2)	9.1 (5.9–14.5)

Stiffness estimates from scans 1 and 2, from both reconstruction methods and shear-compression wave ratios (MRE data quality). The MRE data quality is higher in the more peripheral regions of interest (ROIs) than in the deep gray matter ROIs toward the center of the brain, with the exception of hippocampus, where the data quality lie between that of the deep gray matter and cortical gray matter regions.

TABLE 2. Repeatability and Reliability for Different Brain Regions

ROI	Curl reconstruction			FEM reconstruction		
	CV [%]	ICC (95% CI)	RC [kPa] (95% CI)	CV [%]	ICC (95% CI)	RC [kPa] (95% CI)
Whole-brain	4.3	0.74 (0.40–0.90)	0.14 (0.10–0.19)	3.8	0.60 (0.17–0.84)	0.17 (0.12–0.24)
Caudate nucleus	8.5	0.72 (0.36–0.89)	0.23 (0.16–0.31)	9.5	0.51 (–0.01–0.80)	0.41 (0.27–0.52)
Hippocampus	12.8	0.32 (–0.22–0.71)	0.43 (0.29–0.55)	5.2	0.45 (–0.04–0.77)	0.26 (0.18–0.34)
Putamen	11.7	0.34 (–0.21–0.72)	0.39 (0.26–0.49)	9.6	0.15 (–0.41–0.61)	0.48 (0.32–0.61)
Thalamus	8.8	0.20 (–0.29–0.62)	0.23 (0.16–0.31)	8.3	0.48 (–0.01–0.79)	0.33 (0.22–0.43)
Frontal cortex	4.2	0.89 (0.56–0.97)	0.11 (0.09–0.18)	5.5	0.69 (0.12–0.90)	0.20 (0.17–0.34)
Occipital cortex	4.2	0.89 (0.69–0.96)	0.13 (0.09–0.17)	5.4	0.75 (0.20–0.92)	0.19 (0.17–0.32)
Parietal cortex	4.8	0.78 (0.45–0.92)	0.16 (0.12–0.22)	5.3	0.65 (0.15–0.87)	0.21 (0.17–0.33)
Temporal cortex	4.3	0.80 (0.51–0.93)	0.17 (0.11–0.21)	4.0	0.62 (0.19–0.85)	0.19 (0.14–0.27)
White matter	5.1	0.70 (0.32–0.88)	0.18 (0.13–0.24)	4.5	0.51 (0.05–0.80)	0.22 (0.15–0.29)
Comparison curl-FEM *P*-value	0.82	0.16	0.10	-	-	-

Coefficients of variation (CV), intraclass correlation coefficients (ICC), and repeatability coefficients (RC) for the brain and its subregions, using curl reconstruction and the FEM reconstruction, respectively. There were no significant differences in the reliability and repeatability measurements ICC, CV, nor RC, between the curl- and FEM reconstruction methods.

RELATIONSHIP BETWEEN SHEAR-COMPRESSION WAVE RATIO AND TISSUE STIFFNESS. The median shear-compression wave ratio for the whole-brain ROI was 7.7 (range 5.9–15.5, N = 15) for the first scan and 9.5 (range 6.3–14.9) in the second scan. (Table 1). The median absolute difference between the shear-compression wave ratio of the two scans was 1.7 (range 0.03–4.7).

Grouped together, the deep gray matter regions caudate nucleus, hippocampus, putamen, and thalamus had a lower shear-compression wave ratio than white matter ($P < 0.05$), and the cortical gray matter regions had a higher ratio than white matter ($P < 0.05$).

No significant correlations were found between the shear-compression wave ratio and stiffness in the whole-brain ROI for either reconstruction method (curl: P = 0.08 in scan 1 and P = 0.04 in scan 2, FEM: P = 0.07 in scan 1 and P = 0.12 in scan 2). (See Fig. 6a,b.) Further, no significant correlations were found between median shear-compression wave ratio for a subregion ROI and the median stiffness in that ROI for either reconstruction method (curl: P = 0.19, FEM: P = 0.43). (See Fig. 6c,d.)

ASSOCIATION BETWEEN DATA QUALITY AND REPEATABILITY. No significant correlation was observed between difference in shear-compression wave ratio between scans and stiffness difference between scans (P = 0.09 for curl reconstruction, P = 0.12 for FEM reconstruction), nor between the lowest data quality and the difference in whole-brain stiffness (P = 0.09 for curl reconstruction, P = 0.49 for FEM reconstruction).

Discussion

This study measured tissue stiffness of the healthy brain and its subregions using two different MRE reconstruction methods. The variation in stiffness estimates due to normal biologic and technical factors was quantified, and MRE was found to be a reliable method for assessing brain stiffness. The results suggest that MRE can be used to track changes in tissue stiffness caused by disease, and to track the biomechanical effects of treatment.

Stiffness Estimates Depend on Reconstruction Method

In 15 healthy subjects, stiffness estimates depended on the reconstruction method, where the FEM reconstruction yielded a 39% higher stiffness estimate than the curl reconstruction. This is consistent with earlier results, which found 10–42% higher stiffness values in phantom regions when the data were reconstructed using the FEM compared with the curl approach.[21] As Fovargue et al suggest, this may be due to noise sensitivity. Results are further expected to vary with different acquisition strategies and processing pipelines.

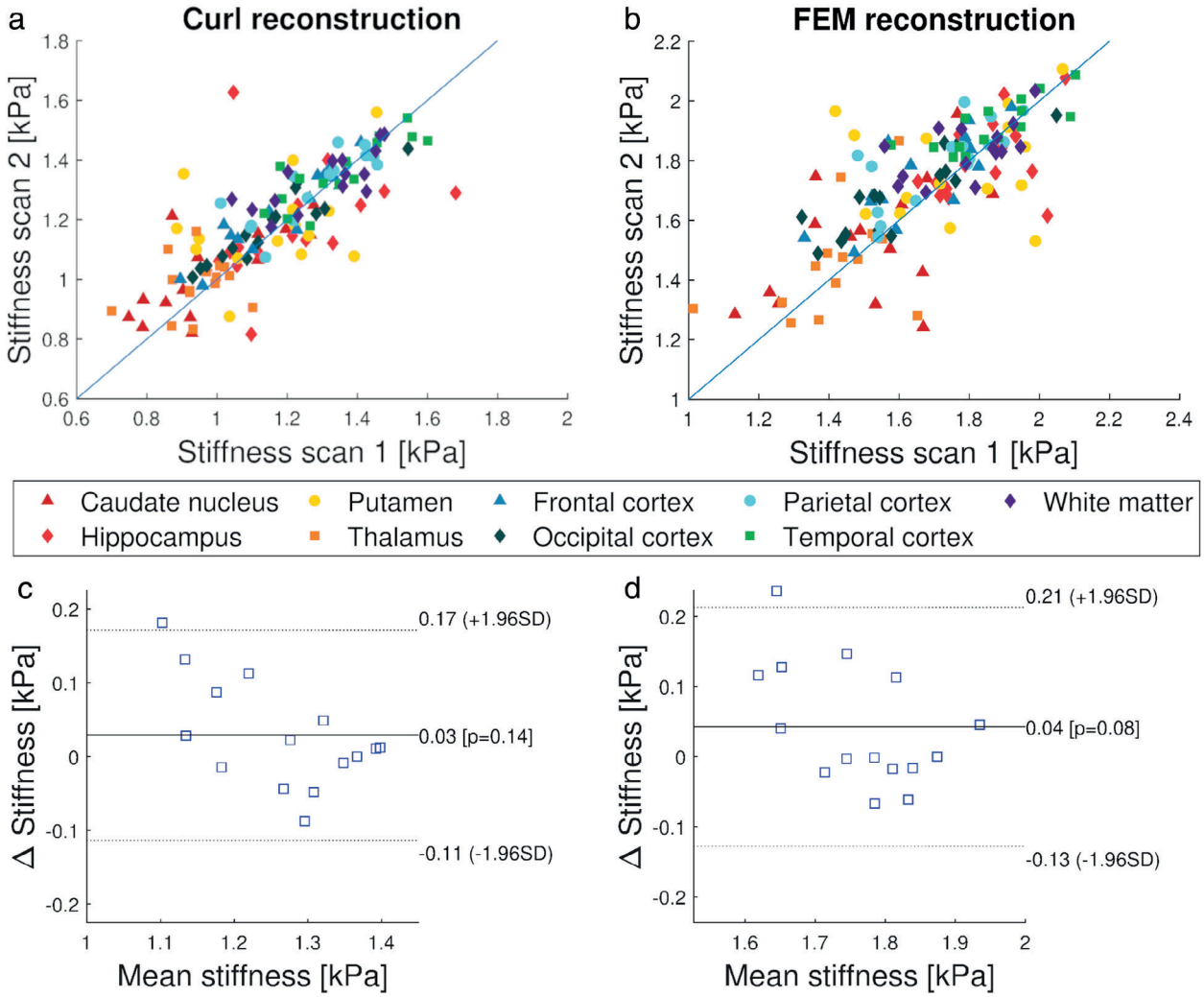

FIGURE 5: (a) Parametric plot of stiffness in each ROI between scan 1 and scan 2 for the curl reconstruction. (b) Similar for the FEM reconstruction. (c) Bland–Altman plots of stiffness in whole-brain ROI for the curl reconstruction. (d) Similar for the FEM reconstruction.

Circumspection is therefore required when comparing stiffness values obtained with different techniques.

Measured stiffness depends on the choice of data acquisition and image reconstruction technique. A way to address this issue it to normalize stiffness measurements to a reference tissue in each subject.[2] In studies of brain cancer patients, tissue stiffness is usually measured relative to healthy white matter.[28–30] This study presents both absolute and normalized measurements. Because stiffness has been shown to vary with age and sex, normalizing within each subject is even more critical with a more heterogeneous subject population.[31,32]

Relationship Between MRE Data Quality and Estimated Stiffness

MRE data quality was quantified by the ratio between the shear waves and the compressional waves, namely, the magnitude of the curl of the displacement field relative to the magnitude of the divergence of the displacement field. Brain tissue is nearly incompressible in vivo. As a consequence, the divergence should be close to zero, while the curl carries the shear signal used to calculate the shear modulus.[16]

This study was not able to identify a relationship between MRE data quality and brain stiffness. Regardless of reconstruction method, the estimated correlation was insignificant at the 0.05 level. MRE was performed twice in each subject. For most subjects, the difference in tissue stiffness between the two scans was small, even when the MRE data quality of the two scans differed.

For a subset of subjects, data quality varied substantially between the two scans. Half of the subjects had a relative difference in shear-compression wave ratio of more than 20% between scans. Subject movement may have contributed to these differences. Moreover, despite the differences in data quality, the median difference in measured brain stiffness for these cases was only 2%. Can the difference between stiffness measurements in the first and second scan be due to differences in data quality? For example, are large differences in

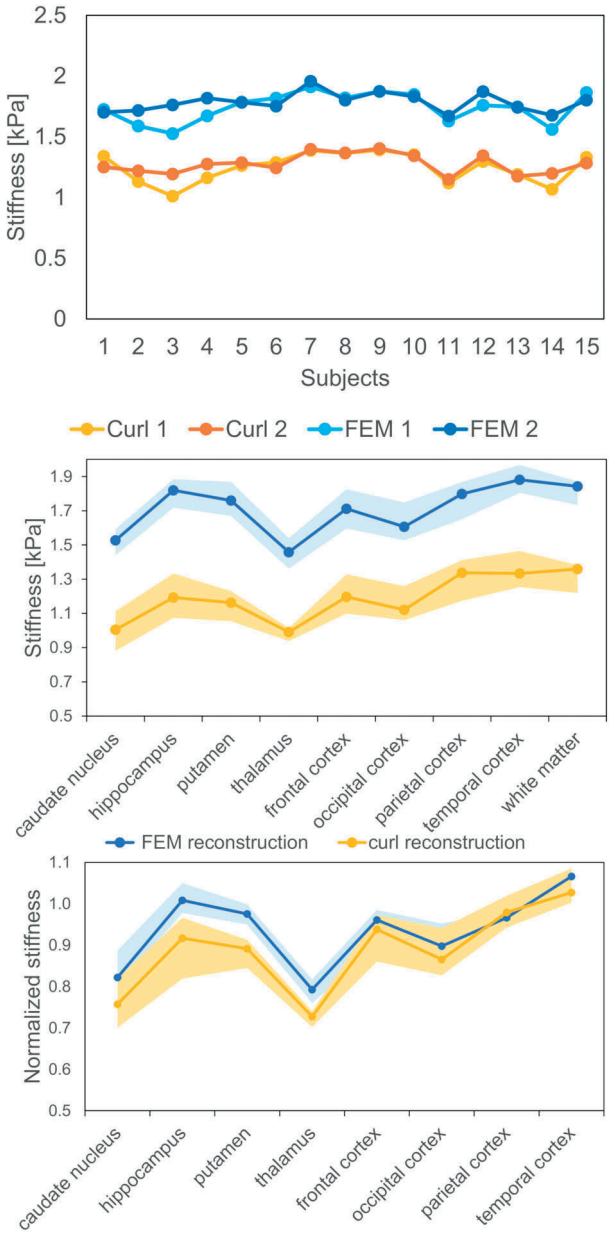

FIGURE 4: (a): Summary plot of mean stiffness in whole-brain ROI from scans 1 and 2 in all 15 subjects, with the two scans taken ~25 minutes apart, shown for both the curl and the FEM reconstruction. Tissue stiffness from the FEM reconstruction is higher than for the curl reconstruction for all subjects and scans. (b) Median stiffness estimates (average of both scans for each subject), ribbon showing first and third quartile range, from both the curl reconstruction and the FEM reconstruction for all the investigated brain regions. The FEM reconstruction yields higher stiffness values than the curl reconstruction for all regions, while the relationship between regions show similar trends for the two reconstructions, for most of the regions. White matter is measured to be stiffer than gray matter using the curl reconstruction, while white and gray matter show similar stiffness using the FEM reconstruction. (c) Median stiffness estimates normalized to values in white matter, from the curl reconstruction and the FEM reconstruction for all the ROIs. The difference between the reconstructions is more apparent after normalization, as the white matter is stiffer relatively to the other regions with curl reconstruction compared to FEM reconstruction.

stiffness measurements associated with substantial differences in MRE data quality? The answer appears to be no. There was no significant correlation between the difference in data quality and differences in tissue stiffness estimates between scans.

Regions of low stiffness, such as caudate nucleus and thalamus, tended toward low shear-compression wave ratios, while regions of high stiffness, such as white matter, tended to have higher shear-compression wave ratios. In general, the shear-compression wave ratio was higher in the brain regions lying closest to the skull, and decreased toward the center of the brain. As the shear waves propagate from the skull inwards, the waves are attenuated, possibly causing a lower MRE signal for the central regions.

Factors Affecting MRE Data Quality

While all subjects were scanned using the same setup, the MRE data quality differed between subjects. The subject with the highest shear-compression wave ratio had twice that of the subject with the lowest shear-compression wave ratio. These challenges may be further exacerbated in a clinical setting. A useful MRE techniques should therefore be robust to data quality.

MRE relies on the transmission of vibrations into the brain tissue. In this study, the vibrations were transmitted by a mechanical transducer placed on the side of the subject's head. Specifically, the transducer was applied on the side of the subject's head, and firmly placed using padding on both sides of the head, leaving no room for head movement. The positioning of the transducer was controlled by visual inspection of images from the localizer scan.

In practice, a central challenge is producing consistent vibrations. Effective transmission requires a firm contact between the transducer and the subject's head. To ensure this contact, the transducer was modified with a curved piece of plastic that lay flush with the side of the test subject's head, slightly behind and above the temple. This piece of plastic was 3D-printed to match the average curvature of the human head, and lined with a thin silicon pad. This is in contrast to the only available commercial MRE hardware, which uses a passive acoustic driver underneath the subject's head.[33]

Using a mechanical transducer positioned on the side of the head has potential drawbacks and advantages relative to using a passive driver beneath the head. The setup used in this study may be susceptible to small movements of the transducer relative to the head. For example, there may be less friction with the transducer for subjects with long or smooth hair. However, an advantage of positioning the transducer on the side of the head rather than on a passive driver underneath the head, avoiding that vibrations are dampened by the weight of the head.[12]

The mechanical vibration inside the applied transducer is caused by a cable with a rotating central axis. Bends in the

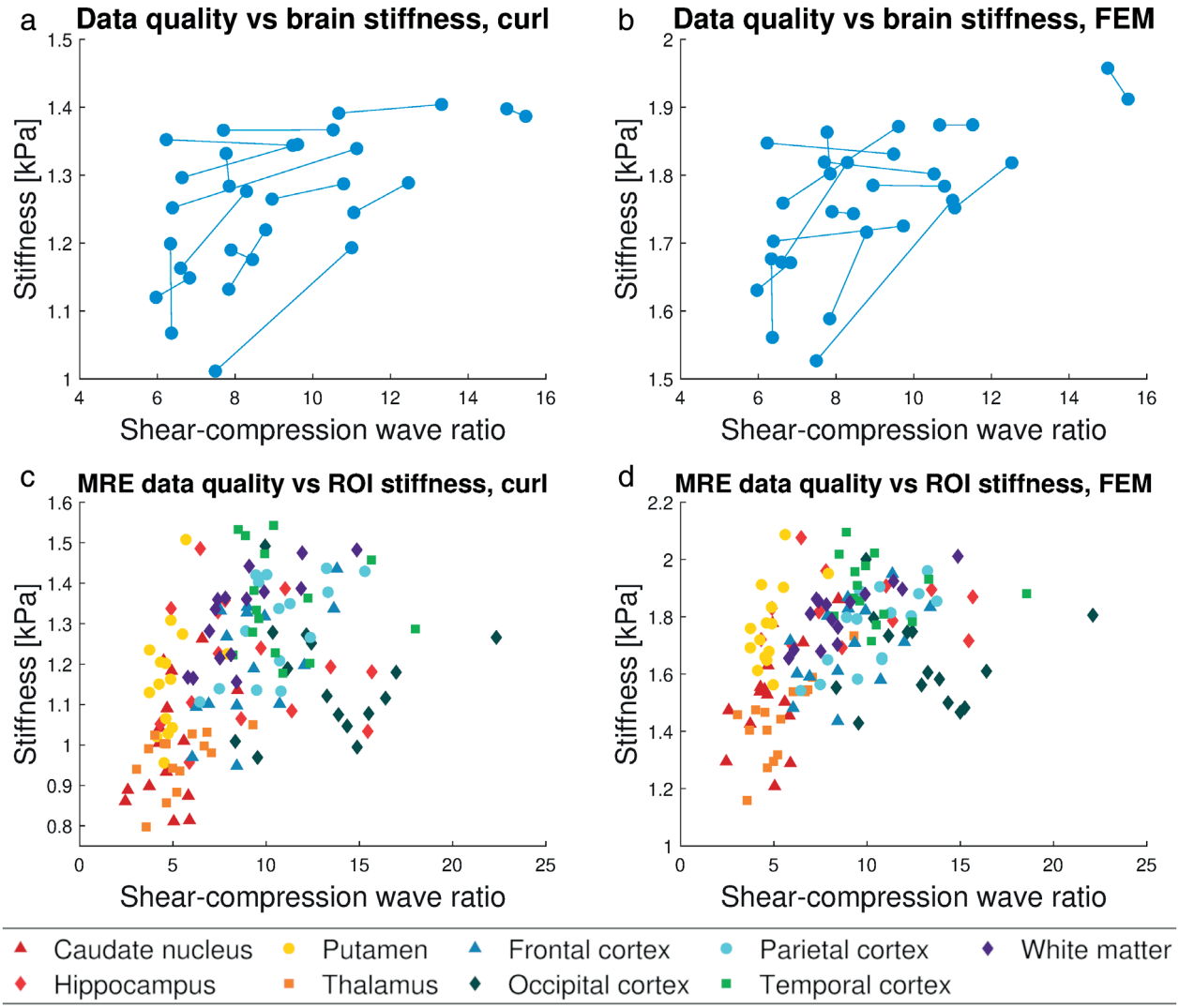

FIGURE 6: (a) The shear-compression wave ratio vs. the stiffness in the whole-brain ROI for the curl reconstruction, showing the two scans for each subject linked with a line. (b) Similar for the FEM reconstruction. (c) Shear-compression wave ratio for each subregion vs. the stiffness in that region for the curl reconstruction, where every entry corresponds to the average of the two scans, and shown for all subjects (N = 15). (d) Similar for the FEM reconstruction. The only significant correlation between the global shear-compression wave ratio and whole-brain ROI stiffness was observed for the FEM reconstruction (Spearman's rho = 0.49, $P < 0.05$ for scan 1 and rho = 0.59, $P < 0.05$ for scan 2).

axis can lead to upper harmonics in the vibration. This effect was minimized by placing the cable as straight as possible from the motor to the scanner isocenter. A different room layout with the MRI scanner placed differently relative to the motor could affect the data quality. The ideal setup would be one where the axis would go straight without bends from the motor to the isocenter.

Repeatability

The RCs found in this study suggest that in order to track whole-brain stiffness changes in a patient over time, this change would need to be larger than 0.14 kPa for the curl reconstruction, and larger than 0.17 kPa for the FEM reconstruction. For the regions deep in the brain, with higher measurement errors, changes would have to be larger than 0.4 kPa. Earlier studies in patients found a 10% reduction of the whole brain |G*| in patients with Alzheimer's disease compared to healthy controls,[34] while a 10% reduction of the whole brain G′ was found for patients with normal pressure hydrocephalus,[35] and for patients with multiple sclerosis,[36] compared to healthy controls. As this study has shown that a significant change in whole-brain stiffness would have to be 11% and 10% for the curl and FEM reconstruction, respectively, this could pose a challenge. However, for several of the brain disorders, for example, brain tumors, a potential stiffness change could be local, and a localized stiffness change could be easier to detect than a global stiffness change of the whole brain. For brain tumors, a large heterogeneity of tumor biomechanics has been shown, with G′ ranging from –60% to +70% of the value in the patient's normal-appearing white

matter. When planning a study in patients, the effect size and repeatability needs to be taken into account to be sure to obtain adequate statistical power.

In addition to assessing repeatability, test–retest reliability was estimated using both relative and absolute indices. The results showed moderate reliability in terms of ICC. The ICC, unlike the CV, depends on the underlying distribution of subjects. Hence, a more homogeneous distribution will result in a lower ICC, as ICC is a measure of how much the measurements for one subject align compared to those of other subjects. For a homogeneous subject group, such as the one used in this study, the test–retest reliability is better assessed by repeatability coefficients, which provide the reliability assessments in kPa, the same units as the tissue stiffness estimates.

Limitations

A general challenge for work in this area is the lack of a gold standard for in vivo tissue stiffness measurements. Limited knowledge of the underlying true values makes comparing reconstruction methods with different stiffness estimates difficult.

The applicability of the results from this study is limited by the relatively small sample comprised of healthy volunteers. Future work should include a larger cohort, and include patients with neurological disease in addition to healthy volunteers. Furthermore, the MRE-derived shear modulus is a frequency-dependent quantity, so measures performed at 50 Hz will only be valid at 50 Hz.[37] This frequency was chosen as it balances resolving power and penetration, and is commonly used in MR elastography.[38]

In this study the test and the retest scan were performed during the same session. The goal was to minimize the factors that could affect the result. A future study where subjects were repositioned between scans or scanned on different days would be clinically interesting and add to the understanding of factors affecting repeatability, as larger variability can be included both in subjects' biological variation, but also introducing uncertainty in varying the placement of equipment. For a full evaluation of brain MRE reliability, reproducibility of stiffness estimates between imaging systems and manufacturers is warranted.

Conclusion

This study found MRE of the human brain to be a robust technique in terms of repeatability and reliability. The RC values suggest that in order to track stiffness changes in a patient over time, the change needs to be on the order of 0.2 kPa, and up to 0.5 kPa for deeper-lying regions with higher measurement error. The estimated tissue stiffness was higher when using the divergence-free FEM reconstruction than using the curl-based reconstruction. Data quality was higher in the more peripheral brain regions than in its central regions. Caution is warranted when comparing stiffness values obtained with different techniques, and normalizing stiffness values to healthy matter is recommended in a patient population.

Conflict of Interest

K.E.E.: NordicNeuroLab AS, Bergen, Norway. Intellectual property rights.

References

1. Murphy MC, Huston J 3rd, Ehman RL. MR elastography of the brain and its application in neurological diseases. Neuroimage 2019;187: 176-183.
2. Bunevicius A, Schregel K, Sinkus R, Golby A, Patz S. Review: MR elastography of brain tumors. Neuroimage Clin 2019;25:102109.
3. Muthupillai R, Ehman RL. Magnetic resonance elastography. Nat Med 1996;2(5):601-603.
4. Pepin KM, Ehman RL, McGee KP. Magnetic resonance elastography (MRE) in cancer: Technique, analysis, and applications. Prog Nucl Magn Reson Spectrosc 2015;90-91:32-48.
5. Venkatesh SK, Yin M, Ehman RL. Magnetic resonance elastography of liver: Technique, analysis, and clinical applications. J Magn Reson Imaging 2013;37(3):544-555.
6. Fovargue D, Nordsletten D, Sinkus R. Stiffness reconstruction methods for MR elastography. NMR Biomed 2018;31(10):e3935.
7. McGarry M, Johnson CL, Sutton BP, et al. Including spatial information in nonlinear inversion MR elastography using soft prior regularization. IEEE Trans Med Imaging 2013;32(10):1901-1909.
8. Johnson CL, McGarry MD, Gharibans AA, et al. Local mechanical properties of white matter structures in the human brain. Neuroimage 2013; 79:145-152.
9. Johnson CL, Schwarb H, McGarry DJM, et al. Viscoelasticity of subcortical gray matter structures. Hum Brain Mapp 2016;37(12):4221-4233.
10. Murphy MC, Huston J 3rd, Jack CR Jr, et al. Measuring the characteristic topography of brain stiffness with magnetic resonance elastography. PLoS One 2013;8(12):e81668.
11. McGarry MD, Van Houten EE, Perrinez PR, Pattison AJ, Weaver JB, Paulsen KD. An octahedral shear strain-based measure of SNR for 3D MR elastography. Phys Med Biol 2011;56(13):N153-N164.
12. Runge JH, Hoelzl SH, Sudakova J, et al. A novel magnetic resonance elastography transducer concept based on a rotational eccentric mass: Preliminary experiences with the gravitational transducer. Phys Med Biol 2019;64(4):045007.
13. Guenthner C, Runge JH, Sinkus R, Kozerke S. Analysis and improvement of motion encoding in magnetic resonance elastography. NMR Biomed 2018;31(5):e3908.
14. Pruessmann KP, Weiger M, Scheidegger MB, Boesiger P. SENSE: Sensitivity encoding for fast MRI. Magn Reson Med 1999;42(5):952-962.
15. Costantini M. A novel phase unwrapping method based on network programming. IEEE Trans Geosci Remote Sens 1998;36(3):813-821.
16. Patz S, Fovargue D, Schregel K, et al. Imaging localized neuronal activity at fast time scales through biomechanics. Sci Adv 2019;5(4): eaav3816.
17. Garteiser P, Sahebjavaher RS, Ter Beek LC, et al. Rapid acquisition of multifrequency, multislice and multidirectional MR elastography data with a fractionally encoded gradient echo sequence. NMR Biomed 2013;26(10):1326-1335.
18. Guenthner C, Sethi S, Troelstra M, Dokumaci AS, Sinkus R, Kozerke S. Ristretto MRE: A generalized multi-shot GRE-MRE sequence. NMR Biomed 2019;32(5):e4049.

19. Sinkus R, Tanter M, Xydeas T, Catheline S, Bercoff J, Fink M. Viscoelastic shear properties of in vivo breast lesions measured by MR elastography. Magn Reson Imaging 2005;23(2):159-165.

20. Savitzky A, Golay M. Smoothing and differentiation of data by simplified least squares procedures. Am Chem Soc 1964;36(8):1627-1639.

21. Fovargue D, Kozerke S, Sinkus R, Nordsletten D. Robust MR elastography stiffness quantification using a localized divergence free finite element reconstruction. Med Image Anal 2018;44:126-142.

22. Tofts P. *Quantitative MRI of the brain: Measuring changes caused by disease*. Chichester, UK, Hoboken, NJ: Wiley; 2003. p 120.

23. Tzourio-Mazoyer N, Landeau B, Papathanassiou D, et al. Automated anatomical labeling of activations in SPM using a macroscopic anatomical parcellation of the MNI MRI single-subject brain. Neuroimage 2002; 15(1):273-289.

24. Bykowski JL, Latour LL, Warach S. More accurate identification of reversible ischemic injury in human stroke by cerebrospinal fluid suppressed diffusion-weighted imaging. Stroke 2004;35(5):1100-1106.

25. Shrout PE, Fleiss JL. Intraclass correlations: Uses in assessing rater reliability. Psychol Bull 1979;86(2):420-428.

26. Klein R. Bland-Altman and Correlation Plot. Available from https://www.mathworks.com/matlabcentral/fileexchange/45049-bland-altman-and-correlation-plot: MATLAB Central File Exchange; 2020.

27. Barnhart HX, Barboriak DP. Applications of the repeatability of quantitative imaging biomarkers: A review of statistical analysis of repeat data sets. Transl Oncol 2009;2(4):231-235.

28. Simon M, Guo J, Papazoglou S, et al. Non-invasive characterization of intracranial tumors by magnetic resonance elastography. New J Phys 2013;15:085024.

29. Streitberger KJ, Reiss-Zimmermann M, Freimann FB, et al. High-resolution mechanical imaging of glioblastoma by multifrequency magnetic resonance elastography. PLoS One 2014;9(10):e110588.

30. Reiss-Zimmermann M, Streitberger KJ, Sack I, et al. High resolution imaging of viscoelastic properties of intracranial tumours by multi-frequency magnetic resonance elastography. Clin Neuroradiol 2015;25(4):371-378.

31. Sack I, Beierbach B, Wuerfel J, et al. The impact of aging and gender on brain viscoelasticity. Neuroimage 2009;46(3):652-657.

32. Hiscox LV, McGarry MDJ, Schwarb H, et al. Standard-space atlas of the viscoelastic properties of the human brain. Hum Brain Map 2020;41: 5282-5300.

33. Murphy MC, Huston J 3rd, Jack CR Jr, et al. Decreased brain stiffness in Alzheimer's disease determined by magnetic resonance elastography. J Magn Reson Imaging 2011;34(3):494-498.

34. Gerischer LM, Fehlner A, Kobe T, et al. Combining viscoelasticity, diffusivity and volume of the hippocampus for the diagnosis of Alzheimer's disease based on magnetic resonance imaging. Neuroimage Clin 2018;18:485-493.

35. Streitberger KJ, Wiener E, Hoffmann J, et al. In vivo viscoelastic properties of the brain in normal pressure hydrocephalus. NMR Biomed 2011;24(4):385-392.

36. Wuerfel J, Paul F, Beierbach B, et al. MR-elastography reveals degradation of tissue integrity in multiple sclerosis. Neuroimage 2010;49(3): 2520-2525.

37. Hamhaber U, Klatt D, Papazoglou S, et al. In vivo magnetic resonance elastography of human brain at 7 T and 1.5 T. J Magn Reson Imaging 2010;32(3):577-583.

38. Hiscox LV, Johnson CL, Barnhill E, et al. Magnetic resonance elastography (MRE) of the human brain: Technique, findings and clinical applications. Phys Med Biol 2016;61(24):R401-R437.

Paper II

Decreased tissue stiffness in glioblastoma by MR elastography is associated with increased cerebral blood flow

Siri F. Svensson, Elies Fuster-Garcia, Anna Latysheva, Jorunn Fraser-Green, Wibeke Nordhøy, Omar I. Darwish, Ivar T. Hovden, Sverre Holm, Einar O. Vik-Mo, Ralph Sinkus and Kyrre E. Emblem

In: *European Journal of Radiology*. Vol. 147, article 110136 (2022), DOI: 10.1016/j.ejrad.2021.110136.

II

European Journal of Radiology 147 (2022) 110136

Contents lists available at ScienceDirect

European Journal of Radiology

journal homepage: www.elsevier.com/locate/ejrad

Research article

Decreased tissue stiffness in glioblastoma by MR elastography is associated with increased cerebral blood flow

Siri Fløgstad Svensson [a,b,*], Elies Fuster-Garcia [a,c], Anna Latysheva [d], Jorunn Fraser-Green [e], Wibeke Nordhøy [a], Omar Isam Darwish [f], Ivar Thokle Hovden [a,b], Sverre Holm [b], Einar O. Vik-Mo [g], Ralph Sinkus [f,h], Kyrre Eeg Emblem [a]

[a] Dept. of Diagnostic Physics, Oslo University Hospital, Oslo, Norway
[b] Department of Physics, University of Oslo, Oslo, Norway
[c] Biomedical Data Science Laboratory, Instituto Universitario de Tecnologías de la Información y Comunicaciones, Universitat Politècnica de València, Valencia, Spain
[d] Department of Radiology, Oslo University Hospital, Oslo, Norway
[e] The Intervention Centre, Oslo University Hospital, Oslo, Norway
[f] Division of Imaging Sciences and Biomedical Engineering, King's College, London, United Kingdom
[g] Vilhelm Magnus Laboratory, Dept. of Neurosurgery, Oslo University Hospital, Oslo, Norway
[h] INSERM U1148, LVTS, University Paris Diderot, Paris, France

ARTICLE INFO

Keywords:
Magnetic Resonance Elastography
Tumor stiffness
Glioblastoma
Brain tumor
Viscoelastic properties

ABSTRACT

Purpose: Understanding how mechanical properties relate to functional changes in glioblastomas may help explain different treatment response between patients. The aim of this study was to map differences in biomechanical and functional properties between tumor and healthy tissue, to assess any relationship between them and to study their spatial distribution.

Methods: Ten patients with glioblastoma and 17 healthy subjects were scanned using MR Elastography, perfusion and diffusion MRI. Stiffness and viscosity measurements G′ and G″, cerebral blood flow (CBF), apparent diffusion coefficient (ADC) and fractional anisotropy (FA) were measured in patients' contrast-enhancing tumor, necrosis, edema, and gray and white matter, and in gray and white matter for healthy subjects. A regression analysis was used to predict CBF as a function of ADC, FA, G′ and G″.

Results: Median G′ and G″ in contrast-enhancing tumor were 13% and 37% lower than in normal-appearing white matter ($P < 0.01$), and 8% and 6% lower in necrosis than in contrast-enhancing tumor, respectively ($P < 0.05$). Tumors showed both inter-patient and intra-patient heterogeneity. Measurements approached values in normal-appearing tissue when moving outward from the tumor core, but abnormal tissue properties were still present in regions of normal-appearing tissue. Using both a linear and a random-forest model, prediction of CBF was improved by adding MRE measurements to the model ($P < 0.01$).

Conclusions: The inclusion of MRE measurements in statistical models helped predict perfusion, with stiffer tissue associated with lower perfusion values.

1. Introduction

Glioblastoma (GBM) is the most common primary malignant tumor in the central nervous system, and is usually rapidly fatal [1]. With a standard treatment regimen of surgery and radiochemotherapy the median survival time is only 12–15 months [1].

Perfusion and diffusion magnetic resonance imaging (MRI) are considered important methods for understanding the tumor biology and quantifying physiological processes [2]. However, the changing biomechanical properties of a solid tumor and its surrounding tissue *in vivo* are less studied. Moreover, understanding how the mechanical properties of tissue relate to functional changes, may help explain the substantial variation in appearance and treatment response between patients.

MR Elastography (MRE) is a technique for non-invasively measuring the biomechanical properties of tissue [3]. Earlier studies have found that glioma tumors differ from the healthy brain in terms of stiffness and viscosity [4–7]. Most studies on MRE in brain tumors present mean

* Corresponding author at: Department for Diagnostic Physics, Building 20 Gaustad, Oslo University Hospital, PB 4959 Nydalen, 0424 Oslo, Norway.
E-mail address: siriflo@uio.no (S. Fløgstad Svensson).

https://doi.org/10.1016/j.ejrad.2021.110136
Received 16 August 2021; Received in revised form 9 November 2021; Accepted 27 December 2021
Available online 29 December 2021
0720-048X/© 2022 The Authors. Published by Elsevier B.V. This is an open access article under the CC BY license (http://creativecommons.org/licenses/by/4.0/).

values for the tumor stiffness, yet glioblastomas display a large degree of heterogeneity, both between patients, and within the tumor [8]. Furthermore, glioblastomas are known to infiltrate the surrounding tissue beyond the contrast-enhancing tumor, and this peritumoral area appears to play a key role in tumor growing and recurrence [9].

In this study, we combine MRE of GBM patients with diffusion and perfusion imaging. Using a deep learning approach [10], we segmented tumors into contrast-enhancing and necrotic regions, and FLAIR-enhanced edema region in order to study tumor heterogeneity and infiltration. The objective of our study is to map the differences between tumor and healthy tissue with regard to biomechanical and functional properties, to study their spatial distribution, and to assess any possible relationship between biomechanical and functional parameters.

2. Materials and methods

2.1. Acquisition

Data was collected prospectively from 10 patients, 5 females and 5 males (44–74 years, median 55 years), prior to any treatment. Eligibility criteria for patients were an IDH-wildtype glioblastoma diagnosis and ability to undergo a pre-surgical extended MR examination including MR elastography, as evaluated by the patient and responsible surgeon. All patients signed informed consent. In addition, 17 healthy subjects were scanned, 8 females and 9 males (21–34 years, median 25 years). Eligibility was based on health and age between 20 and 40 years. In addition, 17 healthy subjects were scanned, 8 females and 9 males (21–34 years, median 25 years). All subjects signed an informed consent form. The study was approved by the National Research Ethics Committee and the institutional review board. The examination was tolerated well by all subjects. Apart from the subjects included in the study, three healthy subjects and two patients were excluded due to inadequate MRE data quality.

The scans were performed on a 3 T clinical MRI scanner (Ingenia, Philips Medical Systems, Best, the Netherlands) using a 32-channel head coil. Scan parameters for all sequences used are presented in Table 1. The MRE was performed using a gravitational transducer [11] attached on the side of the subject's head to induce shear waves of 50 Hz into the brain.

2.2. Image processing

Perfusion and diffusion imaging was analysed in the nordicICE (NordicNeuroLab AS, Bergen, Norway) software. Details about the MRE acquisition and processing can be found in [12]. Fig. 1 shows resulting maps of cerebral blood flow (CBF), apparent diffusion coefficient (ADC) and fractional anisotropy index (FA) for both patients and healthy subjects**.** MRE produced maps of the shear storage modulus G′ (as a measure for stiffness) and loss modulus G″ (related to the viscosity, meaning the tissue's ability to dissipate energy) (Fig. 1**E-F, L-M**).

Patient data was segmented into contrast-enhancing tumor, edema, necrosis, and normal-appearing gray and white matter (Fig. 1**N**). Data from healthy subjects was segmented into gray and white matter. Gray matter was further subdivided into the deep gray and cortical regions. Deep gray matter regions included in the study were head of the caudate nucleus, putamen, thalamus and hippocampus. Cortical gray matter regions included were the frontal, occipital, parietal and temporal lobe (Fig. 1**G**). In addition to absolute measurements, elastography and diffusion measurements in gray matter regions were normalized to the mean value in each subject's white matter. Details about image processing and segmentation can be found in Supplementary information.

2.3. Statistics

For each individual, we computed the mean value of each measurement in all regions of interest (ROIs). In the results below, we present the median of these mean values across individuals, with the range in parenthesis. Measurements in different regions were compared using a Wilcoxon signed-rank test. The relationship between the different parameters for mean values in each ROI was assessed by a Spearman rank-order test.

To visualize each tissue's signature across parameters, mean measurements in each region for each subject was dimensionally reduced using t-distributed stochastic neighbor embedding (t-SNE).

Voxel-wise regression analysis was performed using both a simple linear model and a random forest model for perfusion as a function of ADC, FA, G′ and G″. The performance of the regression models was evaluated by their root-mean-square error (RMSE) with a leave-one-patient-out cross-validation strategy. The different models were compared using a Wilcoxon signed-rank test.

A significance level of $P < 0.05$ was assumed for all tests, after Holm-Bonferroni corrections for multiple comparisons. All statistical analyses were done using Matlab (version R2021a, MathWorks, Natick, MA, USA).

Table 1
Scan parameters for patients and healthy subjects. Abbreviations: Gradient-echo (GRE), spin-echo (SE), echo-planar imaging (EPI), sensitivity encoding (SENSE), Diffusion tensor imaging (DTI), pseudo-Continuous Arterial Spin Labelling (pCASL), Proton-density weighted (PD).

Sequence	Repetition time [ms]	Echo time [ms]	Acquisition matrix	Resolution [mm^3]	Additional information	Used for
T_2-weighted	3000	80	420 × 270 × 28	0.6 × 0.6 × 4	Turbo-SE sequence	Patients
FLAIR	4800	320	252 × 249 × 183	1 × 1 × 1	Turbo-SE sequence, inversion time = 1650 ms	Patients
DSC GRE-SE	1500	25 (GRE)/ 105 (SE)	100 × 125 × 11	1.8 × 1.8 × 5	Combined single-shot 2D GRE-SE, SENSE-factor 2, EPI readout	Patients
T_1-weighted	5.2	2.3	256 × 256 × 368	1 × 1 × 1	3D inversion recovery turbo field echo, flip angle = 8°, shot interval = 3000 ms, inversion delay = 853 ms	All subjects
DTI	9800	60	94 × 94 × 50	2.5 × 2.5 × 2.5	SE, single-shot, EPI readout, SENSE-factor 2, 15 gradient directions, b-values 0 s/mm^2 and 800 s/mm^2	All subjects
MRE	295	12	72 × 70 × 15	3.1 × 3.1 × 3.1	MEG strength 13.2 mT/m, SENSE-factor 2	All subjects
ASL	4400	14.8	72 × 70 × 15	3.6 × 3.6 × 5.5	2D pCASL, labelling duration 1.8 s, post-label delay 1.8 s, 35 pairs of label and control volumes, EPI readout	Healthy subjects
PD	12,000	12	72 × 70 × 15	3.6 × 3.6 × 5.5	Used for calibration of the subtracted and averaged ASL images	Healthy subjects

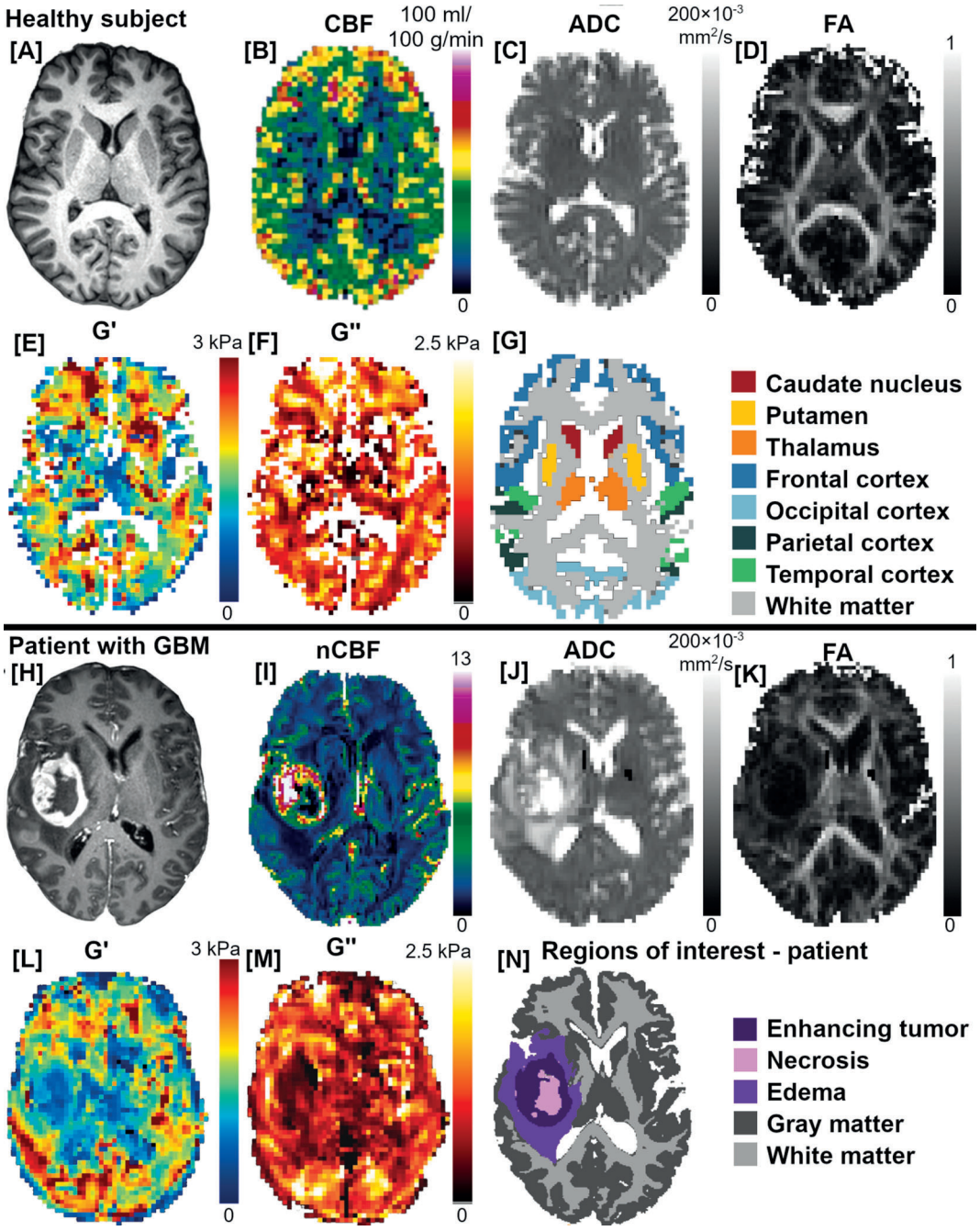

Fig. 1. Image example of a healthy subject and patient. A) T1-weighted image, B) CBF, C) ADC, D) FA E) G′, and F) G″, maps for a healthy subject. G) ROIs used for the healthy subjects, except from hippocampus (not visible in this slice). H) Contrast-enhanced T1-weighted image, I) normalized CBF, J) ADC, K) FA, L) G′, M) G″ maps for a patient with glioblastoma. N) Patient ROIs.

3. Results

3.1. Glioblastoma tissue is structurally degraded compared to healthy tissue

The results of the measurements in the different ROIs are summarized in Table 2.

The median value of G′ in the contrast-enhancing tumor was 13 % lower than in contralateral normal-appearing white matter (cNAWM) ($P < 0.01$). G″ was 37 % lower ($P < 0.01$) and FA was 52 % lower ($P < 0.01$) in contrast-enhancing tumor than in cNAWM. ADC was 48 % higher ($P < 0.01$) and CBF was 2.9 times higher ($P < 0.01$) in tumor than in cNAWM. Especially CBF showed a large variability between patients, with the highest patient tumor CBF 3.2 times higher than the lowest patient tumor CBF.

In edema surrounding the tumor, median G′ was similar to cNAWM ($P = 0.6$), while G″ was 16 % lower than in cNAWM ($P < 0.01$). FA was 48 % lower ($P < 0.05$) and ADC was 53 % higher in edema than in cNAWM ($P < 0.01$). CBF was similar in edema and cNAWM ($P = 0.3$).

3.2. Tumor stiffness is heterogeneous, both between patients and within tumor

The median value of G′ and G″ was 18 % and 6 % lower in necrosis than in contrast-enhancing tumor, respectively ($P < 0.05$). This suggests a within-tumor heterogeneity, illustrated in Fig. 2: G'_{norm} and G''_{norm}

Table 2
Measurements in patients (n = 10) and healthy subjects (n = 17). Upper part: G′, G′′, G'_{norm}, G''_{norm} (normalized to each subject's cNAWM), ADC, FA, and normalized CBF for patients. Lower part: Corresponding measurements in healthy subjects' ROIs. CBF measurements in healthy subjects were acquired using ASL and are not directly comparable to patient CBF (using DSC).

PATIENTS	Median G′ [kPa] (range)	Median G′′ [kPa] (range)	Median G'_{norm} (range)	Median G''_{norm} (range)	Median ADC [10^{-3} mm^2/s] (range)	Median FA (range)	Median nCBF (range)
Contrast-enhancing tumor	1.40 (1.15–1.62)	0.66 (0.55–0.80)	0.86 (0.70–1.02)	0.66 (0.51–0.83)	1.21 (1.00–1.47)	0.19 (0.14–0.25)	3.77 (2.98–9.64)
Necrotic region	1.15 (0.70–1.76)	0.63 (0.37–0.81)	0.70 (0.50–1.11)	0.63 (0.40–0.74)	1.36 (0.94–1.90)	0.10 (0.09–0.16)	2.14 (1.48–3.61)
Edema	1.61 (1.43–2.16)	0.88 (0.68–1.09)	1.01 (0.86–1.33)	0.90 (0.66–1.03)	1.25 (1.01–1.47)	0.20 (0.16–0.34)	1.50 (0.97–2.46)
Average gray matter	1.65 (1.34–1.73)	1.02 (0.90–1.16)	1.01 (0.87–1.07)	0.99 (0.91–1.09)	0.91 (0.85–1.08)	0.16 (0.14–0.17)	2.39 (2.06–2.94)
Average white matter	1.61 (1.36–1.90)	1.04 (0.91–1.23)	–	–	0.82 (0.77–0.89)	0.39 (0.34–0.43)	1.29 (1.11–1.45)
HEALTHY SUBJECTS	**Median G′ [kPa] (range)**	**Median G′′ [kPa] (range)**	**Median G'_{norm} (range)**	**Median G''_{norm} (range)**	**Median ADC [10^{-3} mm^2/s] (range)**	**Median FA (range)**	**Median CBF [ml/100 g/min] (range)**
Caudate nucleus	1.49 (1.25–1.83)	0.84 (0.45–1.15)	0.82 (0.71–1.00)	0.72 (0.40–0.95)	0.74 (0.70–0.81)	0.22 (0.18–0.24)	20 (7–35)
Hippocampus	1.83 (1.30–2.31)	0.96 (0.72–1.14)	1.01 (0.76–1.22)	0.80 (0.59–0.93)	0.88 (0.83–0.93)	0.18 (0.16–0.23)	20 (8–31)
Putamen	1.78 (1.46–2.16)	1.11 (0.77–1.58)	0.96 (0.83–1.17)	0.91 (0.70–1.33)	0.73 (0.71–0.76)	0.20 (0.17–0.23)	24 (12–37)
Thalamus	1.40 (1.21–1.55)	0.73 (0.50–1.03)	0.76 (0.65–0.88)	0.60 (0.46–0.80)	0.80 (0.76–0.84)	0.29 (0.27–0.30)	24 (12–44)
Frontal lobe	1.65 (1.39–1.90)	1.14 (0.88–1.33)	0.91 (0.76–1.10)	0.94 (0.76–1.09)	0.88 (0.86–0.91)	0.17 (0.15–0.18)	44 (23–71)
Occipital lobe	1.44 (1.11–2.15)	1.17 (0.89–1.39)	0.78 (0.61–1.20)	1.01 (0.70–1.26)	0.85 (0.83–0.87)	0.16 (0.15–0.18)	40 (25–62)
Parietal lobe	1.74 (1.38–2.55)	1.23 (0.96–1.35)	0.95 (0.75–1.30)	1.01 (0.81–1.16)	0.86 (0.84–0.88)	0.16 (0.15–0.18)	40 (20–68)
Temporal lobe	1.81 (1.55–2.28)	1.32 (1.18–1.63)	1.00 (0.81–1.23)	1.10 (0.95–1.45)	0.87 (0.85–0.89)	0.16 (0.15–0.17)	36 (21–60)
Average gray matter	1.68 (1.48–1.97)	1.16 (1.01–1.23)	0.89 (0.81–1.07)	0.97 (0.85–1.09)	0.86 (0.85–0.88)	0.17 (0.16–0.18)	40 (22–62)
Average white matter	1.84 (1.70–1.96)	1.19 (1.10–1.32)	–	–	0.80 (0.77–0.82)	0.33 (0.32–0.37)	NA

voxels distributions for each patient differed between contrast-enhancing tumor, necrosis and edema. The differences between patients were also larger in these regions than in normal-appearing gray matter, illustrating the interpatient tumor heterogeneity.

This variability is also illustrated in Fig. 3, which shows the distribution of G′, G′′, ADC and FA among healthy subjects and patients. Measurements in tumor and edema showed a larger inter-patient variability than the values in patient white and gray matter.

3.3. Patient normal-appearing white matter shows lower stiffness, viscosity and anisotropy than white matter in healthy subjects

The white matter region in patients had 12 % lower G′ and G′′ (both $P < 0.001$) compared to white matter in healthy subjects. White matter ADC and FA was 3 % and 16 % higher in patients than in healthy subjects (ADC: $P < 0.05$, FA: $P < 0.001$).

For the healthy subjects, G′ was 9 % higher and G′′ was 39 % higher in the cortical gray matter than in deep gray matter ($P < 0.001$). Comparing white matter to deep gray matter, G′ was 18% higher ($P < 0.01$) and G′′ was 37 % higher in white matter ($P < 0.001$). G′ was 8% higher in white than in cortical gray matter ($P < 0.01$), while G′′ was similar between the two ($P = 0.99$).

The t-SNE plot (Fig. 4) illustrates the separation between pathological and healthy brain regions in both patients and healthy subjects, for ADC, FA, G'_{norm} and G''_{norm}. Most regions of interest in healthy subjects tracked together, and showed a separation between deep and cortical gray matter regions. The contrast-enhancing tumor, edema and necrosis were close to each other and separated from the healthy ROIs.

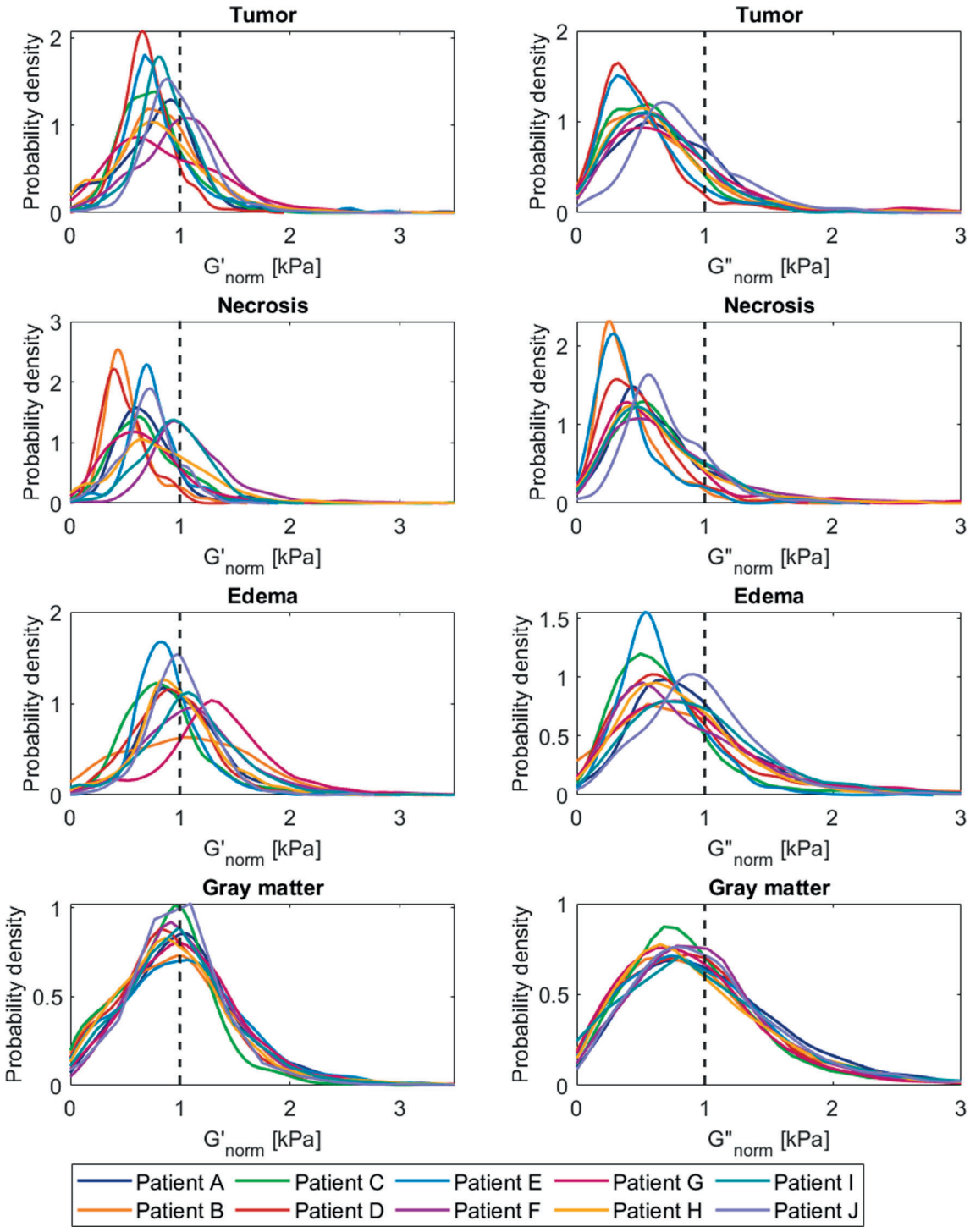

Fig. 2. Distribution of biomechanical properties in pathological regions and gray matter. Distribution of voxel values for G'_{norm} and G''_{norm} in A-B) contrast-enhancing tumor, C-D) necrosis, E-F) edema and G-H) normal-appearing gray matter.

3.4. Tissue properties approach normal values further away from tumor core

Fig. 5 shows gradients of measurements moving radially out from the tumor core. For most patients, G′ and G″ started from low values within the tumor and increased toward values found in cNAWM at the distal edge of the edema region. ADC was high in necrosis, tumor and edema, and was still 29 % (median value) higher than in cNAWM at the edema edge—although with large variation among patients. FA was low in the tumor core and increased away from it; the median value was 46 % lower at the edema edge than in cNAWM. CBF, leakage and vessel size were largest in the contrast-enhancing tumor, and gradually decreased toward the mean cNAWM value at the edema edge.

3.5. Tissue may have abnormal properties outside lesion area

Fig. 6 illustrates gradients moving radially outward from the lesion, defined as necrosis, tumor or edema. For several of the patients, the tissue properties remained abnormal (outside the 25th and 75th percentile of cNAWM) for more than 5 mm into the normal-appearing

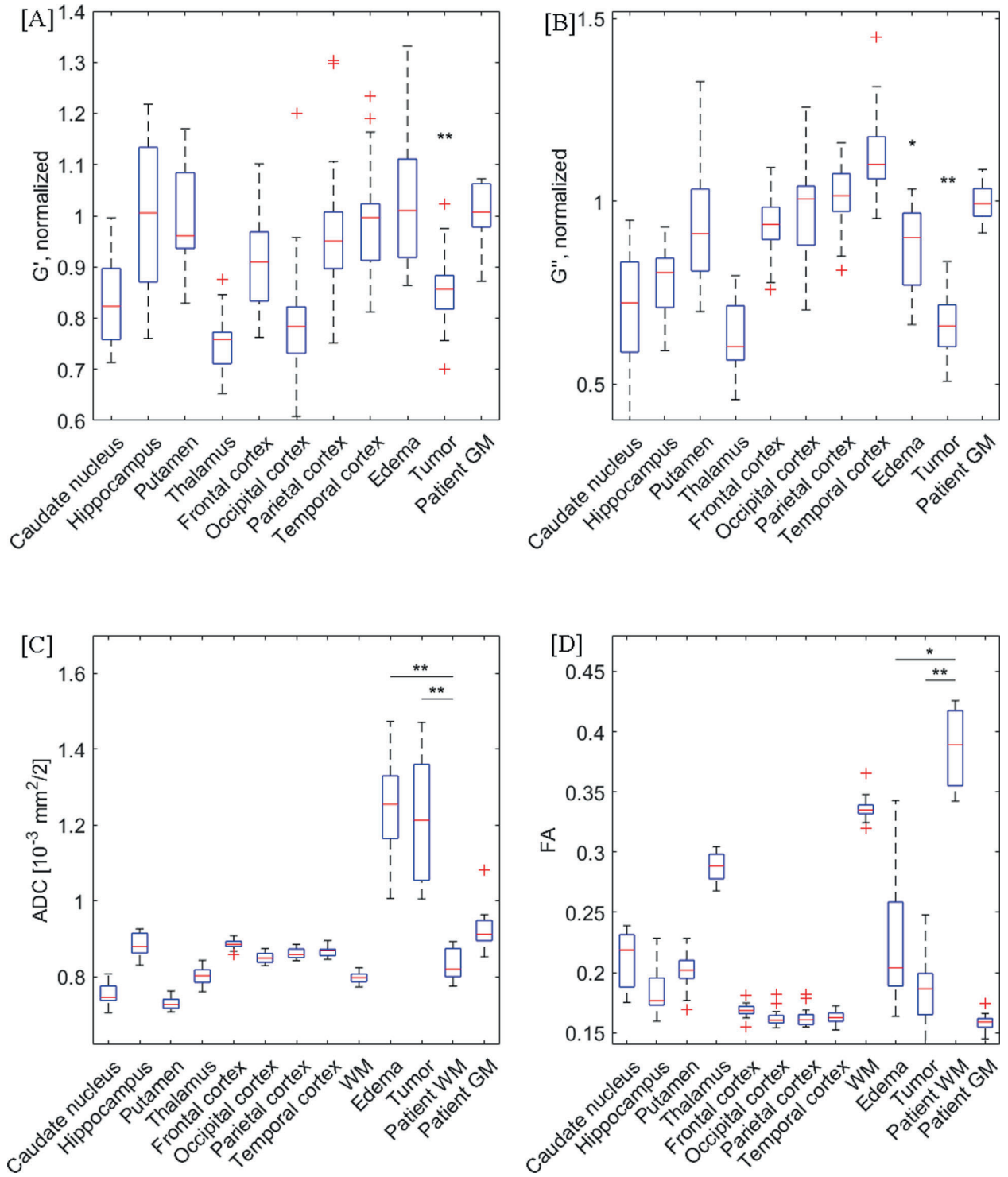

Fig. 3. Box plots of healthy brain regions vs tumors. A) G'_{norm}, B) G''_{norm}, C) ADC, and D) FA for all ROIs in healthy subjects and in edema, contrast-enhancing tumor, white and gray matter in patients. The red line shows the median value, the blue box the 25th and 75th percentile of the mean values, with red crosses indicating outliers. Asterisks show significant differences from patient's cNAWM (*=P < 0.05, **=P < 0.01). (For interpretation of the references to colour in this figure legend, the reader is referred to the web version of this article.)

tissue.

No correlations were found between tumor stiffness and the distance to the skull, nor between tumor stiffness and tumor volume.

3.6. High cerebral blood flow is associated with low stiffness

A positive correlation was found between mean G′ and G″ in contrast-enhancing tumor (Spearman's rho 0.76, P < 0.05) and in patient white matter (rho 0.78, P < 0.05). No correlations across patients were found in the contrast-enhancing tumor between mean G′ and mean CBF, ADC, leakage or vessel size, nor between G″ and the perfusion and diffusion parameters. The same was true for the other patient ROIs. For the healthy subjects, the only correlation between parameters was between G′ and G″ in gray (P < 0.01) and white matter (P < 0.01).

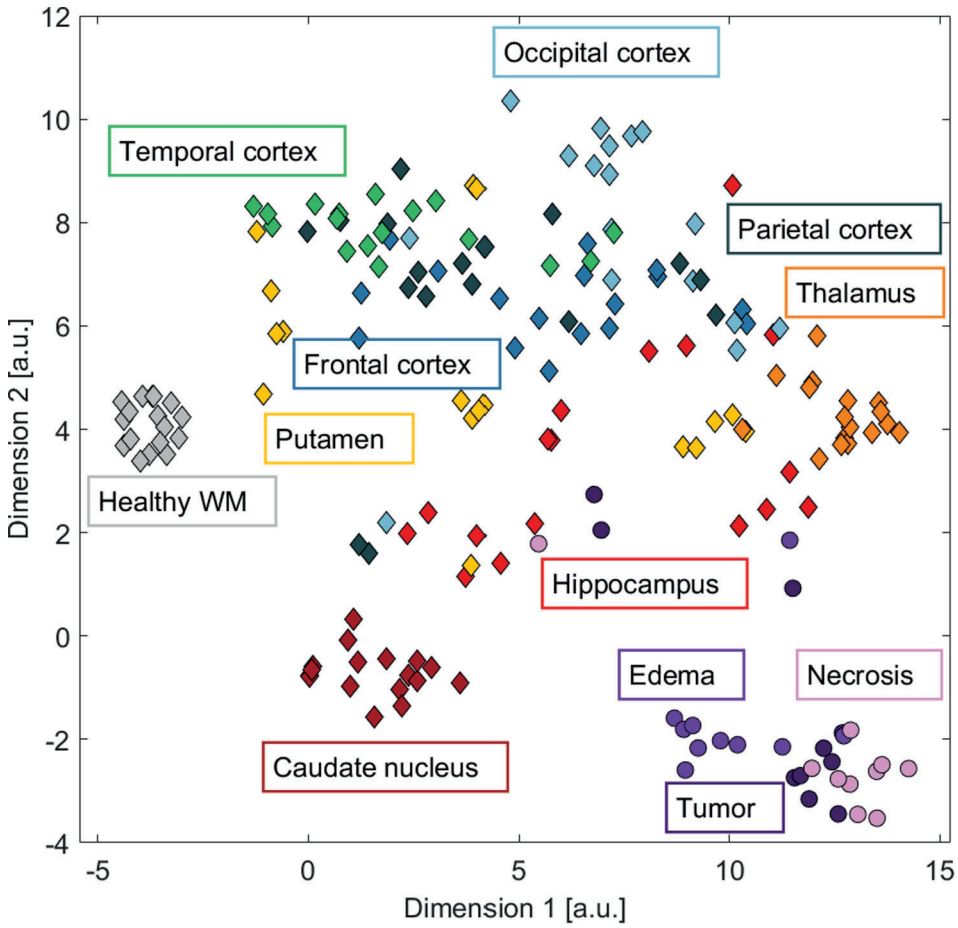

Fig. 4. Brain regions in healthy subjects and patients with ADC, FA, G'_{norm} and G''_{norm} reduced into two dimensions. T-distributed stochastic neighbour embedding of mean measurements, arbitrary units (a.u) on axes. Diamond markers: mean values in healthy subjects, circles: patients.

We estimated voxel-by-voxel regressions to explain CBF as a function of the other measurements, all normalized to cNAWM. Our baseline model was a linear model with ADC_{norm} and FA_{norm} as predictors. Using RMSE as a criterion, we investigated how predictive power increased as we added first G'_{norm} and then both G'_{norm} and G''_{norm} to the model. Results are presented in Table 3, and show that predictive power increased significantly with the inclusion of each additional predictor. After the assessment of each model, the linear model was trained using all data, and the final linear model is:

$$CBF = 1.7 - 0.16 \cdot G'_{norm} - 0.15 \cdot G''_{norm} + 0.35 \cdot ADC - 0.44 \cdot FA$$

In addition to the linear model, we investigated the predictive ability of a random-forest model (Table 3, right column). Again, we compared a baseline model including ADC_{norm} and FA_{norm} to models including G'_{norm}, and both G'_{norm} and G''_{norm}. All three random-forest models performed better than the linear models ($P < 0.01$). In addition, the performance of the random forest model improved by including G'_{norm} ($P < 0.01$), and further improved by including both G'_{norm} and G''_{norm} ($P < 0.01$).

3.7. Data accessibility

All the data and the associated *meta*-data generated as a part of this study is publicly available by request through Zenodo (https://doi.org/10.5281/zenodo.4926005).

4. Discussion

In this study, we used MR elastography, perfusion and diffusion imaging in patients with glioblastoma and healthy subjects. We found that glioblastoma tissue was structurally degraded compared to healthy tissue in terms of all measurements. Measurements approached normal values when moving away from the tumor core, but we still found abnormal tissue properties in regions that appear normal on anatomical images. Finally, we constructed a predictive model for CBF, which showed that perfusion increased with decreased G' and G''.

Stiffness and viscosity in tumors, here measured by G' and G'', were significantly lower than in normal-appearing matter. This is consistent with previous reports: Gliomas have been found to be softer than normal tissue [4,6,7,13] and substantially less viscous [4,5,7]. A reduction in both G'' and G' can be interpreted as a softening of the mechanical rigidity of the tissue [14].

Most studies of MRE in gliomas have presented mean tumor values. Streitberger et al. noted that glioblastomas were composed of stiff and soft compartments, and that the source of heterogeneity may be that glioblastomas consist of both solid masses and possibly cystic and necrotic fractions [4]. In our study, tumors were segmented into contrast-enhancing and necrotic regions. We found necrotic tumor regions to have even lower stiffness and viscosity than the contrast-enhancing parts of the tumor and the distribution of stiffness and viscosity to vary more in tumors than in normal-appearing matter. In a study of MRE in mouse-model gliomas, Schregel et al. found that tumors became softer and more heterogeneous over time with tumor progression and that softer sub-regions of the tumor were characterised by a high heterogeneity [15].

Areas displaying high FLAIR signal is presumed to represent edema due to cancer infiltration, and are considered important elements of treatment planning [9]. We found that tissue properties in edema had

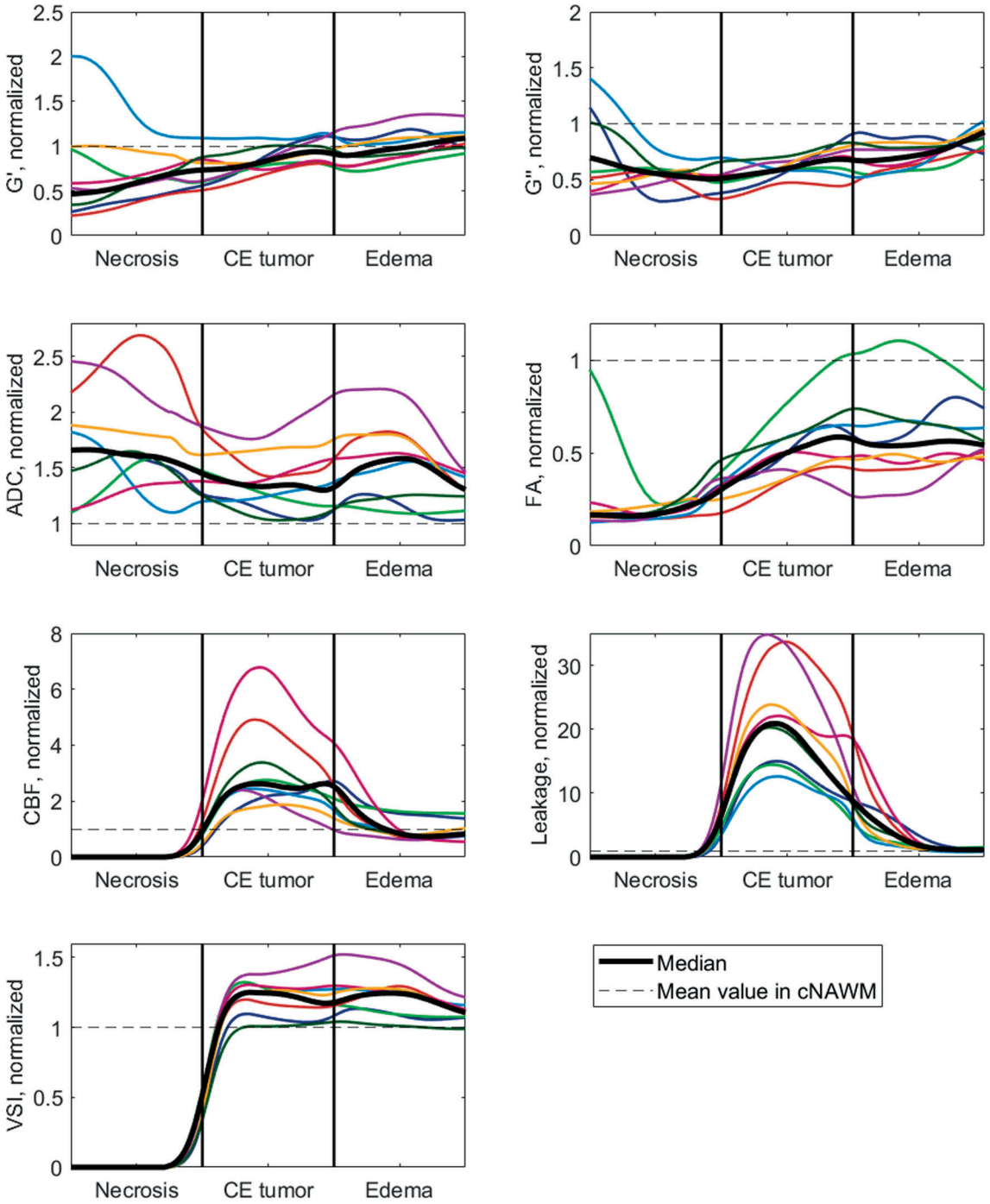

Fig. 5. Gradients of the different measurements in the lesion, moving radially out from the tumor core. All distances were normalized to the maximum distances between necrotic core and contrast-enhancing tumor, inner contrast-enhancing tumor and edema, inner edema and edge to normal-appearing matter, respectively. Colored lines show individual patients (n = 8 included), the black line shows the patient median. Abbreviation: Vessel size index (VSI).

different characteristics than contralateral healthy tissue, which is illustrative of the tumors' infiltrative character [16]. For some patients, abnormal tissue measurements were also found even further away from the tumor core, in regions appearing normal on anatomical scans, implying that infiltration may extend beyond the increased FLAIR signal.

The only association between the different measurements on a region level in patients was between G′ and G″ in contrast-enhancing tumor and in white matter. The lack of correlation between biomechanical and functional properties at the region level may be due to a small sample size and low power; it may also be due to spatial variation within regions. If tissue perfusion depends on diffusion and stiffness properties, such a relationship would depend on the spatial distribution of the tumor and surrounding tissue, due to the GBM heterogeneity. Therefore, all voxels for all patients were considered when constructing regression models of perfusion as a function of the diffusion parameters. Even for a simple linear model, MRE added to the performance of the model, suggesting that MRE provides independent data. Biomechanical properties of the tissue may play an integral role in explaining the tumor vascularity. The simple linear model showed that CBF increased when G′ and G″ decreased, an effect that could possibly be caused by vessels being compressed by stiff tissue and hence reduced perfusion [17]. Of

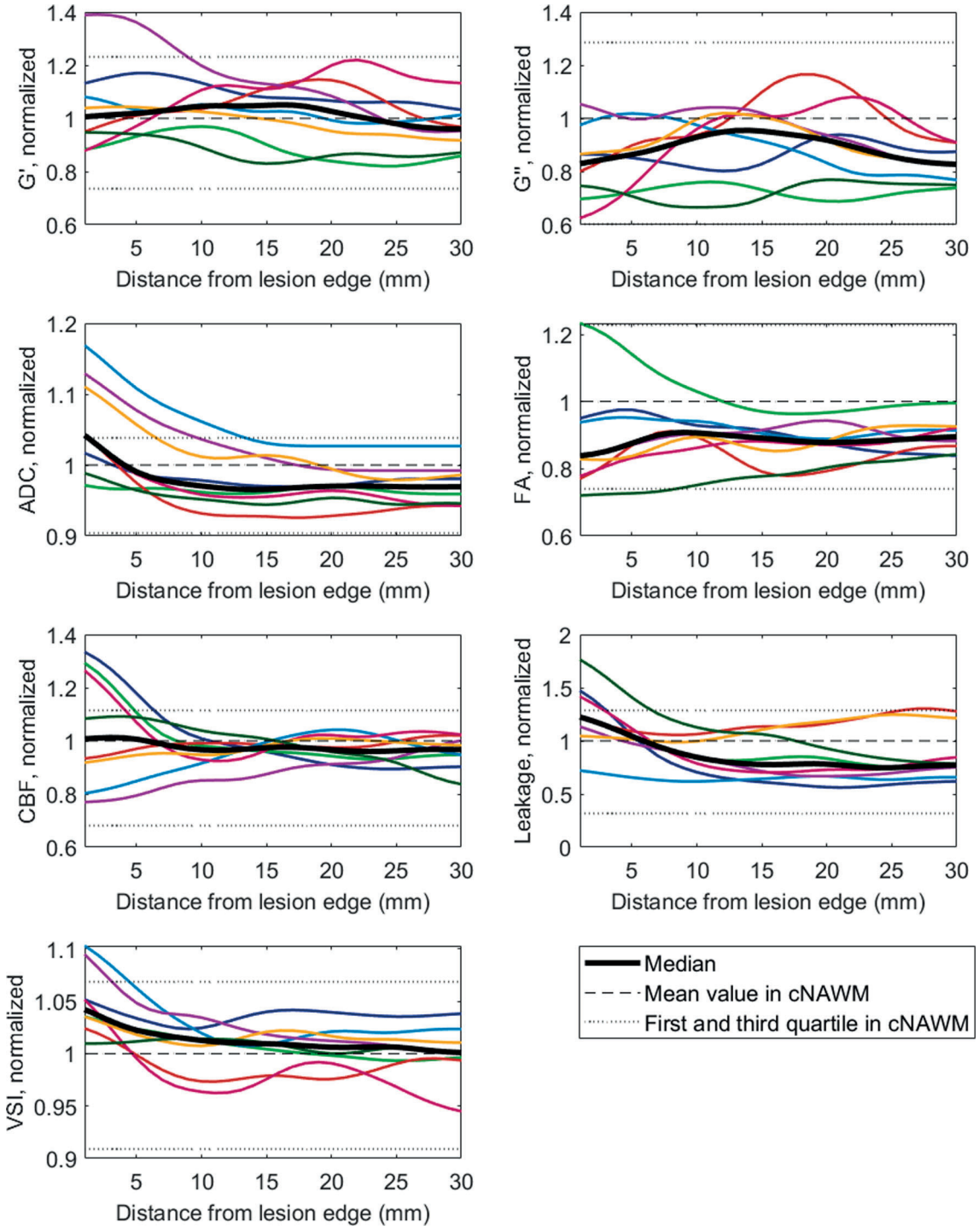

Fig. 6. Gradients of the different measurements, moving radially outwards from the lesion edge. Measurements in tissue labelled as white matter, normalized to each patient's cNAWM. Colored lines show individual patients (n = 8 included), black line shows patient median. Abbreviation: Vessel size index (VSI).

course, there might be a more complex relationship between various characteristics. Other studies have found that tumor stiffness may be affected by factors such as increased cellularity, increased vessel density, and interstitial fluid pressure [6]. A preclinical study suggests that tissue stiffness is influenced by the architecture of the blood vessels, rather than their state of perfusion [18]. Further work is warranted to corroborate our findings, as understanding the mechanisms behind impaired perfusion in glioblastoma could be important for development of new treatment.

The stiffness and viscosity of the contralateral normal-appearing white matter in the patients differed significantly from the measurements in healthy subjects' white matter. Several studies have found brain stiffness to decrease with age [19–21]. The difference between median white matter G′ between patients and healthy subjects in our study was 0.22 kPa, corresponding to −0.007 kPa/year (range 0.002–0.012 kPa/year). This amount of change is roughly comparable to earlier studies. The difference in stiffness and viscosity between patients and healthy subjects shows the importance of normalizing measurements to each subject's normal-appearing white matter. This is typically done in MRE studies of brain cancer patients [4,5,13]. Such a

Table 3
Performance of models predicting CBF_{norm}. Median RMSE (range) for a linear and random forest model using only diffusion parameters to predict CBF_{norm} in patients (upper row), versus including G'_{norm} (middle row) and both G'_{norm} and G''_{norm} (lower row). Asterisk indicates improvement from the row above ($P < 0.01$).

	Linear model	Random forest
CBF_{norm} as a function of ADC_{norm}, FA_{norm}	0.864 (0.844–0.872)	0.695 (0.676–0.701)
CBF_{norm} as a function of ADC_{norm}, FA_{norm}, G'_{norm}	0.860 (0.840–0.869)**	0.674 (0.654–0.680)**
CBF_{norm} as a function of ADC_{norm}, FA_{norm}, G'_{norm}, G''_{norm}	0.859 (0.839–0.867)**	0.626 (0.606–0.630)**

normalization can also remove confounding effects in the case of different MRE acquisition techniques [22].

Our study focused on the differences between pathological and healthy tissue, and contrast-enhancing and necrotic tumor, edema, and normal-appearing gray and white matter ROIs were used for patients. For healthy subjects, we further subdivided the gray matter regions to compare with earlier studies of MRE in the healthy brain. We found white matter to be stiffer than gray matter, consistent with earlier studies [23]. We found cortical gray matter to be stiffer than deep gray matter. This is in contrast to a large recent study, where deep gray matter was reported to be stiffer than both white and cortical gray matter [24]. A second study reported the stiffness to be lower in the deep gray matter than white matter [25], while a third study found white and gray matter stiffness to be very similar in both adults and paediatric subjects [26]. This last study also noted a data quality bias in the calculations due to the attenuation of the applied shear waves causing low MRE signal in the central regions of the brain [26,27]. In an earlier study using this MRE method in healthy subjects, MRE data quality was found to be lower in the deep gray matter regions than in regions closer to the skull. No significant correlation between this data quality and stiffness measurements was found [12]. The existing studies differ with respect to both MRE hardware and reconstruction methods, making it challenging to conclude about the reasons for discrepancies between studies.

4.1. Limitations

A general challenge for MR elastography is the lack of a gold standard for *in vivo* tissue stiffness measurements. A specific challenge for our study is the limited sample size, especially for patient data.

We expect some partial-volume effects with our current image resolution, possibly contributing to less precise measurements in small regions and thin structures such as the cerebral cortex. To ensure statistical validity, we only included regions with greater than 80 voxels. To avoid interpolation effects, MRE, diffusion and perfusion data were all analysed in their native spaces for the calculation of mean values.

The median age of the healthy subjects in our study was 25, and the median age of the patients was 53 years. In order to make direct comparisons between the groups, a larger study of age- and sex-matched cohorts should be performed. Measurements normalized to normal-appearing white matter was used in all parts of the work considering both patients and healthy subjects to account for the age difference.

Perfusion in healthy subjects was measured using ASL, as it is non-invasive, in contrast to DSC, where a gadolinium-based contrast agent is administered intravenously. This hindered direct perfusion comparison between the two groups. In a potential future study comparing MRE and perfusion in both patients and healthy subjects, ASL could be used for all participants. No EPI-distortion correction was performed for ASL images, which may have contributed to less precise coregistration to the anatomical labels.

The repeatability (coefficient of variation) of the employed MRE technique is 4 % [12]. This should be taken into account if comparing small stiffness differences between subjects.

In summary, we found that glioblastoma differed from healthy tissue in terms of G' and G'', CBF, ADC and FA, with heterogeneity both between patients and within tumors. Abnormal tissue properties were present in regions appearing normal on anatomical images. Finally, we showed that inclusion of MRE measurements in statistical models helped predict perfusion, with stiffer tissue associated with lower perfusion values.

CRediT authorship contribution statement

Siri Fløgstad Svensson: Conceptualization, Methodology, Software, Validation, Formal analysis, Investigation, Data curation, Writing – original draft, Writing – review & editing, Visualization, Project administration. **Elies Fuster-Garcia:** Software, Formal analysis, Writing – review & editing, Supervision. **Anna Latysheva:** Resources, Writing – review & editing. **Jorunn Fraser-Green:** Methodology, Investigation, Resources. **Wibeke Nordhøy:** Methodology, Writing – review & editing. **Omar Isam Darwish:** Methodology. **Ivar Thokle Hovden:** Software. **Sverre Holm:** Supervision. **Einar O. Vik-Mo:** Conceptualization, Resources, Writing – review & editing. **Ralph Sinkus:** Methodology, Software, Funding acquisition. **Kyrre Eeg Emblem:** Conceptualization, Writing – review & editing, Supervision, Project administration, Funding acquisition.

Acknowledgements

Grant Support: We gratefully acknowledge support from the European Union's Horizon 2020 Programme: ERC Grant Agreement No. 758657-ImPRESS, Research and Innovation Grant Agreements No. 668039-FORCE and Marie Skłodowska-Curie grant agreement (No 844646-GLIOHAB), South-Eastern Norway Regional Health Authority (Grant Agreement No. 2017073, 2013069 and 2021057), The Research Council of Norway FRIPRO (Grant Agreement No. 261984), the National Institutes of Health R21 grant (Grant Agreement No. EB030757), and the German Research Foundation (DFG, SCHR 1542/1-1).

Appendix A. Supplementary material

Supplementary data to this article can be found online at https://doi.org/10.1016/j.ejrad.2021.110136.

References

[1] R. Stupp, W.P. Mason, M.J. van den Bent, M. Weller, B. Fisher, M.J.B. Taphoorn, K. Belanger, A.A. Brandes, C. Marosi, U. Bogdahn, J. Curschmann, R.C. Janzer, S. K. Ludwin, T. Gorlia, A. Allgeier, D. Lacombe, J.G. Cairncross, E. Eisenhauer, R. O. Mirimanoff, Radiotherapy plus Concomitant and Adjuvant Temozolomide for Glioblastoma, N Engl J Med 352 (10) (2005) 987–996.

[2] P.Y. Wen, D.R. Macdonald, D.A. Reardon, T.F. Cloughesy, A.G. Sorensen, E. Galanis, J. Degroot, W. Wick, M.R. Gilbert, A.B. Lassman, C. Tsien, T. Mikkelsen, E.T. Wong, M.C. Chamberlain, R. Stupp, K.R. Lamborn, M.A. Vogelbaum, M.J. van den Bent, S.M. Chang, Updated response assessment criteria for high-grade gliomas: response assessment in neuro-oncology working group, J. Clin. Oncol. 28 (11) (2010) 1963–1972.

[3] K.M. Pepin, R.L. Ehman, K.P. McGee, Magnetic resonance elastography (MRE) in cancer: Technique, analysis, and applications, Prog Nucl Magn Reson, Spectrosc 90–91 (2015) 32–48.

[4] K.-J. Streitberger, M. Reiss-Zimmermann, F.B. Freimann, S. Bayerl, J. Guo, F. Arlt, J. Wuerfel, J. Braun, K.-T. Hoffmann, I. Sack, W. Zhan, High-resolution mechanical imaging of glioblastoma by multifrequency magnetic resonance elastography, PLoS ONE 9 (10) (2014) e110588, https://doi.org/10.1371/journal.pone.0110588.

[5] M. Reiss-Zimmermann, K.-J. Streitberger, I. Sack, J. Braun, F. Arlt, D. Fritzsch, K.-T. Hoffmann, High Resolution Imaging of Viscoelastic Properties of Intracranial Tumours by Multi-Frequency Magnetic Resonance Elastography, Clin. Neuroradiol. 25 (4) (2015) 371–378.

[6] K.M. Pepin, K.P. McGee, A. Arani, D.S. Lake, K.J. Glaser, A. Manduca, I.F. Parney, R.L. Ehman, J. Huston, MR Elastography Analysis of Glioma Stiffness and IDH1-Mutation Status, AJNR Am. J. Neuroradiol. 39 (1) (2018) 31–36.

[7] K.-J. Streitberger, L. Lilaj, F. Schrank, J. Braun, K.-T. Hoffmann, M. Reiss-Zimmermann, J.A. Käs, I. Sack, How tissue fluidity influences brain tumor progression, Proc. Natl. Acad. Sci. U. S. A. 117 (1) (2020) 128–134.

[8] A.P. Patel, I. Tirosh, J.J. Trombetta, A.K. Shalek, S.M. Gillespie, H. Wakimoto, D. P. Cahill, B.V. Nahed, W.T. Curry, R.L. Martuza, D.N. Louis, O. Rozenblatt-Rosen,

M.L. Suvà, A. Regev, B.E. Bernstein, Single-cell RNA-seq highlights intratumoral heterogeneity in primary glioblastoma, Science 344 (6190) (2014) 1396–1401.
[9] A. D'Alessio, G. Proietti, G. Sica, B.M. Scicchitano, Pathological and Molecular Features of Glioblastoma and Its Peritumoral Tissue, Cancers (Basel) 11 (4) (2019) 469, https://doi.org/10.3390/cancers11040469.
[10] J. Juan-Albarracin, E. Fuster-Garcia, G.A. Garcia-Ferrando, J.M. Garcia-Gomez, ONCOhabitats: A system for glioblastoma heterogeneity assessment through MRI, Int. J. Med. Inform. 128 (2019) 53–61.
[11] J.H. Runge, S.H. Hoelzl, J. Sudakova, A.S. Dokumaci, J.L. Nelissen, C. Guenthner, J. Lee, M. Troelstra, D. Fovargue, J. Stoker, A.J. Nederveen, D. Nordsletten, R. Sinkus, A novel magnetic resonance elastography transducer concept based on a rotational eccentric mass: preliminary experiences with the gravitational transducer, Phys. Med. Biol. 64 (4) (2019), 045007.
[12] S.F. Svensson, J. De Arcos, O.I. Darwish, J. Fraser-Green, T.H. Storas, S. Holm, E.O. Vik-Mo, R. Sinkus, K.E. Emblem, Robustness of MR Elastography in the Healthy Brain: Repeatability, Reliability, and Effect of Different Reconstruction Methods, J. Magn. Reson. Imaging (2021).
[13] M. Simon, J. Guo, S. Papazoglou, H. Scholand-Engler, C. Erdmann, U. Melchert, M. Bonsanto, J. Braun, D. Petersen, I. Sack, J. Wuerfel, Non-invasive characterization of intracranial tumors by magnetic resonance elastography, New J. Phys. 15 (8) (2013) 085024, https://doi.org/10.1088/1367-2630/15/8/085024.
[14] K. Riek, J.M. Millward, I. Hamann, S. Mueller, C.F. Pfueller, F. Paul, J. Braun, C. Infante-Duarte, I. Sack, Magnetic resonance elastography reveals altered brain viscoelasticity in experimental autoimmune encephalomyelitis, Neuroimage Clin 1 (1) (2012) 81–90.
[15] K. Schregel, N. Nazari, M.O. Nowicki, M. Palotai, S.E. Lawler, R. Sinkus, P. E. Barbone, S. Patz, Characterization of glioblastoma in an orthotopic mouse model with magnetic resonance elastography, NMR Biomed. 31 (10) (2018), e3840.
[16] A. Latysheva, O.M. Geier, T.R. Hope, M. Brunetti, F. Micci, E.O. Vik-Mo, K. E. Emblem, A. Server, Diagnostic utility of Restriction Spectrum Imaging in the characterization of the peritumoral brain zone in glioblastoma: Analysis of overall and progression-free survival, Eur. J. Radiol. 132 (2020), 109289.
[17] R.K. Jain, J.D. Martin, T. Stylianopoulos, The role of mechanical forces in tumor growth and therapy, Annu. Rev. Biomed. Eng. 16 (1) (2014) 321–346.
[18] L. Juge, B.T. Doan, J. Seguin, M. Albuquerque, B. Larrat, N. Mignet, G.G. Chabot, D. Scherman, V. Paradis, V. Vilgrain, B.E. Van Beers, R. Sinkus, Colon tumor growth and antivascular treatment in mice: complementary assessment with MR elastography and diffusion-weighted MR imaging, Radiology 264 (2) (2012) 436–444.
[19] I. Sack, B. Beierbach, J. Wuerfel, D. Klatt, U. Hamhaber, S. Papazoglou, P. Martus, J. Braun, The impact of aging and gender on brain viscoelasticity, Neuroimage 46 (3) (2009) 652–657.
[20] A. Arani, M.C. Murphy, K.J. Glaser, A. Manduca, D.S. Lake, S.A. Kruse, C.R. Jack, R.L. Ehman, J. Huston, Measuring the effects of aging and sex on regional brain stiffness with MR elastography in healthy older adults, Neuroimage 111 (2015) 59–64.
[21] T. Takamura, U. Motosugi, Y.u. Sasaki, T. Kakegawa, K. Sato, K.J. Glaser, R. L. Ehman, H. Onishi, Influence of Age on Global and Regional Brain Stiffness in Young and Middle-Aged Adults, J. Magn. Reson. Imaging 51 (3) (2020) 727–733.
[22] A. Bunevicius, K. Schregel, R. Sinkus, A. Golby, S. Patz, REVIEW: MR elastography of brain tumors, Neuroimage Clin 25 (2020) 102109, https://doi.org/10.1016/j.nicl.2019.102109.
[23] L.V. Hiscox, C.L. Johnson, E. Barnhill, M.D.J. McGarry, J. Huston, E.J.R. van Beek, J.M. Starr, N. Roberts, Magnetic resonance elastography (MRE) of the human brain: technique, findings and clinical applications, Phys. Med. Biol. 61 (24) (2016) R401–R437.
[24] L.V. Hiscox, M.D.J. McGarry, H. Schwarb, E.E.W. Van Houten, R.T. Pohlig, N. Roberts, G.R. Huesmann, A.Z. Burzynska, B.P. Sutton, C.H. Hillman, A. F. Kramer, N.J. Cohen, A.K. Barbey, K.D. Paulsen, C.L. Johnson, Standard-space atlas of the viscoelastic properties of the human brain, Hum. Brain Mapp. 41 (18) (2020) 5282–5300.
[25] J. Guo, S. Hirsch, A. Fehlner, S. Papazoglou, M. Scheel, J. Braun, I. Sack, A. A. Oberai, Towards an elastographic atlas of brain anatomy, PLoS ONE 8 (8) (2013) e71807, https://doi.org/10.1371/journal.pone.0071807.
[26] J. Yeung, L. Jugé, A. Hatt, L.E. Bilston, Paediatric brain tissue properties measured with magnetic resonance elastography, Biomech. Model. Mechanobiol. 18 (5) (2019) 1497–1505.
[27] M.A. Green, L.E. Bilston, R. Sinkus, In vivo brain viscoelastic properties measured by magnetic resonance elastography, NMR Biomed. 21 (7) (2008) 755–764.

Paper III

MR elastography identifies regions of extracellular matrix reorganization associated with shorter survival in glioblastoma patients

Siri F. Svensson*, Skarphéðinn Halldórsson*, Anna Latysheva, Elies Fuster-Garcia, Trine Hjørnevik, Jorunn Fraser-Green, Robin A.B Bugge, Jack Grinband, Sverre Holm, Einar O. Vik-Mo, Ralph Sinkus and Kyrre E. Emblem

**Shared first-authorship. Submitted for publication.* DOI: 10.1101/2022.11.07.22282021.

III

MR Elastography Identifies Regions of Extracellular Matrix Reorganization Associated with Shorter Survival in Glioblastoma Patients

Siri Fløgstad Svensson[1,2*], Skarphéðinn Halldórsson[3*], Anna Latysheva[4], Elies Fuster-Garcia[5], Trine Hjørnevik[1], Jorunn Fraser-Green[6], Robin A. B. Bugge[1], Jack Grinband[7,8], Sverre Holm[2], Ralph Sinkus[9,10], Einar O. Vik-Mo[3] & Kyrre Eeg Emblem[1]

[1]Dept. of Physics and Computational Radiology, Division of Radiology and Nuclear Medicine, Oslo University Hospital, Oslo, Norway;
[2]Department of Physics, University of Oslo, Oslo, Norway;
[3]Vilhelm Magnus Laboratory, Dept. of Neurosurgery, Oslo University Hospital, Oslo, Norway;
[4]Department of Radiology, Division of Radiology and Nuclear Medicine, Oslo University Hospital, Oslo, Norway;
[5]BDSLab, Instituto Universitario de Tecnologías de la Información y Comunicaciones, Universitat Politècnica de València, València, Spain;
[6]The Intervention Center, Oslo University Hospital, Oslo, Norway;
[7]Department of Radiology, Columbia University, New York, USA;
[8]Department of Psychiatry, Columbia University, New York, USA;
[9]Division of Imaging Sciences and Biomedical Engineering, King's College, London, United Kingdom;
[10]INSERM U1148, LVTS, University Paris Diderot, Paris, France

** Shared first-authorship.*

Abstract

Purpose: The biomechanical tissue properties of glioblastoma tumors are heterogeneous, but the molecular mechanisms involved and the biological implications are poorly understood. Here, we combine magnetic resonance elastography (MRE) measurement of tissue stiffness with RNA sequencing of tissue biopsies to explore the molecular characteristics of the stiffness signal.

Experimental design: MRE was performed preoperatively in 13 patients with glioblastoma. Navigated biopsies were harvested during surgery and later classified as 'stiff' or 'soft' according to MRE stiffness measurements ($|G^*|_{norm}$). Twenty-two biopsies from eight patients were analysed by RNA sequencing.

Results: The mean whole-tumor stiffness was lower than in normal-appearing white matter. The surgeon's biopsy stiffness evaluation did not correlate with the MRE measurements, which suggests that they measure different properties. Gene set enrichment analysis of the differentially expressed genes between 'stiff' and 'soft' biopsies showed that genes involved in extracellular matrix reorganization and cellular adhesion were overexpressed in 'stiff' biopsies. Supervised dimensionality reduction identified a gene expression signal separating 'stiff 'and 'soft' biopsies. Using the NIH Genomic Data Portal, 265 patients with glioblastoma were divided into patients with (n=63) and without (n=202) this gene expression signal. The median survival time of patients with tumors expressing the gene expression signal associated with 'stiff' biopsies was 100 days shorter than that of patients not expressing it (360 versus 460 days, hazard ratio: 1.45, $P<0.05$).

Conclusions: MRE imaging of glioblastoma can provide non-invasive information on intratumoral heterogeneity. Regions of extracellular matrix reorganization showed an expression signal correlated to shorter survival time in patients with glioblastoma.

Introduction

Intratumoral heterogeneity is characteristic of glioblastoma (GBM) and is believed to be one of the key determinants of therapy failure (1). Intratumoral heterogeneity stems from intrinsic genetic alterations as well as the inherent plasticity of GBM tumor cells that adapt to various microenvironmental factors (2,3). One such factor is the biomechanical properties of the tumor and its microenvironment. The biomechanical properties of GBM affect how tumor cells interact with the local microenvironment and can contribute to tumor invasion (4,5). Despite its importance intraoperatively and for tumor progression, little data exists on the physical characteristics and genetic determinants of biomechanical heterogeneity in GBM.

The biomechanical properties of the tissue within a GBM tumor can be highly variable, with subregions ranging from a soft and gel-like to a solid and dense consistency. These differences in biomechanical properties can impact the technical ease of resection and be an important determinant for operative planning. Resection of a stiff tumor that adheres to pia and vessels can result in damage to neighboring structures, while soft, liquescent tumors are more readily removed through gentle suction.

MR elastography (MRE) is an imaging technique that noninvasively measures the biomechanical properties of tissue. In contrast to intraoperative palpation by the surgeon, MRE provides a quantitative and objective measure of tissue stiffness, and characterizes its spatial distribution. Previous MRE studies in humans have found that GBM tumors differ from healthy brain in terms of shear stiffness and viscosity, and are spatially heterogeneous with respect to measured tissue stiffness (6,7).

Here, we examine the intratumoral biomechanical heterogeneity of GBM tumors using preoperative MRE and MRI-localized biopsies. A comparison of high and low stiffness biopsies using RNA sequencing showed that genes involved in extracellular matrix organization were overexpressed in high stiffness biopsies and were a negative prognostic factor for patient survival. Our data demonstrates that MRE imaging of GBM provides unique information on tumor heterogeneity and helps identify probable regions of active extracellular matrix reorganization.

Methods

This study was approved by the National Research Ethics Committee and the Institutional Review Board (2018/2464 and 2016/1791) and all patients gave written and informed consent. Thirteen patients (eight women and five men, median 56 years, range 38-75 years) with subsequent neuropathologically confirmed IDH wild-type GBM were prospectively included in the study. Four patients were excluded due to technically unsuccessful MRE and one patient was excluded due to MRI susceptibility artifacts caused by a cranium fixation item. Finally, one patient was excluded due to failed registration of biopsy coordinates.

MR imaging

MRI exams were performed on a 3T clinical MRI scanner (Ingenia, Philips Medical Systems, Best, the Netherlands) using a 32-channel head coil. In addition to MRE, a clinical preoperative

protocol was used, including a T1-weighted MPRAGE sequence (3D inversion recovery gradient echo, 1×1×1 mm^3 resolution, 256×256×368 matrix, TR/TE=5.2/2.3 ms, shot interval 3000 ms, inversion delay 853 ms) acquired before and after administration of a gadolinium-based contrast agent, as well as T2-weighted (turbo spin echo, 0.6×0.6×4 mm^3 resolution, 420×270×28 matrix, TR/TE=3000/80 ms) and T2-FLAIR sequences (turbo spin echo, 1×1×1 mm^3 resolution, 252×249×183 matrix, TR/TE=4800/320 ms, inversion time 1650 ms). For the MRE, a gravitational transducer was attached to the side of the subject's head to induce shear waves of 50 Hz in the brain (8). Image acquisition was performed using a multi-shot gradient-echo MRE sequence, synchronized to the wave generator by a trigger signal (9). Fifteen contiguous transversal slices were placed according to the tumor site and scanned using an isotropic resolution of 3.1 mm^3, matrix size of 72 × 70, and FOV = 22 cm. Other scan parameters were: Flip angle = 20°, TR/TE = 384/12 msec, Cartesian readout, and a sensitivity encoding factor of 2. Hadamard motion encoding was performed using bipolar 13 mT/m motion-encoding gradients at 115 Hz in four directions (10). Eight mechanical phase offsets were acquired throughout the period of the 25-Hz frequency component of the waveform. The actual mechanical vibration frequency was shifted to the second index of the Fourier transform, thus filtering out potential contributions from the 25, 75, and 100 Hz frequencies. The MRE acquisition time was 5.5 minutes, and was well tolerated across all patients.

Surgery and tissue sampling

The surgery was performed by two neurosurgeons. In order to guide sampling, surgeons evaluated MRE data prior to surgery to plan for biopsies covering a range of MRE signal. During resection, 2-7 biopsies were taken from different parts of the tumor. All biopsies were situated in tumor or adjacent parts of the brain included in the planned resection prior to MRE evaluation, and covered both contrast-enhanced T1-weighted (CE-T1w) images and more diffusely infiltrating tumor demarcated by non-enhancing T1-weighted and pathological T2-FLAIR signal. Biopsies were taken early in the resection, prior to any major shift in the navigational accuracy. The biopsy locations were chosen according to varying stiffness as evaluated by the neurosurgeon. The surgeon evaluated tumor consistency according to a modified version of the grading scale from Zada et al. as either (1) softer than normal brain tissue, (2) similar in consistency to normal brain tissue, or (3) firmer than normal brain tissue (11). Stereotactic guidance was provided by preoperative CE-T1w and T2-FLAIR images on a neuronavigation system (Brainlab Curve; Brainlab, Feldkirchen, Germany). The biopsies were snap-frozen immediately after extraction. The frozen biopsies were weighed, homogenized in a Tissuelyser (Qiagen, the Netherlands), and aliquoted for biomolecule extraction.

Biopsy co-registration

The biopsy locations were recorded by screen captures of the neuronavigation interface at the time of tissue sampling and co-registered to the CE-T1w images using a semiautomated screen capture registration tool, allowing the determination of the Cartesian coordinates of each biopsy (12). Next, a robust binary region-of-interest (ROI) was made for each coordinate by expanding one voxel in all three directions from the coordinate seed point. Finally, the positions of all ROIs were visually controlled by an experienced neuroradiologist. The same neuroradiologist

also classified each biopsy as collected from either (1) contrast-enhancing tumor, (2) necrotic tissue, or (3) a nonenhancing region with pathological T2-FLAIR signal.

MR Image Processing

From the MRE scan, maps of the magnitude of the shear storage modulus |G*| (tissue stiffness) and the shear phase angle φ (related to tissue viscosity, i.e. its ability to dissipate energy) were produced. Details about the MRE reconstruction can be found in Svensson et al. (7). The volumetric CE-T1w images were co-registered to the MRE image space, using a nearest-neighbor interpolation in the nordicICE software (NordicNeuroLab AS, Bergen, Norway). The resulting transformations were applied to the binary ROI masks in CE-T1w space, resulting in a one-voxel seed point in MRE space. To make the analysis more robust to brain shift and co-registration issues, a ROI consisting of a trimmed mean of nine MRE voxels around the seed point was used, where the voxel with the highest and the lowest value were removed before averaging. **Figure 1A** shows an example of a biopsy location on a CE-T1w image and the corresponding |G*| map.

Tissue segmentation was performed using Oncohabitats, a multiparametric system for glioblastoma heterogeneity assessment through MRI (13). This segmentation was performed for each patient based on pre- and post-contrast T1-weighted, T2-weighted and T2-FLAIR MRI scans, and resulted in segmentation of contrast-enhancing tumor, necrosis, peritumoral region of high signal on T2-FLAIR, and normal-appearing gray and white matter. The mean value of each patient's contralateral normal-appearing white matter was used to normalize MRE measurements, resulting in $|G^*|_{norm}$ (14).

RNA Sequencing

For each patient, 2-4 biopsies were selected for RNA sequencing. Total RNA sequencing returned sequence counts for 22510 genes and other transcripts. The analyzed biopsies were classified as 'stiff' or 'soft' based on MRE, i.e., higher or lower $|G^*|_{norm}$ than the mean value of all biopsies within each tumor, respectively. Batch correction of RNA sequencing data was performed with the ComBat-seq package in R (15). Normalization and differential expression of RNA sequencing data was done with the DESeq2 package in R (16). The differential expression results were corrected for multiple testing using the Benjamini and Hochberg method, and adjusted p-value threshold was set to 0.05.

Statistical analysis

Comparison of MRE measurements in tumor and normal-appearing tissue was performed using a Wilcoxon signed-rank test. MRE measurements and tumor volumes were compared using a Spearman's rank order test. $|G^*|_{norm}$ measurements were compared to the surgeon's evaluation using ordered logistic regression and to the radiological tissue type using multinomial regression. A significance level of $P = 0.05$ was assumed for all tests. Logistic regression was performed using Stata (version 17.0, StataCorp LLC, College Station, Texas, USA). Over-representation (OR) analysis and gene-set enrichment analysis (GSEA) were performed using the clusterProfiler package in R (17). Principal component analysis (PCA), partial least-squares

discriminant analysis (PLS-DA) and sparse PLS-DA were performed with the mixOmics package in R (18).

Survival analysis

Raw RNA sequencing reads from the The Cancer Genome Atlas (TCGA) and the Clinical Proteomic Tumor Analysis Consortium (CPTAC) projects were downloaded from the NIH Genomic Data Commons Data Portal along with sample metadata. Normal samples, control samples and duplicate samples were excluded, leaving 265 patient samples. Values were batch-corrected with ComBat-seq followed by normalization and rlog transformation in DESeq2. A sparse PLS-DA model containing 22 genes was trained using 22 patient samples, annotated as 'stiff' or 'soft', using the mixOmics package. Expression of these 22 genes was used to classify the external data using the 'predict()' function in the mixOmics package. Kaplan-Meier survival curves were produced with the survminer package in R. Cox regression analysis on survival data was performed in SPSS (version 28.0, IBM Corp, Armonk, NY).

Code and Data Availability

The source code and RNA sequencing data to reproduce all analyses and figures in this manuscript is available at https://github.com/SkabbiVML/stiffR. Imaging data is available upon request.

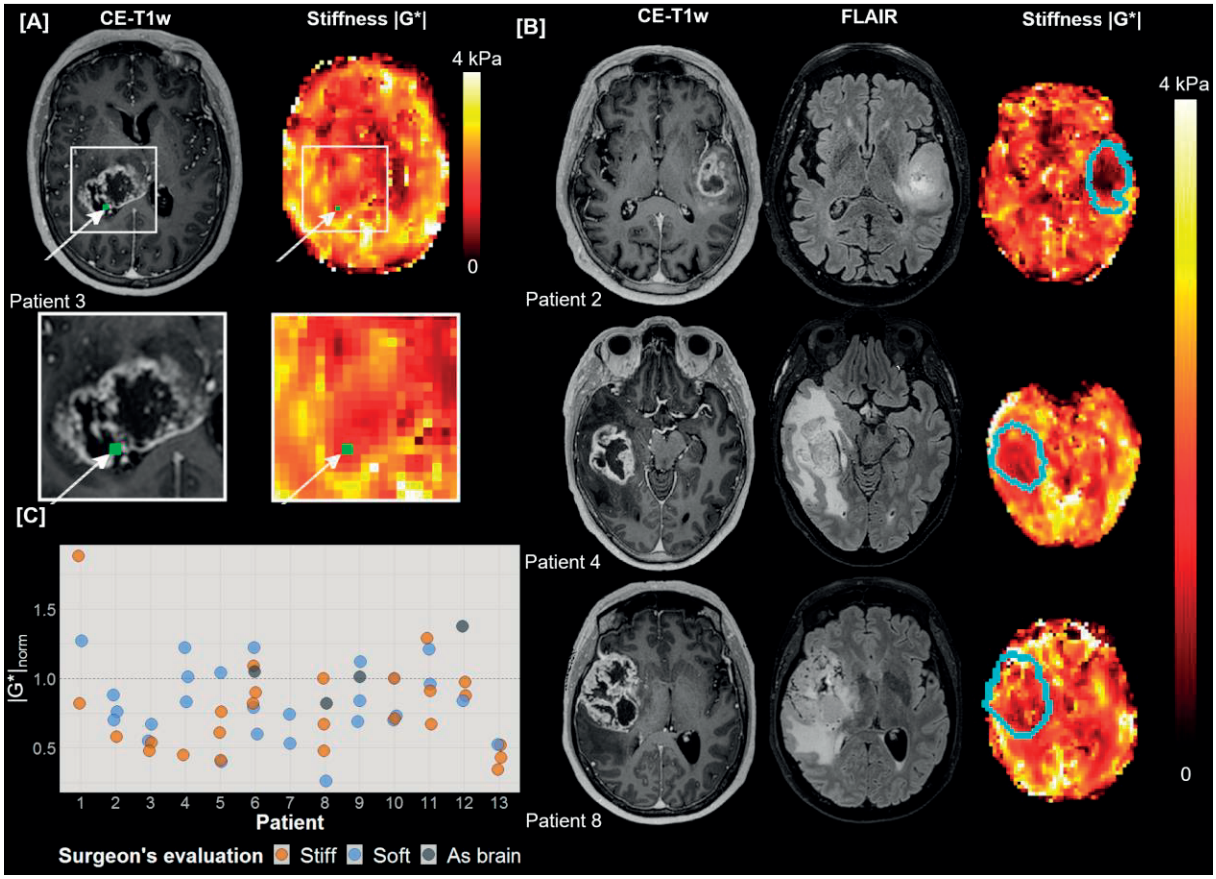

***Figure 1**: (A) Example of MRE imaging. The location of the tissue biopsy is shown in green in the contrast-enhanced T1-weighted image (CE-T1w) and the MRE stiffness map (|G*|). (B) Representative images for three patients. From left to right: CE-T1w images, T2-FLAIR images*

and |G| map, with tumor outline shown in blue. (C) Stiffness measurements for all biopsies per patient (n=56). Normalized MRE-based stiffness $|G^*|_{norm}$ for all biopsies acquired for all patients (n=13). Biopsies evaluated by the surgeon as stiff are shown in orange (median = 0.71), biopsies evaluated as soft are shown in blue (median = 0.79) and biopsies found by the surgeon to be similar in consistency to healthy brain tissue are shown in gray (median = 1.03). The horizontal line at $|G^*|_{norm}$ = 1 shows the mean stiffness in each patient's contralateral normal-appearing white matter.*

Results

The demographic data of the patient, tumor volumes, and mean $|G^*|_{norm}$ and φ_{norm} values are listed in **Supplementary Table 1.** Example MRE images are shown in **Fig. 1B**.

GBM tumors are heterogeneous and softer than normal-appearing brain tissue

The mean stiffness |G*| was 20% lower in contrast-enhancing tumor than in normal-appearing white matter (P<0.001) and 30 % lower in necrosis than normal-appearing white matter (P<0.001). The mean shear phase angle φ was 10% lower in contrast-enhancing tumor than in normal-appearing white matter (P<0.001) and 8% lower in necrosis than in normal-appearing white matter (P<0.005). In the nonenhancing T2-FLAIR hyperintense regions, stiffness did not differ significantly from in normal-appearing white matter (P=0.8), but φ was 15% lower than in normal-appearing white matter (P<0.001). The median tumor volume (contrast-enhancing and necrotic regions combined) was 33 cm^3 (range 7-78 cm^3), and the median volume of the high signal region on T2-FLAIR was 45 cm^3 (range 2-162 cm^3). Mean $|G^*|_{norm}$ and φ_{norm} values did not correlate with the volume of tumor or edema.

The stiffness was heterogeneous both between and within tumors (**Fig. 1C**). Some patients (e.g., patient 13) had $|G^*|_{norm}$ <1 for all biopsies, while others displayed higher stiffness values for some biopsies (e.g., patient 1). The median ratio between the biopsy with highest and lowest stiffness of a patient was 1.6 (range 1.4-3.9). **Table 1** shows $|G^*|_{norm}$ and the surgeon's evaluation of biopsies that were analyzed by RNA sequencing. The table also shows whether the biopsy was taken from contrast-enhancing tumor, necrosis or a region with high signal on T2-FLAIR. Measured stiffness $|G^*|_{norm}$ was not correlated to the radiological tissue type of the biopsy (P=0.06).

Patient number	Sample number	Tissue type	Surgeon's evaluation	$\|G^*\|_{norm}$	MRE soft/stiff
1	1	CE	Stiff	0.82	'Soft'
	2	FLAIR	Stiff	1.88	'Stiff'
	3	CE	Soft	1.27	'Soft'
2	1	FLAIR	Soft	0.76	'Soft'
	2	CE	Soft	0.88	'Stiff'
	3	CE	Soft	0.70	'Soft'
3	1	CE	Soft	0.67	'Stiff'
	2	Necrosis	Stiff	0.54	'Soft'
	3	Necrosis	Stiff	0.48	'Soft'
4	1	FLAIR	Soft	1.22	'Stiff'
	2	CE	Soft	1.01	'Stiff'
	3	Necrosis	Stiff	0.45	'Soft'
5	1	FLAIR	Soft	0.40	'Soft'
	2	Necrosis	Soft	1.04	'Stiff'
	3	CE	Stiff	0.76	'Stiff'
6	1	CE	Soft	0.79	'Stiff'
	2	CE	Soft	0.60	'Soft'
	3	CE	Stiff	0.82	'Stiff'
7	1	CE	Soft	0.53	'Soft'
	2	CE	Soft	0.74	'Stiff'
8	1	CE	Stiff	1.00	'Stiff'
	2	CE	Stiff	0.48	'Soft'

Table 1. ***Biopsies used in RNA sequencing***. *The tissue type of each biopsy point was radiologically evaluated, using CE-T1w and T2-FLAIR images, as contrast-enhancing tumor (CE), region with high signal on T2-FLAIR (FLAIR) or necrosis. Surgeon's evaluation of the consistency of each biopsy (stiff or soft compared to normal brain parenchyma),* $|G^*|_{norm}$*, and MRE biopsy classification ('stiff' or 'soft', i.e. higher or lower* $|G^*|_{norm}$ *than the mean value of all biopsies within each tumor, respectively).*

The surgeon's evaluation of biopsy stiffness during surgery and $|G^*|_{norm}$ did not correlate (P=0.58), suggesting that the two entities are independent measures.

Gene expression associated with GBM stiffness

To evaluate the molecular differences between stiff and soft tissue biopsies, we performed total RNA sequencing on 22 biopsies from 8 GBM tumors (patients 1-8). Unsupervised dimensionality reduction by principal component analysis (**Supplementary Fig. 1A**) did not identify tissue stiffness as measured by MRE as a strong source of variance within the data. However, supervised dimensionality-reduction with partial least-squares discriminant analysis (PLS-DA) identified an expression signal that separated 'stiff' from 'soft' biopsies within each tumor. Tuning of the PLS-DA parameters (5-fold cross-validation, 100 repeats) indicated that a minimal sparse PLS-DA model containing 22 genes was sufficient to separate 22 patient samples based on the measured tissue stiffness (**Supplementary Fig. 1C**).

Differential gene expression analysis between ‘stiff’ and the ‘soft’ biopsies per patient found that 196 genes were differentially expressed based on an adjusted p-value of 0.05 (**Fig. 2A, Supplementary Table 2**). Of these, 122 were upregulated in ‘stiff’ biopsies, while 74 were upregulated in ‘soft’ biopsies. Normalized expression levels of differentially expressed genes in every biopsy show that ‘stiff’ or ‘soft’ biopsies tend to cluster together, and biopsies within individual patients also show similar expression profiles (**Fig. 2B**). Due to the limited size of the dataset, differential expression may depend on samples from a single patient. Therefore, to explore the robustness of the differential expression, we performed sequential differential expression analysis, leaving out all samples from a single patient in each iteration. Patient-wise leave-one-out cross-validation identified a set of 43 genes (35 in ‘stiff’ biopsies and 8 in ‘soft’ biopsies) that were found to be differentially expressed on every iteration (**Table 2**).

Classifying biopsies into stiff or soft by the surgeon’s evaluation was also performed, but no significant difference in gene expression was found between biopsies classified in this way.

ENTREZ ID	Gene ID	Association	Gene Name
84935	MEDAG	‘stiff’	mesenteric estrogen dependent adipogenesis
1378	CR1	‘stiff’	complement C3b/C4b receptor 1 (Knops blood group)
23213	SULF1	‘stiff’	sulfatase 1
3875	KRT18	‘stiff’	keratin 18
9332	CD163	‘stiff’	CD163 molecule
100628315	DNM3OS	‘stiff’	DNM3 opposite strand/antisense RNA
728264	CARMN	‘stiff’	cardiac mesoderm enhancer-associated non-coding RNA
5325	PLAGL1	‘stiff’	PLAG1 like zinc finger 1
8829	NRP1	‘stiff’	neuropilin 1
54885	TBC1D8B	‘stiff’	TBC1 domain family member 8B
7373	COL14A1	‘stiff’	collagen type XIV alpha 1 chain
1282	COL4A1	‘stiff’	collagen type IV alpha 1 chain
79839	CCDC102B	‘stiff’	coiled-coil domain containing 102B
1601	DAB2	‘stiff’	DAB adaptor protein 2
3672	ITGA1	‘stiff’	integrin subunit alpha 1
4121	MAN1A1	‘stiff’	mannosidase alpha class 1A member 1
55075	UACA	‘stiff’	uveal autoantigen with coiled-coil domains and ankyrin
5205	ATP8B1	‘stiff’	ATPase phospholipid transporting 8B1
5139	PDE3A	‘stiff’	phosphodiesterase 3A
22925	PLA2R1	‘stiff’	phospholipase A2 receptor 1
5592	PRKG1	‘stiff’	protein kinase cGMP-dependent 1
1909	EDNRA	‘stiff’	endothelin receptor type A
1290	COL5A2	‘stiff’	collagen type V alpha 2 chain
1368	CPM	‘stiff’	carboxypeptidase M
9060	PAPSS2	‘stiff’	3’-phosphoadenosine 5’-phosphosulfate synthase 2
10351	ABCA8	‘stiff’	ATP binding cassette subfamily A member 8
8654	PDE5A	‘stiff’	phosphodiesterase 5A
3759	KCNJ2	‘stiff’	potassium inwardly rectifying channel subfamily J
5175	PECAM1	‘stiff’	platelet and endothelial cell adhesion molecule 1
2321	FLT1	‘stiff’	fms related receptor tyrosine kinase 1
115548	FCHO2	‘stiff’	FCH and mu domain containing endocytic adaptor 2
84910	TMEM87B	‘stiff’	transmembrane protein 87B
9169	SCAF11	‘stiff’	SR-related CTD associated factor 11
23216	TBC1D1	‘stiff’	TBC1 domain family member 1
2803	GOLGA4	‘stiff’	golgin A4
875	CBS	‘soft’	cystathionine beta-synthase
728875	LINC00623	‘soft’	long intergenic non-protein coding RNA 623
93145	OLFM2	‘soft’	olfactomedin 2
1600	DAB1	‘soft’	DAB adaptor protein 1
767	CA8	‘soft’	carbonic anhydrase 8
441381	LRRC24	‘soft’	leucine rich repeat containing 24
81551	STMN4	‘soft’	stathmin 4
345630	FBLL1	‘soft’	fibrillarin like 1

Table 2 Differentially expressed genes: *List of most stable differentially expressed genes between ‘stiff’ and ‘soft’ biopsies after patient-wise leave-one-out validation.*

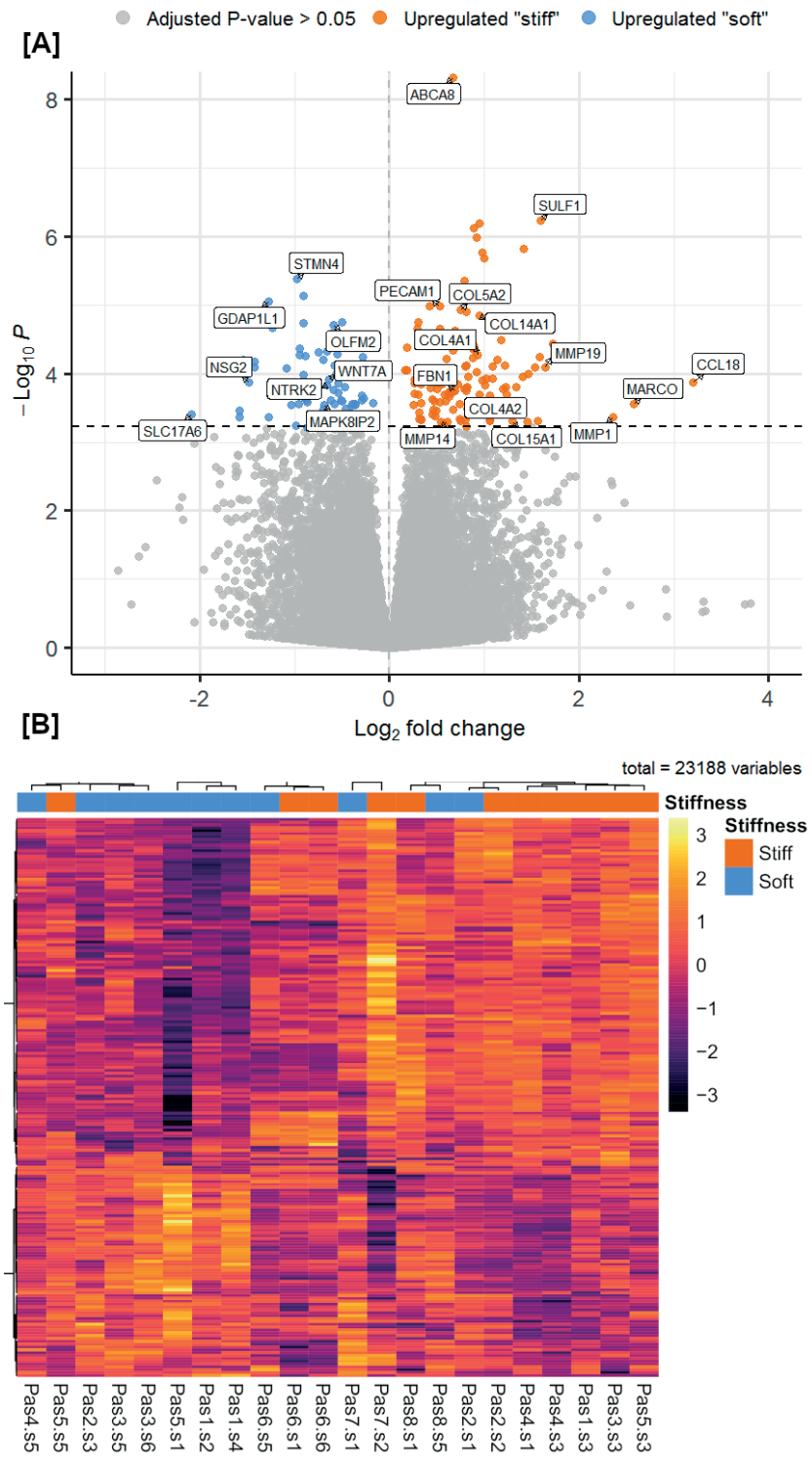

Figure 2. Differential gene expression between 'stiff' and 'soft' biopsies in GBM tumors. *(A) Volcano plot summarizing the results of differential gene expression between 'stiff' and 'soft' biopsies. The magnitude of change in expression between 'stiff' and 'soft' biopsies is shown along the x-axis, and the statistical significance is shown along the y-axis. 521 genes were found to have differential expression between the groups with an adjusted p-value < 0.1, 196 genes with an adjusted p-value < 0.05 (shown in blue and red). (B) Heatmap of differentially expressed genes, where biopsies are grouped according to the pattern of gene expression. All*

genes that passed an adjusted p-value threshold of 0.05 (196 genes) are included in the heat map, along the y-axis. The analyzed biopsies are shown along the x-axis. The color gradient shows the changes of gene expression, the expression of genes is scaled across all biopsies. "Pas" represents patient number, "s" represents biopsy number.

Functional annotation of stiffness-associated gene expression

To evaluate the structural and functional importance of differentially expressed genes, we performed a gene set enrichment analysis (GSEA) of genes associated with increased biopsy stiffness using the Gene Ontology (GO) and Reactome databases (19,20). The GO-terms with the highest association to 'stiff' biopsies represent components of the extracellular matrix, cellular adhesion and innate immunity (**Fig. 3A**). Similarly, among the most significantly enriched Reactome pathways associated with 'stiff' biopsies were extracellular matrix organization, integrin cell surface interactions, and neutrophil degranulation (**Supplementary Fig. 2).** In contrast, GO-terms and Reactome pathways with highest association with 'soft' biopsies largely represented normal neuronal functions such as regulation of membrane potential and neurotransmitter receptor complex although associations to DNA methylation and rRNA regulation were also found. Pathway enrichment maps show three distinct clusters of GO-terms with varying degrees of overlap. GO-terms associated with extracellular matrix reconstruction are upregulated in stiff samples. There is some overlap of genes associated with extracellular matrix terms and terms associated with effector cells of the innate immune system (neutrophils and granulocytes) which are also upregulated in stiff samples **(Fig. 3B)**. A third cluster of pathways, representing neuronal synapses and synaptic membranes, is upregulated in 'soft' biopsies.

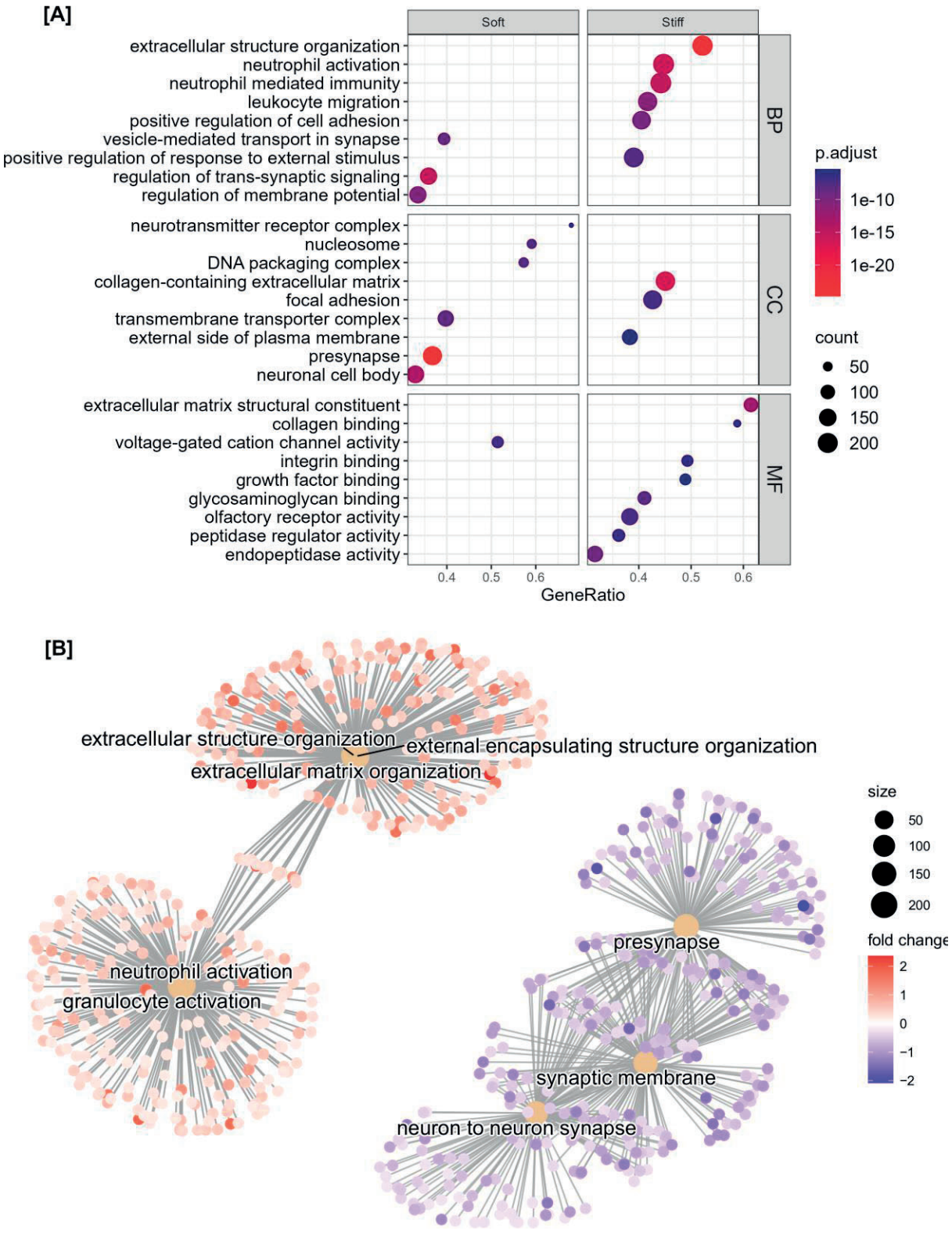

Figure 3. Gene-set enrichment analysis of differentially expressed genes in 'soft' and 'stiff' tumor biopsies. *(A) Dot plot representing the terms most highly enriched in each Gene Ontology category. BP = Biological process, CC = cellular component, MF = molecular function, p.adjust = p-value adjusted for multiple testing. (B) Pathway enrichment map of the*

GSEA results. Central nodes represent Gene Ontology terms, colored dots represent differentially expressed genes (red = upregulated in 'stiff' biopsies, blue = upregulated in 'soft' biopsies).

Over-representation analysis of the 196 genes found to be upregulated in 'stiff' or 'soft' biopsies (adjusted P-value < 0.05, **Supplementary Table 2)** was largely concordant with the results from the GSEA: 'Stiff' biopsies were associated with collagen-containing matrix reorganization, focal adhesion, and immune cell activation/migration, while 'soft' biopsies were associated with normal synaptic activity and, to a lesser extent, DNA packaging and nucleosomes. Over-representation analysis of Reactome pathways identified 'Extracellular matrix organization' as strongly associated with 'stiff' biopsies while DNA methylation and RNA polymerase I promoter opening were associated with 'soft' biopsies (**Supplementary Fig. 3).**

Tissue stiffness is a negative prognostic factor for patient survival

Extracellular matrix reorganization and increased tissue stiffness have been associated with tumor cell infiltration in glioma (5). Based on our findings, we hypothesized that stiffer tumor regions could represent regions of the GBM important for tumor progression and hence patient survival. To further study the effect of the gene expression signal that distinguished our 'stiff' and 'soft' biopsies, we evaluated RNA transcription profiles of 265 GBM tumors from two studies available in the NIH Genomic Data Commons Data Portal (168 biopsies from TCGA and 97 biopsies from CPTAC) (21). Expression patterns of the 22 stable genes selected by PLS-DA were used to classify the tumors *with* this gene expression signal (n = 63) and tumors *without* it (n = 202). Survival analysis showed that the median survival time of patients carrying tumors expressing this gene signal was 100 days shorter than that of patients without this gene expression signal, from a median of 460 to 360 days (**Fig. 4**). Cox regression analysis showed that this gene expression signal had a significant impact on survival, with a 45% higher risk of death at any given time for patients with this gene expression signal. This result was significant after adjusting for age, sex, and type of treatment (hazard ratio: 1.45, 95% confidence interval: 1.043-2.015, P<0.05).

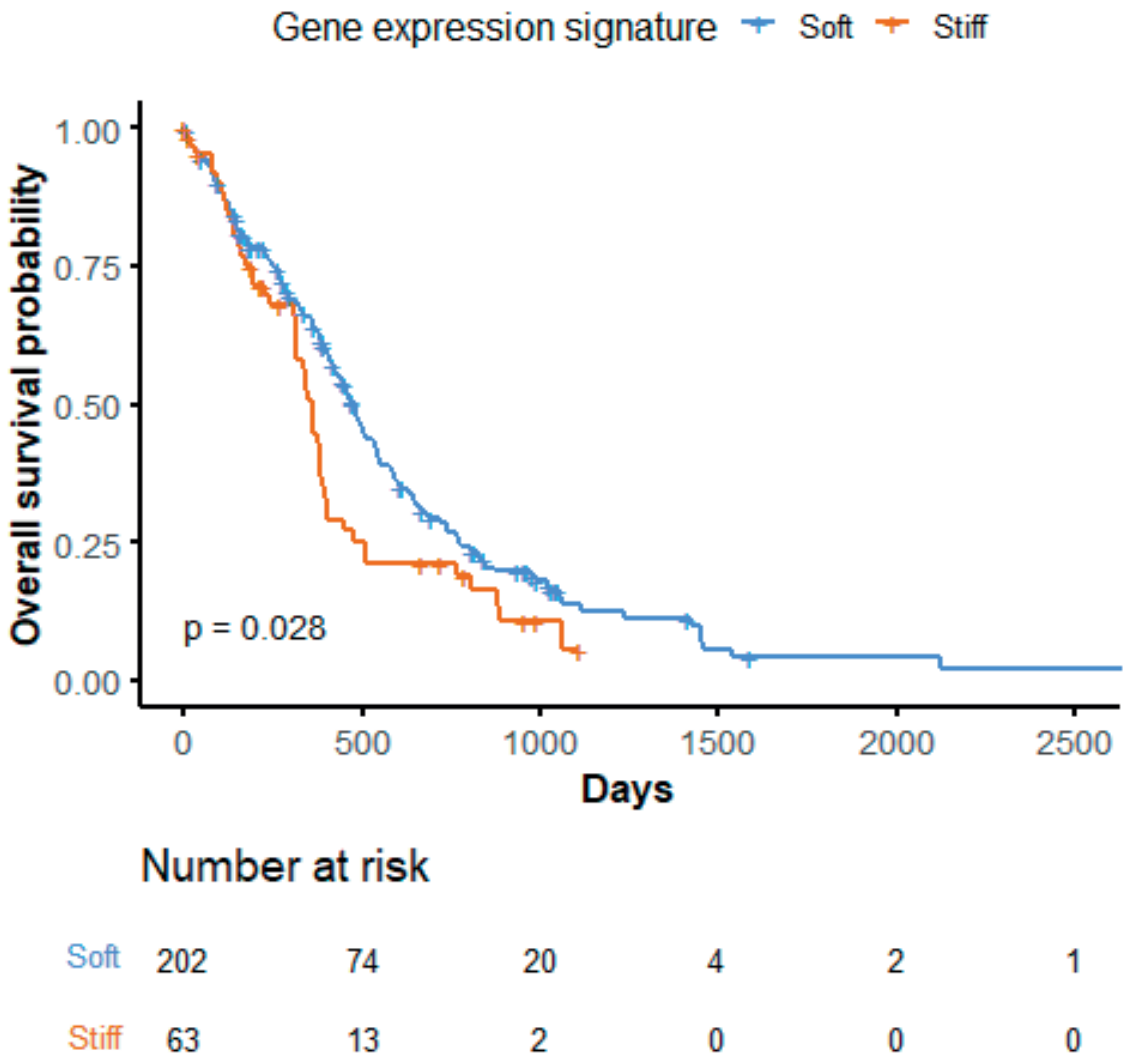

***Figure 4**: Survival analysis using data from TCGA and CPTAC. The median survival time of patients carrying tumors expressing the 22 genes associated with 'stiff' biopsies (n = 63, shown in orange) was 100 days shorter than that of patients who did not express these genes (n = 202, shown in blue).*

Discussion

In our study, we compared the transcriptomic profiles of stiff and soft GBM tissue biopsies as measured by MRE. We found that extracellular matrix reorganization, focal adhesion, and neutrophile-mediated immune responses were associated with increased stiffness within the tumor. Our quantitative measure of stiffness in each biopsy location did not correlate with the surgeon's subjective evaluation based on palpation. The 'stiff' and 'soft' biopsies as quantified by MRE could be separated by a gene expression signal of 22 genes. Finally, we showed that the expression signal found in 'stiff' biopsies is associated with decreased survival in patients with GBM.

Previous MRE studies on GBM tumors have reported decreased mean tumor stiffness of GBM compared to radiographically normal-appearing white matter (6). This is in accordance with our findings that tumor tissue is on average softer than contralateral white matter. However, the stiffness within each tumor was also highly variable with regions of both high and low values compared to normal-appearing tissue.

The level of tissue stiffness in and around a glioblastoma *in vivo* is not well understood. At the single-cell level, glioma cells have been measured to be stiffer than normal brain cells (22,23). On the nanoscale level, several studies using atomic force microscopy (AFM) report that GBM tissue is stiffer than non-tumor tissue (24-26). However, GBM has also been reported to be softer than the normal brain using AFM in animal models (27). Additionally, several *in vitro* studies have found GBM cells to be softer than normal fibroblasts and grade III glioma cells (28,29). Ciesluk *et al.* found GBM tumor stiffness, as measured by AFM, to be higher on average than healthy tissue but also highly heterogeneous (26). These findings on a microscale level are in contrast to previous bulk measurements obtained by MRE (6). Hence, the measured stiffness in GBM varies both with the method and on the scale at which it is measured (26,30). In contrast to these *in vitro* methods, MRE uniquely measures tissue stiffness *in vivo* and *in situ*.

A major source of tissue stiffening in GBM is believed to be restructuring of the extracellular matrix although definitive evidence of this is yet to be produced (24). To the best of our knowledge, this is the first time molecular profiling of GBM tissue has been correlated with *in vivo* MRE stiffness measurements. The transcriptomic profiles of 'stiff' and 'soft' biopsies in our study showed that extracellular matrix reorganization was strongly associated with 'stiff' biopsies, in particular collagen-related processes. Levels of fibrillar collagens in the healthy brain are low compared to the rest of the body, but in glioma, collagen levels are elevated and play a vital role in driving tumor progression (31). Gene sets associated with innate immune processes, such as neutrophil activation, were also upregulated in 'stiff' biopsies, indicating that these are active regions of the tumor (32). Thus, our findings support the idea that as the tumor progresses, it remodels its environment, producing a stiffening of the extracellular matrix. Elevated extracellular matrix stiffness has been shown to increase GBM aggression (33) and increase proliferation (5,34). Several of the genes found in our study to be upregulated in 'stiff' biopsies have previously been shown to play a role in glioma malignancy. *NRP1* and *DAB2* have been linked to glioma progression (35,36), *PECAM1* correlates with GBM aggressiveness (37), *CD163* is positively associated with the glioma malignancy grade (38), and *Flt1* promotes invasion and migration of glioblastoma cells (39). *CR1, PLAGL1, COL4A1,* and *COL5A2* have all been shown to correlate with shorter survival (40-43).

When our data was compared to previously published transcriptomic profiles of GBM samples, we found that median survival was significantly shorter in patients with tumors that exhibited the gene expression signal associated with 'stiff' biopsies. This indicates that the genetic and molecular processes we detect in 'stiff' tumor biopsies play a role in the malignant progression of tumors. It should be noted that while our data consists of multiple biopsies per patient with MRE stiffness evaluations, only one tissue biopsy per patient was available in the external data sets. We assume that this tissue biopsy is representative of the entire tumor. We do not claim

that the tumors in these datasets are stiff or soft, rather, we examined the prognostic relevance of stiff or soft expression signals for GBM patients. However, a significant correlation between the proportion of highly stiff ECM areas within a GBM tumor and worse patient prognosis has previously been shown, suggesting that elevated ECM stiffness can foster GBM aggression (33).

In contrast to AFM, MRE provides a stiffness map of the entire tumor and the surrounding tissue, and is therefore uniquely able to capture the heterogeneity of the biomechanical properties of a tumor prior to surgery. Previous work comparing the evaluation of tumor stiffness by neurosurgeons with MRE in meningiomas and in pituitary adenomas found that the measured stiffness correlated positively with the surgeon's evaluation (44,45). However, in these studies, the mean stiffness value for the entire tumor was reported. From tumor to tumor, meningiomas are known to vary in stiffness, from very firm to very soft (44). In patients with gliomas, the surgeons' haptic impression has been found to vary widely and therefore was not suitable as a gold standard of tumor consistency (46). This illustrates the challenge of comparing MRE measurements with the surgeon's impression, especially for small regions of interest. MRE probes the shear properties of tissue, while the probing by surgical tools involves a more complex process, as the tissue could also be compressed and compromised. Furthermore, tumor growth can compress surrounding tissue, generating solid stress due to swelling (47,48). Several studies have found that MRE is sensitive to compressive stress (49,50). Opening the skull during a craniotomy changes the pressure conditions in the brain, which may affect the perceived tissue stiffness compared to the MRE measurements, performed while the skull was still intact. When classifying biopsies using the surgeon's evaluation rather than MRE, no significant difference in gene expression was found between biopsies evaluated as stiff and soft.

In conclusion, MRE identifies regions of malignant extracellular matrix reorganization with an expression signal correlated to shorter survival time in patients with glioblastoma. Thus, MRE may be a powerful tool for characterizing tumor heterogeneity during pre-surgical planning.

References

1. Qazi MA, Vora P, Venugopal C, Sidhu SS, Moffat J, Swanton C*, et al.* Intratumoral heterogeneity: pathways to treatment resistance and relapse in human glioblastoma. *Ann Oncol* 2017;**28**(7):1448-56 doi 10.1093/annonc/mdx169.
2. Lombardi MY, Assem M. Glioblastoma Genomics: A Very Complicated Story. In: De Vleeschouwer S, editor. Glioblastoma. Brisbane, Australia: Codon Publications; 2017.
3. Dirkse A, Golebiewska A, Buder T, Nazarov PV, Muller A, Poovathingal S*, et al.* Stem cell-associated heterogeneity in Glioblastoma results from intrinsic tumor plasticity shaped by the microenvironment. *Nat Commun* 2019;**10**(1):1787 doi 10.1038/s41467-019-09853-z.
4. Ciasca G, Sassun TE, Minelli E, Antonelli M, Papi M, Santoro A*, et al.* Nano-mechanical signature of brain tumours. *Nanoscale* 2016;**8**(47):19629-43 doi 10.1039/c6nr06840e.
5. Ulrich TA, de Juan Pardo EM, Kumar S. The mechanical rigidity of the extracellular matrix regulates the structure, motility, and proliferation of glioma cells. *Cancer Res* 2009;**69**(10):4167-74 doi 10.1158/0008-5472.CAN-08-4859.
6. Bunevicius A, Schregel K, Sinkus R, Golby A, Patz S. REVIEW: MR elastography of brain tumors. *Neuroimage Clin* 2019;**25**:102109 doi 10.1016/j.nicl.2019.102109.
7. Svensson SF, Fuster-Garcia E, Latysheva A, Fraser-Green J, Nordhoy W, Isam Darwish O*, et al.* Decreased tissue stiffness in glioblastoma by MR elastography is associated with increased cerebral blood flow. *Eur J Radiol* 2022;**147**:110136 doi 10.1016/j.ejrad.2021.110136.
8. Runge JH, Hoelzl SH, Sudakova J, Dokumaci AS, Nelissen JL, Guenthner C*, et al.* A novel magnetic resonance elastography transducer concept based on a rotational eccentric mass: preliminary experiences with the gravitational transducer. *Phys Med Biol* 2019;**64**(4):045007 doi 10.1088/1361-6560/aaf9f8.
9. Guenthner C, Sethi S, Troelstra M, Dokumaci AS, Sinkus R, Kozerke S. Ristretto MRE: A generalized multi-shot GRE-MRE sequence. *NMR Biomed* 2019;**32**(5):e4049 doi 10.1002/nbm.4049.
10. Guenthner C, Runge JH, Sinkus R, Kozerke S. Analysis and improvement of motion encoding in magnetic resonance elastography. *NMR Biomed* 2018;**31**(5):e3908 doi 10.1002/nbm.3908.
11. Zada G, Yashar P, Robison A, Winer J, Khalessi A, Mack WJ*, et al.* A proposed grading system for standardizing tumor consistency of intracranial meningiomas. *Neurosurg Focus* 2013;**35**(6):E1 doi 10.3171/2013.8.FOCUS13274.
12. Petridis PD, Horenstein CI, Pereira B, Wu PB, Samanamud J, Marie T*, et al.* BOLD asynchrony elucidates tumor burden in IDH-mutated gliomas. *Neuro Oncol* 2022;**24**(1):78-87 doi 10.1093/neuonc/noab154.
13. Juan-Albarracin J, Fuster-Garcia E, Manjon JV, Robles M, Aparici F, Marti-Bonmati L*, et al.* Automated glioblastoma segmentation based on a multiparametric structured unsupervised classification. *PLoS One* 2015;**10**(5):e0125143 doi 10.1371/journal.pone.0125143.
14. Svensson SF, De Arcos J, Darwish OI, Fraser-Green J, Storas TH, Holm S*, et al.* Robustness of MR Elastography in the Healthy Brain: Repeatability, Reliability, and Effect of Different Reconstruction Methods. *J Magn Reson Imaging* 2021 doi 10.1002/jmri.27475.
15. Zhang Y, Parmigiani G, Johnson WE. ComBat-seq: batch effect adjustment for RNA-seq count data. *NAR Genomics and Bioinformatics* 2020;**2**(3) doi 10.1093/nargab/lqaa078.

16. Love MI, Huber W, Anders S. Moderated estimation of fold change and dispersion for RNA-seq data with DESeq2. *Genome Biol* 2014;**15**(12):550 doi 10.1186/s13059-014-0550-8.
17. Yu G, Wang L-G, Han Y, He Q-Y. clusterProfiler: an R Package for Comparing Biological Themes Among Gene Clusters. *OMICS* 2012;**16**(5):284-7 doi 10.1089/omi.2011.0118.
18. Rohart F, Gautier B, Singh A, Lê Cao K-A. mixOmics: An R package for 'omics feature selection and multiple data integration. *PLoS Comput Biol* 2017;**13**(11):e1005752-e doi 10.1371/journal.pcbi.1005752.
19. Gene Ontology C. The Gene Ontology resource: enriching a GOld mine. *Nucleic Acids Res* 2021;**49**(D1):D325-D34 doi 10.1093/nar/gkaa1113.
20. Gillespie M, Jassal B, Stephan R, Milacic M, Rothfels K, Senff-Ribeiro A*, et al.* The reactome pathway knowledgebase 2022. *Nucleic Acids Res* 2022;**50**(D1):D687-D92 doi 10.1093/nar/gkab1028.
21. Grossman RL, Heath AP, Ferretti V, Varmus HE, Lowy DR, Kibbe WA*, et al.* Toward a Shared Vision for Cancer Genomic Data. *N Engl J Med* 2016;**375**(12):1109-12 doi 10.1056/NEJMp1607591.
22. Khan ZS, Vanapalli SA. Probing the mechanical properties of brain cancer cells using a microfluidic cell squeezer device. *Biomicrofluidics* 2013;**7**(1):11806 doi 10.1063/1.4774310.
23. Graybill PM, Bollineni RK, Sheng Z, Davalos RV, Mirzaeifar R. A constriction channel analysis of astrocytoma stiffness and disease progression. *Biomicrofluidics* 2021;**15**(2):024103 doi 10.1063/5.0040283.
24. Miroshnikova YA, Mouw JK, Barnes JM, Pickup MW, Lakins JN, Kim Y*, et al.* Tissue mechanics promote IDH1-dependent HIF1α–tenascin C feedback to regulate glioblastoma aggression. *Nat Cell Biol* 2016;**18**(12):1336- doi 10.1038/NCB3429.
25. Chen X, Wanggou S, Bodalia A, Zhu M, Dong W, Fan JJ*, et al.* A Feedforward Mechanism Mediated by Mechanosensitive Ion Channel PIEZO1 and Tissue Mechanics Promotes Glioma Aggression. *Neuron* 2018;**100**(4):799-815 e7 doi 10.1016/j.neuron.2018.09.046.
26. Ciesluk M, Pogoda K, Deptula P, Werel P, Kulakowska A, Kochanowicz J*, et al.* Nanomechanics and Histopathology as Diagnostic Tools to Characterize Freshly Removed Human Brain Tumors. *Int J Nanomedicine* 2020;**15**:7509-21 doi 10.2147/IJN.S270147.
27. Seano G, Nia HT, Emblem KE, Datta M, Ren J, Krishnan S*, et al.* Solid stress in brain tumours causes neuronal loss and neurological dysfunction and can be reversed by lithium. *Nature Biomedical Engineering* 2019 doi 10.1038/s41551-018-0334-7.
28. Ning D, Duong B, Thomas G, Qiao Y, Ma L, Wen Q*, et al.* Mechanical and Morphological Analysis of Cancer Cells on Nanostructured Substrates. *Langmuir* 2016;**32**(11):2718-23 doi 10.1021/acs.langmuir.5b04469.
29. Alibert C, Pereira D, Lardier N, Etienne-Manneville S, Goud B, Asnacios A*, et al.* Multiscale rheology of glioma cells. *Biomaterials* 2021;**275**:120903 doi 10.1016/j.biomaterials.2021.120903.
30. Zanetti-Dallenbach R, Plodinec M, Oertle P, Redling K, Obermann EC, Lim RYH*, et al.* Length Scale Matters: Real-Time Elastography versus Nanomechanical Profiling by Atomic Force Microscopy for the Diagnosis of Breast Lesions. *Biomed Res Int* 2018;**2018**:3840597 doi 10.1155/2018/3840597.
31. Payne LS, Huang PH. The pathobiology of collagens in glioma. *Molecular cancer research : MCR* 2013;**11**(10):1129-40 doi 10.1158/1541-7786.MCR-13-0236.

32. Lin Y-J, Wei K-C, Chen P-Y, Lim M, Hwang T-L. Roles of Neutrophils in Glioma and Brain Metastases. *Front Immunol* 2021;**12**:701383- doi 10.3389/fimmu.2021.701383.
33. Miroshnikova YA, Mouw JK, Barnes JM, Pickup MW, Lakins JN, Kim Y*, et al.* Tissue mechanics promote IDH1-dependent HIF1alpha-tenascin C feedback to regulate glioblastoma aggression. *Nat Cell Biol* 2016;**18**(12):1336-45 doi 10.1038/ncb3429.
34. Umesh V, Rape AD, Ulrich TA, Kumar S. Microenvironmental stiffness enhances glioma cell proliferation by stimulating epidermal growth factor receptor signaling. *PLoS One* 2014;**9**(7):e101771 doi 10.1371/journal.pone.0101771.
35. Hu B, Guo P, Bar-Joseph I, Imanishi Y, Jarzynka MJ, Bogler O*, et al.* Neuropilin-1 promotes human glioma progression through potentiating the activity of the HGF/SF autocrine pathway. *Oncogene* 2007;**26**(38):5577-86 doi 10.1038/sj.onc.1210348.
36. Guven E, Afzal M, Kazmi I. Screening the Significant Hub Genes by Comparing Tumor Cells, Normoxic and Hypoxic Glioblastoma Stem-like Cell Lines Using Co-Expression Analysis in Glioblastoma. *Genes (Basel)* 2022;**13**(3) doi 10.3390/genes13030518.
37. Musumeci G, Castorina A, Magro G, Cardile V, Castorina S, Ribatti D. Enhanced expression of CD31/platelet endothelial cell adhesion molecule 1 (PECAM1) correlates with hypoxia inducible factor-1 alpha (HIF-1alpha) in human glioblastoma multiforme. *Exp Cell Res* 2015;**339**(2):407-16 doi 10.1016/j.yexcr.2015.09.007.
38. Liu S, Zhang C, Maimela NR, Yang L, Zhang Z, Ping Y*, et al.* Molecular and clinical characterization of CD163 expression via large-scale analysis in glioma. *Oncoimmunology* 2019;**8**(7):1601478 doi 10.1080/2162402X.2019.1601478.
39. Jiang K, Wang YP, Wang XD, Hui XB, Ding LS, Liu J*, et al.* Fms related tyrosine kinase 1 (Flt1) functions as an oncogene and regulates glioblastoma cell metastasis by regulating sonic hedgehog signaling. *Am J Cancer Res* 2017;**7**(5):1164-76.
40. Pilgaard L, Mortensen JH, Henriksen M, Olesen P, Sorensen P, Laursen R*, et al.* Cripto-1 expression in glioblastoma multiforme. *Brain Pathol* 2014;**24**(4):360-70 doi 10.1111/bpa.12131.
41. Li C, Cho HJ, Yamashita D, Abdelrashid M, Chen Q, Bastola S*, et al.* Tumor edge-to-core transition promotes malignancy in primary-to-recurrent glioblastoma progression in a PLAGL1/CD109-mediated mechanism. *Neurooncol Adv* 2020;**2**(1):vdaa163 doi 10.1093/noajnl/vdaa163.
42. Wang H, Liu Z, Li A, Wang J, Liu J, Liu B*, et al.* COL4A1 as a novel oncogene associated with the clinical characteristics of malignancy predicts poor prognosis in glioma. *Exp Ther Med* 2021;**22**(5):1224 doi 10.3892/etm.2021.10658.
43. Pencheva N, de Gooijer MC, Vis DJ, Wessels LFA, Wurdinger T, van Tellingen O*, et al.* Identification of a Druggable Pathway Controlling Glioblastoma Invasiveness. *Cell Rep* 2017;**20**(1):48-60 doi 10.1016/j.celrep.2017.06.036.
44. Hughes JD, Fattahi N, Van Gompel J, Arani A, Meyer F, Lanzino G*, et al.* Higher-Resolution Magnetic Resonance Elastography in Meningiomas to Determine Intratumoral Consistency. *Neurosurgery* 2015;**77**(4):653-8; discussion 8-9 doi 10.1227/NEU.0000000000000892.
45. Hughes JD, Fattahi N, Van Gompel J, Arani A, Ehman R, Huston J, 3rd. Magnetic resonance elastography detects tumoral consistency in pituitary macroadenomas. *Pituitary* 2016;**19**(3):286-92 doi 10.1007/s11102-016-0706-5.
46. Reiss-Zimmermann M, Streitberger KJ, Sack I, Braun J, Arlt F, Fritzsch D*, et al.* High Resolution Imaging of Viscoelastic Properties of Intracranial Tumours by Multi-

Frequency Magnetic Resonance Elastography. *Clin Neuroradiol* 2015;**25**(4):371-8 doi 10.1007/s00062-014-0311-9.
47. Fuster-Garcia E, Thokle Hovden I, Flogstad Svensson S, Larsson C, Vardal J, Bjornerud A*, et al.* Quantification of Tissue Compression Identifies High-Grade Glioma Patients with Reduced Survival. *Cancers (Basel)* 2022;**14**(7) doi 10.3390/cancers14071725.
48. Nia HT, Liu H, Seano G, Datta M, Jones D, Rahbari N*, et al.* Solid stress and elastic energy as measures of tumour mechanopathology. *Nat Biomed Eng* 2016;**1** doi 10.1038/s41551-016-0004.
49. Capilnasiu A, Hadjicharalambous M, Fovargue D, Patel D, Holub O, Bilston L*, et al.* Magnetic resonance elastography in nonlinear viscoelastic materials under load. *Biomech Model Mechanobiol* 2019;**18**(1):111-35 doi 10.1007/s10237-018-1072-1.
50. Pogoda K, Chin L, Georges PC, Byfield FJ, Bucki R, Kim R*, et al.* Compression stiffening of brain and its effect on mechanosensing by glioma cells. *New J Phys* 2014;**16**:075002 doi 10.1088/1367-2630/16/7/075002.

Appendices

Appendix A

Supplementary material Paper II

Supplementary information, Paper II

Image processing

Perfusion images of the healthy subjects from ASL were analysed in the nordicICE (NordicNeuroLab AS, Bergen, Norway) software. This resulted in maps of cerebral blood flow (CBF) (**Fig. 1B**) quantified in units of ml/100 g/min, given by the formula (1):

$$CBF = \frac{6000 \cdot \lambda \cdot (SI_{control} - SI_{label}) \cdot e^{\frac{PLD}{T_{1,blood}}}}{2 \cdot \alpha \cdot T_{1,blood} \cdot SI_{PD} \cdot (1 - e^{-\frac{\tau}{T_{1,blood}}})} [ml/100g/min]$$

The following parameters were applied: $T_{1,blood}$= 1650 ms, labelling efficiency α of 0.85, and brain-blood water partition coefficient λ=0.9 ml/g (1). Motion correction and co-registration between the ASL and the proton density images were performed prior to analysis. Because ASL in general has low sensitivity for subtle perfusion levels in white matter (1), our study includes perfusion values from deep- and cortical gray matter regions only.

The DTI and DSC images were corrected for EPI-distortion effects prior to analysis using the geometric distortion correction method FSL TOPUP (2,3). Thereafter, diffusion tensor imaging analysis was performed in nordicICE with motion correction, automatic detection of noise threshold and noise level cutoff. The tissue diffusivity was measured by the apparent diffusion coefficient (ADC), and the tissue anisotropy was measured by the fractional anisotropy index (FA). Patient perfusion images were also analysed in nordicICE (4) utilizing both motion- and leakage-correction on DSC data. This produced map of cerebral blood flow normalized to white matter (nCBF), leakage, and vessel size index (VSI). The two latter maps were available for seven of the nine patients.

For the MRE, phase-unwrapping and pixel-wise temporal Fourier transformation were performed on the displacement phase data in order to obtain the tissue displacement in the frequency domain. The data was filtered in image space using an 11th order Blackmann Harris filter (5), before the curl operator was applied in the image to eliminate information originating from the compressional wave component (6). Through inversion, we then obtained maps of the shear storage modulus G′ (as a measure for stiffness) and the shear loss modulus G″ (related to the viscosity, meaning the tissue's ability to dissipate energy). To avoid artefacts from MRE reconstruction at the edge of the brain, elastography maps were eroded by 2 pixels. MRE data quality was assessed by degree of temporal nonlinearity in the MRE data, which is a measure of noise in the original phase data (7), and the ratio between the amplitude of the curl and the amplitude of the divergence (8). This ratio quantifies the signal (curl) to noise (divergence) since the divergence of the displacement is approximately zero due to the incompressible nature of tissue. All scans had a mean curl-divergence ratio above 5 and any voxels with nonlinearity above 50 % were excluded in the MRE maps.

Image registration and analysis

Segmentations of patient data

Segmentations of contrast-enhancing tumor, edema, necrosis, and normal-appearing gray and white matter was performed automatically using a convolutional neural network (CNN). This

CNN is based on the 3D-Unet architecture defined by Juan-Albarracín et al. (9), trained with 262 BRATS (10,11) pre-surgical exams and 222 follow-up exams from our institution. The segmentations were done for each patient based on pre- and post-contrast $T1_w$, images, $T2_w$ and FLAIR images. Contrast-enhancing and necrotic tumor were defined as the enhancing and non-enhancing tumor region on post-contrast $T1_w$ images, respectively. Edema was defined as the hyperintense region on the FLAIR images. Gray- and white-matter masks were eroded by one voxel, and only the opposite hemisphere of the brain from the tumor was used for the normal-appearing gray- and white-matter masks. For the cases where the tumor affected both hemispheres, a 3 cm margin from the distal edge of the tumor and edema was used for the gray and white matter masks.

For comparisons between patients on an image voxel level, and for calculations of gradients outward from the patients, all maps were registered to the Montreal Neurological Institute (MNI) space (12), by means of an affine transformation and using a nearest-neighbour interpolation to preserve image voxel integrity. For the regression analysis on the voxel level, all maps were smoothed with a 3D Gaussian filter with sigma 1. The analysis was performed in Matlab (version R2021a, MathWorks, Natick, MA, USA).

To assess the spatial distribution of the parameters in necrosis, the distance to contrast-enhancing tumor was calculated for all points in the necrosis, and normalized to the maximum distance to contrast-enhancing tumor. This was repeated in contrast-enhancing tumor, using the distance to edema, and in edema, using the distance to normal-appearing tissue. For visualization, the gradients were smoothed using a Gaussian-weighted moving average filter of window length 70.

In order to make gradients outward from the lesion edge, here defined as the distal edema, an ROI consisting of necrosis, contrast-enhancing tumor and edema was dilated 1 mm at a time, 30 times. For each dilation, the last ROI was subtracted and the mean value of each new layer calculated. The gradients were smoothed using a Gaussian-weighted moving average filter of window length 10.

Regions of interest in healthy subjects

All image registrations in healthy subjects were performed using Matlab and SPM12 (version 7487, Wellcome Trust Centre for Neuroimaging, London). First, anatomical $T1_w$ images were warped to the MNI brain region template (13), and the inverse deformation fields were used to reorient the binary maps of the brain regions of interest into the each subject's anatomical space. T1 images and labels were then co-registered by affine transformations, using nearest-neighbour interpolation, into the native spaces of the MRE, DTI and the ASL images.

ROIs in the healthy subjects were extracted from the MNI template. The deep gray matter regions included in our study were head of the caudate nucleus, putamen, thalamus and hippocampus. The cortical gray matter regions included were the frontal lobe, the occipital lobe, the parietal lobe and the temporal lobe. For MRE and DTI images, a white matter ROI was also included. ADC maps from the diffusion acquisition was used to reduce any potential errors from partial volume effects. A mask with a cut-off ADC value of $< 1.2 \times 10^{-3}$ mm^2/s was used to exclude voxels with free diffusion from DTI and MRE maps, to ensure no voxels with cerebrospinal fluid were included (14).

References

1. Alsop DC, Detre JA, Golay X, et al. Recommended implementation of arterial spin-labeled perfusion MRI for clinical applications: A consensus of the ISMRM perfusion study group and the European consortium for ASL in dementia. Magn Reson Med 2015;73(1):102-116.
2. Andersson JL, Skare S, Ashburner J. How to correct susceptibility distortions in spin-echo echo-planar images: application to diffusion tensor imaging. Neuroimage 2003;20(2):870-888.
3. Hovden IT, Geier OM, Digernes I, et al. The impact of EPI-based distortion correction of dynamic susceptibility contrast MRI on cerebral blood volume estimation in patients with glioblastoma. Eur J Radiol 2020;132:109278.
4. Bjornerud A, Emblem KE. A fully automated method for quantitative cerebral hemodynamic analysis using DSC-MRI. J Cereb Blood Flow Metab 2010;30(5):1066-1078.
5. Albrecht HH. A family of cosine-sum windows for high-resolution measurements. Volume 5: IEEE; 2001. p. 3081-3084 vol.3085.
6. Sinkus R, Tanter M, Xydeas T, Catheline S, Bercoff J, Fink M. Viscoelastic shear properties of in vivo breast lesions measured by MR elastography. Magn Reson Imaging 2005;23(2):159-165.
7. Yeung J, Juge L, Hatt A, Bilston LE. Paediatric brain tissue properties measured with magnetic resonance elastography. Biomech Model Mechanobiol 2019;18(5):1497-1505.
8. Svensson SF, De Arcos J, Darwish OI, et al. Robustness of MR Elastography in the Healthy Brain: Repeatability, Reliability, and Effect of Different Reconstruction Methods. J Magn Reson Imaging 2021.
9. Juan-Albarracin J, Fuster-Garcia E, Garcia-Ferrando GA, Garcia-Gomez JM. ONCOhabitats: A system for glioblastoma heterogeneity assessment through MRI. Int J Med Inform 2019;128:53-61.
10. Menze BH, Jakab A, Bauer S, et al. The Multimodal Brain Tumor Image Segmentation Benchmark (BRATS). IEEE Trans Med Imaging 2015;34(10):1993-2024.
11. Bakas S, Akbari H, Sotiras A, et al. Advancing The Cancer Genome Atlas glioma MRI collections with expert segmentation labels and radiomic features. Sci Data 2017;4:170117.
12. Brett M, Johnsrude IS, Owen AM. The problem of functional localization in the human brain. Nat Rev Neurosci 2002;3(3):243-249.
13. Tzourio-Mazoyer N, Landeau B, Papathanassiou D, et al. Automated anatomical labeling of activations in SPM using a macroscopic anatomical parcellation of the MNI MRI single-subject brain. Neuroimage 2002;15(1):273-289.
14. Bykowski JL, Latour LL, Warach S. More accurate identification of reversible ischemic injury in human stroke by cerebrospinal fluid suppressed diffusion-weighted imaging. Stroke 2004;35(5):1100-1106.

Appendix B

Supplementary material Paper III

MR Elastography Identifies Regions of Extracellular Matrix Reorganization Associated with Shorter Survival in Glioblastoma Patients – Supplementary material

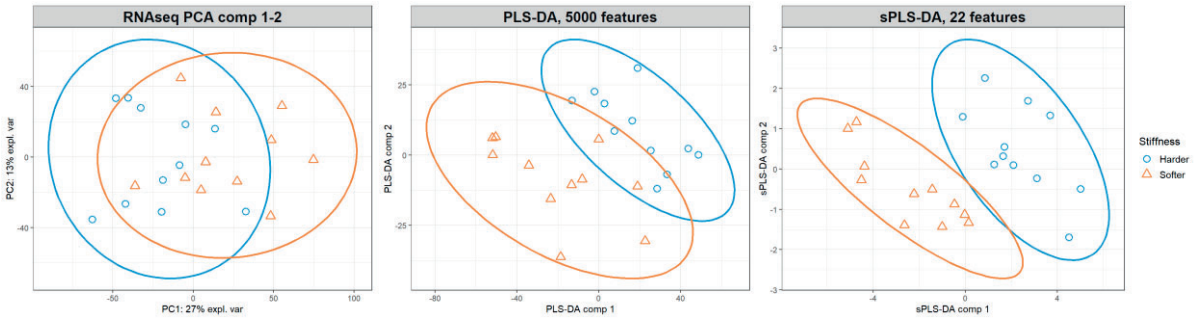

Supplementary Figure 1: Clustering of glioblastoma biopsies based on $|G^*|_{norm}$. *Biopsies from each patient were classified as 'stiff' (blue circles) or 'soft' (orange triangles) based on the mean stiffness of all biopsies from the same patient. A) Multilevel principal component analysis, accounting for patient variability, shows weak separation of 'stiff' and 'soft' biopsies along the first principal component. B) Partial least squares differential analysis (PLS-DA) based on the 5000 RNA transcripts with highest variance in the data shows that an expression signal can be found along the first component that distinguishes 'stiff' biopsies from 'soft' biopsies. C) The tuning of the PLS-DA results revealed that a set of 20 genes along the first component and 2 genes along the second component was sufficient to completely separate the 'stiff' and 'soft' biopsies.*

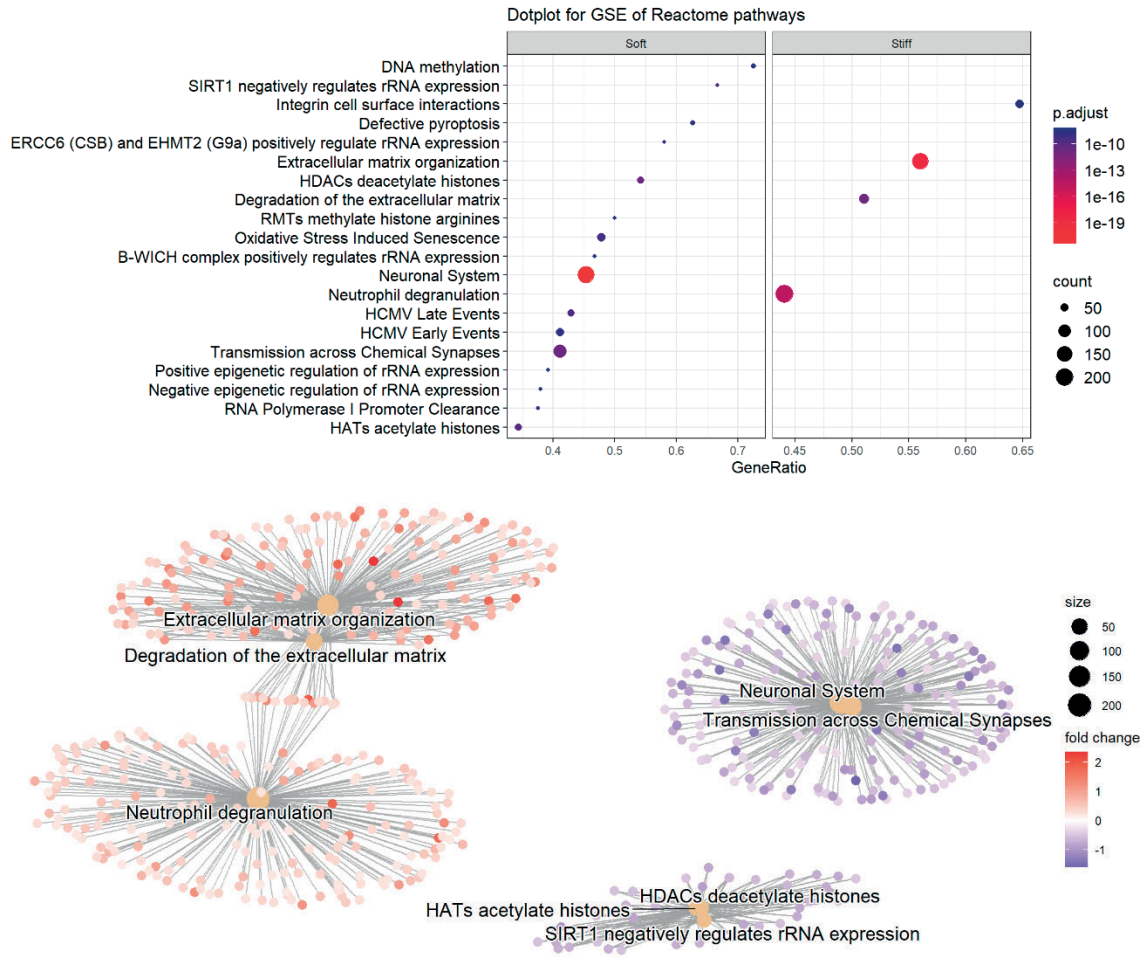

Supplementary Figure 2. Gene-set enrichment analysis (Reactome pathways) of differentially expressed genes in 'soft' and 'stiff' tumor biopsies. *A) Dotplot representing the terms most highly enriched in Reactome pathways, p.adjust = p-value adjusted for multiple testing. B) Pathway enrichment map of the GSEA results. Central nodes represent Reactome pathways, colored dots represent differentially expressed genes (red = upregulated in 'stiff' biopsies, blue = upregulated in 'soft' biopsies).*

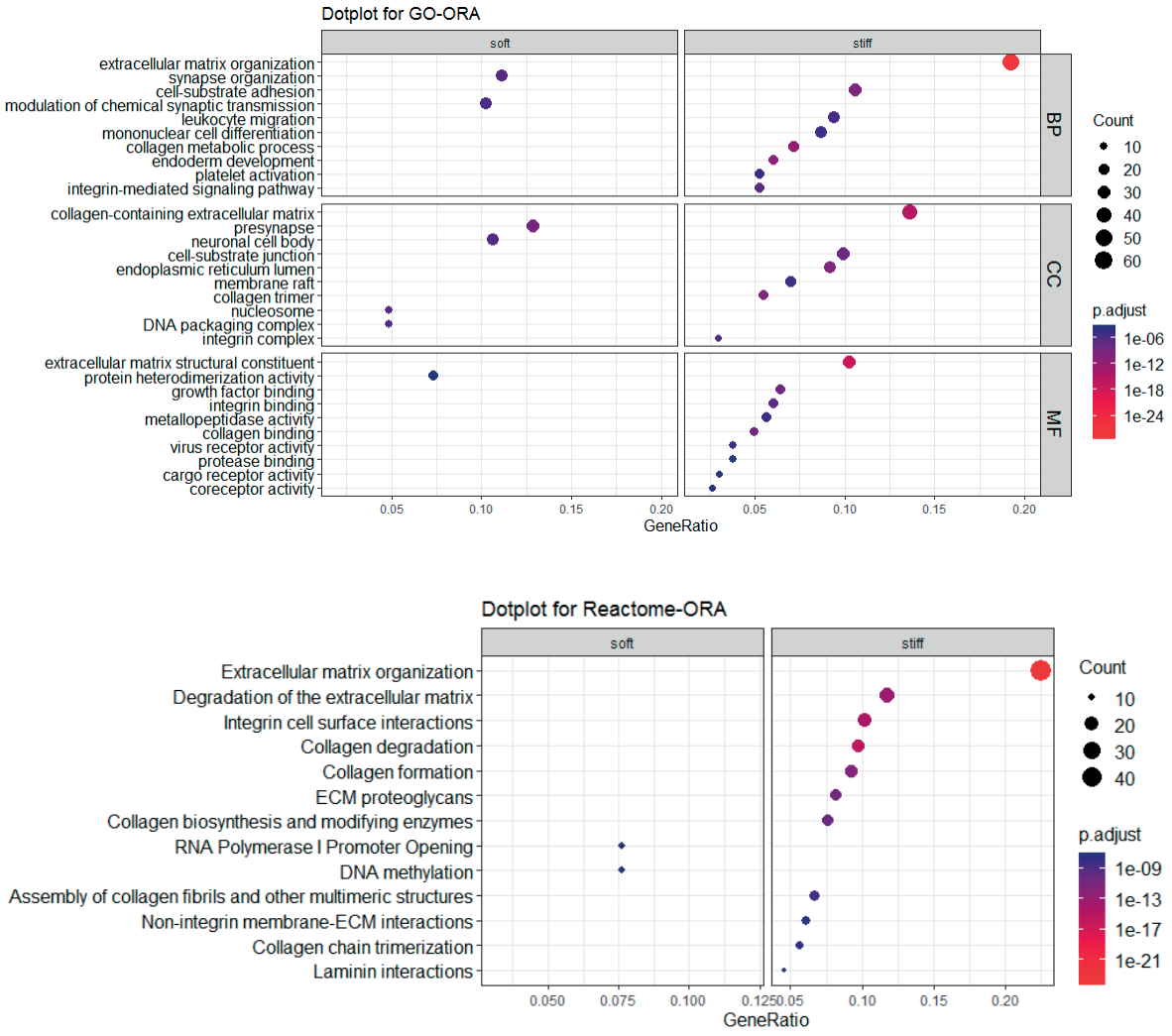

Supplementary Figure 3: GO and Reactome Over-representation analysis. *A) Top 10 GO gene sets in each category (BP = biological process, CC = Cellular component, MF = Molecular function) with lowest adjusted p-value in 'stiff" and 'soft' biopsies. B) Top 13 Reactome pathways with lowest adjusted p-value in 'stiff" and 'soft' biopsies.*

To evaluate the cellular and microenvironmental signatures within biopsies based on gene expression profiles, we performed a cell type enrichment analysis using the xCell signature set [1]. Although we found a high variability in cellular composition as predicted by xCell between the biopsies, the stiffer biopsies tended towards higher astrocyte composition, while the 'soft biopsies' showed a higher score for neurons. Furthermore, a higher aggregated microenvironment score was seen in the 'stiff' biopsies **(Supplementary Fig. 4).**

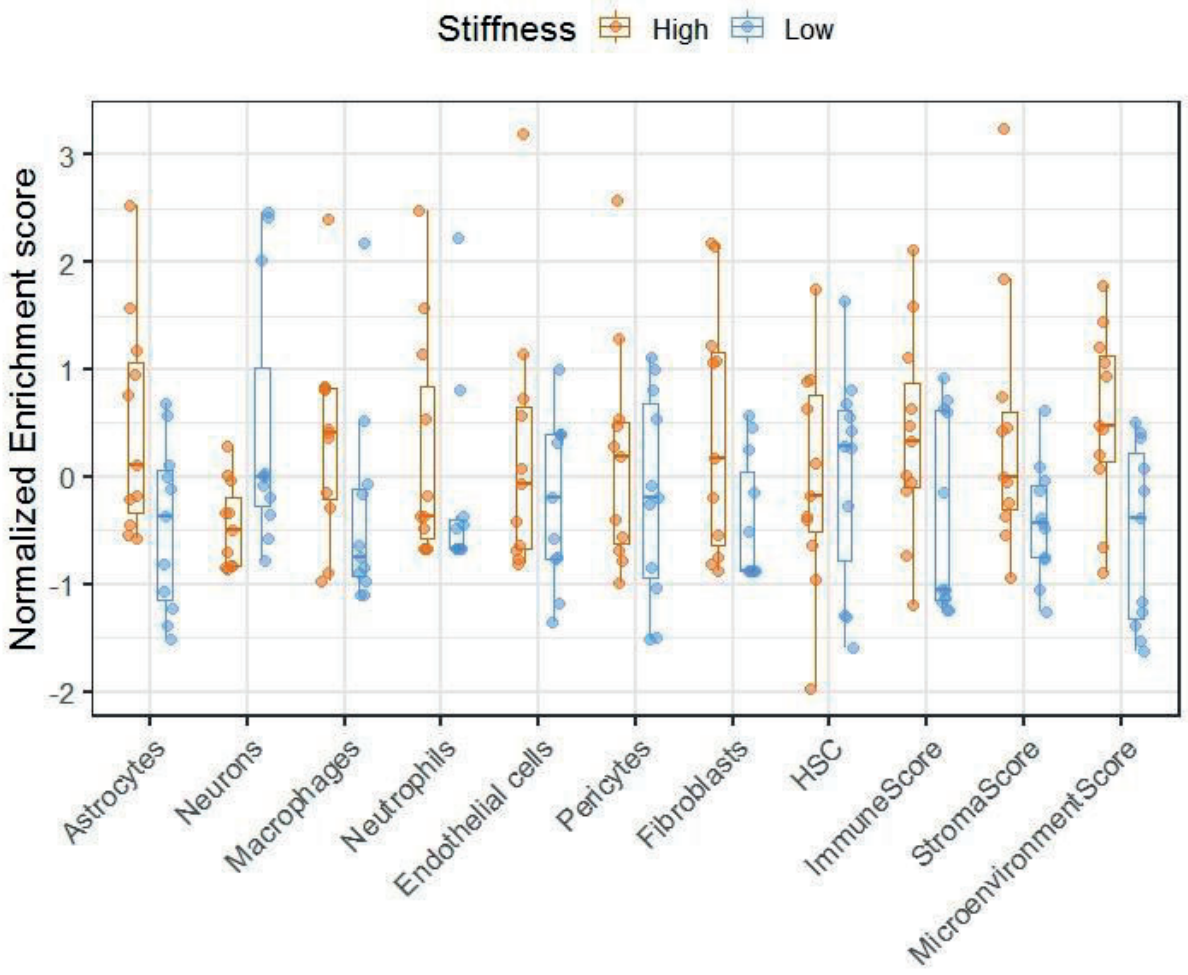

Supplementary Figure 4: Cell-type enrichment in bulk RNA sequencing with xCell. *'Stiff' biopsies shown in blue, 'soft' biopsies shown in orange.*

Patient age	Patient gender	Tumor location	Volume CE tumor [cm^3]	Volume necrosis [cm^3]	Volume FLAIR signal [cm^3]	Mean $\|G^*\|_{norm}$ CE tumor	Mean $\|G^*\|_{norm}$ necrosis	Mean $\|G^*\|_{norm}$ FLAIR signal	Mean φ_{norm} CE tumor	Mean φ_{norm} necrosis	Mean φ_{norm} FLAIR signal
45-49	Male	Parietal	7	4	51	0.80	0.66	0.99	0.99	1.01	0.95
75-79	Male	Temporal	21	12	40	0.78	0.48	1.08	0.75	0.79	0.91
60-64	Female	Basal ganglia	29	13	43	0.73	0.69	0.83	0.82	0.97	0.83
55-59	Male	Temporal	28	11	162	0.80	0.64	0.89	0.79	0.67	0.82
35-39	Female	Parietal	14	4	92	0.74	0.76	1.05	0.71	0.54	0.80
60-64	Male	Temporal	28	19	39	0.90	0.98	1.01	0.81	0.71	0.83
50-54	Male	Temporal	7	3	45	0.84	0.65	1.21	0.97	0.98	0.80
50-54	Female	Temporal	49	25	61	0.80	0.80	0.95	0.97	0.92	0.86
40-44	Female	Temporal	5	2	50	0.81	0.85	1.09	0.75	0.71	0.93
65-69	Female	Parietal	11	8	2	0.98	0.77	1.21	0.88	0.82	0.85
65-69	Female	Parieto-occipital	39	10	42	0.93	0.70	0.99	0.88	1.00	0.95
60-64	Female	Parieto-occipital	33	45	35	0.81	0.75	0.94	0.78	1.26	0.87
45-49	Female	Parietal	13	13	52	0.61	0.56	0.92	0.76	0.97	0.76

Supplementary Table 1: ***Patient characteristics.*** *Patient age group, tumor location, volume, and MRE measurements (normalized to each patient's contralateral normal-appearing white matter*) *in contrast-enhancing tumor, necrosis, and region with high signal on T2-FLAIR. The first eight patients were used in RNA sequencing analysis.*

ENREZ_ID	Symbol	baseMean	log2Fold Change	lfcSE	P-value	Adju. P-value
10351	ABCA8	1204.883261	0.671257	0.114681	4.82E-09	7.70E-05
23213	SULF1	2151.787754	1.595155	0.319137	5.78E-07	0.003052
54885	TBC1D8B	118.289721	0.950754	0.190976	6.41E-07	0.003052
4121	MAN1A1	903.7229709	0.890446	0.180097	7.64E-07	0.003052
79839	CCDC102B	1032.172753	0.922098	0.188653	1.02E-06	0.003258
3875	KRT18	62.60869999	1.415651	0.294371	1.52E-06	0.003951
8829	NRP1	4671.780854	0.982309	0.205396	1.73E-06	0.003951
5325	PLAGL1	113.3530688	0.996035	0.209931	2.09E-06	0.004172
5592	PRKG1	463.8615734	0.792318	0.172652	4.45E-06	0.007111
81551	STMN4	407.1583395	-0.97506	0.211744	4.13E-06	0.007111
2803	GOLGA4	4826.145609	0.274702	0.060761	6.15E-06	0.008938
767	CA8	198.8150717	-0.9019	0.201271	7.43E-06	0.009888
1909	EDNRA	900.7642216	0.760681	0.17067	8.31E-06	0.010156
78997	GDAP1L1	109.6847843	-1.2734	0.286655	8.90E-06	0.010156
5175	PECAM1	829.4028375	0.52938	0.12002	1.03E-05	0.010502
115548	FCHO2	1475.189333	0.419033	0.0951	1.05E-05	0.010502
1290	COL5A2	8963.612758	0.747587	0.170538	1.17E-05	0.010964
5205	ATP8B1	252.8700371	0.809535	0.185212	1.24E-05	0.010983
7373	COL14A1	860.8016235	0.945786	0.217792	1.41E-05	0.011838
9332	CD163	12876.52315	1.308098	0.306163	1.93E-05	0.013013
9169	SCAF11	4011.135905	0.300244	0.069986	1.79E-05	0.013013
875	CBS	961.7247316	-0.49534	0.11545	1.78E-05	0.013013
93145	OLFM2	808.9923179	-0.58671	0.137404	1.96E-05	0.013013
441381	LRRC24	33.97029124	-0.90986	0.212358	1.83E-05	0.013013
3759	KCNJ2	563.1353637	0.537025	0.126575	2.21E-05	0.013239
23216	TBC1D1	1671.086313	0.291718	0.068805	2.24E-05	0.013239
345630	FBLL1	33.27600773	-1.23017	0.289728	2.18E-05	0.013239
26136	TES	368.73219	0.691061	0.16345	2.36E-05	0.013454
79187	FSD1	176.8332367	-0.60704	0.14422	2.56E-05	0.014123
4124	MAN2A1	2722.209833	0.500494	0.119305	2.73E-05	0.014524
22925	PLA2R1	289.4342541	0.796937	0.190545	2.88E-05	0.014864
1.01E+08	DNM3OS	135.1473547	1.177743	0.283332	3.23E-05	0.015651
84910	TMEM87B	790.3001554	0.373412	0.089841	3.23E-05	0.015651
5139	PDE3A	650.0727524	0.808889	0.195392	3.48E-05	0.016329
1378	CR1	428.468695	1.721665	0.417006	3.65E-05	0.016655
84935	MEDAG	187.4729426	1.736515	0.422237	3.91E-05	0.016886
1601	DAB2	1367.228764	0.89499	0.217557	3.89E-05	0.016886
3672	ITGA1	3155.083673	0.892766	0.218458	4.38E-05	0.01705
55075	UACA	2801.043162	0.879256	0.215	4.32E-05	0.01705
4253	MIA2	751.9145183	0.190349	0.046427	4.13E-05	0.01705
128312	H2BU1	56.06297646	-0.94549	0.231187	4.32E-05	0.01705
10184	LHFPL2	2846.391379	0.668107	0.1639	4.58E-05	0.017402
57026	PDXP	301.3936541	-0.66022	0.162233	4.71E-05	0.017496
1600	DAB1	56.07243773	-0.74573	0.183607	4.87E-05	0.017697
4060	LUM	1454.232745	1.585698	0.394083	5.73E-05	0.0182
728264	CARMN	714.9461116	1.138235	0.284377	6.27E-05	0.0182

1282	COL4A1	25705.42138	0.927032	0.229689	5.44E-05	0.0182
1396	CRIP1	139.1756583	0.882014	0.219741	5.97E-05	0.0182
3676	ITGA4	1081.835497	0.598904	0.149273	6.02E-05	0.0182
29803	REPIN1	985.3827012	-0.28253	0.070259	5.79E-05	0.0182
728875	NA	71.47935093	-0.54967	0.135915	5.25E-05	0.0182
1468	SLC25A10	69.37581705	-0.70006	0.174792	6.20E-05	0.0182
1152	CKB	2415.056651	-0.88914	0.220577	5.55E-05	0.0182
494470	RNF165	193.396958	-0.94091	0.232927	5.36E-05	0.0182
11075	STMN2	428.509595	-1.54268	0.385229	6.21E-05	0.0182
9568	GABBR2	317.4056257	-1.42335	0.356861	6.65E-05	0.018965
4327	MMP19	498.6702733	1.640407	0.416131	8.08E-05	0.020003
9509	ADAMTS2	357.1242342	1.535422	0.389542	8.09E-05	0.020003
948	CD36	401.8675628	1.213807	0.306493	7.49E-05	0.020003
9358	ITGBL1	219.7353646	1.084708	0.274643	7.83E-05	0.020003
219623	TMEM26	150.0464163	0.815724	0.206018	7.51E-05	0.020003
81792	ADAMTS12	312.2400418	0.801566	0.202922	7.81E-05	0.020003
285203	EOGT	659.0670372	0.484049	0.12306	8.37E-05	0.020003
359845	RFLNB	399.7972356	0.467286	0.118812	8.39E-05	0.020003
7067	THRA	1744.471032	-0.57394	0.145132	7.67E-05	0.020003
283248	RCOR2	193.5926837	-1.0851	0.275763	8.32E-05	0.020003
375704	ENHO	168.7048087	-1.41831	0.360117	8.20E-05	0.020003
23317	DNAJC13	3629.359927	0.181268	0.046274	8.96E-05	0.020776
90268	OTULIN	1024.722629	0.164369	0.041965	8.97E-05	0.020776
7855	FZD5	453.0463433	0.510575	0.130528	9.17E-05	0.020922
140738	TMEM37	115.1899765	0.92	0.23587	9.60E-05	0.021364
1496	CTNNA2	2181.699365	-0.4864	0.124725	9.63E-05	0.021364
1803	DPP4	393.6808038	1.46781	0.377505	0.000101	0.022
51310	SLC22A17	1001.60094	-0.55445	0.142678	0.000102	0.022
57524	CASKIN1	89.75823766	-0.90651	0.233705	0.000105	0.02235
3559	IL2RA	322.7840705	1.407741	0.364006	0.00011	0.022532
1295	COL8A1	785.7219972	0.829723	0.214528	0.00011	0.022532
7048	TGFBR2	1865.961745	0.557067	0.143881	0.000108	0.022532
1303	COL12A1	2159.00124	1.090289	0.283196	0.000118	0.023709
2335	FN1	90865.15825	1.020001	0.265024	0.000119	0.023709
7476	WNT7A	60.23711675	-0.64025	0.166501	0.00012	0.023743
23075	SWAP70	1735.632773	0.261018	0.068001	0.000124	0.02412
4320	MMP11	136.6725256	0.979662	0.255476	0.000126	0.024199
6362	CCL18	165.8221877	3.206418	0.8398	0.000134	0.024614
3487	IGFBP4	1330.361348	1.005899	0.264911	0.000146	0.024614
9060	PAPSS2	534.3162319	0.717231	0.188686	0.000144	0.024614
4162	MCAM	3578.341451	0.554437	0.145774	0.000143	0.024614
2321	FLT1	3181.634308	0.525557	0.137997	0.00014	0.024614
4094	MAF	1185.587343	0.470618	0.123125	0.000132	0.024614
9208	LRRFIP1	1882.434969	0.334148	0.087816	0.000142	0.024614
5311	PKD2	1730.840704	0.267787	0.070224	0.000137	0.024614
4597	MVD	198.203436	-0.53868	0.141385	0.000139	0.024614
4915	NTRK2	10188.32693	-0.65318	0.171955	0.000146	0.024614
26232	FBXO2	188.0271482	-0.90256	0.237649	0.000146	0.024614

51617	NSG2	330.3962473	-1.48427	0.38894	0.000136	0.024614
4625	MYH7	116.0433084	-0.7667	0.202208	0.00015	0.024902
1278	COL1A2	10955.85651	1.338037	0.354165	0.000158	0.025246
54829	ASPN	244.8656243	1.23206	0.325763	0.000156	0.025246
57125	PLXDC1	1016.990503	0.824465	0.218261	0.000158	0.025246
154141	MBOAT1	132.9346344	0.808017	0.21415	0.000161	0.025246
30061	SLC40A1	1744.7296	0.43417	0.115026	0.00016	0.025246
138311	DIPK1B	300.7735757	-0.46717	0.123724	0.000159	0.025246
6781	STC1	751.7672591	1.197282	0.317934	0.000166	0.025498
54796	BNC2	387.8907464	0.787387	0.208994	0.000165	0.025498
4026	LPP	7269.585995	0.49995	0.132952	0.00017	0.025568
6538	SLC6A11	255.5257214	-1.00746	0.267829	0.000169	0.025568
8338	H2AC20	610.1125553	-0.58486	0.155735	0.000173	0.025828
2444	FRK	45.02494024	0.807139	0.215587	0.000181	0.02634
2200	FBN1	3836.740463	0.689311	0.184011	0.00018	0.02634
10924	SMPDL3A	308.1054271	0.670435	0.179163	0.000183	0.02634
9697	TRAM2	777.0399409	0.634394	0.169563	0.000183	0.02634
8654	PDE5A	931.6264987	0.644951	0.172872	0.000191	0.02706
51560	RAB6B	1252.662182	-0.53887	0.144465	0.000191	0.02706
55803	ADAP2	953.2199966	0.61838	0.165884	0.000193	0.027066
203522	INTS6L	432.7831097	0.268365	0.072046	0.000195	0.027139
5551	PRF1	194.6917989	1.233593	0.331646	0.0002	0.027242
4643	MYO1E	1517.086364	0.580884	0.156161	0.000199	0.027242
3912	LAMB1	6558.519009	0.952069	0.256399	0.000205	0.027469
27	ABL2	2714.176905	0.308347	0.08303	0.000204	0.027469
11326	VSIG4	3914.818203	1.06168	0.286626	0.000212	0.02801
10522	DEAF1	529.1343407	-0.28902	0.078005	0.000211	0.02801
144402	CPNE8	334.4890902	0.631622	0.170661	0.000215	0.028114
23175	LPIN1	1576.370062	-0.27185	0.073812	0.000231	0.029701
1826	DSCAM	836.6862168	-0.89297	0.242412	0.00023	0.029701
121457	IKBIP	710.8423048	0.456273	0.124168	0.000238	0.03044
5300	PIN1	505.7290614	-0.2893	0.078845	0.000243	0.030466
23580	CDC42EP4	2054.20444	-0.5124	0.139757	0.000246	0.030466
844	CASQ1	102.851126	-0.62236	0.169543	0.000242	0.030466
55964	SEPTIN3	919.5956037	-0.87965	0.239917	0.000246	0.030466
677828	SNORA47	176.1461107	-0.49527	0.135231	0.00025	0.030707
221395	ADGRF5	1868.792441	0.592567	0.162029	0.000255	0.030861
59342	SCPEP1	1196.295538	0.478	0.130639	0.000253	0.030861
57089	ENTPD7	391.9679173	0.532667	0.145848	0.00026	0.031226
8685	MARCO	535.2883966	2.576484	0.70937	0.000281	0.031385
114904	C1QTNF6	189.8862482	0.889486	0.245128	0.000285	0.031385
1368	CPM	886.7084237	0.739726	0.203536	0.000279	0.031385
11214	AKAP13	6303.945295	0.338091	0.092877	0.000272	0.031385
10921	RNPS1	1012.036306	-0.16959	0.046521	0.000267	0.031385
51222	ZNF219	186.2433482	-0.36032	0.099032	0.000274	0.031385
79007	DBNDD1	248.8072732	-0.39024	0.107414	0.00028	0.031385
3757	KCNH2	289.7502657	-0.5773	0.158908	0.00028	0.031385
23542	MAPK8IP2	253.6324494	-0.69246	0.190819	0.000285	0.031385

9363	RAB33A	76.79579553	-0.86168	0.236206	0.000264	0.031385
162494	RHBDL3	397.04649	-0.95185	0.261879	0.000278	0.031385
10690	FUT9	1111.737231	-1.03623	0.28554	0.000285	0.031385
51696	HECA	1206.177572	0.254234	0.070139	0.000289	0.031558
374875	HSD11B1L	155.8397076	-0.35897	0.09906	0.00029	0.031558
84892	POMGNT2	534.3183284	-0.39647	0.109508	0.000294	0.031737
5799	PTPRN2	575.3596982	-0.46404	0.129048	0.000323	0.034659
132720	FAM241A	76.4253114	0.88035	0.245329	0.000333	0.034731
22795	NID2	874.5732207	0.822026	0.228902	0.000329	0.034731
9695	EDEM1	1378.143463	0.459338	0.12798	0.000332	0.034731
155185	AMZ1	90.55429743	-0.70038	0.195173	0.000333	0.034731
4017	LOXL2	1457.428712	0.995069	0.277577	0.000337	0.034986
51393	TRPV2	314.0000926	0.668317	0.186517	0.000339	0.034987
1374	CPT1A	1281.279583	0.492052	0.137443	0.000344	0.035179
23040	MYT1L	219.6461449	-1.58061	0.441958	0.000348	0.035445
7402	UTRN	8581.245903	0.315511	0.088689	0.000374	0.037852
1284	COL4A2	11792.98347	0.860112	0.242032	0.00038	0.038159
2261	FGFR3	971.5925916	-0.73788	0.207961	0.000388	0.038734
10052	GJC1	1509.788124	0.453422	0.127883	0.000392	0.038853
57084	SLC17A6	62.45771606	-2.08441	0.588143	0.000394	0.038853
1E+08	WHAMMP1	332.1194823	0.488077	0.138238	0.000414	0.040369
4713	NDUFB7	564.652786	-0.42705	0.120918	0.000413	0.040369
4312	MMP1	333.0243407	2.357464	0.669073	0.000426	0.041023
10912	GADD45G	122.9919302	-1.2734	0.361557	0.000428	0.041023
114794	ELFN2	170.5098342	-1.57895	0.448354	0.000429	0.041023
4642	MYO1D	416.4996328	0.805727	0.23039	0.00047	0.043232
1075	CTSC	3371.493764	0.737876	0.210894	0.000467	0.043232
55614	KIF16B	690.9023115	0.338261	0.096565	0.00046	0.043232
5978	REST	1979.939898	0.336081	0.096128	0.000472	0.043232
23607	CD2AP	1148.566558	0.310308	0.088542	0.000457	0.043232
130612	TMEM198	185.5749796	-0.45957	0.131483	0.000474	0.043232
56967	C14orf132	2304.611287	-0.55489	0.158338	0.000458	0.043232
53826	FXYD6	1795.861564	-0.776	0.222009	0.000473	0.043232
8600	TNFSF11	17.21627915	1.563785	0.448565	0.00049	0.043657
3101	HK3	469.1411728	1.060946	0.303903	0.000481	0.043657
133584	EGFLAM	198.9539668	1.056084	0.303028	0.000492	0.043657
8038	ADAM12	1172.340227	0.752182	0.2158	0.000491	0.043657
23086	EXPH5	272.076768	-0.593	0.170044	0.000488	0.043657
5069	PAPPA	487.7788881	1.45492	0.417961	0.0005	0.043837
1306	COL15A1	500.8326701	1.293265	0.371434	0.000498	0.043837
4323	MMP14	4320.572043	0.607981	0.174775	0.000504	0.043837
3688	ITGB1	11064.35875	0.540154	0.155421	0.00051	0.043837
29965	CDIP1	575.7181599	-0.3303	0.095043	0.00051	0.043837
55228	PNMA8A	1059.662381	-0.52364	0.150668	0.00051	0.043837
23640	HSPBP1	306.095839	-0.28365	0.081887	0.000532	0.04548
79812	MMRN2	390.28342	0.577056	0.166768	0.00054	0.045616
83539	CHST9	431.0490011	-0.60842	0.175791	0.000538	0.045616
10882	C1QL1	281.9994608	-0.775	0.224379	0.000552	0.04644

9890	PLPPR4	779.0493132	-0.6626	0.192343	0.000571	0.047567
2066	ERBB4	707.39527	-0.98605	0.286254	0.000572	0.047567
1824	DSC2	431.3027964	0.806546	0.234836	0.000594	0.049132
284716	RIMKLA	240.5064459	-0.5165	0.150504	0.0006	0.049369
9211	LGI1	126.2127386	-0.86347	0.251749	0.000604	0.049465
55702	YJU2	270.6322614	-0.26324	0.076798	0.000609	0.049608

Supplementary Table 2: Differential expression results*. Differential gene expression between 'stiff' and 'soft' biopsies in 8 glioblastoma patients (22 biopsies). Only genes with an adjusted p-value (Benjamini and Hochberg method) below 0.05 are shown. Genes with higher expression in 'stiff' biopsies have log2foldchange>0, genes with higher expression in 'soft' biopsies have log2foldchange<0.*

References

1. Aran D, Hu Z, Butte AJ. xCell: digitally portraying the tissue cellular heterogeneity landscape. *Genome Biol.* 2017; 18(1):220.